Methods for Expanding the Diversity in the Response of Metal Oxide Based Gas Sensors

Dissertation

der Mathematisch-Naturwissenschaftlichen Fakultät

der Eberhard Karls Universität Tübingen

zur Erlangung des Grades eines

Doktors der Naturwissenschaften

(Dr. rer. nat.)

vorgelegt von

Anna Friederike Staerz

aus Denver, Colorado, Vereinigte Staaten von Amerika

Tübingen

2019

Gedruckt mit Genehmigung der Mathematisch-Naturwissenschaftlichen Fakultät der Eberhard Karls Universität Tübingen.

Tag der mündlichen Qualifikation: 28.04.2020
Dekan: Prof. Dr. Wolfgang Rosenstiel
1. Berichterstatter: Prof. Udo Weimar
2. Berichterstatter: Prof. Reinhold Fink
3. Berichterstatter: Prof. Elisabetta Comini

For Mieze

Table of Contents

List of Figures

List of Abbreviations

a.u.	Arbitrary Units
BF	Bright Field
CSNs	Core-Shell Nanofibers
DRIFT	Diffuse Reflectance Infrared Fourier Transform
FSP	Flame Spray Pyrolysis
HAADF	High-Angle Annular Dark-Field
HR-STEM	High Resolution-Scanning Transmission Electron Microscopy
HVAC	Heating, Ventilation, and Air Conditioning
LPG	Liquefied Petroleum Gas
MEMS	Micro-Electromechanical Systems
ppm	Parts per Million
RH	Relative Humidity
SEM	Scanning Electron Microscopy
SMOX	Semiconducting Metal Oxide
TEM	Transmission Electron Microscopy
TGS	Taguchi Gas Sensor
VOCs	Volatile Organic Compounds
XAS	X-ray Absorption Spectroscopy
XANES	X-ray Absorption Near Edge Structure
XRD	X-ray Diffraction

List of Symbols

$e\Delta V_s$	Band Bending
k	Boltzmann Constant
n_b	Concentration of Electrons in the Conduction Band
n_s	Concentration of Electrons in the Conduction Band at the Surface
R_0	Resistance in the Absence of a Target Gas
R_{gas}	Resistance in the Presence of a Target Gas
s	Sensor Signal
T	Temperature

List of Publications
Research Papers

1. **Staerz, A**., Kobald, A., Russ, T., Ewald, C., Weimar, U., Hémeryck, A., Barsan, N. (2020): Hydrogen Production from Humidity using WO_3, in process.

Conceptualization: Nicolae Barsan, Anne Hémeryck, and Udo Weimar, Formal Analysis and experiments: Anna Staerz, Arne Kobald, Tamara Russ and Carolin Ewald, Investigation: Anna Staerz, Writing-Original Draft Preparation: Anna Staerz, Writing-Review & Editing: Anna Staerz, Arne Kobald, Tamara Russ and Nicolae Barsan. Supervision: Udo Weimar and Nicolae Barsan.

2. **Staerz, A**., Somacescu, S., Epifani, M., Kida, T., Weimar, U., Barsan, N. (2020): WO_3 Based Gas Sensors: Identifying Inherent Qualities and Understanding the Sensing Mechanism, in publishing.

Conceptualization: Nicolae Barsan, and Udo Weimar, Formal Analysis and experiments: Anna Staerz, Mauro Epifani, Tetsuya Kida. Simona Somacescu, Investigation: Anna Staerz, Writing-Original Draft Preparation: Anna Staerz, Writing-Review & Editing: Anna Staerz, Mauro Epifani, Tetsuya Kida. Simona Somacescu and Nicolae Barsan. Supervision: Udo Weimar and Nicolae Barsan.

This paper is reprinted at the end of this thesis with permission. Copyright 2020, American Chemical Society.

3. **Staerz, A**., Bahri, M., Geyik, U., Brinkmann, H., Ersen, O., Weimar, U., Barsan N (2020), Direct Microscopic Proof of the Fermi Level Pinning Gas Sensing Mechanism, The Journal of Physical Chemistry Letters, (11) 166-171.

Conceptualization: Nicolae Barsan, Udo Weimar and Ovidiu Ersen, Formal Analysis and experiments: Anna Staerz, Mounib Bahri, Ugur Geyik, and Helena Brinkmann, Investigation: Anna Staerz, and Mounib Bahri, Writing-Original Draft Preparation: Anna Staerz, and Mounib Bahri, Writing-Review & Editing: Anna Staerz, and Nicolae Barsan, Supervision: Nicolae Barsan.

This paper is reprinted at the end of this thesis with permission. Copyright 2020, American Chemical Society.

4. **Staerz, A**., Gao, X., Cetmi, F., Weimar, U., Zhang, T., Barsan, N. (2020), The Dominant Role of Heterojunctions in Gas Sensing with Composite Materials, ACS Applied Materials & Interfaces, (12), 21127-21132.

Conceptualization: Nicolae Barsan, Tong Zhang and Udo Weimar, Formal Analysis and experiments: Anna Staerz, Faruk Cetmi, Gao Xing, and Zhang Ming, Investigation: Anna Staerz, and Faruk Cetmi, Writing-Original Draft Preparation: Anna Staerz, Writing-Review & Editing: Anna Staerz, and Nicolae Barsan, Supervision: Nicolae Barsan and Tong Zhang.

This paper is reprinted at the end of this thesis with permission. Copyright 2019, American Chemical Society.

5. **Staerz, A**., Liu, Y., Geyik, U., Brinkmann, H., Weimar, U., Zhang, T., Barsan, N. (2019): The effect of platinum loading on WO_3 based sensors. In: Sensors Actuators B Chemical. (291), 378-384.

Conceptualization: Nicolae Barsan, Tong Zhang and Udo Weimar, Formal Analysis and experiments: Anna Staerz, Yunshi Liu, and Ugur Geyik, Investigation: Anna Staerz and Ugur Geyik, Writing-Original Draft Preparation: Anna Staerz, Writing-Review & Editing: Anna Staerz, Yunshi Liu, Ugur Geyik, Tong Zhang and Nicolae Barsan. Supervision: Udo Weimar, Tong Zhang and Nicolae Barsan.

This paper is reprinted at the end of this thesis as allowed by Elsevier for authors of the original work.

6. **Staerz, A**., Boehme, I., Degler, D., Bahri, M., Doronkin, D., Zimina, A., Brinkmann, H., Hermann, S., Junker, B., Ersen, O., Grunwaldt, J.D., Weimar, U., Barsan N. (2018): Rhodium Oxide Surface Loaded Gas Sensors. In: Nanomaterials. (8), 892.

Anna Staerz and Inci Boehme contributed equally to this work. Conceptualization: Nicolae Barsan, Udo Weimar Ovidiu Ersen, and Jan-Dierk Grunwaldt, Formal Analysis and experiments: Anna Staerz, Inci Boehme, David Degler, Mounib Bahri, and Dmitry Doronkin, Investigation: Anna Staerz, Inci Boehme, David Degler, Mounib Bahri, Dmitry E. Doronkin, Anna Zimina, Helena Brinkmann, Sina Herrmann, and Benjamin Junker, Writing-Original Draft Preparation: Anna Staerz, Inci Boehme, David Degler, and Mounib Bahri, Writing-Review & Editing: Anna Staerz, David Degler, Jan-Dierk Grunwaldt and Nicolae Barsan, Supervision: Nicolae Barsan.

This paper is reprinted at the end of this thesis as allowed by MDPI.

7. **Staerz, A**., Kim, T.H., Lee, J.H., Weimar, U., Barsan, N. (2017): Nano-Level Control of Gas Sensing Characteristics via P-N Heterojunction between Rh_2O_3 Clusters and WO_3 Crystallites. In: Journal of Physical Chemistry C. 121 (44), 24701-24706.

Conceptualization: Nicolae Barsan, Udo Weimar and Jong Heun Lee, Formal Analysis and experiments: Anna Staerz, and Tae Hyung Kim, Investigation: Anna Staerz, and Tae Hyung Kim, Writing-Original Draft Preparation: Anna Staerz, Writing-Review & Editing: Anna Staerz, Jong Heun Lee and Nicolae Barsan, Supervision: Nicolae Barsan.

This paper is reprinted at the end of this thesis with permission. Copyright 2017, American Chemical Society.

8. **Staerz, A**., Berthold, C., Russ, T., Wicker, S., Weimar, U., Barsan, N. (2016): The Oxidizing Effect of Humidity on WO_3 Based Sensors. In: Sensors Actuators B Chemical. (237), 54-58.

Conceptualization: Nicolae Barsan, and Udo Weimar, Formal Analysis and experiments: Anna Staerz, Christoph Berthold, Tamara Russ and Susanne Wicker, Investigation: Anna Staerz, Writing-Original Draft Preparation: Anna Staerz, Writing-Review & Editing: Anna Staerz, Tamara Russ, Susanne Wicker, and Nicolae Barsan. Supervision: Udo Weimar and Nicolae Barsan.

This paper is reprinted at the end of this thesis as allowed by Elsevier for authors of the original work.

Review Papers and Book Chapters

1. **Staerz, A.,** Roeck, F., Weimar, U., Barsan N. (2019): Electronic Nose: Current Status and Future Trends. In: Surface and Interface Science Volume 9: Applications, Eds. Wandelt, K. (Wiley).
2. **Staerz, A.,** Suzuki, T., Weimar, U., Barsan N. (2019): SnO_2 as a Gas Sensor. In: Tin Oxide Materials: Synthesis, Properties and Applications, Eds. Orlandi, M. (Elsevier).
3. Izawa, K., Ulmer, H., **Staerz, A.**, Weimar, U., Barsan N. (2018): Application of SMOX Based Sensors. In: Gas Sensors Based on Conducting Metal Oxides (1st), Eds. Barsan, N., Schierbaum, K. (Elsevier).
4. **Staerz, A**., Weimar, U., Barsan, N. (2016): Understanding the Potential of WO_3 Based Sensors for Breath Analysis. In: Sensors, 16 (11).

Conference Proceedings

1. **Staerz, A**, Weimar, U., Barsan, N., (2019): Gold Beladene WO_3 –Sensoren, AMA Science Proceedings of the 14. Dresdner Sensor-Symposium at Dresden Germany, December 2019.
2. **Staerz, A**, Russ, T., Weimar, U., Barsan, N. (2019): Understanding the Sensing Mechanism of WO_3 based Gas Sensors. Proceedings of the 18th International Symposium on Olfaction and Electronic Nose, Fukuoka, Japan, May 2019, 256-258.
3. **Staerz, A**, Somacescu, S., Epifani, M., Russ, T., Weimar, U., Barsan N. (2019): WO_3 Based Gas Sensors. Proceedings of Eurosensors Conference, Graz, Austria, September 2018, 826.
4. Boehme, I., Herrmann, S., **Staerz, A**., Brinkmann, H., Weimar, U., Barsan, N. (2018): Understanding the Sensing Mechanism of Rh_2O_3 loaded In_2O_3. Proceedings of Eurosensors Conference, Graz, Austria, September 2018, 821.
5. Suzuki, T., Lauxmann, R., Sackmann, A., **Staerz**, **A.,** Weimar, W., Berthold, C., Barsan, N. (2018): Operando Investigations of Rare-Earth Oxycarbonate CO_2 Sensors. Proceedings of Eurosensors Conference, Graz, Austria, September 2018, 80.
6. **Staerz, A**., Geyik, U., Brinkmann, H., Weimar, U., Barsan, N., Sensing with Noble Metal Oxide Loaded WO_3. (2018): AMA Science Proceedings of the 17th International Meeting on Chemical at Vienna, Austria, July 2018, 68-69.
7. Suzuki, T., Sackmann, A., **Staerz, A**., Weimar, U., Barsan, N. (2018): Crystal Structure and CO_2 Sensing Properties of Rare-earth oxycarbonates. AMA Science Proceedings of the 17th International Meeting on Chemical Sensors at Vienna, Austria, July 2018, 541-542.
8. **Staerz, A.**, Weimar, U., Barsan, N. (2017): The Fundamental Characteristics of WO_3. Proceedings of the 12th Asian Conference on Chemical Sensors at Hanoi, Vietnam, November 2017, 94.
9. Arndt, G., Suchy, S., Vialkowitsch, D., **Staerz, A**., Oprea, A., Weimar, U., Rosenstiel, W. (2017): Multi-criteria/multi-sensor early fire detection in the engine compartment of road vehicles: Evaluation process of gas sensors. Proceedings of the 16th International Conference on Automatic Fire Detection at MD, USA, September 2017.
10. **Staerz, A**., Epifani, M., Barsan, N., Weimar, U. (2016): Surface reactions effect on selectivity of WO_3 based Sensors. Proceedings of I*SOCS-MINAB*-ICT at Otranto, Italy, June 2016.
11. **Staerz, A**, Wicker, S., Barsan, N., Weimar, U. (2015): Eine systematische Untersuchung von der Wechselwirkung zwischen Wolframtrioxid Gassensoren und Luftfeuchtigkeit. AMA Science Proceedings of the 12. Dresdner Sensor-Symposium at Dresden Germany, December 2015, 307-310.

Awards

FY2019 JSPS Doctoral Fellowship, Three Month Research Stay in Kumamoto, Japan

Best Speaker Award 12th Asian Conference on Chemical Sensors 2017

Abstract English

As all aspects of life become more automated and interconnected, sensors will be needed in various applications. In particular, gas sensors will find widespread use, in e.g. indoor air quality monitoring and breath analysis. Versus other detection methods, semiconducting metal oxide (SMOX) based sensors are more compact, sensitive, robust and inexpensive. Their major drawback is their inherent lack of selectivity. This limitation could be addressed by using arrays of SMOX materials with complementary sensing behavior. Today as a result of the historical development, despite the decades of research, most commercially available sensors are still based on SnO_2. The work here examines three different options for creating complementary sensors: using a different *n*-type base metal oxide (WO_3), noble surface loading and the creation of metal-oxide-metal-oxide mixtures. Based on a literature review, WO_3 appeared promising and here its complementarity was verified. It was identified that the sensing behavior of WO_3 is robust against changes in synthesis. Using operando diffuse reflectance infrared Fourier transform (DRIFT) spectroscopy, it was possible to identify why the resistance of WO_3 increases with humidity. From this finding it became apparent why the response to oxidizing gases strongly decreases in the presence of atmospheric humidity. In order to tune the sensing behavior, surface loading with metal oxides is commonly used. Although two mechanisms, chemical sensitization and Fermi level pinning, were already suggested in the 1980s, experimental evidence was limited. Here, the effect of rhodium, palladium and platinum loading on WO_3 was examined. Using operando DRIFT spectroscopy, in situ transmission electron microscopy (TEM) and X-ray absorption spectroscopy (XAS) it was shown that the Fermi level pinning mechanism dominates. As a result, Rh-loading reduces the complementarity of WO_3 and SnO_2 based sensors. Finally, sensors based on SnO_2 and Cr_2O_3 mixtures were examined. Reports of gas sensors based on combinations of metal oxides, in particular mixtures of *n*- and *p*-type materials, are common in literature. These mixed materials are usually created using sophisticated and expensive methods, like the electrospinning of nanofibers. Here sensors based on nanofibers were compared to those based on randomly dispersed particles. By breaking apart the nanofibers using soft mechanical grinding, it was possible, for the first time, to clearly separate the effects of the secondary structure from the coupling between the materials. It was identified that the junctions between the materials are largely responsible for the changed sensing. Furthermore, it was shown that by varying the ratio of the metal oxides, the sensor response can be tuned, i.e. shows a *p*- or *n*- type response, and in some cases no response. In total it has been shown that other *n*-type materials should be considered for integration into arrays with SnO_2. It has been found that the applicability of noble metal oxide surface loadings to increase the complementarity of materials is limited. It has been shown that metal-oxide-metal-oxide mixtures can be used to tune the sensing behavior and that the mechanical mixing of materials is a sufficient preparation method to attain the desired results.

Zusammenfassung Deutsch

In Zeiten der zunehmenden digitalen Vernetzung und Automatisierung von unterschiedlichen Anwendungen im Lebensalltag werden Sensoren immer wichtiger. Insbesondere Gassensoren können für eine Vielzahl von Anwendungen eingesetzt werden, bspw. für die Raumluftüberwachung oder in der Atemgasanalyse. Hierbei sind auf metalloxidische Halbleiter (SMOX) basierende Gassensoren besonders interessant, da sie im Vergleich zu anderen Detektionsmethoden sehr robust, kompakt, kostengünstig und sensitiv sind. Ein Nachtteil dieser Sensoren liegt in ihrer geringen Selektivität. Durch die Integration von unterschiedlichen und komplementären Sensoren in Arrays, können Gase jedoch selektiv detektiert werden. Heutzutage basieren die meisten Gassensoren immer noch auf Zinnoxid, obwohl auch andere Basismaterialien seit Jahrzehnten erforscht werden. Diese Arbeit untersucht drei verschiedene Möglichkeiten, komplementäre Sensoren zu SnO_2 herzustellen: WO_3 als Grundmaterial (ein weiterer *n*-typ Halbleiter), Oberflächenbeladung mit Edelmetall-Nanocluster und die Benutzung von Metalloxidmischungen. Für WO_3 konnte die Komplementarität zu SnO_2 bestätigt werden. Zudem wurde entdeckt, dass unterschiedliche Herstellungsmethoden die Sensoreigenschaften kaum beeinflussen. Mit operando diffuse Reflexions-Fouriertransformationsinfrarotspektroskopie (DRIFT) konnte gezeigt werden, warum der Widerstand von WO_3 mit Feuchtigkeit zunimmt und weshalb das Signal zu oxidierenden Gasen abnimmt. Sensoreigenschaften können auch durch Edelmetall-Nanocluster verändert werden. Schon in den 80-iger Jahren wurden hierfür zwei Erklärungen vorgeschlagen, Ferminiveau-Pinning und Chemische Aktivierung. Bisher gab es jedoch keinen experimentellen Nachweis dafür. Hier konnte mit DRIFT-Spektroskopie, in situ Transmissionselektronenmikroskopie (TEM) und Röntgenabsorptionsspektroskopie (XAS) erstmals gezeigt werden, dass im Falle von Oberflächenbeladung mit Rhodium, Palladium und Platin der Ferminiveau-Pinning Mechanismus dominiert. Dadurch konnte auch erklärt werden, warum eine Oberflächenbeladung mit Rhodium die Komplementarität von WO_3 und SnO_2 zueinander verringert. Zuletzt wurden Sensoren basierend auf Mischungen aus Cr_2O_3 und SnO_2, ein *n*- und ein *p*-typ Halbleiter, untersucht, welche gemäß bisheriger Studien günstige Eigenschaften aufweisen sollten. Zumeist werden durch komplexe und teure Herstellungsmethoden, bspw. Elektrospinnen für Nanofasern, die Proben für die Sensoren bereitgestellt. In der vorliegenden Arbeit wurden auf Nanofaser basierende Sensoren mit Proben verglichen, in denen eine zufällige Verteilung der oxidischen Partikel herrscht. Durch eine sanfte Zerlegung der Nanofasern konnte gezeigt werden, dass die Kontakte zwischen den Oxiden hauptverantwortlich für die Änderung der Sensoreigenschaften sind und dass die Fasermorphologie keine dominante Rolle spielt. Zusammenfassend konnte gezeigt werden, dass WO_3 ein komplementäres Verhalten zu SnO_2 aufweist, die Oberflächenbeladung mit den Edelmetallen Rh, Pd und Pt nicht nützlich für die Diversifizierung der Eigenschaften ist und das die einfache Vermischung von Metalloxide eine ausreichende Methode ist um das erwünschte Verhalten zu erreichen.

Introduction and Background Information

History

In 1962, Seiyama et al. from Kyushu University in Japan reported that the resistance change of a metal oxide (ZnO) could be used to detect changes in the surrounding atmosphere [1]. At the same time a second inventor, Naoyoshi Taguchi filed a patent for a sensor based on SnO_2 activated with palladium oxide [2,3]. In the 1960s, the use of liquefied petroleum gas (LPG) for cooking had become popular in Japan, and as a result, the number of domestic gas explosions skyrocketed. In 1968, Taguchi founded the company Figaro Engineering Inc. (Japan) and began to sell the Taguchi Gas Sensor (TGS) 109 manufactured for residential gas alarms. The gas alarms, using TGS109 were inexpensive, costing roughly one-third as much as the predecessor which was based on catalytic-type sensors [4]. Detection systems became widespread resulting in a drastic decrease of domestic gas explosions [4].
In the 1980s, there was renewed interest in SMOX based sensors as a method with which the air intake into the car passenger cabin could be monitored. Car exhaust contains toxic gases like CO, NO_x and various other hydrocarbons [5]. The concentrations are usually given in the volume mass ratio of the target gas to air in parts per million (ppm). Values between 30 and 100 ppm (ca. 0.035 – 0,116 mg/L) for CO and 2 to 10 ppm (0.003-0.019 mg/L) for NO_2 are relevant for outdoor air monitoring [6]. These concentrations can be easily monitored using SMOX based sensors. In order to ensure the comfort of the passengers, especially as the number of cars increased and people spent more time waiting in traffic, an automatic ventilation system was desired [7]. The packaging of the sensor needed to address several challenges [7]: the extremely harsh sensing environment due to the presence of water and dust, the extreme variations in temperature (-40 °C to 125 °C), and the continuous vibration of the motor [7]. In addition, in order to be viable for the automotive industry, the sensor cost had to be reduced. Standardized high-volume manufacturing processes were developed [7]. In 1986, the first control unit based on a single Figaro sensor, developed for gasoline powered BMWs, was sold [8]. Shortly after the Robert Bosch GmbH (Germany) developed a two sensor array which could also detect NO_x, making it useful for diesel exhaust gases [8]. In the 1990s, in order to meet the increasing demand, thick film layers were first coupled with

microelectromechanical system (MEMS) substrates [8]. Today, this is the standard sensor production method [8–10]. [1]

Motivation

As the world becomes more interconnected and automated, sensors will be widely needed. In 2018, the global gas sensor market was valued at over USD 2 billion, and the market is projected to continue growing [11]. Research is being done on the use of gas sensors for a wide array of applications, ranging from indoor air quality monitoring to breath analysis [12–16], see Figure 1.

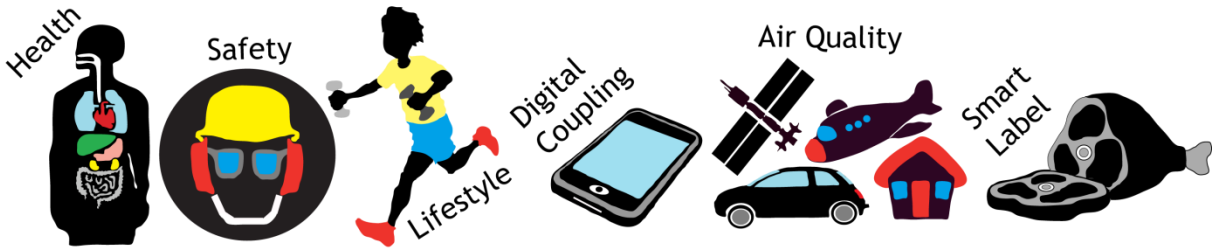

Figure 1: Possible application fields for SMOX based gas sensors.

SMOX based sensors are a robust, sensitive, inexpensive and compact alternative to other gas detection methods [3,17]. Specifically, SMOX based sensors can be used in battery operated devices [17]. This simplifies the installation of sensor networks, for example for automated heating, ventilation, and air conditioning (HVAC) control [11]. For this application, monitoring volatile organic compounds (VOCs), which can be released as a gas into indoor air at room temperatures is particularly interesting. VOCs encompass a variety of chemical compound groups, e.g. ketones, alcohols, and aromatics. Governments in developed regions, such as North America and Europe, have issued guidelines about the indoor concentrations of such harmful contaminants [18,19]. For example, the Canadian government, set a short-term indoor air exposure limit of the aromatic compound toluene at 4 ppm (0,015 mg/L) [19]. Ethanol is another common indoor contaminant that originates from human activities.

VOCs are also relevant in other applications. For example, the detection of acetone in breath is interesting as a means for diabetes monitoring [20] or in order to monitor diet changes [21,22]. An acetone concentration between 0.5 and 2 ppm (0.001-0.004 mg/L) is relevant [20].

[1] For a more detailed history of gas sensors please see the book chapter by Izawa et al. [16].

Currently, however, the low selectivity of SMOX based sensors is a significant limitation for most of these applications. The use of sensor arrays (i.e. the simultaneous use of two or more sensors) is now a promising solution to this issue because miniaturization is possible and computation power is readily available [12,23]. Over the last decades, however, most research has continued to concentrate on SnO_2 [24]. As a result, most commercially available sensors are still based on this material [16]. Although the sensing characteristics of SnO_2 can be tuned using different preparation methods and additives, overall, the use of a single base material significantly limits the variability of the sensors. In the future, a higher diversity in the sensor behavior of the materials will be needed. The presented work examines three different options for creating SMOX materials complementary to SnO_2. Based on a literature review, WO_3 appeared to be a promising base material. Here, the complementarity is verified and it is examined if the preparation method of WO_3 significantly changes its sensing behavior. Another way in which the sensing behavior of metal oxides can be tuned is through surface additives. Specifically noble metals are widely used. Here, the effect of rhodium and platinum loading on WO_3 was examined. The results of surface loading WO_3 with rhodium are compared to those achieved with loaded SnO_2. Using operando diffuse reflectance infrared Fourier transform (DRIFT) spectroscopy, in situ transmission electron microscopy TEM and X-ray absorption spectroscopy (XAS), the mechanism responsible for the change in sensor response is identified. Finally, the applicability of preparing metal-oxide-metal-oxide mixtures to create desirable sensing behavior is examined. The response of sensors based on SnO_2-Cr_2O_3 nanofibers will be compared to samples without a secondary structure. By using a soft mechanical grinding to destroy the secondary fiber structure to create randomly dispersed samples, it is possible to rule out variations in the samples as a result of the synthesis method. This examination allows changes in sensing behavior of the oxide mixtures compared to the pure materials to be attributed to the secondary structure, contacts between the materials or a combination of both.

In total, this work explores three possibilities to create sensors that are complementary to those based on SnO_2. The results of the work are highly relevant for the future use of SMOX based sensors.

General Operation Principle

Variations in the surrounding atmosphere result in a change of the gas sensitive material which is translated into a detectable output [25]. In the case of SMOX based sensors, the presence of a target gas in the atmosphere results in a resistance change [26,27]. In the work here, the metal oxide powder and 1,2- propanediol (Sigma-Aldrich, 99.5+% ACS reagent) was ground with mortar and pestle into a viscous paste. The paste was then screen-printed onto an inert Al_2O_3 substrate containing platinum electrodes and a backside platinum heater (300 µm electrode gap, 300 µm width and 5 µm thickness; Ceramtec AG, Germany) using an EKRA Microtronic II. The sensors were left at room temperature for 1 h and then dried overnight at 80 °C (Heraeus UT12). The sensors were annealed for 10 min each at 400−500−400 °C with two steps to cool down in a tube furnace (Heraeus ROK 6/30). A layer thickness of approximately 50 µm, is attained (see Figure 2). As such, the sensing layer is considered to be a thick film [28].

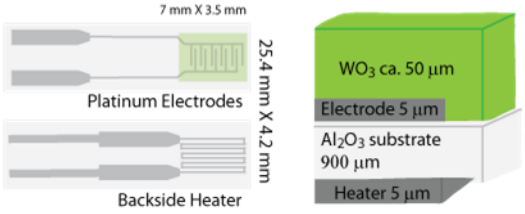

Figure 2: Schematic of screen printed SMOX based gas sensors.

In the used porous thick film layers, the gas can interact at different sites on the sensor, e.g. with the grain surface, the substrate and the electrodes [29]. The influence of the chemically inert substrate (alumina) is considered negligible [30]. The platinum electrons can, however, have significant catalytic effects. In the work here, the electrodes are always made of platinum and the effect is not examined further.

Here, both *n*-type materials, e.g. WO_3 and SnO_2, and *p*-type materials, e.g. Cr_2O_3, were examined. In *n*-type semiconductors, the major charge carriers are electrons while for *p*-type semiconductors, they are holes [31]. The reaction of the atmospheric gases with the surface of the metal oxide grains is the reception mechanism of the sensor. The translation of this reaction into an electronic change is the transduction mechanism.

It is assumed that the sensitive layer is made up of loosely sintered monocrystalline grains which are larger than the Debye length [32]. In air, between 100 and 500 °C, atmospheric oxygen adsorbs onto the surface, leaving the bulk largely unaffected [29]. This results in a resistive electron depletion surface layer for *n*-type materials

and correspondingly a hole accumulation layer for *p*-type materials. It is, thus, generally accepted that under standard operation conditions the conduction of *n*-type sensors is depletion layer controlled while for *p*-type an accumulation layer control dominates.

In order for the electrons to take part in the conduction process of *n*-type materials, they must pass between the grains and go over the surface energy barrier caused by the adsorbed oxygen [33]. In the equivalent circuits of *n*-type gas sensors, the resistance of the grain boundaries and the bulk resistance are considered to be in series to one another. If the electrode gap is large enough, the resistance originating from the junction between the platinum electrode and *n*-type metal oxide is considered negligible because it is in series with a large number of resistances (the grain to grain boundaries and the bulk resistance) [30]. As a result of the reaction between the surface oxygen and reducing gases, electrons are released back into the material decreasing the energy barrier between the grains [29]. It is assumed that the Boltzmann distribution accurately describes the relationship between the electron concentration that can reach the surface $n_{s,}$ and the band bending $e\Delta V_s$ [32]:

$$n_{\mathrm{s}} = n_{\mathrm{b}} \exp\left(-\frac{eV_{\mathrm{s}}}{kT}\right). \qquad \text{Eq. 1}$$

Then, the relative change of the band bending under gas exposure can be directly calculated as follows from the changes in the resistance [32]:

$$\frac{R_0}{R_{\mathrm{gas}}} = \exp\left(\frac{e\Delta V_{\mathrm{s}}}{kT}\right). \qquad \text{Eq. 2}$$

In the case of a sensor based on a *p*-type material, the resistance of the narrow accumulation layer on the grain surface (as a result of oxygen adsorption) is parallel to that of the large highly resistive bulk region [24,33,34]. The electrons injected into the material as a result of the reaction between the reducing gas and the surface oxygen then decrease the concentration of holes in the accumulation layer resulting in a higher sensor resistance. In the case of large grains, the contribution of the bulk cannot be neglected. A major difference between n-type and p-type SMOX results from the depletion versus accumulation layer transduction. In an accumulation layer, the relative change of the band bending under gas exposure can be directly calculated as follows from the changes in the resistance [33]:

$$\frac{R_0}{R_{gas}} = \exp\left(\frac{e\Delta V_s}{2kT}\right). \qquad \text{Eq. 3}$$

Therefore, the sensor response of a *p*-type material (dominant accumulation layer controlled transduction) is equal to the square root of that of an *n*-type based gas

sensor (dominant depletion layer controlled transduction) with identical morphology [34]. Pokhrel et al. additionally found that unlike for *n*-type materials the resistance corresponding to the junction between the metal oxide grains and the electrodes is not negligible for the *p*-type material Cr_2O_3 [35]. However, this resistance is not affected by the atmospheric gas. This explains the low sensor signal of the *p*-type material in comparison to the *n*-type materials.

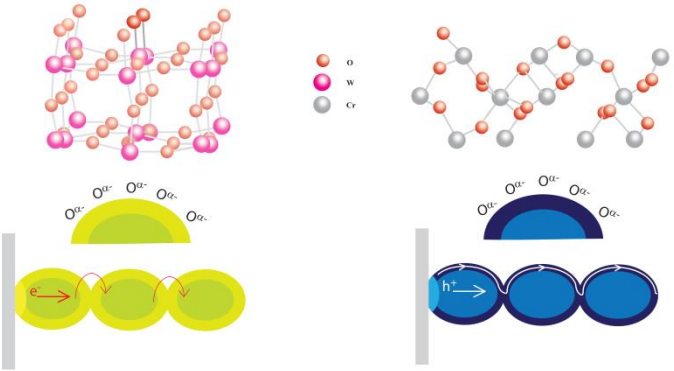

Figure 3: Schematic representation of the sensitive layer and contacts between the WO_3 (left)/ Cr_2O_3 (right) grains and the electrode.

The response of SMOX based gas sensors is a complex interplay between their reception and transduction mechanisms, see a schematic representation in Figure 3. Both aspects must be considered when interpreting the results. More information about WO_3, SnO_2, and Cr_2O_3 will be presented in the following sections.

Tin Oxide Based Sensors

Today, most commercially available gas sensors are based on SnO_2 [16]. There is a large amount of research on SnO_2 based gas sensors. Comprehensive reviews on the material characteristics have been published by Batzill and Diebold [36], and about the sensor response by Das and Jayaraman and Barsan et al. [37,38]. In addition to a general overview of reception and transduction mechanisms, the reviews by Barsan et al. give a great deal of specific information about SnO_2 sensors [39,40]. In their review, Das and Jayaraman concentrated on the analyte gases LPG, NH_3, ethanol, CO, H_2, and NO_2 [38]. Unsurprisingly, noble metal loaded SnO_2 is suited for the detection of LPG [38,41]. This explains why the first commercially available gas sensor developed by Taguchi was based on palladium loaded SnO_2 [2,3]. In order to understand why the material is so well suited for sensing, and in order to identify methods for further optimization, surface science techniques were applied [42,43].

The results, however, were obtained far from realistic conditions, resulting in differences caused by variation in material state, pressure and temperature [44,45]. The necessity of studying SMOX based sensors under realistic operation conditions became apparent [46]. Following earlier powder measurements [47] and emission spectroscopy [48], in 2003, Harbeck et al. first used operando DRIFT spectroscopy on SnO_2 based sensors activated with Pd [49]. This method allows the surface reactions of SMOX that result in the sensor response to be identified. A reflectance spectrum is taken under gas exposure and then referenced to a spectrum taken in standard atmosphere, e.g. dry synthetic air. During the infrared measurements, the sensors are heated and the resistance changes are measured [50]. Ideally, the intensity of the bands visible in the DRIFT spectra should be linear with the adsorbate surface concentration. This calculation is not trivial and the Kubelka-Munk theory is poorly suited as many of the required conditions are not met by the porous layers of the sensors, e.g. matrix absorption [51]. Olinger and Griffiths propose that in the case of absorbing matrices, the best linear representation of the concentration is given by log (1/R) [52]. This method is successfully applied to calculate the operando DRIFT spectra taken of the sensors [52,53].

Most research on the sensor mechanism of SnO_2 and the effect of humidity has been done using the chemically simple gas CO. Wicker et al. examined two different SnO_2 samples: for the sample calcined at 1000 °C, the presence of humidity drastically decreased the baseline resistance, while for commercially available powder (from Sigma Aldrich, calcined to 500°C) the response was negligible. The authors attribute the decrease in resistance of the highly calcined sample to the mechanisms suggested by Heiland and Kohl: the dissociation of water and subsequent reaction with surface lattice oxygen to form either two terminal hydroxyl groups or a terminal and rooted hydroxyl group [54–56]. The authors postulate a charge neutral reaction for the commercial powder in which water fills a vacancy and reacts with a surface lattice oxygen to form two rooted hydroxyl groups [56]. CO reacts with the surface lattice oxygen of SnO_2 to form CO_2 [57]. In both cases, CO competes with humidity for oxygen vacancies, resulting in the decreased sensor response [56]. Unlike the other reducing gases, the sensor response of SnO_2 to ethanol, however, is generally found to increase in the presence of humidity [38,58]. It has been postulated that the adsorption of the ethanol molecules is enhanced by a hydroxylated surface due to hydrogen bonding [58].

In addition to operando DRIFT spectroscopy, operando XAS spectroscopy is a powerful tool for monitoring material structural properties [45,59]. In 2009, Koziej et al. first studied sensors based on SnO_2 loaded with palladium using operando XAS [59]. This method is particularly well suited to identify changes in the small nanocluster surface loadings. Recently, Degler et al. were able to identify the dominant Fermi level pinning mechanism using operando DRIFT spectroscopy coupled with operando XAS for platinum loaded SnO_2 [60].

During the decades of research on SnO_2, many sophisticated measurement methods were developed from which insight into the sensing mechanisms can be attained [61,62]. More recently, these methods have been applied to different metal oxides, e.g. WO_3.[2]

Tungsten Trioxide Based Sensors

Although less popular than SnO_2, there is literature examining gas sensing with the *n*-type semiconductor WO_3. Most of the studies, however, examine only how the sensor response of the material can be altered through changes in the crystal structure [63–65], morphology [66–69] and through surface dopants [70–72]. In literature, there are few examinations of differently prepared WO_3 samples from which sensing characteristics inherent to the material can be identified. This becomes apparent in the review of WO_3 by Long et al. [65]. Here, very often the authors are unable to identify sensor responses of pure WO_3 and instead report largely on loaded samples [65]. The limited studies that identify inherent material properties and examine which surface reactions are responsible for the sensor response will be reviewed here.

In 2009, Pokhrel et al. examined the sensor response of three differently prepared WO_3 samples to CO and NO_2 in dry air and humidity [73]. Of the three, only the sample prepared using hexadecyltrimethylammoniumbromide in acetylacetone responded well to CO in dry air [73]. Huebner et al. examined the interaction between this sample and CO using operando DRIFT spectroscopy [53]. The WO_3 sensor operated at 300 °C was exposed to CO in both the presence and the absence of atmospheric oxygen. In both cases, CO_2 was detected in the exhaust (gas leaving the measurement chamber) [53]. In the simultaneously measured DRIFT spectra, in both cases, there was a visible decrease of bands attributed to tungsten-oxygen

[2] For a comprehensive review of SnO_2 in general and specific information to its application as a gas sensor please see the chapter by Staerz et al.[130]

bonds, 2065 and 1858 cm^{-1} [53,74,75]. This led the authors to postulate that CO reduces the surface of WO_3, which results in the detected decrease in resistance [53].

The sensitivity of WO_3 to NO_2 at 300 °C was first reported by Akiyama et al. in 1991 [76]. It has also been found that WO_3 sphere structures or nanolamellae respond well to NO_2 [77,78]. All three of the differently prepared samples examined by Pokhrel et al. showed high sensor signals to NO_2 in dry air [73]. Similar results were attained by Baumann who further examined WO_3 samples using impedance spectroscopy [79]. He suggested a major and a minor mechanism for the interaction between the WO_3-surface and NO_2 [79]. The major reaction is the adsorption of NO_2 via one of the oxygen atoms to form a nitrite. The minor reaction is the subsequent oxidation of the WO_3 surface and the release of NO [79]. Akamatsu et al. investigated the interaction between WO_3 and NO_2 using DRIFT spectroscopy done on powder samples [80]. Their work supports the mechanisms suggested by Baumann. The WO_3 sample was exposed to 1 ppm of NO_2. In the DRIFT spectra, the bands attributed to tungsten-oxygen bonds are increasing [74,75,80]. In addition, a nondescript band visible around 1400 cm^{-1} was found to increase during exposure to NO_2 [81]. The vibration of surface nitrites is expected in this region, but no additional measurements were done to conclusively identify the origin of the band [81]. The work of Bauman and Akamatsu et al. does not examine the effect of humidity. In all of the samples examined by Pokhrel et al., the response of the samples to NO_2 significantly decreases in the presence of humidity. A similar behavior is also known for the other oxidizing gas, ozone [82]. In all of the samples examined by Pokhrel et al. humidity exposure, also, resulted in an increase of the resistance [73].

There is also a large body of literature which examines the response of WO_3 to VOCs. There are reports that the ε-phase (stabilized using either chrome or silicon) responds particularly well to acetone [63,83]. It has been found that microtubes (unintentionally carbon doped) respond better than commercial WO_3 to toluene [84]. In all cases, only a limited number of WO_3 samples (maximum two) were considered and information about the surface reaction responsible for the signal is missing.

From this brief literature review, WO_3 appears to be a complementary material for application in arrays with SnO_2.

Chromium Sesquioxide Based Sensors

p-type oxide semiconductors like Cr_2O_3, have received significantly less attention than their n-type counterparts [24]. Cr_2O_3 has been used for the detection of H_2, toluene, and NO_2 [85,86]. It is considered that the adsorbed oxygen on the Cr_2O_3 surface act as an acceptor and its interaction with the valence band determines the generation of holes [87]. This theory was supported by the simultaneously performed work function and resistance change measurements by Pokhrel et al. [35]. In general, it is considered that the exposure of a metal oxide to a reducing gas, i.e. ethanol decreases the concentration of the ionosorbed oxygen. The electrons go back into the valence band and decrease the concentration of holes [35]. Overall, however, the sensor response to ethanol was low due to the large influence of the gas insensitive resistive component of the metal oxide and electrode junction [35]. In order to make them relevant for practical applications, the sensor response for p-type semiconductors must be enhanced [24].

The combination of Cr_2O_3 with SnO_2 seems to be a promising option to enhance the sensor response. The creation of core-shell nanofibers (CSNs) containing SnO_2 and Cr_2O_3 is reported to result in high responding *p*-type sensors for acetylene [88]. The addition of SnO_2 to Cr_2O_3 increased the sensors response to ethanol [89]. On the other hand, SnO_2-Cr_2O_3 CSNs showed an increased n-type response to trimethylamine [90]. A systematic study is needed to understand when the sensor responds as *p*-type or n-type. In addition, the role of the secondary structure should be examined.

Mixed Materials

In order to increase the stability and tune the response, noble metals are usually added to the sensitive layer of commercially available SMOX based sensors [3]. For a general review, please see the work of Degler et al. [91]. Palladium was already added to the first commercially available gas sensor based on SnO_2 [2,3]. There is a great deal of existing work which describes variation in the sensing behavior of SnO_2 and WO_3 as a result of noble metal surface additives, e.g. rhodium [72], platinum [92–94], palladium [95,96], and gold [95,96].

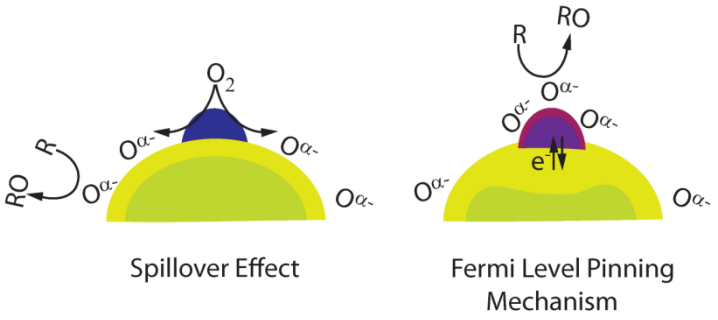

Figure 4: (left) Schematic of the spillover effect, in which the reaction between the base metal oxide and the analyte gas is enhanced by the presence of the noble metal surface additive. (right) Schematic of the Fermi level pinning mechanism, in which the analyte gas reacts with the noble metal surface clusters resulting in a change of the electronic coupling between the materials.

Two possible interaction mechanisms were postulated by Morrison et al. and Yamazoe et al. in the 1980s: Spillover and Fermi level control, see Figure 4 [97–99]. In the case of a spillover effect, the additive activates the reaction of the metal oxide surface with the target gas. This increases the sensor response but effectively leaves the mechanism the same. In the case of the Fermi level pinning mechanism, the additive and the metal oxide are electronically coupled. The reaction takes place on the additive, changing its oxidation state. This, in turn results in an electronic change of the base metal oxide, which results in the sensor response [97–99]. Most work attributes the change in sensing behavior to one of the mechanisms with little or no experimental evidence. Knowing which of these mechanisms dominates for which combination of material is, however, a prerequisite for the intentional development of sensors.

In addition to surface loading, variation in sensing behavior can also be attained by combining nanoparticles of two or more different metal oxides. Due to their inverse sensing behavior (the resistance of *n*-type materials decrease in the presence of reducing gases while that of a *p*-type increases), it would be advantageous to incorporate materials of each category into arrays. The chemiresistive variation of *p*-type materials, however, is significantly lower than that of *n*-type semiconductors [24]. One way in which the *p*-type sensing qualities can be enhanced is through combination with *n*-type metal oxides [90].

In their review, Korotcenkov at al. list three possible methods of attaining metal-oxide-metal-oxide mixtures [100]. They can be formed using layer by layer deposition of the materials. They can be simply attained by mixing together already-synthesized materials in certain proportions. They can be directly prepared during the process of either synthesis or deposition of the initial material [100]. In this work, only the second

two methods will be considered further. Korotcenkov at al. specifically identify electrospinning as a promising method for the preparation of metal-oxide-metal-oxide materials [100]. It ensures the formation of metal oxide nanofibers with minimal grain size and maximal porosity of the gas sensing matrix [100]. Electrospinning is particularly well-suited for the preparation of CSNs [101]. In general, CSNs consist of an inner layer of nanoparticles encapsulated by a different material [102]. It is important to note that the nanofibers are polycrystalline. Gas sensors based on CSNs are reported to show a large number of advantages over pure nanofibers [103]. However, in their review Korotcenkov at al. conclude that the sensing mechanism with metal-oxide-metal-oxide mixtures is not known [100]. In most cases the explanations are solely based on speculations [100]. Specifically, the role of the secondary structure (e.g. nanofibers) remains unclear. In their review, Ding et al. conclude that nanofiber-based sensors show much higher sensitivity and quicker responses to target gases in comparison to sensors based on flat films [104]. Abideen et al. argue that the conduction channel of nanofibers can be tailored to enhance the gas sensing properties [103]. Yamazoe et al., however, theorize that even if the arrangement of the grains in the sensitive layer is not random, as long as the contact geometry is the same and changes in gas diffusion are negligible, the response remains unchanged [105]. Although there are a large number of studies that compare the response of pure nanofibers to those of nanofibers containing several metal oxides, no study was found that compares CSNs with randomly dispersed particles. The commercial applicability of electrospinning for gas sensor production is limited due to its low throughput rate, requirement for specialized equipment needing high voltage, and conducting targets [106]. In comparison, the mechanical mixing of metal oxides is a far simpler way to achieve the desirable sensor qualities. A systematic examination is done to identify if the variation in the sensor response can be attributed to the secondary morphological structure, the junctions between the metal oxides or a combination of both.

Results and Discussion

Tungsten Trioxide Based Sensors

The research described here is covered in papers 1, 2, and 8.

To identify the inherent sensor qualities of WO_3, seven differently prepared samples were examined. The platelets were prepared using the methods suggested by Kida et al. [107]. In order to increase the anisotropy of the samples the synthesis temperature was either 100 °C or 5 °C. The SA sensor is based on commercially available WO_3 nanopowder (Sigma Aldrich, <100 nm particle size). The ME sensor was based on WO_3 prepared from tungsten chloro-methoxide [108]. The sample was prepared by Mauro Epifani at the Institute for Microelectronics and Microsystems IMM in Lecce, Italy [108]. The RO sensor is based on a sample synthesized via a hydrothermal method using a nonionic surfactant as a structural agent. The powder was provided by Simona Somacescu from the Ilie Murgulescu Institute of Physical Chemistry, Romanian Academy in Bucharest, Romania. The Sphere sensor is based on a sample that was prepared using ultrasonic spray pyrolysis [109]. This sample was prepared by Tae-Hyung Kim from the Lee Group in the Department of Materials Science and Engineering at Korea University in Seoul, Republic of Korea. The Epsilon sample was produced via flame spray pyrolysis (FSP) by members of the Pratsinis Group from the ETH Zurich, Switzerland [110]. The samples are silicon doped [110].

From scanning electron microscope (SEM) images and the X-ray diffraction (XRD) pattern of the sensitive layers (see Figure 5) it is apparent that the sensors show a strong variation in morphology. The platelets prepared at 5 °C are very large while those prepared at 100 °C are significantly smaller. In the XRD pattern, the peak attributed to the crystal facet (002) is reduced in the 100 °C platelets sample, indicative of significant anisotropy. The SA, RO and the ME samples have spherical crystallites. In the Sphere sample, the crystallites are arranged in a hollow sphere structure (secondary morphology is present). In the XRD of the Epsilon sample, the ε-phase is present. The grain size of the samples also varies greatly and was calculated using the Debye Scherrer equation. In the case of the 100 °C platelets, the Debye Scherrer equation could not be applied because the particles are too large (over 100 nm). In the case of the Epsilon sample, the particles are very small and the

value for the grain size was taken from literature because of the large reflex overlap in the XRD.

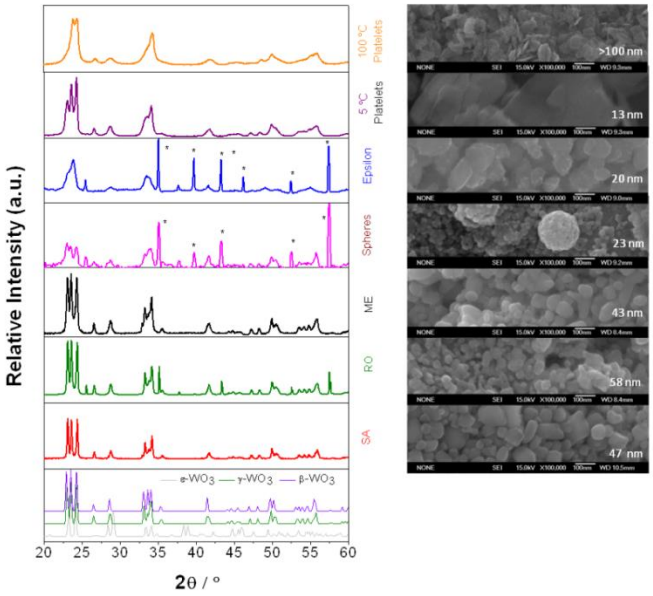

Figure 5: SEM images taken of the sensitive layer of fully fabricated sensors. Reflexes attributed to the substrate are marked with asterisk. The attained diffractograms are compared to those of ε-WO_3[111], **β-WO_3**[112] **and γ-WO_3**[113]**.**

The response of the samples to different test gases was examined. NO_2 and CO were selected as automobile exhaust pollutants. Acetone was selected due to its relevance in breath analysis. Ethanol and toluene were selected as VOCs relevant in indoor air quality monitoring. Application relevant concentrations were selected.

The sensor response was calculated using the following equation:

$$S = \frac{R_0}{R_{gas}} . \qquad \text{Eq. 4}$$

The inverse relation was used for the oxidizing gas NO_2.

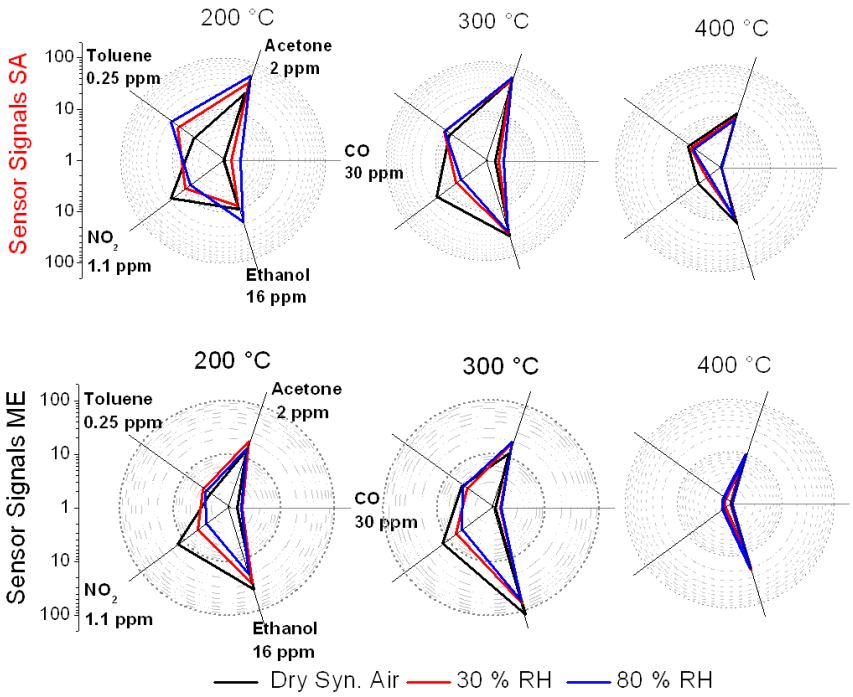

Figure 6: Temperature study of the SA and ME samples.

WO_3 sensors are typically operated between 200 and 400 °C. A temperature study was done of the SA and the ME samples. It was found that the sensors respond similarly at 200 and 300 °C, Figure 6. The response to several gases, e.g. NO_2 significantly decreases at 400 °C. At 300 °C the response and recovery of the sensors was faster. For the systematic study of all the samples, an operation temperature of 300 °C was selected. This temperature is commonly used for WO_3 based sensors [65,73,110].

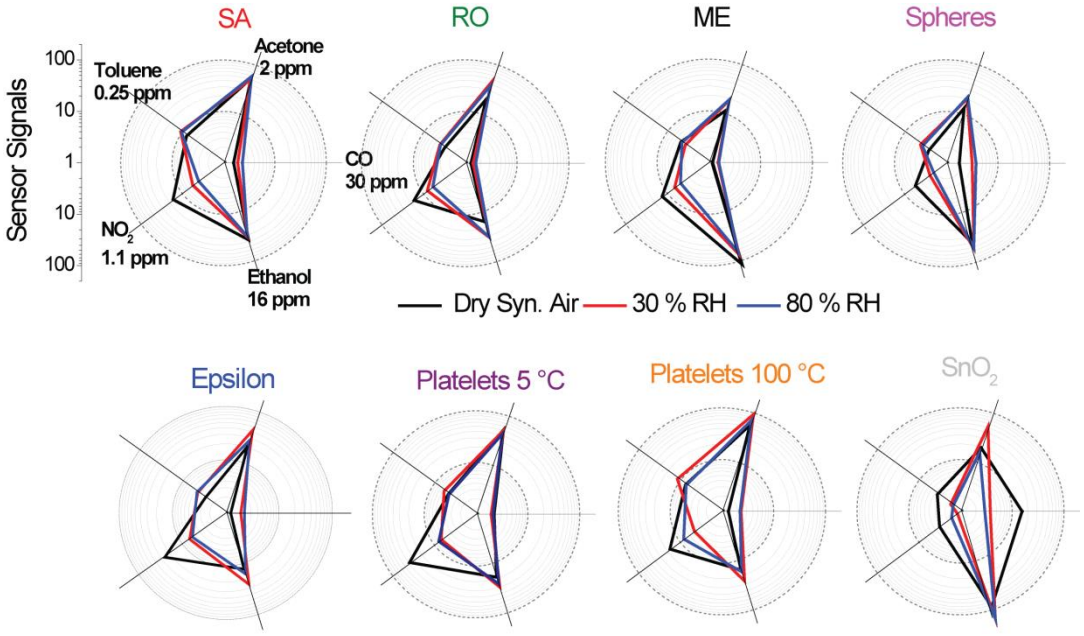

Figure 7: Gas sensor profile of seven different WO_3 samples in comparison to SnO_2 from Sigma Aldrich.

In Figure 7, the sensor responses of each of the materials to one concentration of each gas in different levels of humidity are depicted. Although the sensors are based on WO_3 materials which were prepared using different methods and show variation in morphology and crystal structure, the sensing behavior is remarkably similar. All of the sensors show practically no response to CO and the response always increases in the presence of humidity. The sensors respond well to NO_2 in dry air but the signal degrades in the presence of humidity. The sensors respond well to ethanol. The sensors show high responses to the low concentration of acetone, regardless of the crystal structure. The response to toluene shows the largest variation between the samples.

In line with literature, all of the samples showed an increase of the resistance in the presence of humidity, see Figure 8.

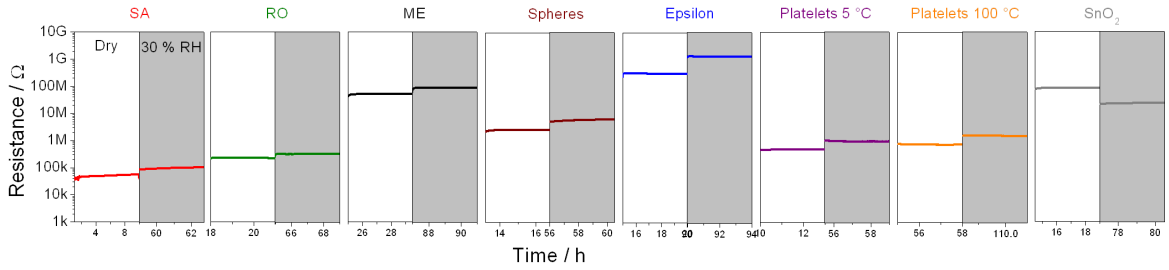

Figure 8: Change in the resistance of the samples as a result of humidity exposure.

In order to understand the surface reaction responsible for the increase of resistance, operando DRIFT spectra were taken during humidity exposure and referenced to dry air. Operando DRIFT has been found to be an infrared method that shows high sensitivity to changes of the surface groups [114]. The very broad band visible at approximately 3450 cm^{-1} in the case of the platelets, and the band at 3500 cm^{-1} for ME and Spheres have previously been ascribed to intercalated water molecules [115,116]. There is no change of the hydroxyl region for RO and SA, but a very clear increase of the bands at 1858 cm^{-1} and 2065 cm^{-1} attributed to tungsten-oxygen bonds.

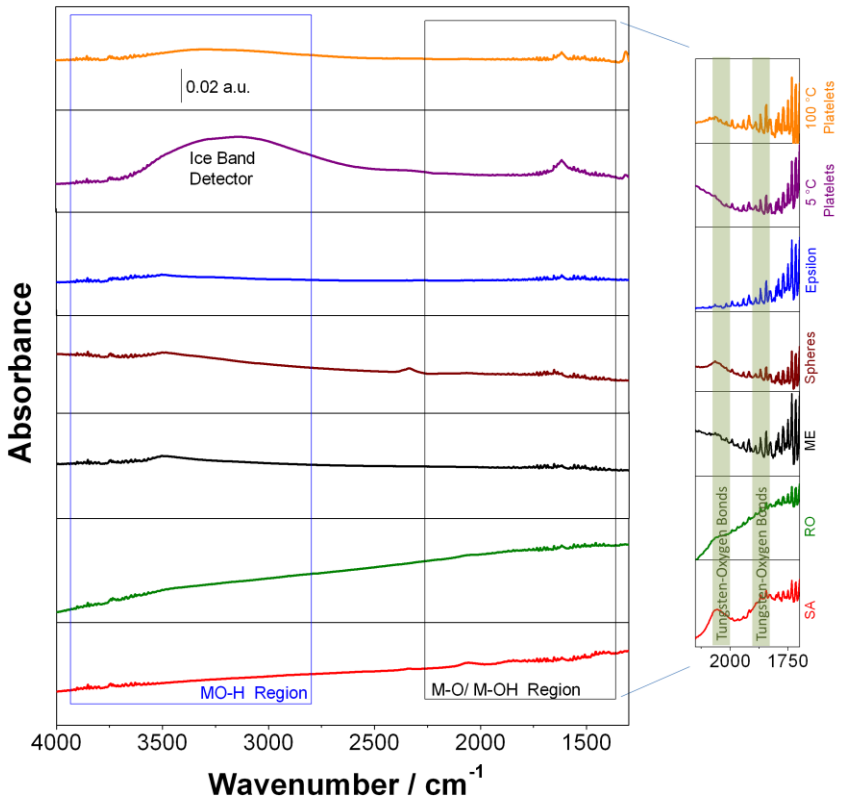

Figure 9: DRIFT spectra taken of the sensors at 300 °C during exposure to 10 % RH referenced to dry synthetic air.

An enlargement of the metal-oxygen bond region reveals that these bands also increase for the other samples (with the exception of the Epsilon sample), see Figure 9. The Epsilon sample is prepared using FSP, which is known to result in very porous materials. It is possible that there is much less of the Epsilon sample on the substrate compared to the other materials and that as a result the signal strength is very low in the infrared measurements. An increase of the bands at 1858 and 2065 cm^{-1} indicates that surface vacancies are filled by the oxygen of water, which explains why the resistance is higher in humidity. This suggests the following reaction:

$$V_O^{\cdot\cdot} + 2e' + H_2O \rightarrow O_O^x + H_2 \qquad \text{Eq. 5}$$

For some samples, e.g. Spheres and ME, the formation of hydroxyl groups is also visible in the DRIFT spectra. In order to understand the origin of these bands, DRIFT spectra of the SA and the ME sample during exposure to H_2 were done.

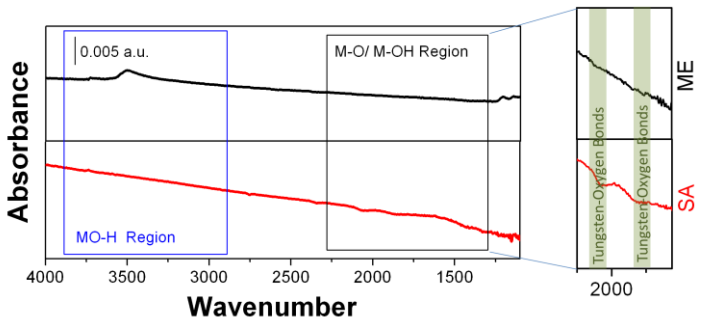

Figure 10: DRIFT spectra taken of the SA and the ME sample during exposure to 250 ppm H_2 referenced to the spectra taken in dry syn. air at an operation temperature of 300 °C .

Both samples show a low response (decreasing resistance) to 250 ppm H_2. SA has a sensor signal of ca. 3.5 while the ME sample has a response of about 2.5. In the DRIFT spectra of the SA sample during exposure to hydrogen, only the reduction of the sample is visible, see Figure 10. In the spectrum of the ME sample, only the formation of the same hydroxyl groups as with water is visible, see Figure 10. In line with the mechanisms suggested by Heiland and Kohl, the formation of hydroxyl groups appears to result in a decrease of the resistance [42,55]. Based on these findings, it is inferred that in the case of humidity, the formation of hydroxyl groups is either a parallel or secondary reaction to the surface oxidation. The dominant reaction for all samples, i.e. the reaction responsible for the increase of resistance, is the oxidation of the surface by humidity.

In order to verify this finding and elucidate the mechanism further, a temperature study was done. The SA sample was selected because the oxidation is clearly visible in the DRIFT spectra. The sensor was exposed to 10 % RH at different operation temperatures. Surprisingly, at temperatures less than 200 °C, humidity results in a significant decrease of the sensors resistance. At 200 °C, the effect of humidity on the resistance is minimal and at higher temperatures the resistance then increases, Figure 11a.

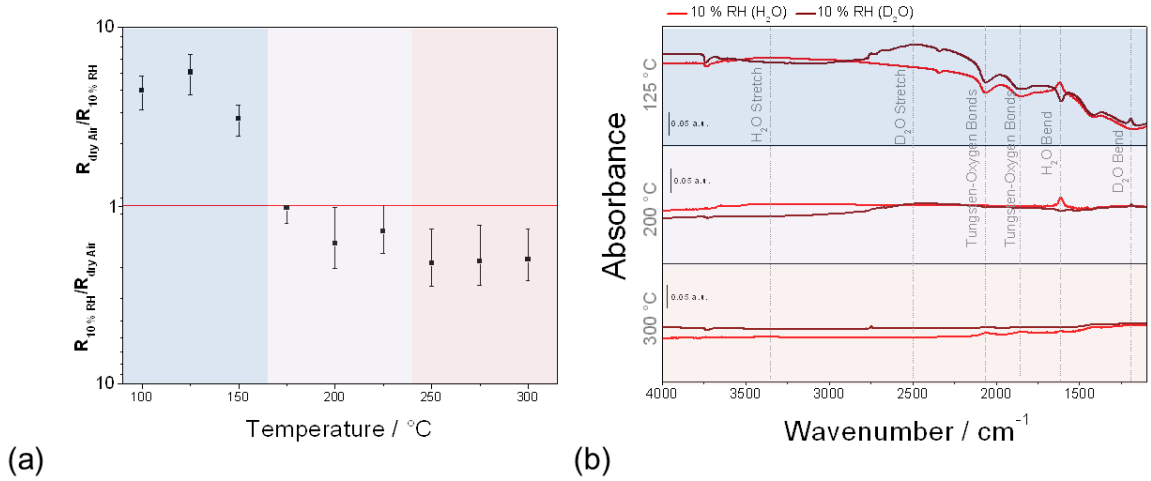

Figure 11: (a) The average sensor signal of four different sensors based on SA during exposure to humidity at different operation temperatures. (b) DRIFT spectra of a sensor measured (in the same position) at different temperatures during exposure to 10 %RH.

In the DRIFT spectra at 125 °C, there is a clear decrease in the bands at 1858 and 2065 cm^{-1}, see Figure 11b. Albanese et al. identified the tendency of H_2O to adsorb onto the surface vacancies of WO_3 using DFT calculations [117]. In addition, the substitution of an oxygen in the tungsten-oxygen octahedral with water is known to occur during hydration of the material [118]. The bending mode unique to the presence of adsorbed water is clearly visible in the DRIFT spectra at 1620 cm^{-1} [74]. Molecular water blocks the oxygen vacancy. The following mechanism at low temperatures is suggested:

$$V_O^{\cdot\cdot} + H_2O \rightleftharpoons H_2O_O^{\cdot\cdot}. \qquad \text{Eq. 6}$$

This disrupts the equilibrium between the vacancies and the atmospheric oxygen, i.e. less tungsten-oxygen surface bonds:

$$V_O^{\cdot\cdot} + O_2 \rightleftharpoons O_O^x. \qquad \text{Eq. 7}$$

This disruption of the equilibrium is in line with the significant decrease of the resistance. In order to verify that the interaction with humidity is restricted to the surface of the material, operando XRD measurements were done. In the operando XRD, there is no change visible after 10 hours at 125 °C in 90 % RH, i.e. even in high humidity water does not enter the lattice, see Figure 12.

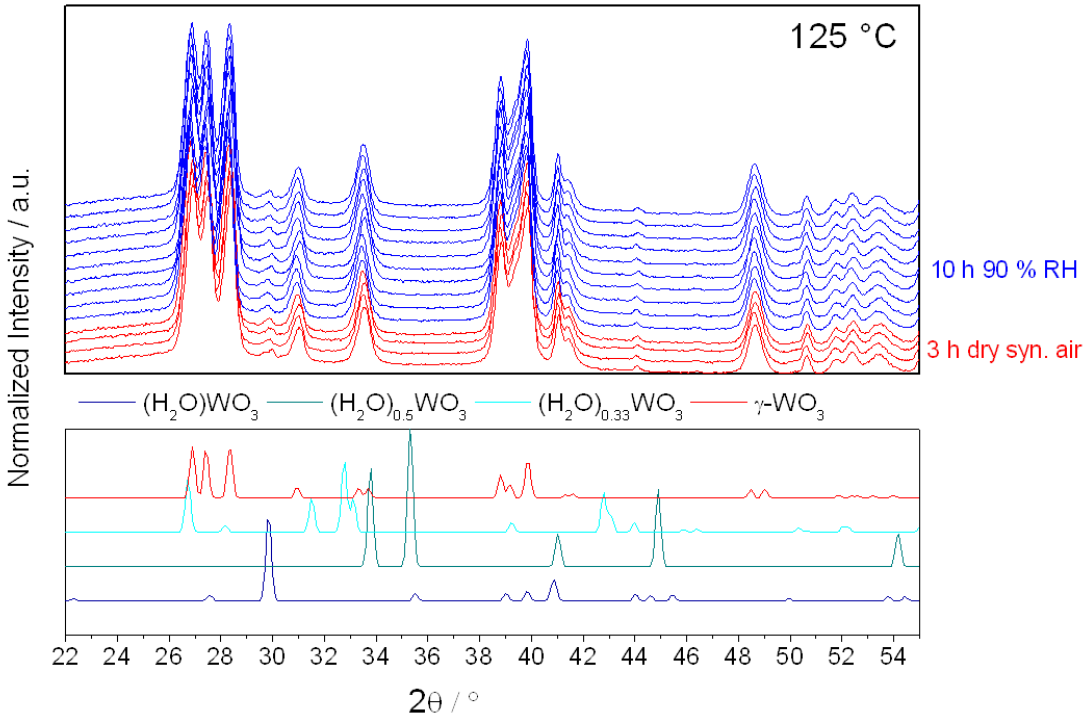

Figure 12: Operando XRD of a SA sensor operated at 125 °C during an initial 3 h exposure to dry synthetic air and then to 90 %RH. The attained diffractograms are compared to those of $(H_2O)WO_3$ [119]**, $(H_2O)0.5WO_3$**[120]**, $(H_2O)0.33WO_3$**[121] **and γ-WO_3**[113]**.**

By considering the DRIFT spectra taken at 300 °C during humidity exposure in the context of the DRIFT spectra at lower temperatures, a mechanism becomes clear. While at 125 °C it molecularly adsorbs onto a surface oxygen vacancy site, at 300 °C water is catalytically split at the surface of WO_3, oxidizing the surface and releasing hydrogen. At 200 °C, both mechanisms are present, explaining why the bands attributed to tungsten-oxygen bonds are barely increasing and a band associated with molecularly adsorbed water (1620 cm^{-1}) is hardly visible. This also fits well to the resistance measurements. At 125 °C there is a significant decrease of the resistance, while at 300 °C there is a slight increase. When both reactions are present, 200 °C, the resistance change is the lowest.

The final verification for the suggested mechanism is the identification of hydrogen in the exhaust. Due to the low concentration, the detection of H_2 in the exhaust is not trivial. The setup shown in Figure 13a was used. 1 g of SA WO_3 was heated to 300 °C. Using a gas mixing system air was guided through the WO_3 powder at a flow rate of 150 ml/min. 3 h of dry synthetic air were then followed by a 2 h exposure to 10 % RH. The exhaust gas was dried using silica gel and molecular sieve and then monitored using a TGS2600 (n-type SMOX sensor from Figaro Engineering Inc.) gas sensor. There is no significant response of the sensors when 10 % RH was added to the dry heated glass tube, see the blue line in Figure 13b.

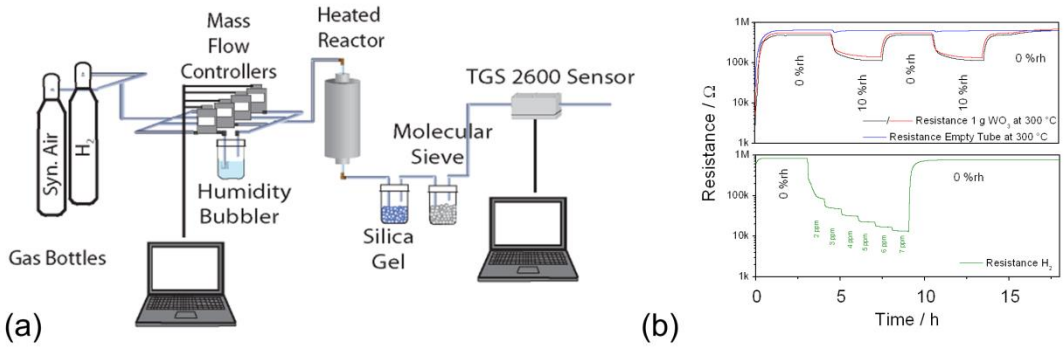

Figure 13: (a) Setup of the hydrogen measurements. (b) Results of the exhaust measurements.

It is likely that the formation of hydrogen during the exposure of the heated WO_3 to humidity is responsible for the decreasing resistance of the TGS2600 sensor, see the red and black line in Figure 13b. Based on measurements done using the TGS sensor during exposure to hydrogen from the bottle, approximately 2 ppm H_2 are released during the exposure of 1 g WO_3 to 10 % RH.

Operando DRIFT spectroscopy was also used to identify the surface reaction between WO_3 and the analyte gases acetone and NO_2. The DRIFT spectra taken of the samples at 300 °C during exposure to acetone is similar to that reported by Huebner et al. for the exposure of WO_3 to CO [53]. The bands at 1858 and 2065 cm^{-1}, attributed to tungsten-oxygen bonds, are decreasing, see Figure 14. The formation of organic groups on the surface or a change in hydroxyl groups is not visible on the samples. This indicates that the major reaction partner of WO_3 with acetone is surface oxygen.

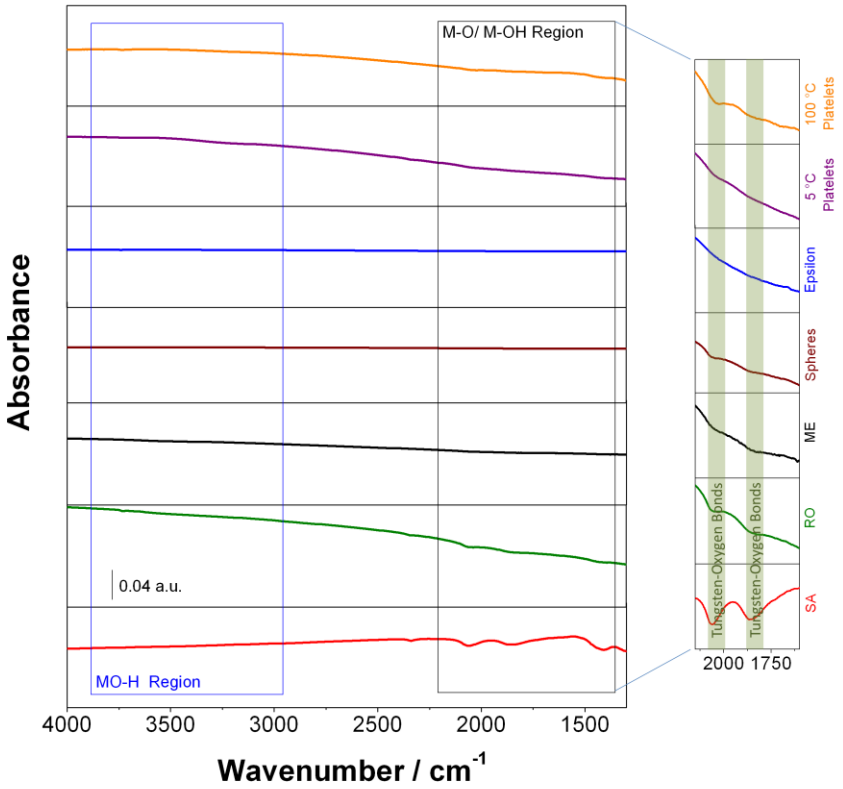

Figure 14: DRIFT spectra of the samples at 300 °C taken during exposure to 1.5 ppm acetone referenced to the spectra taken in dry syn. air.

In order to better understand the reaction steps of acetone with the WO_3 surface, DRIFT spectra of the SA and the ME sample at 200 °C were examined.

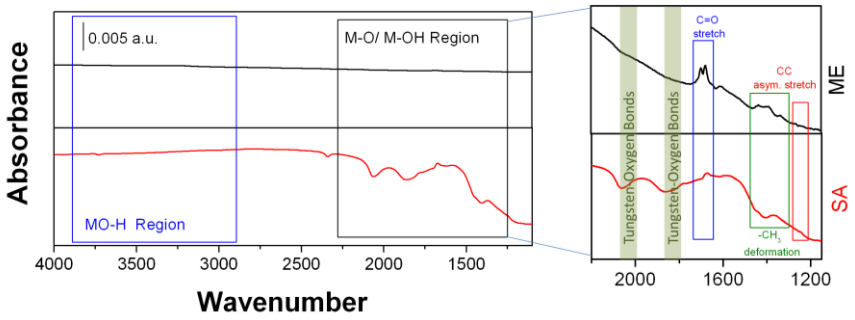

Figure 15: Spectra of the ME and SA samples at 200 °C taken during exposure to 1.5 ppm acetone referenced to the spectra taken in dry syn. air.

At 200 °C, in addition to the decreasing bands attributed to the tungsten-oxygen bonds, there are bands in the carbonyl region, see Figure 15. In the case of the SA sample, there is a single carbonyl band visible at ca. 1680 cm^{-1} which, in literature, is attributed to surface bound acetone [122]. In the case of the ME sample there are two bands visible at ca. 1710 and 1665 cm^{-1}, which is attributed to an acetone diolate [122]. This indicates that acetone reacts with WO_3 analogously to TiO_2. It first

adsorbs via the oxygen of the carbonyl to the surface metal [123]. From there, it is oxidized. In DRIFT spectra taken during exposure to the oxidizing gas NO_2 at 300 °C, the increasing bands at 1858 and 2065 cm^{-1} are visible, Figure 16. The classic nitro symmetric and asymmetric bands are not visible in the spectra taken during NO_2 exposure [81].

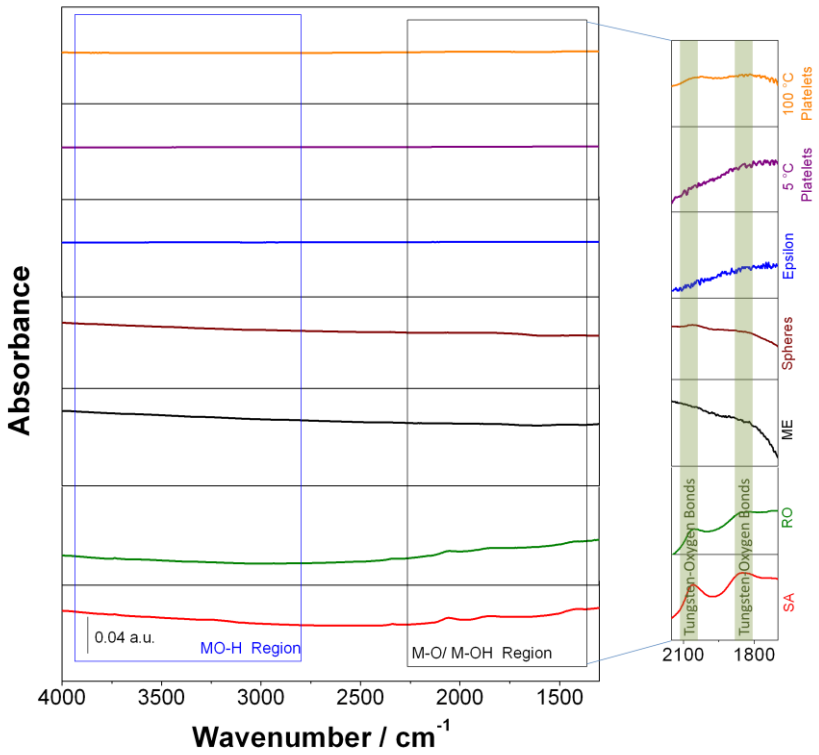

Figure 16: DRIFT spectra taken during exposure to 0.75 ppm NO_2 referenced to the spectra taken in dry synthetic air.

In the SA sample there is an increasing band visible at 1420 cm^{-1}. This band was also detected by Akamatsu et al., and was inconclusively attributed to adsorbed NO_2 [80]. In order to identify the origin of this band, the DRIFT spectrum of the SA sample at 200 °C is consulted, see Figure 17.

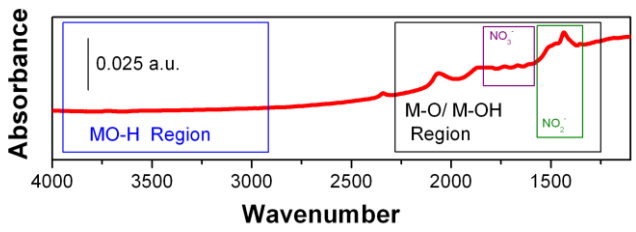

Figure 17: DRIFT spectra of the SA sample taken during exposure to 0.75 ppm NO_2 referenced to the spectra taken in dry synthetic air at 200 °C.

In the spectrum, in addition to the increasing bands attributed to the tungsten-oxygen bonds, there are two strong bands (1487and 1437 cm^{-1}) and two weak bands (1720 and 1624 cm^{-1}) visible. In line with the reports of Akamatsu, the bands in this region can be attributed to either nitrites (NO_2^-) or nitrates (NO_3^-) [81]. Yang et al. attribute the bands at lower wavenumbers to nitrites and the bands at higher wavenumbers to nitrates [81]. This indicates that NO_2 dominantly adsorbs into an oxygen vacancy of the WO_3 surface, resulting in a nitrite. From there, NO is released into the atmosphere (reoxidized with atmospheric oxygen to NO_2) and the surface is oxidized. It is possible that in addition to nitrites there is a band around 1420 cm^{-1} that originates from tungsten-oxygen bonds as, at 300 °C, the band is decreasing in the spectra taken with acetone (and also increases in the presence of humidity).

From this broad study of the material, it was identified that, at 300 °C, the WO_3 surface is always oxidized by humidity. The material responds well to acetone and ethanol. It shows high responses to NO_2 in dry air and a significant decrease of the response in humidity. Conversely, the response to CO is low and increases with humidity. The homogeneous sensing behavior, surprisingly similar despite variations in morphology and preparation method, was attributed to the dominant adsorption of the test gases with surface oxygen vacancies. Overall, WO_3 is a very promising material that is complementary to SnO_2.

Mixed Materials

Noble Metal Additives

The research presented here is covered in papers 3, 5, 6, and 7.

Surface loading is known to drastically change the sensor response of SMOXs. Noble metals are commonly used additives. Here, the effect of platinum, palladium, and rhodium surface clusters on WO_3 based sensors was examined. The Spheres sample was surface loaded with rhodium by the group of Professor Jong-Heun Lee at Korea University in Seoul, Republic of Korea [124]. As a result, the identified inherent characteristics of WO_3 disappeared, see Figure 18. The addition of rhodium onto SA via a sol gel process resulted in very similar results.

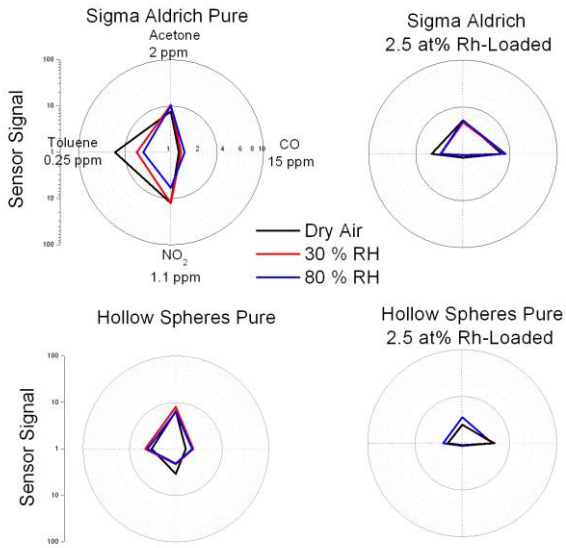

Figure 18: Comparison of two different Rh-loaded WO_3 samples.

In order to understand whether the Fermi level pinning mechanism or the spillover effect is responsible for the drastic change in the response, a thorough examination of the samples was done. Here, the results for the loaded SA sample will be detailed. The analogous results were attained for the loaded Spheres sample.[3]

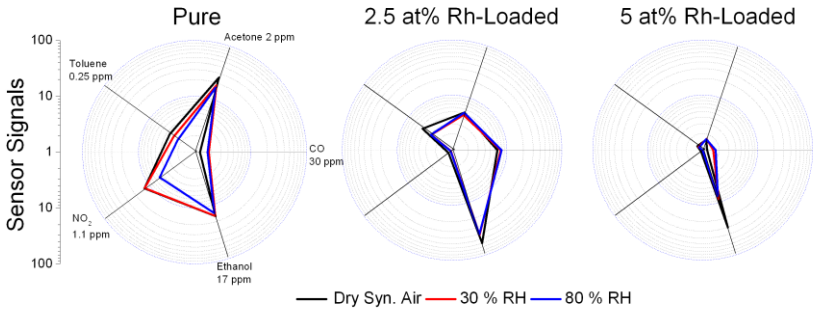

Figure 19: Effect of different Rh-loading concentrations on the sensor response of WO_3.

By increasing the loading concentration to 5 at%, the change in sensor response becomes even more drastic, see Figure 19. The resistance of the loaded samples is much higher than that of the sensor based on pure WO_3, see Figure 20. Simplistically, in the case of *n*-type semiconductors, oxygen absorbed on the surface traps electrons resulting in a potential barrier between the crystallites of the samples. In an inert atmosphere (nitrogen) without the presence of oxygen, it is assumed that the increase in resistance of the loaded sample in comparison to the pure sample is as a result of the coupling between the surface rhodium clusters and WO_3, see Figure 20.

[3] For more detailed infomation please see the paper by Staerz et al. [131]

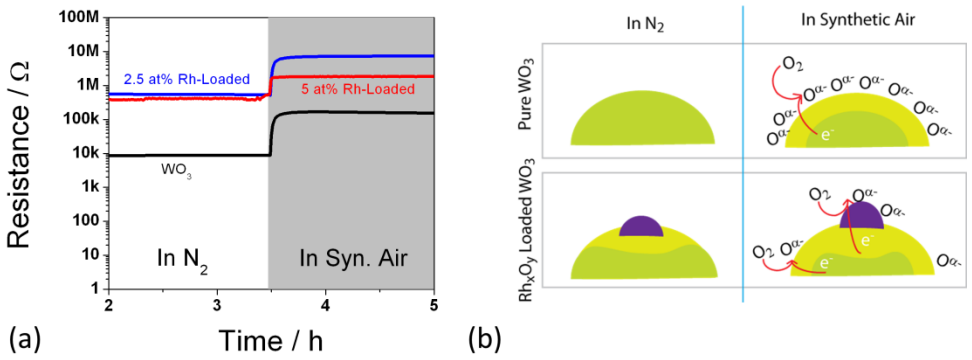

Figure 20: (a) The baseline resistance change as a result of surface loading with rhodium in nitrogen and dry synthetic air. (b) A schematic showing why the resistance increases so significantly as a result of the loading and why the effect of oxygen is lower for the loaded materials.

The rhodium surface clusters result in a band bending of approximately 198 meV for the 2.5 at% and 200 meV for the 5 at% sample, see Figure 21a. In order to understand how the presence of the rhodium clusters changes the surface chemistry of the sensors, operando DRIFT spectroscopy was used. All of the sensors show a strong decrease in the resistance in the presence of ethanol.

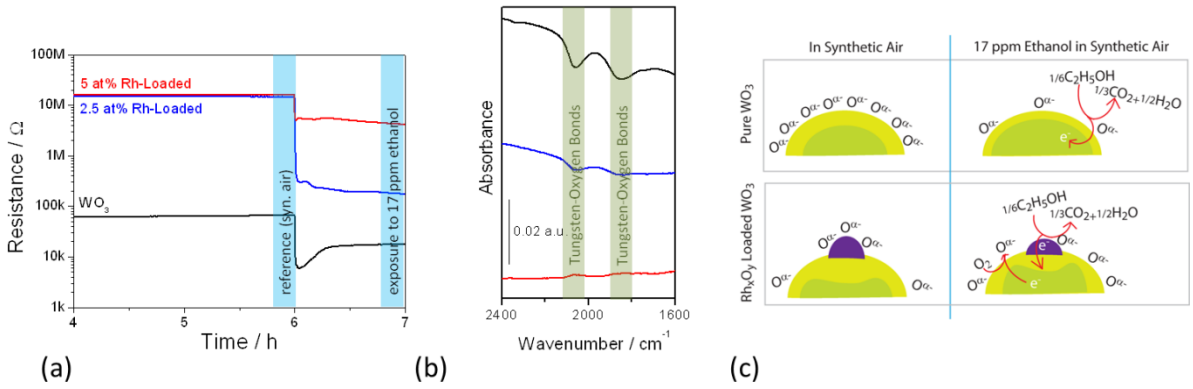

Figure 21: (a) The resistance change as a result of exposure to ethanol for both the loaded samples and the pure material. (b) DRIFT spectra taken of the samples during exposure to 17 ppm ethanol. (c) A schematic showing why the resistance of the loaded sample decreases even if an oxidation is visible in the DRIFT spectra.

For pure WO_3, the absorbance DRIFT spectrum of the ethanol exposure is as expected. There is a decrease in the two bands attributed in literature to tungsten-oxygen bonds. This decrease signalizes a reduction of the surface by ethanol. This surface reaction explains the decrease in resistance. The interpretation is less straightforward for the loaded samples. For the 2.5 at% loaded sample, although the presence of ethanol results in a more significant decrease of the resistance, the reduction of WO_3 is less significantly visible in the DRIFT spectra. Furthermore despite a decrease of the resistance, the bands attributed to the tungsten-oxygen

bonds increase in the spectra of the 5 at% loaded sample, see Figure 21b. These findings, in addition to the very significant increase of the resistance as a result of the rhodium loading, strongly indicate a Fermi level pinning mechanism. In other words, the ethanol reacts dominantly with the oxidized rhodium clusters, significantly changing their stoichiometry. As a result, electrons are released from the junction back into WO_3. More electrons are then available for the base oxide to react with oxygen in the atmosphere. In total, however, the electronic effect is more strongly affected by the release of electrons than by the re-oxidation of WO_3, Figure 21c. To verify the validity of this explanation, DRIFT measurements done in highly reducing backgrounds are helpful.

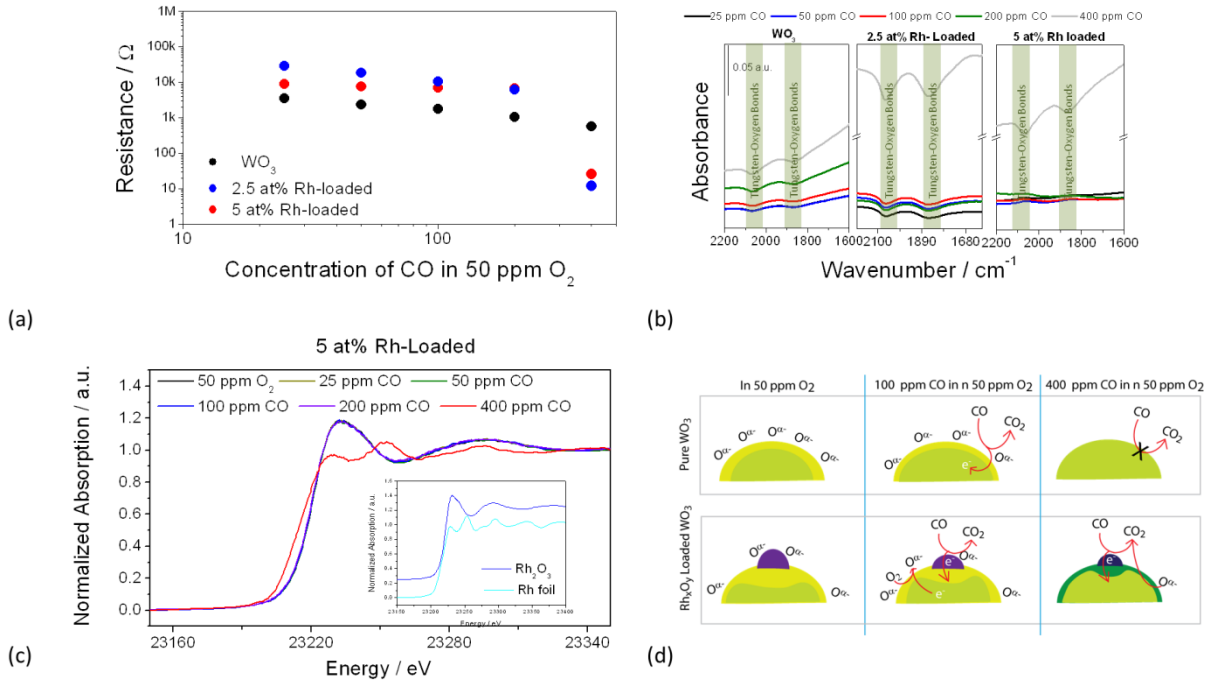

Figure 22: Low oxygen background measurements: (a) Resistance changes of the pure and loaded WO_3 as a function of the CO concentration. (b) Operando DRIFT spectra taken during exposure to CO referenced to the spectra taken in 50 ppm O_2. (c) Operando Rh K-edge XANES spectra of 5.00 at% Rh-loaded WO_3. (d) Schematic of a possible surface mechanism.

The sensors were exposed to increasing concentrations of CO in a background of 50 ppm oxygen in nitrogen. In the case of the sensor based on pure WO_3, the sensor behaves as expected for an *n*-type metal oxide: it shows a power law relation between the concentration of CO and the resistance, see Figure 22a. In the DRIFT spectra, the decrease of the bands attributed to tungsten-oxygen bonds are visible, see Figure 22b. At lower CO concentrations, the behavior of the sensors based on the loaded samples is similar to that of pure WO_3. The DRIFT spectra are very similar

to those under ethanol exposure. At this point, the surface rhodium clusters are oxidized, see Figure 22c. Between 200 and 400 ppm CO, however, there is a drastic drop in the resistance of the sensors based on both loaded samples, see Figure 22a.. At this point, the DRIFT spectra indicate a change in the surface chemistry, see Figure 22b. The 5 at% rhodium loaded sample no longer shows an increase of the bands attributed to the tungsten-oxygen bonds but instead shows a reduction of the surface. In the case of the 2.5 at% loaded sample, the reduction of WO_3 becomes more significant under exposure to 400 ppm CO. At this point, it can be seen using operando XAS that the rhodium surface clusters are fully reduced to their metallic state, see Figure 22c. It is possible that the concentration of the oxygen in the background is too low to allow the WO_3 surface to be fully re-oxidized or that the metallic surface rhodium catalyzes the reaction with CO. It is also possible that electrons are inserted from the metallic rhodium into WO_3. In all cases, a surface charge accumulation layer is responsible for the drastic drop in the resistance. A schematic representation of the different situations identified for the loaded sample is shown in Figure 22d.

Drastic changes in the sensor response were also attained by surface loading the SA WO_3 sample using platinum and palladium chloride, see Figure 23a. In addition, similar results were attained for WO_3 nanofibers surface loaded with platinum.[4]

[4] For more detailed infomation please see the paper by Staerz et al. [132]

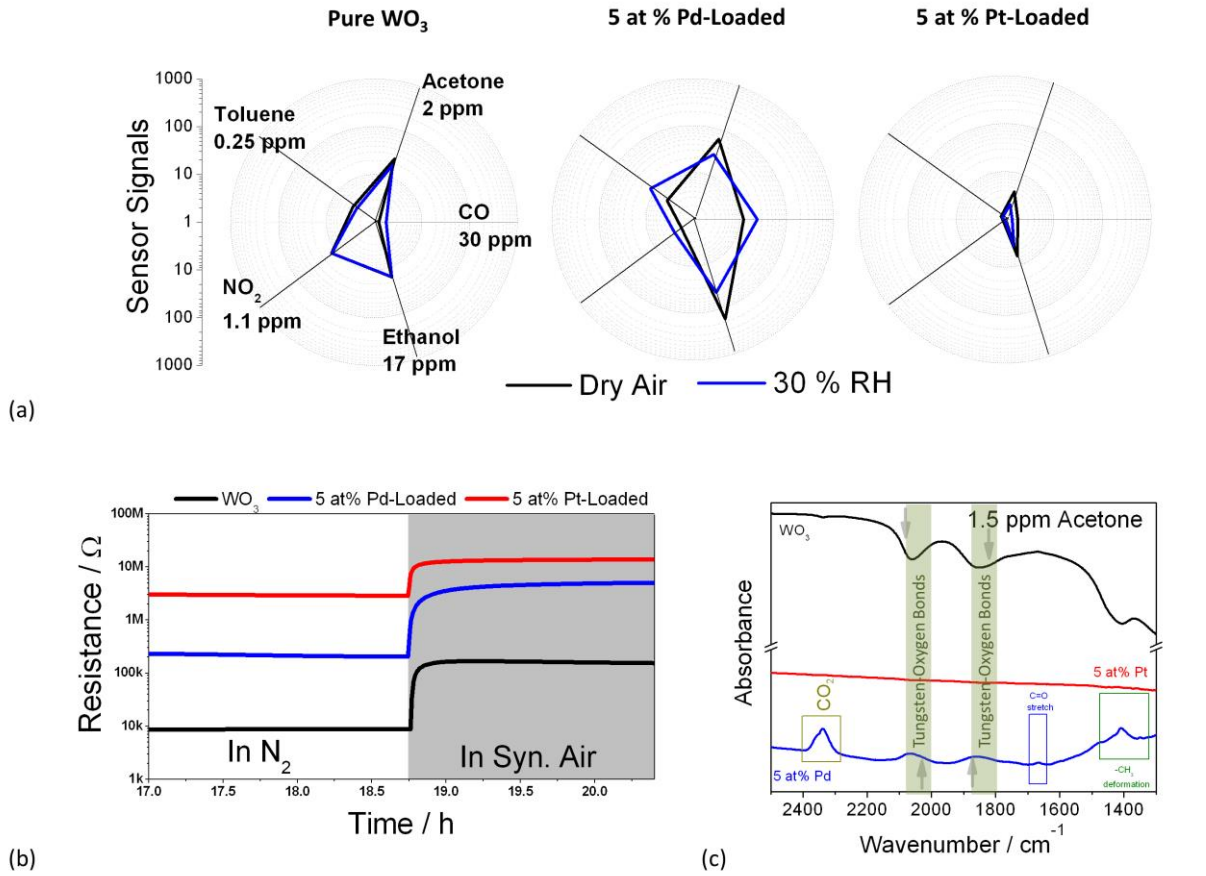

Figure 23: (a) The sensor response of the pure and Pd/Pt- loaded WO_3 samples. (b) The baseline resistance change as a result of surface loading with Pd/Pt in nitrogen and dry synthetic air. (c) DRIFT spectra taken of the samples during exposure to 1.5 ppm acetone.

Both surface loading with palladium and with platinum results in a significant increase of the baseline resistance under N_2 atmosphere, see Figure 23b. This increase is indicative of an initial band bending of 154 meV for palladium and ca. 233 meV for the platinum loading.

Like in the DRIFT spectra taken of Rh-loaded WO_3 during ethanol exposure, the oxidation of WO_3 is visible in the spectra taken of the palladium sample during exposure to acetone, see Figure 23c. In the case of the Pt-loaded sample, no information can be gained from the DRIFT spectra taken in synthetic air background. Analog to the Rh-loaded sample, the samples were examined using low oxygen measurements.

The Pd-loaded sample behaves very similarly to the Rh-loaded sample. During exposure to low CO concentrations an increase of the bands attributed to tungsten-oxygen bonds is visible and the effect on the resistance is minimal. Between 100 and 200 ppm CO, however, there is a drastic drop in the resistance, see Figure 24. Based

on these findings, it is theorized that the effect of palladium on the sensing of WO_3 is analogous to rhodium. In other words the Fermi level pinning mechanism dominates.

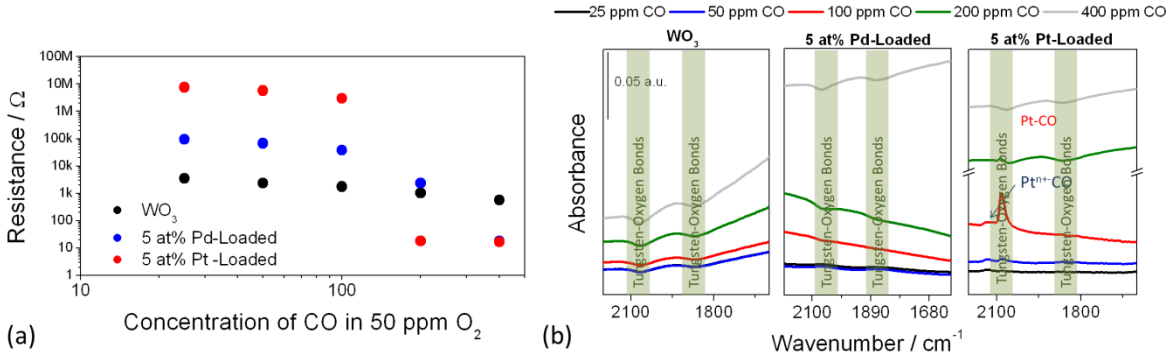

Figure 24: (a) Low oxygen background measurements: (a) Resistance changes of the pure and loaded WO_3 as a function of the CO concentration (b) Operando DRIFT spectra taken during exposure to CO referenced to the spectra taken in 50 ppm O_2.

The behavior of the resistance is also similar in the Pt-loaded sample: initially, a low power law response to CO and then a drastic drop in the resistance between 100 and 200 ppm CO. In the DRIFT spectra taken of the Pt-loaded sample, no increase of the bands attributed to tungsten-oxygen bonds is visible during exposure to low CO concentrations. It is, however, possible to infer a similar situation to the Rh-and Pd-loaded samples based on the presence of different platinum carbonyls. At low CO concentrations, Pt^{n+}-carbonyls are dominantly visible. As the concentration of CO increases, metallic Pt-carbonyls become visible. During exposure to 200 ppm CO, only metallic Pt-carbonyls are visible and the bands attributed to tungsten-oxygen bonds are clearly decreasing. At this point, the surface platinum clusters are fully reduced to their metallic state. Infrared spectroscopy, however, only offers information about the sample on average. Transmission electron microscopy (TEM) supplies localized information about the platinum surface clusters.

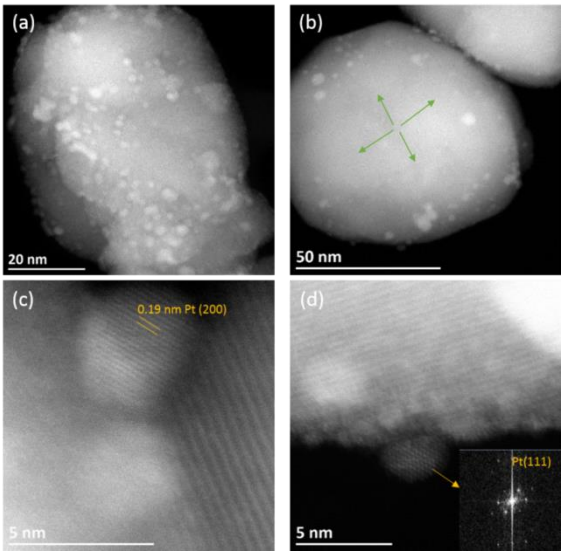

Figure 25: STEM-HAADF images of the PtO_x-WO_3 sample before exposure to CO in (a) and after cooling in CO (b). HR-STEM-HAADF in (c) and (d) shows metallic Pt nanoparticles after cooling in 400 ppm CO. Inset of d): Fast Fourier Transformed of the corresponding high resolution image.

Ex situ high resolution scanning transmission electron microscopy (HR-STEM) images taken of the sample before exposure to CO are shown in Figure 25a. HR-STEM images of a sample cooled in 400 ppm CO are shown in Figure 25b. Before exposure, the platinum oxide clusters are homogeneously dispersed on the surface. In the sample that had been exposed to 400 ppm, the platinum is agglomerated. High resolution images, shown metallic Pt particles with Pt(200) in Figure 25c and Pt(111) in Figure 25d. These results are in line with the operando DRIFT spectra and reveal that under these conditions the platinum clusters are reduced to their metallic state. Using in situ STEM, it was possible to follow the reduction of the platinum cluster optically.

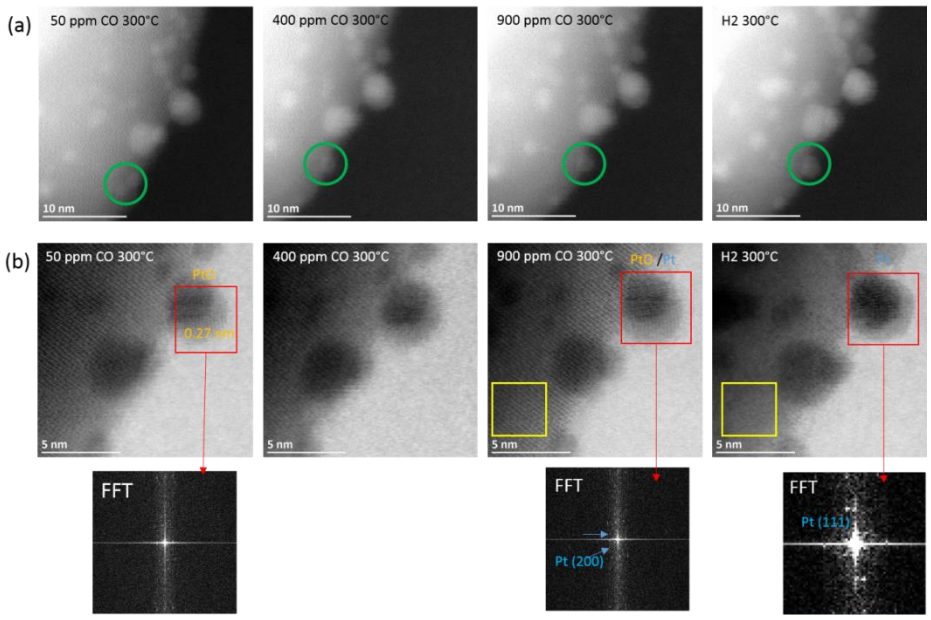

Figure 26 : In situ STEM-HAADF images in different environments showing particle coalescence in (a) and In situ STEM–BF images showing the PtO_x–Pt structural transformation when increasing the CO concentration and under H_2 at 300°C.

In Figure 26, using STEM with high-angle annular dark-field imaging (HAADF) and bright field (BF), the oxidation state of the platinum surface clusters is observed under different atmospheres, see red box. Under exposure to 50 ppm CO, the surface platinum clusters are largely oxidized. During exposure to 900 ppm CO, reflexes belonging to metallic platinum are also detected. The in situ TEM provide information about the drastic resistance associated with the reduction of the noble metal clusters. These results show that, unlike the rhodium oxide surface clusters which are either oxidized or metallic, the surface platinum clusters can be in a partially reduced state. The extreme drop in resistance appears, however, to occur once the clusters are fully reduced, i.e. the Fermi level pinning is completely released.

The resistance drop could be because the WO_3 is initially so drastically depleted by the presence of the platinum oxide clusters that it cannot be sufficiently re-oxidized in the low oxygen atmosphere. Mohammad examined the electrical properties of WO_3 nanopowder at different reduction levels and found that until the material was reduced to WO_2, it showed n-type semiconductor behavior [125]. Venables et al. report that at ca. 300 °C the reduction of WO_3 to WO_2 is slow, needing approximately 40 minutes to reach completion in a flowing H_2 atmosphere [126]. Upon exposure to pure hydrogen, the reduction of WO_3 is visible in the TEM images, in line with the findings of Venables et al. This can be seen by the amorphous structure of the tungsten support under hydrogen exposure. On the sensor cooled in 400 ppm CO in

50 ppm O_2, although the platinum clusters are metallic, no reduction of the WO_3 is visible. These findings indicate that the decrease in resistance is most probably the result of an electronic coupling between the metallic surface clusters and the WO_3.

This study experimentally proves that the Fermi level pinning mechanism dominates on WO_3 based sensors that have been surface loaded with noble metal oxides. As a result, the inherent characteristics of WO_3 are lost and the chemistry of the noble oxide clusters dominates the sensing behavior. Similar findings were reported by Degler et al. for oxidized platinum clusters loaded onto SnO_2 [60]. In this context, it was hypothesized that surface loading with noble metal oxides should decrease the complementarity of the *n*-type base oxides WO_3 and SnO_2. This hypothesis was tested with rhodium oxide surface loadings.

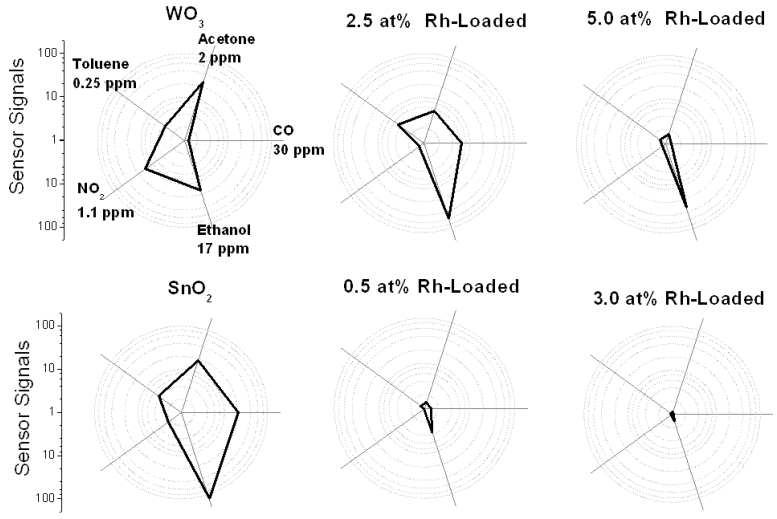

Figure 27: Sensor profile of pure and Rh-loaded WO_3 and SnO_2 in dry synthetic air.

As predicted, surface loading with rhodium reduces the complementarity of the materials and, with higher loadings, the sensors are only responsive to ethanol, see Figure 27. In a comprehensive study using operando DRIFT and X-ray spectroscopy, the Fermi level pinning mechanism was found to dominate for all the samples [46].[5] Based on these findings, it is concluded that the addition of oxidized noble metal surface clusters is not well-suited for creating a large palette of complementary gas sensitive materials.

[5] For more detailed infomation please see the paper by Staerz et al. [133]

Metal-Oxide-Metal-Oxide Mixtures

The research covered here is presented in the paper 4.

In literature it is widely reported that the sensor response of mixed metal oxide materials is drastically different than that of the pure material. In most cases the mixed materials have a secondary structure, e.g. the crystallites are ordered in nanofibers. Here it is examined how the sensing response of SnO_2 changes through the addition of the *p*-type semiconductor Cr_2O_3. In addition, the effect of the contact between the materials is separated from the effect of the secondary fiber structure. Pure nanofibers and CSNs were prepared by Xing Gao from the research group of Prof. Tong Zhang at Jilin University in Changchun, People's Republic of China. The nanofibers (shown in Figure 28a and c) were compared to samples without a secondary morphology (shown in Figure 28b and d). The randomly dispersed materials were prepared by breaking apart the core-shell structure using soft mechanical grinding in a mortar and pestle.

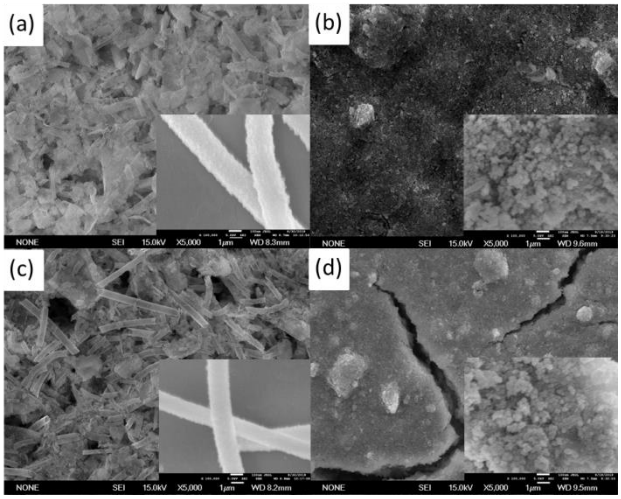

Figure 28: SEM image of the (a) Cr_2O_3- SnO_2 core-shell sensitive layer of a sensor (b) crushed SnO_2-Cr_2O_3 core-shell sensitive layer of a sensor (c) SnO_2-Cr_2O_3 core-shell sensitive layer of a sensor (d) crushed Cr_2O_3- SnO_2 core-shell sensitive layer of a sensor. The higher magnification insets are taken of powder samples.

Analog to the previous studies, the response of the sensors to five different gases in varying background humidity was examined. The ground samples showed responses very similar to their counterparts with intact secondary structure. In most cases, the resistance of the samples containing the nanofibers is higher than the corresponding crushed materials. As expected, the pure SnO_2 based sensors show an *n*-type response, while the Cr_2O_3 sensors show a *p*-type response. Notably, the sensors

based on a mixture of both oxides showed an enhanced *p*-type response for CO and ethanol, Figure 29.

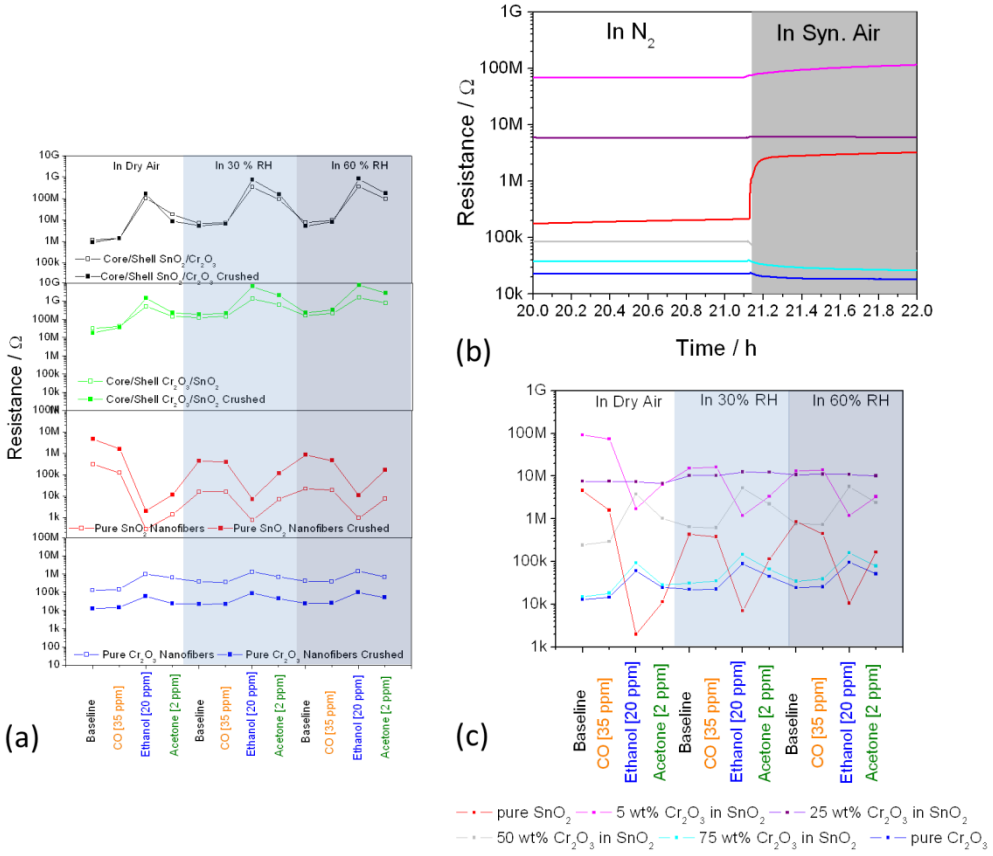

Figure 29: (a) The resistance of the SnO_2 and Cr_2O_3 nanofibers and the randomly dispersed samples to the test gases. (b) The resistance of all the samples to nitrogen and synthetic air. (c) The resistance of samples based on different ratios of Cr_2O_3 to SnO_2 under different test gases.

In order to examine how the *p*-type response of the composite materials is enhanced, samples with varying ratios of the oxides without a secondary structure were prepared. A simple, albeit unprecise, approach to identify band bending is by comparing the resistance of the samples in nitrogen. It is assumed that in N_2, the surface acceptor state related to the ionosorption of O_2 can be neglected. The metal-oxide-metal-oxide mixtures show a higher resistance than the pure materials. In literature, there is a large variation in the reported work functions of the two materials; SnO_2 between 4.7 and 5.7 eV [127] and for Cr_2O_3 between 4.6 [128] and 5.9 [129]. Based on the resistance changes, it appears that electrons migrate from SnO_2 to Cr_2O_3, resulting in a majority charge carrier depletion layer in both oxides.

The sample containing 50 wt% of each metal oxide shows a significantly enhanced *p*-type response over that of pure Cr_2O_3. At the examined operation temperature of

200 °C, oxygen adsorbs onto the surface of the grains resulting in a surface hole accumulation layer and a decrease of the resistance in *p*-type materials. The higher response of the 50 wt% sensor to oxygen indicates a higher surface electron concentration in Cr_2O_3 originating from the heterojunctions. In addition, it is known that the presence of an initial band bending affects the transduction, shifts the conditions for depletion or accumulation layer control [91]. The higher resistance of the sample containing 50 wt% of each metal oxide in oxygen than that of pure Cr_2O_3 in nitrogen, also indicates that a depletion layer control may exist. It is known that for the same band bending change, the resistance change in the case of an accumulation layer is the square root of that in a depletion layer [91]. This change in transduction may be an additional reason for the enhanced sensor response.

Overall no clear advantage could be attributed to the CSNs samples versus the randomly dispersed samples. It was, however, verified that desirable sensor qualities could be attained using metal-oxide-metal-oxide mixtures. It was shown, that when added in an optimal ratio, the *p*-type sensing behavior of Cr_2O_3 could be enhanced. It was postulated that this enhancement is a result of an increased surface reactivity and change in the conduction mechanism. From this study, it can be seen that metal-oxide-metal-oxide, using mechanically mixed oxide samples, is a feasible method to produce sensitive *p*-type samples.

Conclusion

The goal of this work was to examine different possibilities of creating sensors that show complementarity to SnO_2. Based on literature, there were strong indications that WO_3 was suited as a base material. There was, however, no work which examined how variations in morphology and preparation route affected this behavior. Through a systematic study of different WO_3 samples, inherent sensor characteristics of the material were identified. It was found that the interaction between the test gas and the surface vacancies plays a dominant role in sensing with WO_3. This finding explains the homogeneity of the samples (little effect on sensing behavior originating from e.g. surface hydroxyl groups) and the very different behavior of WO_3 to humidity in comparison to SnO_2. It was found that water oxidizes the surface of tungsten trioxide at 300 °C, resulting in the release of hydrogen.

It was examined if the complementarity of the samples could be enhanced through surface loading, a commonly applied method to tune the sensing characteristics. Here, the effect of platinum and rhodium surface clusters on WO_3 was examined. For

the first time, it was possible to prove the Fermi level pinning mechanism already suggested by Yamazoe and Morrison in the 1980s [97–99]. It was proven using the inputs from different sophisticated analytical methods: Information of the sample on average attained using operando infrared and x-ray absorption spectroscopy was coupled with localized visual information from in situ TEM. As a result, it was shown that the sensing behavior is dominated by the noble metal oxide clusters and not the base material. This hypothesis was validated by the fact that the sensor qualities of SnO_2 and WO_3 become more similar as a result of loading with rhodium.

Finally it was examined, whether the sensing behavior can be diversified by creating composite materials. In literature, it is widely reported that the mixing metal oxides can result in improved sensing behavior. Specifically the combination of Cr_2O_3 with SnO_2 in CSNs was found to result in enhanced *p*-type sensor behavior. In literature, the origin of the improved sensor response was unclear. In many reports without experimental verification, however, the importance of the CSN-structure was stressed. Here, in order to unravel the different aspects, Cr_2O_3-SnO_2 samples with and without the secondary morphology were examined. By comparing fibers with the sample in which the secondary morphology had been broken using only a mortar and pestle, it was possible to ensure that any detected differences were not as a result of variation in the preparation method or surface chemistry. Surprisingly, it was found that the secondary morphology, only negligibly changes the sensor behavior. Additionally, the results indicate that the enhanced *p*-type response of the sensors can solely be attributed to the contacts between the different oxides.

In conclusion, the results presented here provide the following practical inputs for the use of metal oxide gas sensors. It was found that there is a natural diversity in the sensing behavior of the different metal oxide base materials, WO_3 and SnO_2. This complementarity is diminished through the addition of noble metal oxide clusters (the chemistry is dominated by the additive). It is possible to enhance the sensor response of materials, e.g. *p*-type oxides, by combining them with other oxides. Here, simply mixing the two oxide materials is sufficient. A secondary morphology in which the grains are rowed in porous structures, e.g. nanofibers, has no significant effect. Instead the ratio between the two oxides and the resulting contacts dominates the sensing behavior.

Bibliography

[1] T. Seiyama, A. Kato, K. Fujishi, M. Nagatani, A New Detector for Gaseous Components Using Semiconductive Thin Films, Anal. Chem. (1962) 2–3. doi:https://doi.org/10.1021/ac60191a001.

[2] N. Taguchi, Gas-Detecting Device, US3695848, 1971.

[3] G. Neri, First Fifty Years of Chemoresistive Gas Sensors, Chemosensors. 3 (2015) 1–20. doi:10.3390/chemosensors3010001.

[4] K. Ihokura, J. Watson, The Stannic Oxide Gas Sensor - Principles and Application, CRC Press, Boca Raton, Florida, 1994.

[5] G. Wiegelb, J. Heitbaum, Semiconductor gas sensor for detecting NO and CO traces in ambient air of road traffic, Sensors Actuators B. 17 (1994) 93–99. doi:https://doi.org/10.1016/0925-4005(94)87035-7.

[6] H. Nakagawa, S. Okazaki, S. Asakura, K. Fukuda, H. Akimoto, H. Takahashi, S. Shigemori, An automated car ventilation system, Sensors Actuators B. (2000) 133–137.

[7] J. Marek, H.-P. Trah, Y. Suzuki, I. Yokomori, Sensor Applications: Sensors for Automotive Applications, 4th ed., WILEY-VCH Verlag, 2003.

[8] N. Barsan, G. Gauglitz, A. Oprea, E. Osterberg, G. Proll, K. Rebner, K. Schierbaum, F. Schleifenbaum, U. Weimar, Chemical and Biochemical Sensors, in: Ullmann's Encycl. Ind. Chem., Wiley VCH GmbH & Co KGaA., 2016.

[9] J.W. Gardner, A. Pike, N.F. de Rooij, M. Koudelka-Hep, P.A. Clerc, A. Hierlemann, W. Göpel, Integrated Array Sensor for Detecting Organic Solvents, Sens. Actuators B. Chem. 26 (1995) 135–139. doi:10.1016/0925-4005(94)01573-Z.

[10] Automatic HVAC Air Recirculation Made Easy with Stepper Motors, (2014) 9. http://www.onsemi.com/pub_link/Collateral/TND416-D.PDF.

[11] Grandview Research, Gas Sensor Market Size and Share | Global Industry Report, 2019-2025, Gd. Res. (2019) 2019–2025. https://www.grandviewresearch.com/industry-analysis/gas-sensors-market?

[12] D. Rüffer, F. Hoehne, J. Bühler, New Digital Metal-Oxide (MOx) Sensor Platform, Sensors (Basel). 18 (2018). doi:10.3390/s18041052.

[13] A.T. Güntner, S. Abegg, K. Königstein, P.A. Gerber, A. Schmidt-Trucksäss, S.E. Pratsinis, Breath sensors for health monitoring, ACS Sensors. 4 (2019) 268–280. doi:10.1021/acssensors.8b00937.

[14] G.P. Wang L, Flame Spray Synthesis of WO_3 for NO Breath Monitors, J. Mater. Sci. Eng. 04 (2015) 3–5. doi:10.4172/2169-0022.1000165.

[15] Indoor Air Monitor, (2015). https://www.airqualitymonitor.ch/?gclid=EAIaIQobChMIsfn2wcem3QIVWouyCh0uuAtUEAAYAyAAEgJPNPD_BwE.

[16] K. Izawa, A. Staerz, U. Weimar, Chapter 5: Applications, in: N. Barsan (Ed.), Gas Sensors Based Conduct. Met. Oxides Basic Understanding, Technol. Appl., Elsevier Science Publishing Co Inc, United States, 2018: pp. 217–262.

[17] J. Burgués, S. Marco, Low power operation of temperature-modulated metal oxide semiconductor gas sensors, Sensors (Switzerland). 18 (2018). doi:10.3390/s18020339.

[18] WHO Regional Office for Europe, Guidelines for indoor air quality, 2010. doi:10.1186/2041-1480-2-S2-I1.

[19] Government of Canada, Residential Indoor Air Quality Guidelines, 2018. http://healthycanadians.gc.ca/healthy-living-vie-saine/environment-environnement/air/guidelines-lignes-directrices-eng.php#a1.

[20] C. Deng, J. Zhang, X. Yu, W. Zhang, X. Zhang, Determination of acetone in human breath by gas chromatography-mass spectrometry and solid-phase microextraction with on-fiber derivatization, J. Chromatogr. B Anal. Technol. Biomed. Life Sci. 810 (2004) 269–275. doi:10.1016/j.jchromb.2004.08.013.

[21] T. Hyodo, T. Kaino, T. Ueda, K. Izawa, Y. Shimizu, Acetone-Sensing Properties of WO3 based

Gas Sensors Operated in Dynamic Temperature Modulation Mode - Effects of Loading of Noble Metal and / or NiO onto WO3-, Sensors Mater. 28 (2016) 1179–1189. doi:10.18494/SAM.2016.1279.

[22] A.T. Güntner, N.A. Sievi, S.J. Theodore, T. Gulich, M. Kohler, S.E. Pratsinis, Noninvasive Body Fat Burn Monitoring from Exhaled Acetone with Si-doped WO_3 -sensing Nanoparticles, Anal. Chem. 89 (2017) 10578–10584. doi:10.1021/acs.analchem.7b02843.

[23] K. Persaud, G. Dodd, Analysis of Discrimination Mechanisms in the Mammalian Olfactory System Using a Model Nose, Nature. 299 (1982) 352–355. doi:10.1038/299352a0.

[24] H.-J. Kim, J.-H. Lee, Highly sensitive and selective gas sensors using p-type oxide semiconductors: Overview, Sens. Actuators B. Chem. 192 (2014) 607–627. doi:10.1016/j.snb.2013.11.005.

[25] V.E. Bochenkov, G.B. Sergeev, Chapter 2: Sensitivity , Selectivity , and Stability of Gas-Sensitive Metal-Oxide Nanostructures, in: Met. Oxide Nanostructures Their Appl., American Scientific Publishers, 2010: pp. 31–52.

[26] R. Jaaniso, O.K. Tan, eds., Semiconductor Gas Sensors, Woodhead Publishing Series in Electric and Optical Materials, 2013.

[27] U.W. Alexander Gurlo, Nicolae Barsan, Metal Oxides: Chemistry and Applications, in: J.L.G. Fierro (Ed.), 2006: pp. 683–730. https://www.crcpress.com/Metal-Oxides-Chemistry-and-Applications/Fierro/9780824723712.

[28] T. Beckera, S. Ahlers, C. Bosch-v.Braunmuehl, G. Mueller, O. Kiesewetter, Gas sensing properties of thin- and thick- tin -oxide materials, Sensors Actuators B Chem. 77 (2001) 55–61. doi:https://doi.org/10.1016/S0925-4005(01)00672-4.

[29] N. Barsan, U. Weimar, Conduction model of metal oxide gas sensors, J. Electroceramics. 7 (2001) 143–167. doi:10.1023/A:1014405811371.

[30] N. Barsan, U. Weimar, M. Hübner, Chapter 2: Conduction mechanisms in semiconducting metal oxides sensing films: impact on transduction, in: Semicond. Gas Sensors, Woodhead Publishing Limited, 2013: pp. 35–63. doi:10.1533/9780857098665.1.35.

[31] P. Atkins, J. de Paula, Physical Chemistry, 8th ed., Oxford University Press, 2006.

[32] N. Barsan, M. Hübner, U. Weimar, Conduction mechanisms in SnO_2 based polycrystalline thick film gas sensors exposed to CO and H_2 in different oxygen backgrounds, Sensors Actuators, B Chem. 157 (2011) 510–517. doi:10.1016/j.snb.2011.05.011.

[33] M. Hübner, C. Simion, A. Tomescu-Stănoiu, S. Pokhrel, N. Barsan, U. Weimar, Influence of humidity on CO sensing with p-type CuO thick film gas sensors, Sensors Actuators B Chem. 153 (2011) 347–353. doi:10.1016/j.snb.2010.10.046.

[34] N. Barsan, C. Simion, T. Heine, S. Pokhrel, U. Weimar, Modeling of sensing and transduction for p-type semiconducting metal oxide based gas sensors, J. Electroceramics. 25 (2010) 11–19. doi:10.1007/s10832-009-9583-x.

[35] S. Pokhrel, C. Simion, V. Quemener, N. Barsan, U. Weimar, Investigations of conduction mechanism in Cr_2O_3 gas sensing thick films by ac impedance spectroscopy and work function changes measurements, Sensors Actuators B Chem. 133 (2008) 78–83. doi:10.1016/j.snb.2008.01.054.

[36] M. Batzill, U. Diebold, The surface and materials science of tin oxide, Prog. Surf. Sci. 79 (2005) 47–154. doi:10.1016/j.progsurf.2005.09.002.

[37] N. Barsan, M. Schweizer-Berberich, W. Göpel, Fundamental and practical aspects in the design of nanoscaled SnO2 gas sensors : a status report, Fresenius J. Anal. Chem. 365 (1999) 287–304. doi:10.1007/s002160051490.

[38] S. Das, V. Jayaraman, SnO_2 : A comprehensive review on structures and gas sensors, Prog. Mater. Sci. 66 (2014) 112–255. doi:10.1016/j.pmatsci.2014.06.003.

[39] N. Barsan, D. Koziej, U. Weimar, Metal oxide-based gas sensor research: How to?, Sens. Actuators, B Chem. 121 (2007) 18–35. doi:10.1016/j.snb.2006.09.047.

[40] N. Barsan, U. Weimar, T. Chemistry, Fundamentals of Metal Oxide Gas Sensors, MCS 2012 – 14th Int. Meet. Chem. Sensors. (2012) 618–621. doi:10.5162/IMCS2012/7.3.3.

[41] M.H.M. Reddy, A.N. Chandorkar, E-beam deposited SnO2 , Pt -SnO2 and Pd-SnO2 thin films for LPG detection, Thin Solid Films. 349 (1999) 260–265. doi:10.1016/S0040-6090(99)00194-7.
[42] D. Kohl, Surface Processes in the Detection of Reducing Gases with SnO2-based Devices, Sensors and Actuators. 18 (1989) 71–113. doi:10.1016/0250-6874(89)87026-X.
[43] W. Göpel, Solid-state chemical sensors: atomistic models and research trends, Sensors and Actuators. 16 (1989) 167–193. doi:10.1016/0250-6874(89)80015-0.
[44] A. Urakawa, Trends and advances in Operando methodology, Curr. Opin. Chem. Eng. 12 (2016) 31–36. doi:10.1016/j.coche.2016.02.002.
[45] D. Degler, Trends and Advances in the Characterization of Gas Sensing Materials Based on Semiconducting Oxides, Sensors. 18 (2018). doi:10.3390/s18103544.
[46] A. Staerz, I. Boehme, D. Degler, M. Bahri, D. Doronkin, A. Zimina, H. Brinkmann, S. Herrmann, B. Junker, O. Ersen, J.-D. Grunwaldt, U. Weimar, N. Barsan, Rhodium Oxide Surface-Loaded Gas Sensors, Nanomaterials. 8 (2018) 892. doi:10.3390/nano8110892.
[47] S. Emiroglu, N. Bârsan, U. Weimar, V. Hoffmann, In situ diffuse reflectance infrared spectroscopy study of CO adsorption on SnO_2, Thin Solid Films. 391 (2001) 176–185. doi:10.1016/S0040-6090(01)00979-8.
[48] R. Pohle, M. Fleischer, H. Meixner, Infrared emission spectroscopic study of the adsorption of oxygen on gas sensors based on polycrystalline metal oxide films, Sensors Actuators, B Chem. 78 (2001) 133–137. doi:10.1016/S0925-4005(01)00803-6.
[49] S. Harbeck, A. Szatvanyi, N. Barsan, U. Weimar, V. Hoffmann, DRIFT studies of thick film un-doped and Pd-doped SnO_2 sensors : temperature changes effect and CO detection mechanism in the presence of water vapour, Thin Solid Films. 436 (2003) 76–83. doi:10.1016/S0040-6090(03)00512-1.
[50] D. Koziej, Phenomenological and Spectroscopic Studies on Gas Detection Mechanism of Selected Gases with Tin Dioxide Based Sensors, Eberhard Karls University of Tuebingen, 2006.
[51] J. Sirita, S. Phanichphant, F.C. Meunier, Quantitative Analysis of Adsorbate Concentrations by Diffuse Reflectance FT-IR, Anal. Chem. 79 (2007) 3912–3918. doi:10.1021/ac0702802.
[52] J.M. Olinger, P.R. Griffiths, Quantitative Effects of an Absorbing Matrix on Near-Infrared Diffuse Reflectance Spectra, Anal. Chem. 60 (1988) 2427–2428. doi:10.1021/ac00172a022.
[53] M. Hübner, C.E. Simion, A. Haensch, N. Barsan, U. Weimar, CO sensing mechanism with WO_3 based gas sensors, Sensors Actuators B Chem. 151 (2010) 103–106. doi:10.1016/j.snb.2010.09.040.
[54] G. Heiland, D. Kohl, Physical and Chemical Aspects of Oxidic Semiconductor Gas Sensors, in: T. Seiyama (Ed.), Chem. Sens. Technol., 1st ed., Elsevier Science, 1992: pp. 43–88.
[55] G. Heiland, Zum einfluss von wasserstoff auf die elektrische leitfaehigkeit von ZnO-kristallen, Zeitschrift Für Phys. 148 (1957) 15–27.
[56] S. Wicker, M. Guiltat, U. Weimar, A. Hémeryck, N. Barsan, Ambient Humidity Influence on CO Detection with SnO_2 Gas Sensing Materials. A Combined DRIFTS/DFT Investigation, J. Phys. Chem. C. 121 (2017) 25064–25073. doi:10.1021/acs.jpcc.7b06253.
[57] D. Degler, S. Wicker, U. Weimar, N. Barsan, Identifying the active oxygen species in SnO_2 based gas sensing materials: an operando IR spectroscopy study, J. Phys. Chem. C. 119 (2015) 11792–11799. doi:10.1021/acs.jpcc.5b04082.
[58] S. Wicker, Influence of humidity on the gas sensing characteristics of SnO_2 - DRIFTS investigation of different base materials and dopants, University of Tuebingen, 2016.
[59] D. Koziej, M. Hübner, N. Barsan, U. Weimar, M. Sikora, J.-D. Grunwaldt, Operando X-ray absorption spectroscopy studies on Pd-SnO_2 based sensors, Phys. Chem. Chem. Phys. 11 (2009) 8620. doi:10.1039/b906829e.
[60] D. Degler, S.A. Müller, D.E. Doronkin, D. Wang, J.-D. Grunwaldt, U. Weimar, N. Barsan, Platinum Loaded Tin Dioxide: A Model System for Unravelling the Interplay between Heterogeneous Catalysis and Gas Sensing, J. Mater. Chem. A. (2018). doi:10.1039/C7TA08781K.
[61] S.A. Müller, D. Degler, C. Feldmann, M. Türk, R. Moos, K. Fink, F. Studt, D. Gerthsen, N. Bârsan, J.D. Grunwaldt, Exploiting Synergies in Catalysis and Gas Sensing using Noble Metal-Loaded

Oxide Composites, ChemCatChem. 10 (2018) 864–880. doi:10.1002/cctc.201701545.
[62] D. Degler, N. Barz, U. Dettinger, H. Peisert, T. Chassé, U. Weimar, N. Barsan, Extending The Toolbox For Gas Sensor Research: Operando UV/vis Diffuse Reflectance Spectroscopy On SnO2 -Based Gas Sensors, Sensors Actuators B Chem. 224 (2016) 256–259. doi:10.1016/j.snb.2015.10.040.
[63] L. Wang, T. A., S.E. Pratsinis, P.I. Gouma, Ferroelectric WO_3 Nanoparticles for Acetone Selective Detection, Chem. Mater. 20 (2008) 4794–4796. doi:10.1021/cm800761e.
[64] M. Righettoni, A. Amann, S.E. Pratsinis, Breath analysis by nanostructured metal oxides as chemo-resistive gas sensors, Mater. Today. 18 (2015) 163–171. doi:10.1016/j.mattod.2014.08.017.
[65] H. Long, W. Zeng, H. Zhang, Synthesis of WO_3 and its gas sensing: a review, J. Mater. Sci. Mater. Electron. (2015) 4698–4707. doi:10.1007/s10854-015-2896-4.
[66] X. Bai, H. Ji, P. Gao, Y. Zhang, X. Sun, Morphology, phase structure and acetone sensitive properties of copper-doped tungsten oxide sensors, Sensors Actuators, B Chem. 193 (2014) 100–106. doi:10.1016/j.snb.2013.11.059.
[67] C.L. Dai, M.C. Liu, F.S. Chen, C.C. Wu, M.W. Chang, A nanowire WO_3 humidity sensor integrated with micro-heater and inverting amplifier circuit on chip manufactured using CMOS-MEMS technique, Sensors Actuators, B Chem. 123 (2007) 896–901. doi:10.1016/j.snb.2006.10.055.
[68] S. Zhuiykov, E. Kats, K. Kalantar-zadeh, Enhanced electrical properties in sub-10-nm WO_3 nanoflakes prepared via a two-step sol-gel-exfoliation method, Nanoscale Res. Lett. 9 (2014) 401. doi:10.1186/1556-276X-9-401.
[69] X.-L. Li, T.-J. Lou, X.-M. Sun, Y.-D. Li, Highly Sensitive WO_3 Hollow-Sphere Gas Sensors, Inorg. Chem. 43 (2004) 5442–5449. doi:10.1021/ic049522w.
[70] T. Samerjai, N. Tamaekong, C. Liewhiran, A. Wisitsoraat, A. Tuantranont, S. Phanichphant, Selectivity towards H_2 gas by flame-made Pt-loaded WO_3 sensing films, Sensors Actuators, B Chem. 157 (2011) 290–297. doi:10.1016/j.snb.2011.03.065.
[71] H. Kawasaki, T. Ueda, Y. Suda, T. Ohshima, Properties of metal doped tungsten oxide thin films for NO_x gas sensors grown by PLD method combined with sputtering process, Sensors Actuators, B Chem. 100 (2004) 266–269. doi:10.1016/j.snb.2003.12.052.
[72] N.H. Kim, S.J. Choi, S.J. Kim, H.J. Cho, J.S. Jang, W.T. Koo, M. Kim, I.D. Kim, Highly sensitive and selective acetone sensing performance of WO_3 nanofibers functionalized by Rh_2O_3 nanoparticles, Sensors Actuators, B Chem. 224 (2016) 185–192. doi:10.1016/j.snb.2015.10.021.
[73] S. Pokhrel, C.E. Simion, V.S. Teodorescu, N. Barsan, U. Weimar, Synthesis, Mechanism, and Gas-Sensing Application of Surfactant Tailored Tungsten Oxide Nanostructures, Adv. Funct. Mater. 19 (2009) 1767–1774. doi:10.1002/adfm.200801171.
[74] S.M. Kanan, Z. Lu, J.K. Cox, G. Bernhardt, C.P. Tripp, Identification of surface sites on monoclinic WO_3 powders by infrared spectroscopy, Langmuir. 18 (2002) 1707–1712. doi:10.1021/la011428u.
[75] G. Ramis, C. Cristiani, A.S. Elmi, P. Villa, G. Busca, Characterization of the surface properties of polycrystaline WO_3, J. Mol. Catal. 61 (1990) 319–331. doi:10.1016/0304-5102(90)80006-5.
[76] M. Akiyama, J. Tamaki, N. Miura, N. Yamazoe, Tungsten Oxide-Based Semiconductor Sensor Highly Sensitive to NO and NO_2, Chem. Lett. (1991) 1611–1614. doi:10.1246/cl.1991.1611.
[77] J.S. Kim, J.W. Yoon, Y.J. Hong, Y.C. Kang, F. Abdel-Hady, A.A. Wazzan, J.H. Lee, Highly sensitive and selective detection of ppb-level NO_2 using multi-shelled WO_3 yolk-shell spheres, Sensors Actuators, B Chem. 229 (2016) 561–569. doi:10.1016/j.snb.2016.02.003.
[78] T. Kida, A. Nishiyama, Z. Hua, K. Suematsu, M. Yuasa, K. Shimanoe, WO_3 Nanolamella Gas Sensor: Porosity Control Using SnO_2 Nanoparticles for Enhanced NO_2 Sensing, (2014). doi:10.1021/la4049105.
[79] S.L. Baumann, Detektions-Mechanismen auf WO_3 bei Einsatz in Verbrennungsabgasen, Jutus Liebig Universität Gießen, 2003.

[80] T. Akamatsu, T. Itoh, N. Izu, W. Shin, NO and NO_2 sensing properties of WO_3 and Co_3O_4 based gas sensors., Sensors (Basel). 13 (2013) 12467–12481. doi:10.3390/s130912467.
[81] Anatoli Davydov, Molecular Spectroscopy of Oxide Catalyst Surfaces, Wiley VCH, 2003.
[82] D.E. Williams, S.R. Aliwell, K.F.E. Pratt, D.J. Caruana, R.L. Jones, R.A. Cox, G.M. Hansford, J. Halsall, Modelling the response of a tungsten oxide semiconductor as a gas sensor for the measurement of zone, Meas. Sci. Technol. 13 (2002) 923–931. doi:10.1088/0957-0233/13/6/314.
[83] M. Righettoni, A. Tricoli, S.E. Pratsinis, Thermally stable, silica-doped ε-WO_3 for sensing of acetone in the human breath, Chem. Mater. 22 (2010) 3152–3157. doi:10.1021/cm1001576.
[84] X. Ding, D. Zeng, S. Zhang, C. Xie, C-doped WO_3 microtubes assembled by nanoparticles with ultrahigh sensitivity to toluene at low operating temperature, Sensors Actuators, B Chem. 155 (2011) 86–92. doi:10.1016/j.snb.2010.11.030.
[85] B.K. Miremadi, R.C. Singh, Z. Chen, S. Roy Morrison, K. Colbow, Chromium oxide gas sensors for the detection of hydrogen, oxygen and nitrogen oxide, Sensors Actuators B. Chem. 21 (1994) 1–4. doi:10.1016/0925-4005(93)01208-L.
[86] H. Ma, Y. Xu, Z. Rong, X. Cheng, S. Gao, X. Zhang, H. Zhao, L. Huo, Highly toluene sensing performance based on monodispersed Cr_2O_3 porous microspheres, Sensors Actuators, B Chem. 174 (2012) 325–331. doi:10.1016/j.snb.2012.08.073.
[87] S.R. Morrison, Surface Satates on a Chromia Catalyst, J. Catal. 47 (1977) 69–78. doi:10.22201/fq.18708404e.2004.3.66178.
[88] X. Gao, Q. Zhou, Z. Lu, L. Xu, Q. Zhang, W. Zeng, Synthesis of Cr_2O_3 Nanoparticle-Coated SnO_2 Nanofibers and C_2H_2 Sensing Properties, Front. Mater. 6 (2019) 1–8. doi:10.3389/fmats.2019.00163.
[89] R.C. Singh, N. Kohli, M.P. Singh, O. Singh, Ethanol and LPG sensing characteristics of SnO_2 activated Cr_2O_3 thick film sensor, Bull. Mater. Sci. 33 (2010) 575–579. doi:10.1007/s12034-010-0088-7.
[90] C.H. Kwak, H.S. Woo, J.H. Lee, Selective trimethylamine sensors using Cr_2O_3- decorated SnO_2 nanowires, Sensors Actuators, B Chem. 204 (2014) 231–238. doi:10.1016/j.snb.2014.07.084.
[91] D. Degler, U. Weimar, N. Barsan, Current understanding of the fundamental mechanisms of doped and loaded semiconducting metal oxide-based gas sensing materials, ACS Sensors. (2019). doi:10.1021/acssensors.9b00975.
[92] Y. Shen, B. Zhang, X. Cao, D. Wei, J. Ma, L. Jia, S. Gao, B. Cui, Y. Jin, Microstructure and enhanced H_2S sensing properties of Pt-loaded WO_3 thin films, Sensors Actuators, B Chem. 193 (2014) 273–279. doi:10.1016/j.snb.2013.11.106.
[93] M. Horprathum, T. Srichaiyaperk, B. Samransuksamer, A. Wisitsoraat, P. Eiamchai, S. Limwichean, C. Chananonnawathorn, K. Aiempanakit, N. Nuntawong, V. Patthanasettakul, C. Oros, S. Porntheeraphat, P. Songsiriritthigul, H. Nakajima, A. Tuantranont, P. Chindaudom, Ultrasensitive hydrogen sensor based on Pt-decorated WO_3 nanorods prepared by glancing-angle dc magnetron sputtering, ACS Appl. Mater. Interfaces. 6 (2014) 22051–22060. doi:10.1021/am505127g.
[94] P.J. Shaver, Activated Tungsten Oxide Gas Detectors, Appl. Phys. Lett. 11 (1967) 255. doi:10.1063/1.1755123.
[95] A. Labidi, E. Gillet, R. Delamare, M. Maaref, K. Aguir, Ethanol and ozone sensing characteristics of WO_3 based sensors activated by Au and Pd, Sensors Actuators, B Chem. 120 (2006) 338–345. doi:10.1016/j.snb.2006.02.015.
[96] S. Kim, S. Park, S. Park, C. Lee, Acetone sensing of Au and Pd-decorated WO_3 nanorod sensors, Sensors Actuators B Chem. 209 (2015) 180–185. doi:10.1016/j.snb.2014.11.106.
[97] N. Yamazoe, New approaches for improving semiconductor gas sensors, Sensors Actuators B. 5 (1991) 7–19. doi:10.1016/0925-4005(91)80213-4.
[98] N. Yamazoe, Y. Kurokawa, T. Seiyama, Effects of Additives on Semiconductor Gas Sensors, Sensors Actuators B Chem. 4 (1983) 283–289. doi:10.1016/0250-6874(83)85034-3.
[99] S.R. Morrison, Selectivity in semiconductor gas sensors, Sensors Actuators B. 12 (1987) 425–440. doi:10.1016/0250-6874(87)80061-6.

[100] G. Korotcenkov, B.K. Cho, Metal oxide composites in conductometric gas sensors: Achievements and challenges, Sensors Actuators, B Chem. 244 (2017) 182–210. doi:10.1016/j.snb.2016.12.117.
[101] R. Khajavi, M. Abbasipour, Electrospinning as a versatile method for fabricating coreshell, hollow and porous nanofibers, Sci. Iran. 19 (2012) 2029–2034. doi:10.1016/j.scient.2012.10.037.
[102] H. Wang, L. Chen, Y. Feng, H. Chen, Exploiting Core- Shell Synergy for Nanosynthesis and Mechanistic Investigation, Acc. Chem. Res. 46 (2013) 1636–1646. doi:10.1021/ar400020j.
[103] Z.U. Abideen, J.H. Kim, J.H. Lee, J.Y. Kim, A. Mirzaei, H.W. Kim, S.S. Kim, Electrospun metal oxide composite nanofibers gas sensors: A review, J. Korean Ceram. Soc. 54 (2017) 366–379. doi:10.4191/kcers.2017.54.5.12.
[104] B. Ding, M. Wang, J. Yu, G. Sun, Gas sensors based on electrospun nanofibers, Sensors. 9 (2009) 1609–1624. doi:10.3390/s90301609.
[105] N. Yamazoe, K. Shimanoe, Chemical Basic approach to the transducer function of oxide semiconductor gas sensors, Sensors Actuators B. Chem. 160 (2011) 1352–1362. doi:10.1016/j.snb.2011.09.075.
[106] Kenry, C.T. Lim, Nanofiber technology: current status and emerging developments, Prog. Polym. Sci. 70 (2017) 1–17. doi:10.1016/j.progpolymsci.2017.03.002.
[107] T. Kida, A. Nishiyama, M. Yuasa, K. Shimanoe, N. Yamazoe, Highly sensitive NO_2 sensors using lamellar-structured WO_3 particles prepared by an acidification method, Sensors Actuators, B Chem. 135 (2009) 568–574. doi:10.1016/j.snb.2008.09.056.
[108] M. Epifani, T. Andreu, J. Arbiol, R. Díaz, P. Siciliano, J.R. Morante, Chloro-alkoxide route to transition metal oxides. Synthesis of WO_3 thin films and powders from a tungsten chloro-methoxide, Chem. Mater. 21 (2009) 5215–5221. doi:10.1021/cm902128r.
[109] Y. Ho Cho, Y. Chan Kang, J.H. Lee, Highly selective and sensitive detection of trimethylamine using WO_3 hollow spheres prepared by ultrasonic spray pyrolysis, Sensors Actuators, B Chem. 176 (2013) 971–977. doi:10.1016/j.snb.2012.10.044.
[110] M. Righettoni, S.E. Pratsinis, Annealing dynamics of WO_3 by in situ XRD, Mater. Res. Bull. 59 (2014) 199–204. doi:10.1016/j.materresbull.2014.07.018.
[111] E.K.H. Salje, S. Rehmann, F. Pobell, D. Morris, K.S. Knight, T. Herrmannsd, M.T. Dove, Crystal structure and paramagnetic behaviour of ε-WO_{3-x}, J. Phys. Condens. Matter. 9 (1997) 6563–6577. doi:10.1088/0953-8984/9/31/010.
[112] E. Salje, The Orthorhombic Phase of WO_3, Acta Cryst. B. 33 (1977) 574–577. doi:10.1107/S0567740877004130.
[113] B.O. Loopstra, H.M. Rietveld, Further refinement of the structure of WO_3, Acta Crystallogr. Sect. B Struct. Crystallogr. Cryst. Chem. 25 (1969) 1420–1421. doi:10.1107/S0567740869004146.
[114] E. Roedel, A. Urakawa, S. Kureti, A. Baiker, On the local sensitivity of different IR techniques: Ba species relevant in NO(x) storage-reduction., Phys. Chem. Chem. Phys. 10 (2008) 6190–8. doi:10.1039/b808529c.
[115] V.B. Kumar, D. Mohanta, Formation of nanoscale tungsten oxide structures and colouration characteristics, Bull. Mater. Sci. 34 (2011) 435–442. doi:10.1007/s12034-011-0117-1.
[116] J. Pfeifer, C. Guifang, P. Tekula-Buxbaum, B. a. Kiss, M. Farkas-Jahnke, K. Vadasdi, A reinvestigation of the preparation of tungsten oxide hydrate WO_3, $1/3H_2O$, J. Solid State Chem. 119 (1995) 90–97. doi:10.1016/0022-4596(95)80013-F.
[117] E. Albanese, C. Di Valentin, G. Pacchioni, H_2O Adsorption on WO_3 and WO_{3-x} (001) Surfaces, ACS Appl. Mater. Interfaces. 9 (2017) 23212–23221. doi:10.1021/acsami.7b06139.
[118] M.F. Daniel, B. Desbat, J.C. Lassegues, Infrared and Raman Study of $W0_3$ Tungsten Trioxide and $W0_3x\ H_2O$ Tungsten Trioxide Hydrates Trioxides, J. Solid State Chem. 247 (1987) 235–247. doi:10.1016/0022-4596(87)90359-8.
[119] J.T. Szymanski, A.C. Roberts, The Crystal Structure of Tungstite, WO_3-H_2O, Can. Mineral. 22 (1984) 681–688.

[120] J.R. Günter, M. Amberg, H. Schmalle, Direct synthesis and single crystal structure determination of cubic pyrochlore-type tungsten trioxide hemihydrate, $WO_3 \cdot 0.5H_2O$, Mater. Res. Bull. 24 (1989) 289–292. doi:10.1016/0025-5408(89)90214-6 Get.

[121] B. Gerand, G. Nowogrocki, M. Figlarz, A new tungsten trioxide hydrate, $WO_3 \cdot 1/3H_2O$: Preparation, characterization, and crystallographic study, J. Solid State Chem. 38 (1981) 312–320. doi:10.1016/0022-4596(81)90062-1.

[122] T. Würger, W. Heckel, K. Sellschopp, S. Müller, A. Stierle, Y. Wang, H. Noei, G. Feldbauer, Adsorption of Acetone on Rutile TiO_2 : A DFT and FTIRS Study, J. Phys. Chem. C. 122 (2018) 19481–19490. doi:10.1021/acs.jpcc.8b04222.

[123] Y. Xia, B. Zhang, J. Ye, Q. Ge, Z. Zhang, Acetone-assisted oxygen vacancy diffusion on TiO_2(110), J. Phys. Chem. Lett. 3 (2012) 2970–2974. doi:10.1021/jz301293y.

[124] K.-I. Choi, S.-J. Hwang, Z. Dai, Y. Chan Kang, J.-H. Lee, Rh-catalyzed WO_3 with anomalous humidity dependence of gas sensing characteristics, RSC Adv. 4 (2014) 53130–53136. doi:10.1039/C4RA06654E.

[125] A. Al Mohammad, Synthesis , Separation and Electrical Properties of WO_{3-x} Nanopowders via Partial Pressure High Energy Ball-Milling, 116 (2009) 240–244. doi:10.12693/APhysPolA.116.240.

[126] D.S. Venables, M.E. Brown, Reduction of tungsten oxides with hydrogen and with hydrogen and carbon, Thermochim. Acta. 285 (1996) 361–382. doi:10.1016/0040-6031(96)02951-6.

[127] A. Klein, C. Körber, A. Wachau, F. Säuberlich, Y. Gassenbauer, S.P. Harvey, D.E. Proffit, T.O. Mason, Transparent Conducting Oxides for Photovoltaics: Manipulation of Fermi Level, Work Function and Energy Band Alignment, Materials (Basel). 3 (2010) 4892–4914. doi:10.3390/ma3114892.

[128] B. Dillmann, F. Rohr, O. Seiferth, G. Klivenyi, M. Bender, K. Homann, I.N. Yakovkin, D. Ehrlich, M. Bäumer, H. Kuhlenbeck, H.-J. Freund, Adsorption on a polar oxide surface: O_2, C_2H_4 and Na on Cr_2O_3(0001)/Cr(110), Faraday Discuss. 105 (1996) 295–315. doi:10.1039/FD9960500295.

[129] K.K. Singh, K.K. Senapati, C. Borgohain, K.C. Sarma, Newly developed Fe_3O_4–Cr_2 O_3 magnetic nanocomposite for photocatalytic decomposition of 4-chlorophenol in water, J. Environ. Sci. 52 (2017) 333–340. doi:10.1016/j.jes.2015.01.035.

[130] A. Staerz, T. Suzuki, U. Weimar, N. Barsan, SnO_2: The most important base material for semiconducting metal-oxide based materials, in: Tin Oxide Mater., 1st ed., Elsevier, 2019: pp. 345–377.

[131] A. Staerz, T.-H. Kim, J.-H. Lee, U. Weimar, N. Barsan, Nanolevel Control of Gas Sensing Characteristics via p–n Heterojunction between Rh_2O_3 Clusters and WO_3 Crystallites, J. Phys. Chem. C. 121 (2017) 24701–24706. doi:10.1021/acs.jpcc.7b09316.

[132] A. Staerz, Y. Liu, U. Geyik, H. Brinkmann, U. Weimar, T. Zhang, The effect of platinum loading on WO_3 based sensors, Sens. Actuators B. Chem. 291 (2019) 378–384. doi:10.1016/j.snb.2019.04.088.

[133] I. Boehme, S. Herrmann, A. Staerz, H. Brinkmann, U. Weimar, Understanding the sensing mechanism of Rh_2O_3 loaded In_2O_3, Proceedings. 2 (2018).

Acknowledgements

I would like to thank my two advisers, Dr. Nicolae Barsan and Prof. Udo Weimar for all of the opportunities you have given me. I have learned to love research during my time in the group.

I would like to thank all the members of the thesis defense committee, Prof. Reinhold Fink, Prof. Atsushi Urakawa and Dr. Marcus Scheele. I would like to thank Prof. Elisabetta Comini for taking the time to write a review of the thesis.

I would like to thank Dr. Alexandru Oprea for always taking the time to help me. I would also like to thank you for all of the knowledge you have shared with me during different projects.

I would like to thank Jochen Mehne, without you my time as a lab assistant would have been much less enjoyable.

I would like to thank Ute Harbusch, Diana Strauß, Egon Merz, and Helen Donath for all of your help and for your patience with my slightly unorganized manner.

I would like to thank all of the additional support I have received during my research. To Prof. Tetsuya Kida, thank you for allowing me to spend three months in your lab and for all of the interesting scientific discussions. To Takeshi Shinkai, Azzah Pramata, Soreli Issasi, Agutaya Jonas Christopher Nuevas, Maria Christina Arboleda, Farhan Haqeem, and Fitrie Anastasia, thank you for making me feel very welcome. To the Japan Society for the Promotion of Science, thank you for financing my stay in Kumamoto, Japan. To Prof. Huan Liu and Prof. Hua-Yao Li, thank you for making me feel welcome in your group during my stay in Wuhan and for allowing me to hold the presentation on infrared spectroscopy. To Zhixiang Hu, Jingyao Liu, Li Long, Bohui Zhai and Licheng Zhou, thank you for showing me around Wuhan. To Anne Hémeryck, thank you for your hospitality during my visit to Toulouse. To Prof. Jong-Heun Lee, thank you for the fruitful scientific exchange and all of the support during the job application process. To Tae Hyung Kim, thank you for the good teamwork during your stay in Tübingen. To Prof. Tong Zhang, Yunshi Liu and Gao Xing, thank you for providing all of the interesting samples and for the very warm welcome I received in Changchun. To Mauro Epifani and Simona Somacescu, thank you for the very interesting samples and inputs to the DRIFT results. To Mounib Bahri and Ovidiu Ersen, thank you for the successful cooperation. To Dmitry Doronkin, Anna Zimina, and Jan-Dierk Grunwaldt, thank you for helping me examine my samples using XAS. To Christoph Berthold and Frieder Lauxmann, thank you for all of the support with XRD measurements. To Elke Nadler, Markus Turad and Ronny Löffler, thank you for helping me examine my samples with SEM. To all the project partners in ‘‘The Burning Bus Project’’ and ‘‘Präbea’’ for the interesting discussions and topics.

I would like to thank all of my office buddies. To Jens Kemmler, Susanne Wicker and David Degler, thank you for warmly welcoming me into the office. To Inci Boehme, thank you for

creating such a fun and familiar office feeling. To Tamara Ruß, thank you for the countless hours of proof reading and for all of the fun adventures we have had together. To Benjamin Junker and Arne Kobald, thank you for all of the constructive office discussions.

I would like to thank all of my colleagues. To Peter Bonanati, Andre Sackmann, Alexander Haensch, and Leonard Pollak, thank you for solving all of my ‘’layer eight issues.’’ To Matthias Böpple and Ugur Geyik, thank you for all of the political and philosophical discussions.

I would like to thank all of the students I have had the opportunity to work with during my thesis. To Helena Brinkmann and Faruk Cetmi, thank you for the great work during your Zulassungsarbeit.

I would like to thank my semester colleagues. To Kim Flaig, thank you for always being ready to try new things and see new places. You are a friend for life. To Torben Saatkamp, Oliver Hess, Amiera Madani and Lea Mehl, thank you for all of the fun times we have had together and all of the support you have given me over the years.

I would like to thank everyone who made my time in Germany so wonderful. To my aunts, uncles, cousins and Traudl Neff, thank you for making me feel at home so far away from Colorado. To all of my great aunts and uncles, and the whole extended family in the Allgäu, thank you for always inviting me and for all of the good times we enjoyed together. To my godfather, Reginhard and his family for always checking in on me. To the whole Merz family, thank you for all of the nice trips we have had together and all of the wonderful weekends in Bittenfeld. To the whole Obergfell family, thank you for always helping me and welcoming me into the community. To Jörg Stark, thank you for helping me settle into life at the University and for all of the help with math. To Meike Tilebein, thank you for all of the encouragement over the years.

I would like to thank everyone in Colorado, even though I have been far away for so long going back always feels like coming home. To Ron, Janina, Paula, Al, Wendy, Heather and Shawn, thank you for being my American family. To Maureen, Jill, Liz, Matthew, Jeffery and Gavin, thank you for being friends for life. I know that, wherever I am in the world I can always count on you.

I would like to thank my family. To both of my grandmothers, Irene and Wally, thank you for the support throughout my life and for teaching me so much about my German heritage. To my little sister Sophie, thank you for always believing in me and making me laugh. I am glad to have you. To my parents, Uwe and Elisabeth, thank you for teaching me to believe in myself and never back away from a challenge. To Markus, thank you for always helping me see the bigger picture and for teaching me how to take time to enjoy life.

Hydrogen Production from Humidity using WO_3

Anna Staerz[1], Arne Kobald[1], Tamara Russ[1], Carolin Ewald[1], Udo Weimar[1], Anne Hémeryck[2] and Nicolae Barsan[1]

[1]Faculty of Science, Department of Chemistry, Institute of Physical and Theoretical Chemistry, Tuebingen University, Auf der Morgenstelle 15, 72076 Tuebingen, Germany

[2]LAAS-CNRS, Université de Toulouse, CNRS, UPS, 31400 Toulouse, France

Introduction

One challenge faced by society today is the production of enough energy to maintain a high living standard for the increasing world population[1]. Oil, coal and natural gas reserves are dwindling and global warming has become a concern[2]. The evolution of hydrogen from water is an attractive carbon-free alternative[2]. Different methods have been classically applied in order to address the high energy requirements of producing hydrogen from water; ranging from thermochemical conversion to photoelectrochemical water splitting[1–3]. The interaction between WO_3 and water has widely been examined for application in the oxygen evolution reaction[4,5]. Thermochemical gaseous water-splitting on WO_3 is, however, less examined. Typically, the two-step redox cycle consists of the endothermic thermal reduction of the metal oxide (typically requiring temperatures over 2200 °C) releasing oxygen followed by the exothermic oxidation of the reduced oxide with H_2O to generate H_2[2,6]. For thermochemical water splitting, bulk processes are usually considered[6]. Recently, however, Daeneke et al. reported that under irradiation, the surface reaction of a molybdenum sulfide and titanium oxide ink with atmospheric humidity resulted in water splitting[7]. As the ink can be coated onto any substrate, the authors argue that the hydrogen production from humidity is easy and inexpensive[7]. Using in operando diffuse reflectance infrared Fourier transform (DRIFT) spectroscopy, it was found that humidity exposure oxidizes the surface of WO_3 nanoparticles at 300 °C[8]. WO_3 is a reducible oxide that can have a high concentration of surface oxygen vacancies[9]. Here, it is examined if the oxidation of the surface of WO_3 results in subsequent hydrogen evolution.

Results

It is known that in the case of porous films made of nanopowder, the reaction between the atmospheric gas and the surface of the grains results in a detectable change of the resistance[10,11]. In the case of an *n*-type material like WO_3, an increase of the resistance is expected for oxidizing gases[12]. This effect is widely used for metal oxide based gas sensors[12–14]. The increase of the baseline resistance of porous WO_3 films at 300 °C in the presence of humidity is known[8,15,16].

Here, films (screen printed film thickness ca. 50 μm) prepared from different WO_3 nanomaterials were examined. In all cases, the film's resistance increases upon exposure to 10 % RH at an operation temperature of 300 °C, see Figure 1[16]. In the DRIFT spectra the bands attributed to tungsten-oxygen bonds are increasing for all samples[17,18]. This indicates that the oxidation of the surface by humidity is an

inherent quality of WO_3. For some samples, the formation of hydroxyl groups is also visible. The formation of the hydroxyl groups is either an intermediary step in the oxidation or a secondary reaction with the formed hydrogen. The formation of hydroxyl groups, however, is known to result in either a decrease of the resistance or no detectable change[19–21]. The oxidation of the surface is responsible for the detected increase of the resistance and is therefore the dominant reaction.

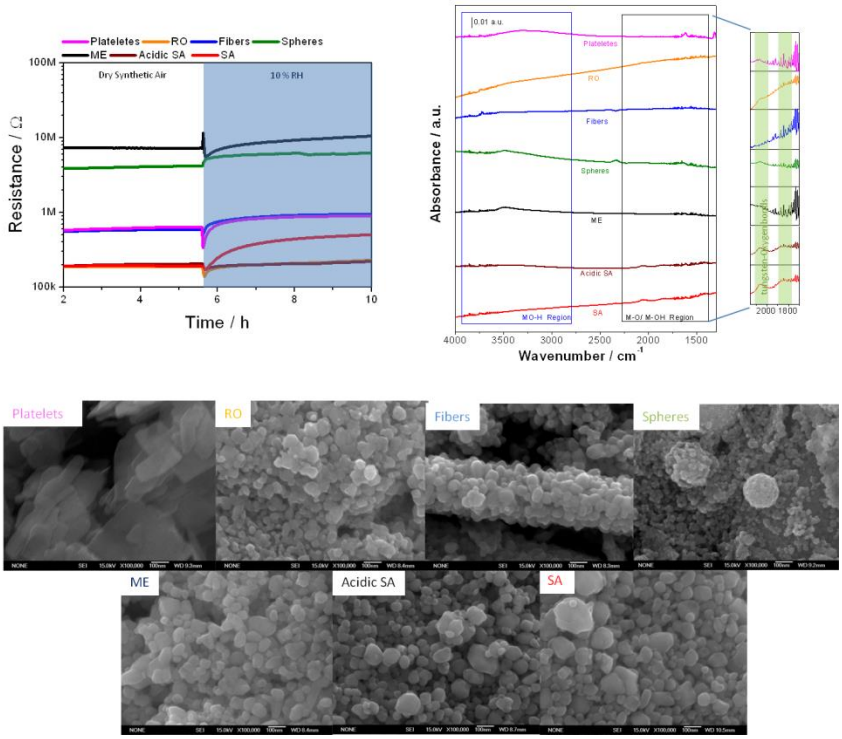

Figure 1: The change in resistance of the different films as a result of exposure to 10 %RH and the corresponding DRIFT spectra. SEM images of the different samples show the variation in morphology.

In order to identify the exact mechanism, a temperature study was done. For this study a film based on commercially available WO_3 powder (Sigma Aldrich, < 100 nm) was used because it showed the strongest oxidizing signal in the DRIFT spectra. The film was heated between 100 and 300 °C. Interestingly, at temperatures less than 175 °C (Figure 2, blue region) the presence of humidity results in a significant decrease of the film's resistance. Around 200 °C (Figure 2, purple region) there is a negligible effect on the resistance and around 300 °C (Figure 2, red region) the resistance is increasing. In order to understand the interaction between the surface of WO_3 and humidity, operando DRIFT spectroscopy was used.

At 125 °C, the bands attributed to overtones and combinations of the tungsten oxide lattice are decreasing. Additionally, increasing bands attributed to the stretching and bending vibrations of molecularly adsorbed water are visible around 3390 and 1620 cm^{-1}, respectively[22]. By using an isotope exchange, the absorption wavenumber of groups containing hydrogen will shift and can therefore be easily identified[23]. The water bands can be identified more clearly through the exchange with D_2O, at 2494 and 1191 cm^{-1}.

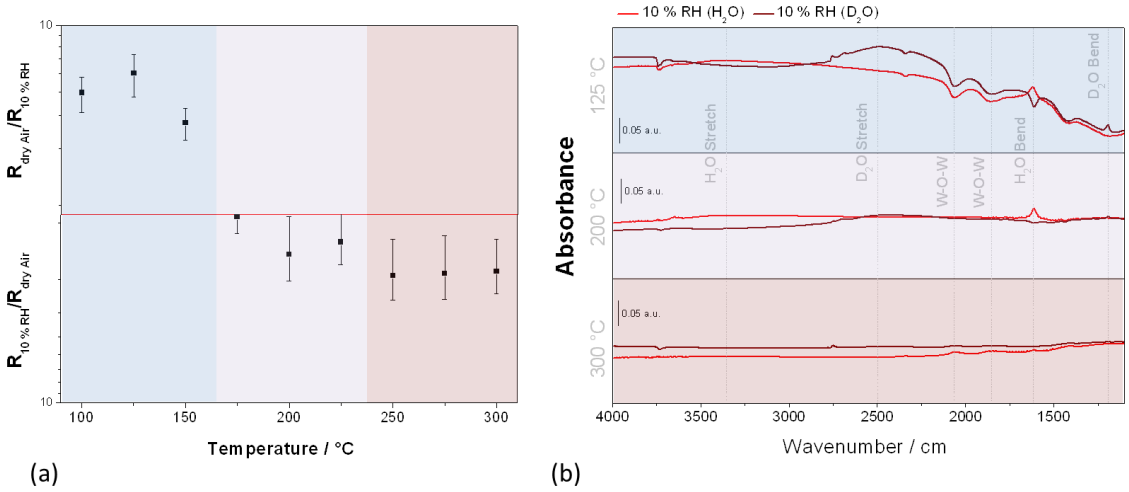

Figure 2: (a) The relative change in the resistance as a result of exposure to 10 % RH. The average of four identically prepared films was taken and the error calculated. (b) The DRIFT spectra taken of the film at three different temperatures during exposure first to 10 % RH (H_2O) followed by 10 % RH (D_2O). The reference state was the spectrum taken in dry synthetic air.

In order to support the measurements, DFT calculations were done. Here, the stoichiometric (001) β–WO_3 surface was modeled. WO_3 is known to have different temperature dependent crystal structures[24–26]. Based on operando XRD, see S. 1, at 300 °C the SA sample is in a mixed γ– and β–phase. As a control, and in order to examine the validity for γ–phase, the findings were compared to work of Albanese et al.[9] Here the bond between the terminal oxygen and tungsten has a length of 1.71 Å (compare Albanese et al. 1.69 Å). This oxygen is stable singly charged with one excess electron[9,27]. Based on theoretical calculations in literature, the dominant surface vacancy (V_0^C) results from the loss of this singly coordinated oxygen (O_{1C}^C)[9,27]. These vacancies are in constant equilibrium with the atmosphere. Based on the calculations, the adsorption of water molecularly into this vacancy is energetically favorable with ΔE_{ads} = -0.75 eV and a distance between the oxygen of water and tungsten of 2.29 Å (compare Albanese et al. ΔE_{ads} =-1.05 eV and a distance between the oxygen of water and tungsten 2.38 Å)[9]. The adsorption of an oxygen molecule into the V_0^C, with ΔE_{ads} = -0.41 eV and a distance between oxygen and tungsten of 1.80 Å is energetically less favorable than that of water. As their work was meant to provide insight into processes occurring in aqueous medium, Albanese et al., did not examine the adsorption energy of molecular oxygen into the vacancy [9]. These calculations and the DRIFT spectra indicate that at 125 °C, the molecularly adsorbed water hinders the equilibrium of the surface with atmospheric oxygen. Overtime, the singly negatively charged surface oxygen is replaced by a neutral water molecule, explaining the detected change of the film's resistance. It is known that water can be integrated into the lattice of WO_3[22], but the reaction here is surface based (no change in operando XRD, see S. 2).

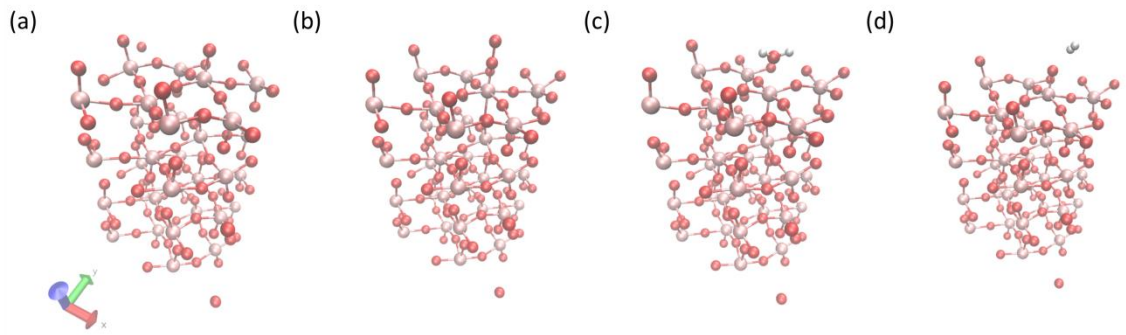

Figure 3: (a) The stoichiometric (001) β-WO_3 surface. (b) Adsorption of O_2 into V_0^C. (C) Adsorption of H_2O into V_0^C. (d) Adsorption of H_2 onto a single terminal oxygen.

In the spectra at 300 °C, the bands attributed to the overtones and combinations of the WO_3 lattice are increasing. At this temperature, the bands attributed to molecularly adsorbed water are weakly visible. This, in addition to the detected increase of the resistance, indicates that the tungsten oxide surface is more oxidized in the presence of humidity. Albanese et al. examined the interaction between the WO_3 surface and hydrogen. They found the tendency of hydrogen to dissociate on the terminal oxygen (O_{1C}^C)[9], as the energetically most favorable interaction, with ΔE_{ads} = -0.56 eV (a similar energy was attained here, ΔE_{ads} = -0.48 eV).
In total, the results here indicate that at the gas-solid interface, the dominant reaction is the reverse of that suggested by Albanese et al.:

$$\mathbf{WO_3 + V_0^C + H_2O \rightarrow WO_3/(2H - O_0^C) \rightarrow WO_3 + H_2} \qquad \textbf{eq. 1}$$

At low temperatures the surface vacancy is filled by the oxygen of water (an exothermic process) and at higher temperatures; hydrogen is released into the atmosphere (an endothermic process). At 200 °C, the degree of molecular water adsorption and the subsequent surface oxidation/ release of hydrogen are similar. As a result the change of the films resistance is also low. In the DRIFT spectra, no change of the bands attributed to tungsten-oxygen bonds is visible.
In order to verify that at 300 °C water is split on the surface, i.e. the evolution of hydrogen, exhaust measurements were done. One gram of WO_3- powder was heated to 300 °C in a reactor. The powder was first exposed to dry synthetic air and then to 10% RH. The exhaust was monitored using a TGS2600 sensor (Figaro Engineering Inc., Japan). The sensor is highly sensitive to low concentrations of hydrogen[28]. As the sensor also responds to humidity the exhaust gas was dried using silica and molecular sieve before arriving at the sensor.

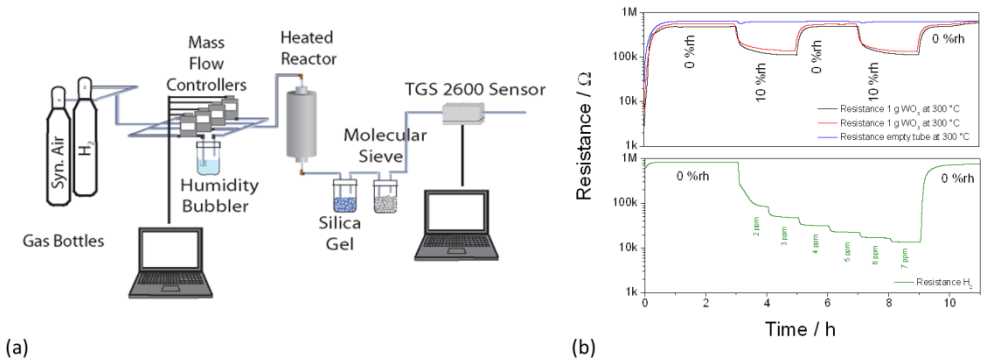

Figure 4: (a) Setup of the catalytic conversion measurements. 1g of WO_3 powder was heated to 300 °C and then exposed to 10% RH. The exhaust was dried using silica gel and molecular sieve and then monitored using a TGS2600 (Figaro Engineering Inc., Japan) metal oxide sensor. (b) The resistance of the TGS2600 sensor. The red and black lines are measurements done of a heated gram of WO_3. The blue line is the same measurement done without WO_3 (heated empty tube). The green line is the resistance change during exposure to different concentrations of hydrogen.

The sensor's responses during the exhaust measurements are shown in Figure 4. The red and black lines are measurements done with one gram of WO_3 in the reactor heated to 300 °C. The measurements were done twice with two samples to show that the results are reproducible and that the process is reversible. The blue line is the same measurement done without WO_3 (only a heated tube) to show that the sensor is not responding to residual humidity. The green line is a measurement done during gas pulses from a bottle, in order to show the response of the sensor to hydrogen. This shows that hydrogen is not eliminated by the molecular sieve or the silica gel. It also indicates that based on the response of the TGS2600 to the exhaust, that the reaction between WO_3 and humidity results in a production of over 1 ppm of H_2.The measurement indicates that the hydrogen evolution is constant and that once humidity is removed the process stops. In addition the measurement was repeated, and the same result is attained. Repetition of the measurement using the same sample showed the same response indicating that the process is fully reversible.
It was found that the oxidation of the surface nanoparticles is an inherent quality of WO_3. By coupling inputs from theoretical calculations, the resistance measurements, DRIFT spectroscopy and exhaust monitoring, it was possible to fully elucidate the mechanism: At low temperatures water absorbs molecularly onto the surface vacancies of WO_3, thus disturbing the equilibrium with atmospheric oxygen. At 300 °C, the surface vacancy is healed by the oxygen from water releasing hydrogen.

Methods

Film Preparation:

Films were made based on differently prepared WO_3 nanopowders. The Platelets were prepared using a variation of the preparation method developed by Kida et al. in which the acidic solution was brought to 100 °C.[29] The RO sample was prepared via a hydrothermal method using a nonionic surfactant- Birj 37- as a structural agent. The Fibers were prepared using electrospinning[30]. The Spheres were prepared using ultrasonic spray pyrolysis[31]. The sample labeled ME was prepared via a Chloro-

Alkoxide Route[32]. The SA sample was based on commercially available nanopowder (< 100nm, Sigma Aldrich). In the case of the acidic SA sample, the nanopowder was stirred in an acidic (HCl. at pH 1) for two hours[33]. The powders were mixed with 1,2-propanediol (Sigma-Aldrich, 99.5+% ACS reagent) and ground with mortar and pestle into a viscous paste which was printed using an EKRA Microtronic II onto an Alumina substrates containing platinum electrodes and a backside platinum heater (300 µm electrode gap, 300 µm width and 5 µm thickness; Ceramtec AG, Germany). The films were dried at room temperature for 1 h, overnight at 80 °C (Heraeus UT12) and then annealed for 10 min each at 400−500−400 °C in a tubular furnace (Heraeus ROK 6/30). The Platelets were only heated to a maximum of 400 °C. Based on the geometry of the screen, a final film thickness of 50 µm is achieved. The sensitive layers were characterized using a JOEL JSM-6500F Scanning Electron Microscopy (SEM) with an acceleration of 15kV, a probe current of 7 and a stage height of 10 mm.

The X-ray diffraction measurements of the heated films under humidity exposure were done using a BRUKER D8 discover GADDS microdiffractometer equipped with a Co-X-ray tube, HOPG-primary monochromator, X-ray optics and a large 2dimensional VANTEC-500 detector covering 40° 2Θ and 40° 2θ and 40° ψ allowing fast and locally resolved measurements of the film[8,34].

DC Resistance Measurements and Operando DRIFT Spectroscopy

The films are mounted into a homemade Teflon chamber and heated using a Agilent E3614A DC power source. The gas flow was regulated using a computer monitored mass flow controller unit. The resistance was monitored using a Keithley 6517B electrometer. For the operando DRIFT spectra, a Vertex80v with a mid-band mercury cadmium telluride (MCT) detector (Bruker, Billerica, MA, USA) and a spectral resolution of 4 cm^{-1} was used. The films were mounted in a homemade chamber with a KBr window. The films were heated and their resistance monitored simultaneously. A single-channel spectrum was recorded every 15 min. The absorbance spectra, was calculates using the relation suggested by Olinger and Griffiths[35]: In this case, bands that are decreasing in the absorbance spectra are attributed to groups that are leaving the surface as a result of exposure to humidity, while those that are increasing are being added.

Theoretical Calculations

The periodic calculations were performed using the DFT method based on the GGA approximation employing the PBE exchange−correlation functional as implemented in the plane-waves program VASP [20,36–38] The projector-augmented wave (PAW) potentials were applied for the core electron representation.[39,40] A converged value of E_{cut} = 500 eV was used asthe cutoff energy of the plane wave. The integration in reciprocal space was performed with a Monkhorst−Pack grid.[41] One simulation cell was used. The stoichiometric (001) β–WO_3 surface was modeled by the period slab shown in S2. The cell is composed of a total number of 128 atoms with 32 W- and 96 O- atoms. A vacuum zone of 15 Å in the z direction was used to create a surface effect. 16 W and 44 O atoms were frozen in their bulk positions at the bottom of the

cell to simulate a bulk effect [42]. All other atoms were free to relax. The periodic slab was repeated in the three directions. A k-point mesh of (4 × 4 x 1) was used. The energy of oxygen vacancy formation ΔE_O was calculates using the following relation:

$$\Delta E_O = E_{vac} + \frac{1}{2} E_{O_2} - E_{surface} \quad \text{eq. 2}$$

and the adsorption energies are calculated using the following formula:

$$\Delta E_{ads} = E_{adsorbed\ molecule} - E_{surface} - E_{gaseous\ molecule} \quad \text{eq. 3}$$

where E_{vac} is the energy of the surface with one terminal oxygen vacancy, E_{O_2} is the energy of the isolated spin polarized O_2, $E_{surface}$ is the total energy of the relaxed surface, $E_{gaseous\ molecule}$ is the total energy of the isolated gaseous molecule, $E_{adsorbed\ molecule}$ is the total energy of the system with a gaseous molecule adsorbed. The visualization of the cell was done using VMD[43]. Pictures were then rendered using POV-Ray[44].

Bibliography

1. Krol, R. van der & Grätzel, M. Photoelectro-chemical hydrogen Production. in (eds. Krol, R. van der & Grätzel, M.) (2012).
2. Tuller, H. L. Solar to fuels conversion technologies: A perspective. *Mater. Renew. Sustain. Energy* **6**, 1–16 (2017).
3. Appleby, A. J. Efficiencies of electrolytic and thermo- chemical hydrogen production. *Nature* **253**, 257–258 (1975).
4. Xin, G., Guo, W. & Ma, T. Effect of annealing temperature on the photocatalytic activity of WO3 for O2 evolution. *Appl. Surf. Sci.* **256**, 165–169 (2009).
5. Ji, X. *et al.* WO3 Nanoarray: An Efficient Electrochemical Oxygen Evolution Catalyst Electrode Operating in Alkaline Solution. *Inorg. Chem.* **56**, 14743–14746 (2017).
6. Abanades, S. Metal Oxides Applied to Thermochemical Water-Splitting for Hydrogen Production Using Concentrated Solar Energy. *ChemEngineering* **3**, 63 (2019).
7. Daeneke, T. *et al.* Surface Water Dependent Properties of Sulfur- Rich Molybdenum Sul fi des: Electrolyteless Gas Phase Water Splitting. (2017) doi:10.1021/acsnano.7b01632.
8. Staerz, A. *et al.* The Oxidizing Effect of Humidity on WO_3 based Sensors. *Sensors Actuators B Chem.* **237**, 54–58 (2016).
9. Albanese, E., Di Valentin, C. & Pacchioni, G. H_2O Adsorption on WO_3 and WO_{3-x} (001) Surfaces. *ACS Appl. Mater. Interfaces* **9**, 23212–23221 (2017).
10. Brattain, W. H. & Bardeen, J. Surface Properties of Germanium. *Bell Labs Tech. J.* **32**, (1953).
11. Seiyama, T., Kato, A., Fujishi, K. & Nagatani, M. A New Detector for Gaseous Components Using Semiconductive Thin Films. *Anal. Chem.* 2–3 (1962) doi:https://doi.org/10.1021/ac60191a001.
12. Barsan, N. & Weimar, U. Conduction model of metal oxide gas sensors. *J. Electroceramics* **7**, 143–167 (2001).
13. Taguchi, N. Gas-Detecting Device. (1971).
14. Neri, G. First Fifty Years of Chemoresistive Gas Sensors. *Chemosensors* **3**, 1–20 (2015).
15. Pokhrel, S., Simion, C. E., Teodorescu, V. S., Barsan, N. & Weimar, U. Synthesis, mechanism,

and gas-sensing application of surfactant tailored tungsten oxide nanostructures. *Adv. Funct. Mater.* **19**, 1767–1774 (2009).

16. Staerz, A. *et al.* WO3 Based Gas Sensors. *Proceedings* **2**, 2–5 (2019).
17. Kanan, S. M., Lu, Z., Cox, J. K., Bernhardt, G. & Tripp, C. P. Identification of surface sites on monoclinic WO_3 powders by infrared spectroscopy. *Langmuir* **18**, 1707–1712 (2002).
18. Ramis, G., Cristiani, C., Elmi, A. S., Villa, P. & Busca, G. Characterization of the surface properties of polycrystaline WO_3. *J. Mol. Catal.* **61**, 319–331 (1990).
19. Heiland, G. Zum einfluss von wasserstoff auf die elektrische leitfaehigkeit von ZnO-kristallen. *Zeitschrift für Phys.* **148**, 15–27 (1957).
20. Wicker, S., Guiltat, M., Weimar, U., Hémeryck, A. & Barsan, N. Ambient Humidity Influence on CO Detection with SnO_2 Gas Sensing Materials. A Combined DRIFTS/DFT Investigation. *J. Phys. Chem. C* **121**, 25064–25073 (2017).
21. Heiland, G. & Kohl, D. Physical and Chemical Aspects of Oxidic Semiconductor Gas Sensors. in *Chemical Sensor Technology* (ed. Seiyama, T.) 43–88 (Elsevier Science, 1992).
22. Daniel, M. F., Desbat, B. & Lassegues, J. C. Infrared and Raman Study of $W0_3$ Tungsten Trioxide and $W0_3x\ H_2O$ Tungsten Trioxide Hydrates Trioxides. *J. Solid State Chem.* **247**, 235–247 (1987).
23. Grossmann, K., Pavelko, R. G., Barsan, N. & Weimar, U. Interplay of H2 , water vapor and oxygen at the surface of SnO2 based gas sensors – An operando investigation utilizing deuterated gases. *Sensors Actuators, B Chem.* **166**–**167**, 787–793 (2012).
24. Arai, M., Hayashi, S. & Yamamoto, K. Raman studies of phase transitions in gas-evaporated WO3 microcrystals. *Solid State Commun.* **75**, 613–616 (1990).
25. Righettoni, M. & Pratsinis, S. E. Annealing dynamics of WO_3 by in situ XRD. *Mater. Res. Bull.* **59**, 199–204 (2014).
26. Salje, E. The Orthorhombic Phase of WO_3. *Acta Cryst. B* **33**, 574–577 (1977).
27. Jin, H., Zhou, H. & Zhang, Y. Insight into the Mechanism of CO Oxidation on WO3(001) Surfaces for Gas Sensing: A DFT Study. *Sensors* **17**, 1–12 (2017).
28. Figaro Engineering Inc. *Technical Information for TGS2600*. (2004).
29. Kida, T., Nishiyama, A., Yuasa, M., Shimanoe, K. & Yamazoe, N. Highly sensitive NO_2 sensors using lamellar-structured WO_3 particles prepared by an acidification method. *Sensors Actuators, B Chem.* **135**, 568–574 (2009).
30. Staerz, A. *et al.* The effect of platinum loading on WO_3 based sensors. *Sens. Actuators B. Chem.* **291**, 378–384 (2019).
31. Staerz, A., Kim, T.-H., Lee, J., Weimar, U. & Barsan, N. Nano-level Control of Gas Sensing Characteristics via p-n Heterojunction between Rh2O3 Clusters and WO3 Crystallites. *J. Phys. Chem. C*.
32. Epifani, M. *et al.* Solvothermal, Chloroalkoxide-based Synthesis of Monoclinic WO 3 Quantum Dots and Gas-Sensing Enhancement by Surface Oxygen Vacancies. (2014) doi:10.1021/am504158r.
33. Staerz, A. *et al.* Rhodium Oxide Surface-Loaded Gas Sensors. *Nanomaterials* **8**, 892 (2018).
34. Berthold, C., Bjeoumikhov, A. & Brügemann, L. Fast XRD2 Microdiffraction with Focusing X-Ray Microlenses. *Part. Part. Syst. Charact.* **26**, 107–111 (2009).
35. Olinger, J. M. & Griffiths, P. R. Quantitative Effects of an Absorbing Matrix on Near-Infrared Diffuse Reflectance Spectra. *Anal. Chem.* **60**, 2427–2428 (1988).
36. Kresse, G. & Hafner, J. Ab initio molecular-dynamics simulation of the liquid-metal–amorphous-semiconductor transition in germanium. *Phys. Rev. B* **49**, 14251–14269 (1994).
37. Kresse, G. & Furthmüller, J. Efficiency of ab-initio total energy calculations for metals and

semiconductors using a plane-wave basis set. *Comput. Mateials Sci.* **6**, 15–50 (1996).

38. Perdew, J. P., Ernzerhof, M. & Burke, K. Rationale for mixing exact exchange with density functional approximations. *J. Chem. Phys.* **105**, 9982–9985 (1996).
39. Joubert, D. From ultrasoft pseudopotentials to the projector augmented-wave method. *Phys. Rev. B - Condens. Matter Mater. Phys.* **59**, 1758–1775 (1999).
40. Blochl, P. E. Projector augmented-wave method. **50**, (1994).
41. Monkhorst, H. J. & Pack, J. D. Special points for Brillouin-zone integrations. *Phys. Rev. B* **13**, 5188–5192 (1976).
42. Köhler, L. & Kresse, G. Density functional study of CO on Rh(111) [78]. *Phys. Rev. B - Condens. Matter Mater. Phys.* **70**, 1–9 (2004).
43. Humphrey, W., Dalke, A. & Schulten, K. VMD: Visual molecular dynamics. *J. Mol. Graph.* **14**, 33–38 (1996).
44. Persistence of Vision Raytracer. (2004).
45. Loopstra, B. O. & Rietveld, H. M. Further refinement of the structure of WO $_3$. *Acta Crystallogr. Sect. B Struct. Crystallogr. Cryst. Chem.* **25**, 1420–1421 (1969).
46. Szymanski, J. T. & Roberts, A. C. the Crystal Structure of Tungsttte, WO3-H2O. *Can. Mineral.* **22**, 681–688 (1984).
47. Günter, J. R., Amberg, M. & Schmalle, H. Direct synthesis and single crystal structure determination of cubic pyrochlore-type tungsten trioxide hemihydrate, $WO_3 \cdot 0.5H_2O$. *Mater. Res. Bull.* **24**, 289–292 (1989).
48. Gerand, B., Nowogrocki, G. & Figlarz, M. A new tungsten trioxide hydrate, $WO_3 \cdot 1/3H_2O$: Preparation, characterization, and crystallographic study. *J. Solid State Chem.* **38**, 312–320 (1981).

Supplementary information:

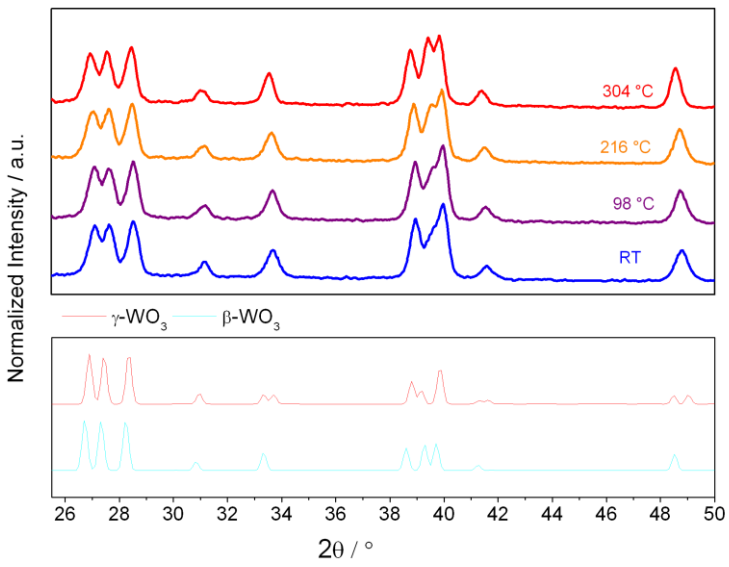

S. 1: Temperature dependent XRD of the film based on SA. The attained diffractograms are compared to those of β-WO_3[26] and γ-WO_3[45].

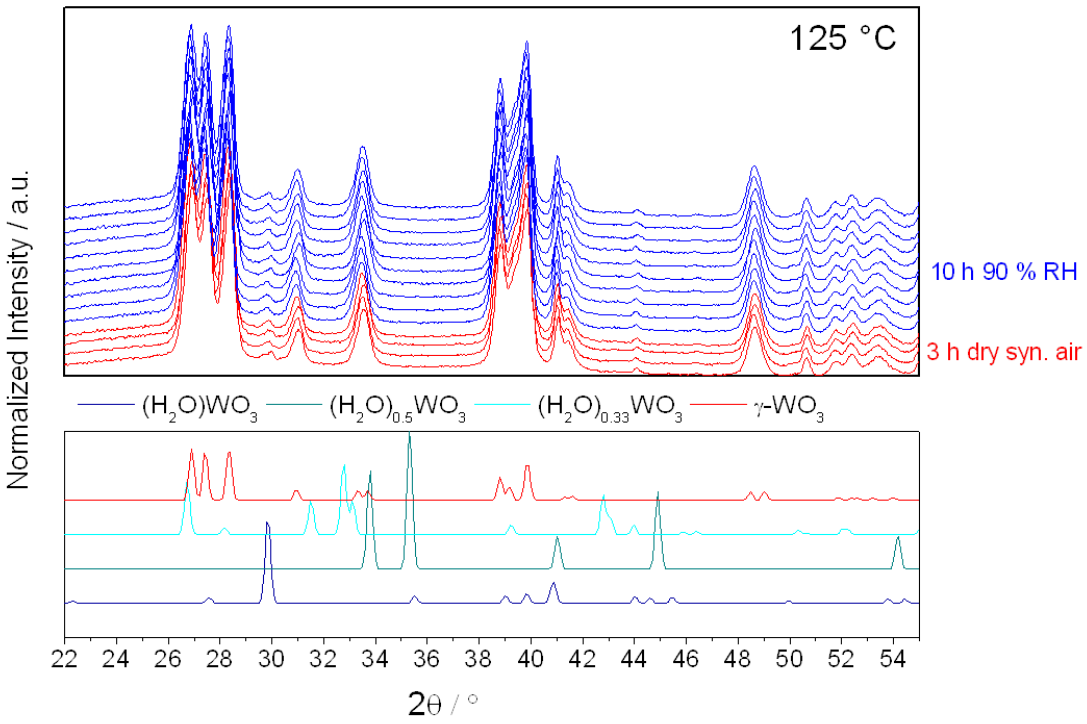

S. 2 Operando XRD of a SA sensor operated at 125 °C during an initial 3 h exposure to dry synthetic air and then to 90 %RH. The attained diffractograms are compared to those of $(H_2O)WO_3$ [46], $(H_2O)0.5WO_3$ [47], $(H_2O)0.33WO_3$ [48] and γ-WO_3 [45].

ACS SENSORS

pubs.acs.org/acssensors Article

WO_3-Based Gas Sensors: Identifying Inherent Qualities and Understanding the Sensing Mechanism

Anna Staerz, Simona Somacescu, Mauro Epifani, Tetsuya Kida, Udo Weimar, and Nicolae Barsan*

Cite This: https://dx.doi.org/10.1021/acssensors.0c00113 Read Online

ACCESS | Metrics & More | Article Recommendations | Supporting Information

ABSTRACT: Semiconducting metal oxide-based gas sensors are an attractive option for a wide array of applications. In particular, sensors based on WO_3 are promising for applications varying from indoor air quality to breath analysis. There is a great breadth of literature which examines how the sensing characteristics of WO_3 can be tuned via changes in, for example, morphology or surface additives. Because of variations in measurement conditions, however, it is difficult to identify inherent qualities of WO_3 from these reports. Here, the sensing behavior of five different WO_3 samples is examined. The samples show good complementarity to SnO_2 (the most commonly used material)-based sensors. A surprising homogeneity, despite variation in morphology and preparation method, is found. Using operando diffuse reflectance infrared Fourier transform spectroscopy, it is found that the oxygen vacancies are the dominant reaction partner of WO_3 with the analyte gas. This surface chemistry is offered as an explanation for the homogeneity of WO_3-based sensors.

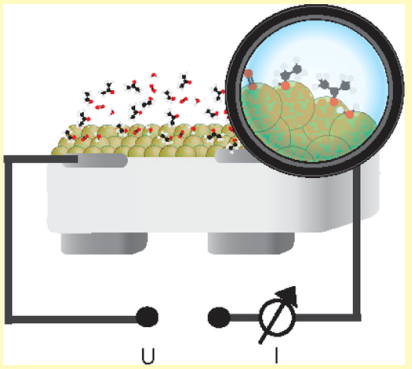

KEYWORDS: *WO_3, metal oxides, gas sensor, DRIFT spectroscopy, acetone, NO_2, humidity, CO*

Sensors based on semiconducting metal oxides (SMOXs) are attractive for a wide array of applications. They are robust, sensitive, and inexpensive. SMOX-based sensors were first developed in the 1960s.[1] The use of natural gas for cooking had become popular in Japan, resulting in an increased number of domestic gas explosions.[2] It was this situation that motivated Naoyoshi Taguchi to develop, and eventually patent, the first commercially available SMOX-based gas sensor.[3] Although they have been commercially available and optimized for over half a century,[4] SMOX-based sensors are inherently unselective, limiting their more widespread use.[4] A promising method to address this limitation is the use of sensor arrays, a combination of several complementary SMOX sensors.[5] Using readily available computing power, the outputs of arrays can be analyzed.[6] Certain gases can then be identified based on patterns instead of a single response.[5,7] This concept is already being implemented by the industry. In 2018, Rüffer et al. introduced the new Sensirion Gas Platform based on sophisticated electronics and sensitive layer deposition methods.[6] It contains four different SMOX materials, each measured separately using a read-out electrode that is deposited onto a 50 μm large hotplate.[6] In order to take full advantage of this versatile setup, however, a large diversity of sensitive materials is needed.[6] The first commercially available gas sensor developed by Taguchi was based on the *n*-type material SnO_2.[3,4] Over the last decades, a disproportionate amount of research has continued to concentrate on this base material.[8] As a result, most commercially available gas sensors are still based on SnO_2.[9] In fact, even in the highly sophisticated array presented by Rüffer et al. the sensitive layers were all based on SnO_2 modified with varying concentrations of Pd.[6] Even though it is possible to change the sensing behavior of SnO_2 through, that is, the addition of surface additives, operation temperature, and preparation methods, the resulting diversity is limited. In order to maximize the potential of arrays, a spectrum of different, well-characterized SMOX-based materials is vital.

Although significantly less investigated than SnO_2, there is literature examining the sensing behavior of WO_3. Already in 1967, Shaver reported a gas detector based on platinum-activated tungsten oxide.[10] Even today, most literature on WO_3-based sensors concentrates on samples activated with various noble metals, platinum,[10−13] palladium,[14,15] gold,[16−19] and rhodium.[20−22] For example, the addition of palladium,[23] gold,[18] and even carbon[24] reportedly results in an increased response to low concentrations of toluene. This is of interest for monitoring indoor air quality.[25] The outgassing of furniture results in increased indoor concentrations.[25] The Canadian government has set a short-term indoor air exposure limit of toluene at 4 ppm (0.015 mg/L).[25]

There are also reports that by controlling the morphology, desirable sensor qualities can be achieved. Nanolamellae of

Received: January 16, 2020
Accepted: April 9, 2020
Published: April 9, 2020

https://dx.doi.org/10.1021/acssensors.0c00113
ACS Sens. XXXX, XXX, XXX−XXX

WO_3 are reported to show a high response to NO_2.[26] NO_2 is an oxidizing gas that is found in low concentrations, between 2 and 10 ppm (0.004−0.019 mg/L), in the exhaust of diesel cars.[27] Favorably, unlike SnO_2, WO_3 is reported to show low cross sensitivity to CO, a reducing gas prominent in car exhaust, between 30 and 100 ppm (ca. 0.035−0.116 mg/L).[27−29] Based on operando diffuse reflectance infrared Fourier transform (DRIFT) spectroscopy performed on crystalline blocks of WO_3, it was found that CO reduces the surface of WO_3.[30−32] On the contrary, NO_2 is found to oxidize the surface.[30−32] In addition to an increase in the two bands attributed to tungsten−oxygen bonds, Akamatsu et al. reported a band at 1421 cm^{-1} which they tentatively attribute to the formation of nitrates.[33] The presence of humidity significantly decreases the response of WO_3 to NO_2, while the response to CO is reported to generally increase.[34] Remarkably, the resistance of WO_3 is found to increase in the presence of humidity.[34] This is the opposite behavior of SnO_2-based sensors, which either show a decrease or no change in the resistance as a result of humidity exposure.[35−37] Recently, based on DRIFT spectra, the oxidation of the surface by humidity was reported for a single WO_3 sample.[32] The decrease in the response to NO_2 was in turn attributed to competing surface oxidation.[32]

WO_3 is known to have six temperature-dependent crystal phases.[38] Variation in the crystal phase has also been reported to affect the sensing behavior of WO_3. In 2008, Wang et al. reported the stabilization of the ε-WO_3 phase at 300 °C (usually only stable under −40 °C) through the integration of Cr.[39] Righettoni et al. attained similar results using silica doping.[40] In both cases, the authors report that at an operation temperature of 300 °C, the ε-WO_3 phase shows a high response to low concentrations of acetone. For diabetes monitoring, a breath acetone concentration between 0.5 and 2 ppm (0.001−0.005 mg/L) is relevant.[41] The authors argue that the ferroelectric nature of ε-WO_3 is responsible for the high signals to acetone.[39] There are also, however, reports that sensors based on WO_3, in general, respond well to low concentrations of acetone.[42,43] In all cases, no examination of the surface chemistry was performed. Although SnO_2 is also found to respond to acetone, based on the prevalence of the literature, WO_3 appears to be the better-suited material.[44]

In conclusion, despite the large amount of literature examining WO_3, it is exceedingly difficult to identify inherent characteristics of the material. Most studies examine only a single sample and the test gases/conditions vary greatly between the different reports. Here, a thorough characterization of WO_3 as a gas-sensing material is presented. The responses of sensors based on differently prepared materials to five different test gases both in the presence and the absence of humidity are examined. The surface reactions of the samples with the different test gases were examined using operando DRIFT spectroscopy. By understanding which behavior is inherent to WO_3, it will be possible to accurately classify changes in the sensing response as a result of, for example, surface loading or morphology in the future. Additionally, it will be possible to understand if WO_3, in general, shows complementary sensing behavior to SnO_2.

EXPERIMENTAL SECTION

Sample Preparation. Sensors based on five different WO_3 samples were examined. The platelet sample was prepared using a variation in the preparation method developed by Kida et al.:[45] 191 mL of H_2SO_4 (conc.) was added to 409 mL of distilled water. A solution of 16.40 g of $Na_2WO_4{\cdot}2H_2O$ dissolved in 100 mL of distilled water was slowly dropped into the acidic solution (a yellow-white precipitate formed). The acidic solution was held at 100 °C. The solution was then allowed to slowly return to RT and stirred overnight. The precipitate was washed with distilled water (centrifuged at 10,000 rpm for 5 min) until the water reached pH 5.3. The precipitate was dried for 18 h at 80 °C and then calcined for 2 h at 400 °C. WO_3 hollow spheres (labeled spheres) were prepared as previously reported.[22] The sample labeled ME was prepared via a chloro-alkoxide route.[46] Another WO_3 sample was prepared via a hydrothermal method using a nonionic surfactant-Birj 37 as a structural agent (labeled RO sample). The sample was calcined at 550 °C in air. As a reference, commercially available WO_3 (Sigma-Aldrich, <100 nm) labeled SA and SnO_2 (Sigma-Aldrich, <100 nm) powder were used.

The powders were ground with 1,2-propanediol using a mortar and pestle into a viscous paste which was screen-printed (EKRA Microtronic II.) onto alumina substrates (CeramTec GmbH, electrode gap 300 μm, front side Pt electrodes and backside Pt heater) as described elsewhere.[35] The samples were dried overnight at 80 °C and then annealed for 10 min each at 400, −500, and −400 °C with two 5 min steps to cool down in a tubular furnace (Heraeus ROK 6/30). The platelets were only calcined to a maximum temperature of 400 °C. As a result of the printing parameters, a layer thickness of approximately 50 μm is attained.

dc Resistance Measurements. The sensors were mounted in a homemade Teflon sensor chamber, and the test gas concentrations in dry synthetic air were supplied using a computer-controlled gas-mixing system. Humidity was added using a bubbler. A constant flow of 200 mL/min was used during the measurements. A Keithley 617 electrometer was used to measure the resistance of the sensors. Agilent E3630A and E3614A voltage sources were used to heat the sensors, via the backside heater. The sensor signal was calculated using the following relation

$$s = \frac{R_{\text{reference}}}{R_{\text{test gas}}} \tag{1}$$

Material Characterization. X-ray powder diffractograms were collected with a Philips X'Pert apparatus (PANalytical Spectris, Egham, UK). A monochromatic Cu Kα radiation source (λ = 1.540598 Å) was used. The diffractograms were recorded from a $2\theta - \omega$ angle of 25−45° with a step size of 0.01° at a rate of 0.01°/s. The diffractograms of the platelet sample were collected using a Rigaku MiniFlex. The XRD data were analyzed using the Match! 3 software (CRYSTAL IMPACT, Bonn, Germany).

Images of the sensitive layers were taken with a JOEL JSM-6500F scanning electron microscope with an acceleration voltage of 15 kV, a probe current of 74 μA, and a stage height of 15 mm.

X-ray photoelectron spectroscopy (XPS) was carried out on a PHI Quantera equipment with a base pressure in the analysis chamber of 10^{-9} Torr. The X-ray source was monochromatized Al Kα radiation (1486.6 eV) and the overall energy resolution is estimated at 0.65 eV by the full width at half-maximum (fwhm) of the Au $4f_{7/2}$ photoelectron line (84 eV). The spectra were calibrated using the internal C 1s line (BE = 284.8 eV) of the unavoidable adsorbed hydrocarbon on the sample surface (C−C or $(CH)_n$ bondings), Supporting Information S.1.

Operando DRIFT Spectroscopy. For operando DRIFT spectroscopy, a Vertex80v containing a mid-band mercury cadmium telluride (MCT) detector (Bruker, Billerica, MA, USA) with a spectral resolution of 4 cm^{-1} was used. The sensors were mounted in a homemade gas chamber with a KBr window. The sensors were heated analogously to the resistance measurements, and the dc resistance was recorded simultaneously. Every 15 min, a single-channel spectrum was recorded. To obtain the absorbance spectra, the single-channel spectra recorded under exposure to the target gases were referenced to the spectra recorded under the carrier gas using the relation suggested by Olinger and Griffiths:[47]

https://dx.doi.org/10.1021/acssensors.0c00113
ACS Sens. XXXX, XXX, XXX−XXX

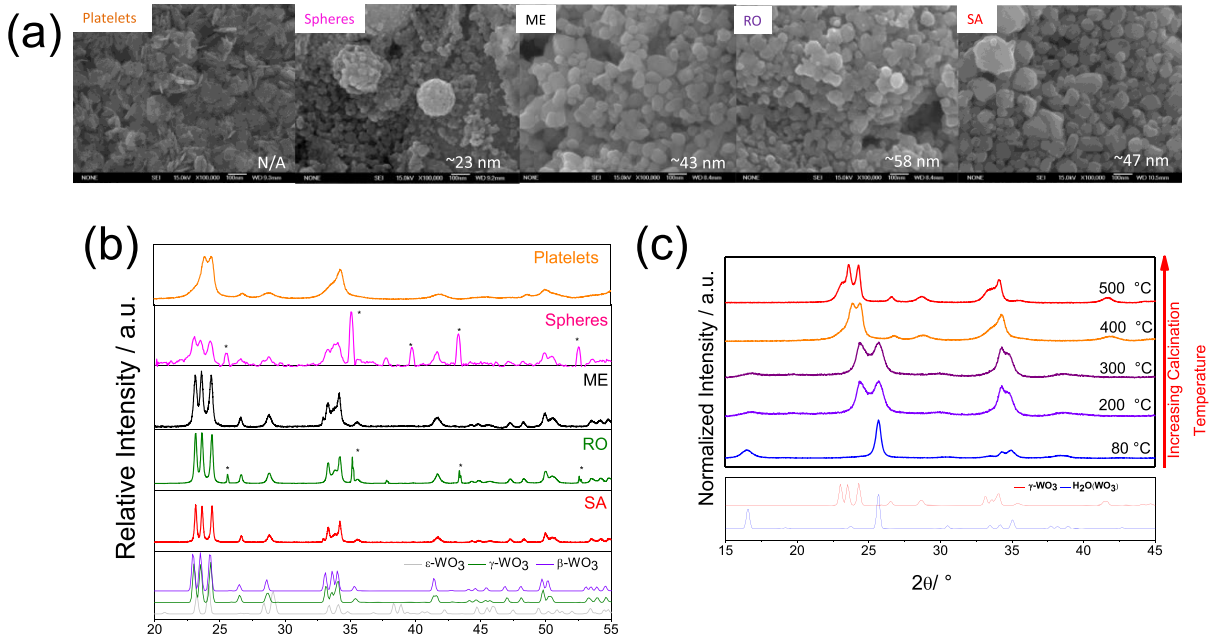

Figure 1. (a) SEM images of the sensitive layer of the different WO_3-based sensors. (b) X-ray diffractometry (XRD) spectra of the WO_3 materials. Peaks associated with the Al_2O_3 substrate are marked using an asterisk. The attained diffractograms are compared to those of ε-WO_3,[68] β-WO_3,[69] and γ-WO_3[70] (c) XRD data of the platelet sample after calcination to different temperatures.

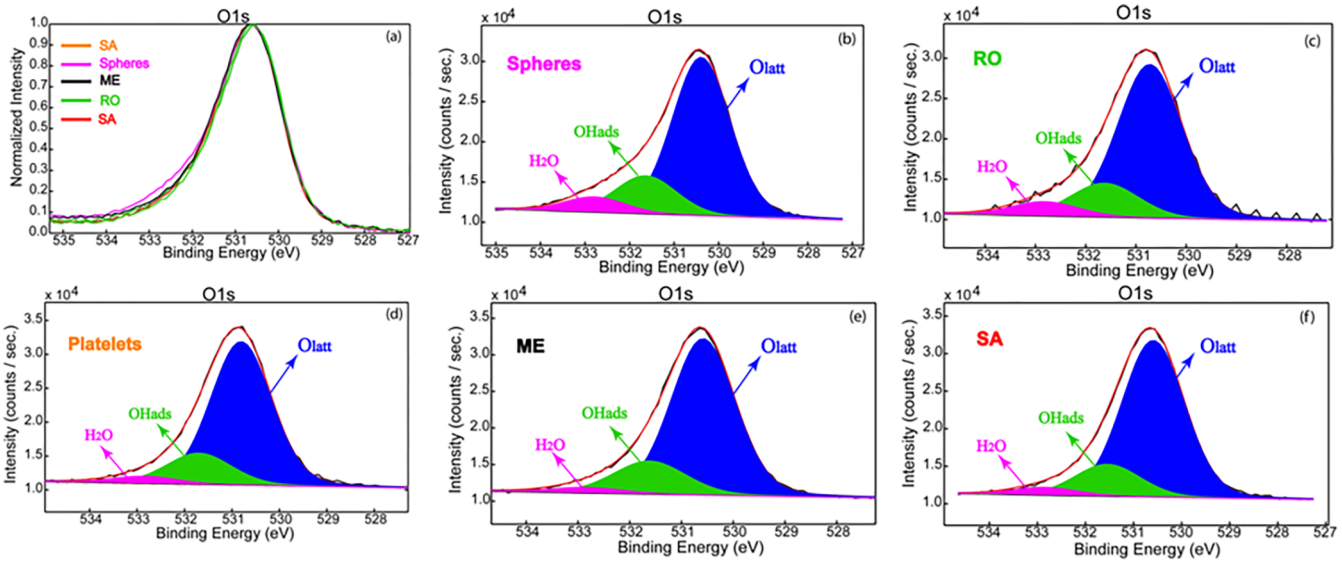

Figure 2. O 1s high resolution superimposed (a) and deconvoluted (b–f) spectra for the samples of the various WO_3 samples.

$$\text{Absorbance} = -\log\left(\frac{\text{single channel test gas}}{\text{single channel reference}}\right) \quad (2)$$

RESULTS AND DISCUSSION

Based on the SEM images of the sensitive layer, as shown in Figure 1, it can be seen that the samples have a large variation in morphology. The ME, RO, and SA samples are made up of largely round particles. In the sphere sample, the particles are arranged in a secondary hollow sphere structure. The grain size of the samples also varies greatly (calculated from the XRD spectra using the Debye Scherrer equation), as shown in Figure 1a,b. As expected, all of the examined WO_3 materials display the γ-phase at room temperature.

Based on the SEM of the platelets, variation in the dominant exposed facets can be suspected. This is further supported by the difference in the XRD pattern of the platelet sample in comparison with the other WO_3 materials. In XRD of the platelets, the reflex attributed to the 002 plane shows such a significant broadening (decrease in crystallite size) that it is not clearly discernible in XRD. It was reported by Choi et al. that this distortion results from the preferential orientation of tungsten dihydrate which is dehydrated to WO_3 at 200–240 °C.[48] This behavior is also seen in XRD spectra of the sample after different calcination steps. The as-prepared sample after drying at 80 °C shows the XRD pattern associated with tungsten hydrate. Reflexes which can be attributed to tungsten oxide begin to appear after calcination for 2 h at 200 °C. After calcination at 400 °C for 2 h, the reflex associated with the

https://dx.doi.org/10.1021/acssensors.0c00113
ACS Sens. XXXX, XXX, XXX−XXX

Table 1. Percentage Associated to Each Chemical Species

	atomic concentrations (atom %)			binding energies (eV) O 1s and W 4f				percentage oxygen chemical species (%)		
sample	C 1s	O 1s	W f	O_{latt}	OH_{ads}	H_2O	W $4f_{7/2}$	O_{latt}	OH_{ads}	H_2O
platelets	10.5	68.5	21.0	530.8	531.7	532.8	35.7	77.7	18.2	4.1
w/Ar^+		76.6	23.4							
spheres	14.7	67.2	18.1	530.7	531.6	532.8	35.7	74.5	18.3	7.2
w/Ar^+		78.7	21.3							
ME	13.2	66.6	20.2	530.6	531.6	532.8	35.8	78.3	18.7	3.0
w/Ar^+		76.7	23.3							
RO	12.6	67.7	19.7	530.7	531.6	532.8	35.6	75.7	17.0	7.3
w/Ar^+		77.5	22.4							
SA	12.9	66.3	20.8	530.8	531.5	532.8	35.7	78.9	16.8	4.3
w/Ar^+		76.4	23.6							

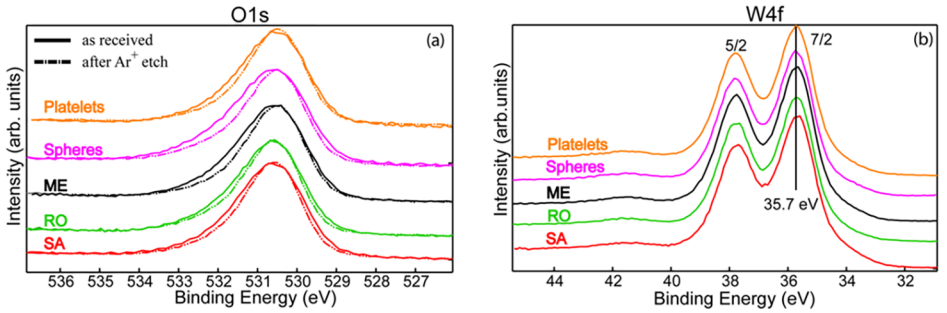

Figure 3. (a) Superimposed O 1s and measurements performed directly with the sample compared to measurements performed after sputtering with Ar ions. (b) W 4f high-resolution spectra of the samples.

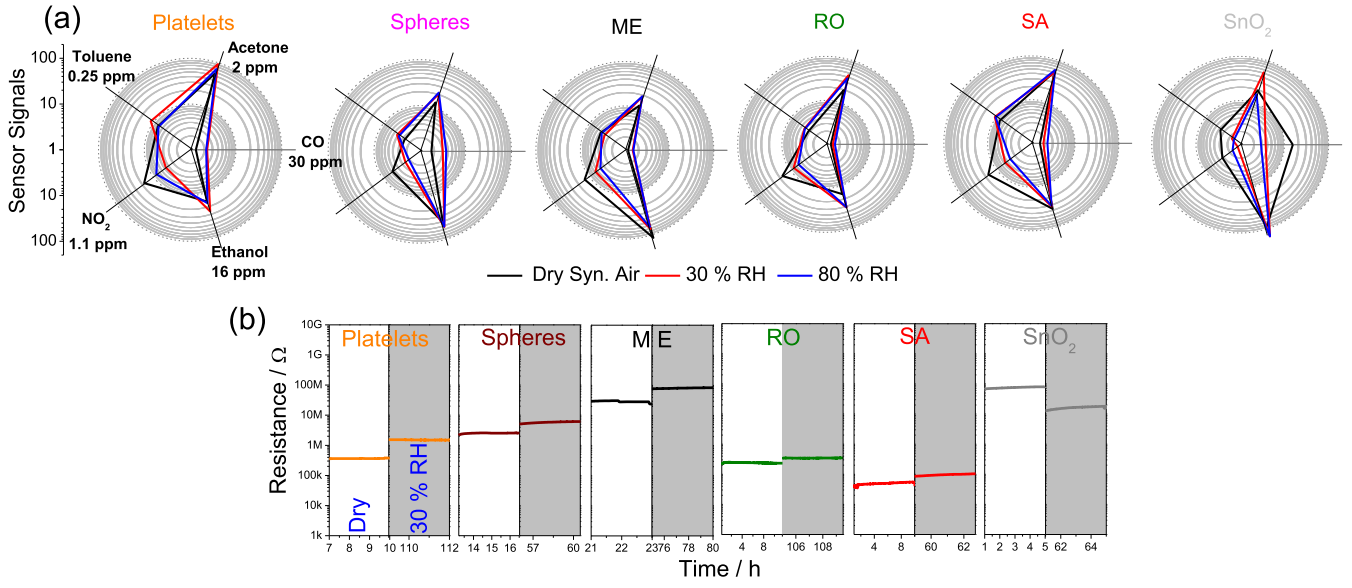

Figure 4. (a) Sensor profile of different WO_3 samples compared to a SnO_2 reference sample at an operation temperature of 300 °C. (b) Resistance of the sensors in dry synthetic air and in 30% RH at an operation temperature of 300 °C.

tungsten hydrate is no longer visible. The XRD pattern after calcination at 500 °C shows more defined peaks, indicating larger crystallites. In total, a pretreatment temperature of 400 °C, however, appears to be sufficient for the complete conversion of the hydrate into the oxide platelet material and thus was used here.

The XPS analysis provides information about the elements and their chemical state, which are present on the surface of the samples (<10 nm). Quantitative assessment allows the relative element concentration and chemical state ratios to be determined. Figure 2 shows the O 1s high-resolution superimposed (a) and deconvoluted (b–f) spectra for the WO_3 samples. Deconvolution of the O 1s singlet indicates three main components: lattice oxygen O_{latt} (530.7 ± 0.2) eV, hydroxyl groups OH_{ads} (531.6 ± 0.2) eV, and surface adsorbed water (532.8 ± 0.2) eV. The percentage attributed to each species is shown in Figure 2. This surface hydroxylation results in the asymmetry of the O 1s spectrum on the higher binding energy (BE) side as this spectral region accommodates the OH groups and the water adsorbed on the surface.

https://dx.doi.org/10.1021/acssensors.0c00113
ACS Sens. XXXX, XXX, XXX−XXX

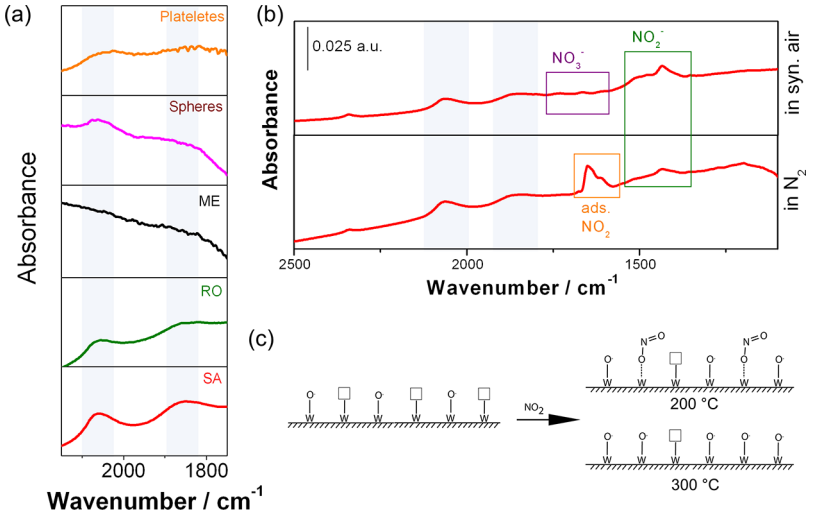

Figure 5. (a) DRIFT spectra recorded during exposure to 0.75 ppm NO_2 and referenced to dry synthetic air at an operation temperature of 300 °C. (b) DRIFT spectra recorded during exposure to 0.75 ppm NO_2 and referenced to dry synthetic air at an operation temperature of 200 °C. (c) Schematic representation of the surface reaction with NO_2.

The deconvolution procedure was carried out according to the guidelines of ISO-TC201 by imposing constraints on the BEs, the fwhm, and the spin−orbit parameter of the spectra in order to get an accurate interpretation. From Figure 2a, it can be seen that the spectrum of the sphere sample displays the most pronounced asymmetry. Quantitatively (see Table 1), the sphere sample shows the lowest amount of the lattice oxygen (O_{latt}) and the maximum percentage of OH and H_2O adsorbed on the surface. In order to gain information about the origin of the hydroxylation, the "as-received" samples were compared to samples after sputtering with Ar ions 1 keV (3 × 3) rastered area and 0.5 min sputter time. This treatment should only remove the first two monolayers of the surface, see Figure 3. A close examination of the superimposed and normalized spectra clearly reveals the removal, after a slight Ar ion etching, of the weak OH surface bonded and the water confined on the top of the surface. In all samples, there is a decrease in the OH groups. This result indicates physically adsorbed surface OH groups and water. Surface hydroxylation is known to affect the sensing behavior of SMOX.[49,50] In Figure 2b, the W $4f_{7/2}$ photoelectron peak assigned to 35.7 ± 0.2 eV which is the typical BE value for the W^{6+} oxidation state as WO_3 is detected.[51]

This material characterization will be useful in understanding the sensing behavior of the materials. The typical operation temperature of WO_3 is between 200 and 400 °C. Here, based on a temperature study with the SA and the ME sample, an operation temperature of 300 °C was selected. At this temperature, the sensing behavior was similar to 200 °C but the response and recovery time were significantly better, see the Supporting Information S.2 and S.3. The response of the sensors to the five test gases, CO, acetone, NO_2, ethanol, and toluene in the absence and in the presence of 30% RH and 80% RH is shown in Figure 4. The sensor profiles of the different WO_3 samples are surprisingly homogeneous.

Like the reference SnO_2 sample, all of the WO_3 sensors respond well to the volatile organic compound, ethanol. For the other examined test gases, however, the sensing behavior of the WO_3-based sensors is found to be generally complementary to the reference SnO_2.[52] All of the samples respond well to acetone and show lower humidity dependence than SnO_2. All of the WO_3-based sensors show a higher response to toluene than SnO_2. Additionally the response to toluene shows practically no humidity dependence for WO_3, while it significantly decreases for the SnO_2 sample. Unlike SnO_2, which shows a high response to CO in dry air and a significant decrease in humidity, the WO_3 sensors barely respond to CO and the signals even slightly increase in humidity. In line with the literature, the response of all of the WO_3 samples to NO_2 in dry air is high but significantly decreases in the presence of humidity. Even in the presence of humidity, however, WO_3 is much better suited to detect NO_2 than the reference SnO_2 sample. The homogeneity of the samples' sensing behavior is remarkable, and in order to understand its origin, the reception mechanism, that is, surface reactions, responsible for the sensor response, will be examined using operando DRIFT spectroscopy.

In an attempt to make the suggested mechanisms easily understandable, simple schematic representations are presented. Albanese et al. simulated different surface layer oxygen vacancies using density functional theory (DFT). They found that the dominant vacancy is the loss of the singly coordinated oxygen which is stable with a single charge (with one excess electron).[53] Therefore, here, only terminal oxygen vacancies are depicted in the schematics. In the literature, absorption bands at 1858 and 2065 cm^{-1} are attributed to various overtones and combinations of the WO_3 lattice, that is, an increase in these bands means surface oxidation and a decrease reduction.[31,54] As a reference, the SA sample was exposed to synthetic air after operation in a nitrogen background, The addition of atmospheric oxygen (in the absorbance spectra calculated by referencing the spectrum in dry synthetic air to that recorded in nitrogen) results in an increase in the bands at 1858 and 2065 cm^{-1}, see the Supporting Information S.4. This verifies that in line with the literature, the increase in these bands is indicative of an increase in surface oxygen. Inversely, then, a decrease in these bands is assumed to indicate a decrease in surface oxygen (a reduction in the surface).

In line with the literature, exposure to NO_2 results (Figure 5a) in an increase in the bands attributed to tungsten−oxygen bonds (1858 and 2065 cm^{-1}) visible in the DRIFT spectra,[33,54,55] that is, the oxidation of the surface by NO_2.

https://dx.doi.org/10.1021/acssensors.0c00113
ACS Sens. XXXX, XXX, XXX−XXX

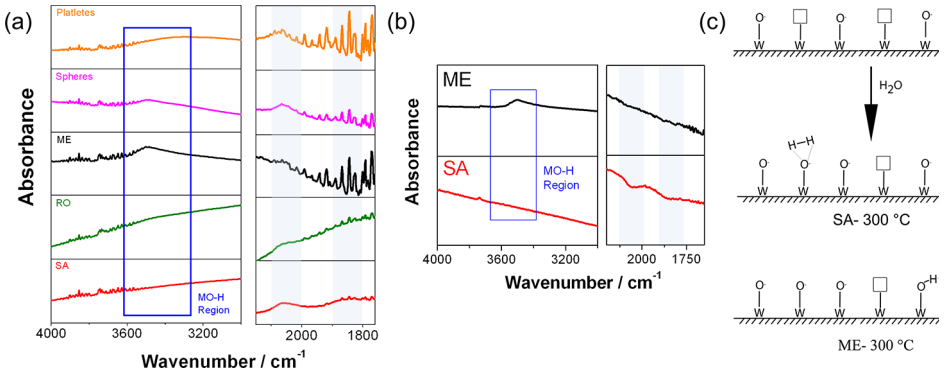

Figure 6. (a) DRIFT spectra recorded during exposure to 10% RH and referenced to dry synthetic air at an operation temperature of 300 °C. (b) Spectra of SA and ME during exposure to 250 ppm H_2 in dry air referenced to the spectra recorded in dry synthetic air at an operation temperature of 300 °C. (c) Schematic representation of the surface reaction with humidity.

In the spectra of the SA sample, an additional band is visible at 1420 cm^{-1}.[32,33] Akamatsu et al. inconclusively attributed this band to surface adsorbed NO_2.[33] However, the classic nitro symmetric and asymmetric bands, visible in the case of NO_2 exposure on In_2O_3, are not visible.[56] In order to gain more information about the surface chemistry, it is often helpful to examine spectra recorded at a lower temperature, where the reaction rate is decreased. The surface reaction between NO_2 and the SA sample at 200 °C was examined using operando DRIFT spectroscopy, as shown in Figure 5b. In this spectrum, there are two strong bands (1487 and 1437 cm^{-1}) and two weaker bands visible (1720 and 1624 cm^{-1}). Bands in this region can be attributed to nitrites (NO_2^-) or nitrates (NO_3^-).[56] Yang et al. attribute the bands at lower wave numbers to nitrites and the bands at higher wave numbers to nitrates.[57] This assignment is additionally supported by spectra of the sample during exposure to NO_2 in nitrogen. Although the bands attributed to nitrites are still clearly visible and increasing, the bands attributed to nitrates are no longer visible. In nitrogen, the level of surface oxidation should be significantly lower (there are fewer possibilities for NO_2 to form nitrates). Additionally, in nitrogen, the bands commonly attributed in the literature to molecular adsorbed NO_2 are visible (between 1642 and 1605 cm^{-1}).

Based on DFT calculations, Han et al. reported that in an O-terminated WO_3 (001), a NO_2 molecule is oxidized into nitrate and is adsorbed onto the surface.[58] They report that in the case of a WO-terminated (001) surface, a NO_2 molecule heals a vacancy.[58] A real surface is of course neither O- or WO-terminated but a complicated combination of both. Based on the results, NO_2 dominantly forms nitrites, the path suggested by Han et al. for a WO-terminated surface. This finding indicates that either there are a large number of surface vacancies (equivalent of a WO-terminated surface if terminal oxygen is considered the dominant vacancy) or the vacancy is a better suited reaction partner for NO_2 than surface oxygen.

Overall, based on the literature and the DRIFT spectra, the following mechanism is suggested, shown schematically in Figure 5c. NO_2 adsorbs into a vacancy of the WO_3 surface. At 300 °C, the vacancy is then healed with the oxygen of NO_2, releasing NO which is easily re-oxidized with atmospheric oxygen. The broad increasing band at 1420 cm^{-1}, seen at 300 °C, appears to be an additional band associated with tungsten−oxygen, as it is not only increasing during exposure to NO_2 but also as a result of the addition of oxygen, Supporting Information S.5. In the subsequent sections, the band will also be found to decrease upon exposure to reducing gases.

In order to understand why the signal to NO_2 strongly decreases in the presence of humidity, the interaction of humidity with WO_3 is examined using dc resistance and DRIFT spectroscopy. The response of the materials to humidity is also very homogeneous. Unlike SnO_2, which, at 300 °C, shows either a significant decrease in the resistance or no response depending on the preparation method,[35,36] WO_3-based sensors consistently show an increase.[52] For the SA WO_3 sample, the increase in the resistance was previously attributed to the direct oxidation of the surface by humidity.[32] In order to determine if this explanation can be applied to all of the other WO_3 samples, operando DRIFT spectra were recorded during exposure to 10% RH referenced to dry synthetic air. A humidity level of 10% was selected, as at higher humidity, the interpretation of the DRIFT spectra is difficult because of large signals of water vapor.

As previously reported, in the DRIFT spectra of the SA sample, there is no formation of hydroxyl groups visible.[32] Only an increase in the two bands (1858 and 2065 cm^{-1}) attributed to the tungsten−oxygen bond is visible.[54,55] This indicates that the surface is directly oxidized by humidity. The spectra of the RO and the platelet samples are similar to that of SA. In the case of the ME and the sphere sample, in addition to the increasing bands attributed to tungsten−oxygen, the formation of hydroxyl groups is visible. This is indicative of a surface hydroxylation in line with the XPS spectra.

In order to better understand the effect of these hydroxyl groups on the sensor response, the reaction between the SA and the ME sample with hydrogen is examined. These two samples are representatives of the two different sample types, those that form hydroxyl groups with humidity and those that do not. Both samples show a low response to hydrogen. SA has a signal of ca. 3.5 and ME has a signal of approximately 2.5−250 ppm H_2. Both samples were exposed to 250 ppm of H_2 in dry synthetic air. The DRIFT spectra, shown in Figure 6b, were attained by referencing to the spectra recorded in dry synthetic air. In the DRIFT spectra of the SA sample, only the direct reduction of the sample is visible. In contrast, in the case of the ME sample, only the formation of hydroxyl groups (identical to those formed with humidity) is visible. The decrease in the resistance, in the case of the ME sample, could be explained using the mechanism suggested by Heiland and Kohl.[53,59,60] Albanese et al. theoretically find that for WO_3, the formation of hydroxyl groups can be followed by hydrogen

https://dx.doi.org/10.1021/acssensors.0c00113
ACS Sens. XXXX, XXX, XXX−XXX

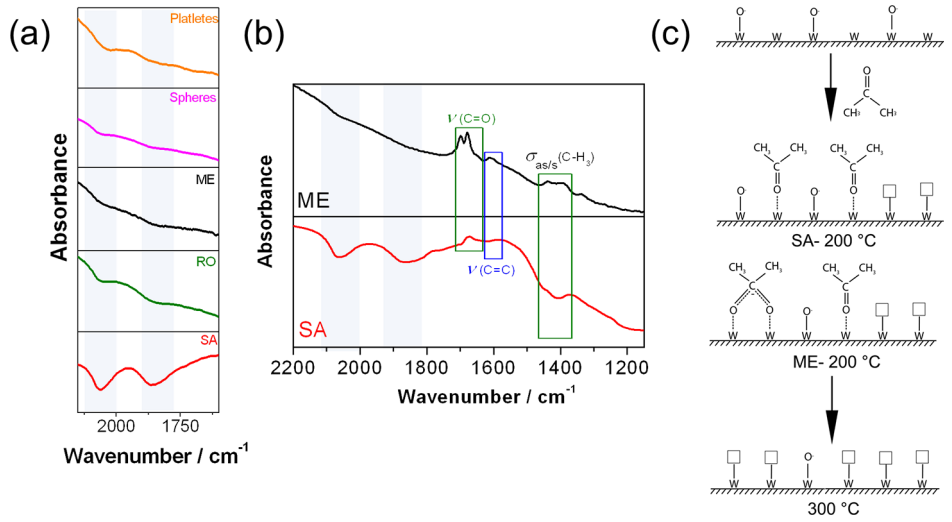

Figure 7. (a) Spectra recorded during exposure to 1.5 ppm acetone referenced to the spectra recorded in dry synthetic air at an operation temperature of 300 °C. (b) Spectra of the ME and SA samples during exposure to 1.5 ppm acetone referenced to the spectra recorded in dry synthetic air at an operation temperature of 200 °C. (c) Schematic representation of the surface reaction with acetone.

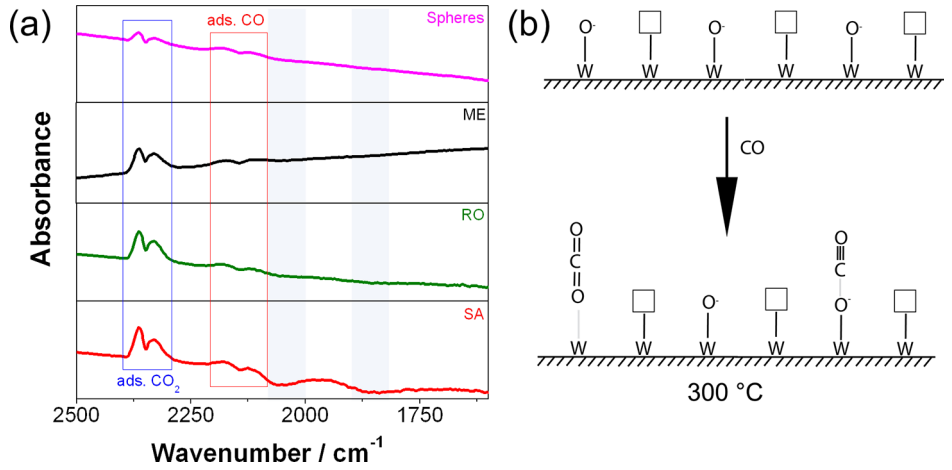

Figure 8. (a) DRIFT spectra recorded during exposure to 500 ppm CO (b) DRIFT spectra of the SA sample upon exposure to 400 ppm CO in 50 ppm O_2 in N_2 (c) schematic representation of the surface reaction with carbon monoxide.

migration and formation of H_2O. Water is then found to desorb from the surface.[53] In other words, the surface reactions with H_2O and H_2 appear to be in equilibrium. Overall, however, the detected increase in resistance as a result of humidity and the clearly increasing bands attributed to tungsten−oxygen show that even for samples which form hydroxyl groups, the direct oxidation of the surface by humidity is the dominant reaction.

The gained insights about the WO_3 surface reactions with oxygen, NO_2, and humidity are helpful for understanding the reaction of WO_3 with more chemically complex gases, such as acetone. In the DRIFT spectra at 300 °C, only a decrease in the bands (1858 and 2065 cm^{-1}) attributed to tungsten−oxygen bonds is visible, a shown in Figure 7a. In order to gain more insight into the surface reaction of WO_3 with acetone, DRIFT spectra recorded at 200 °C of the ME and the SA samples are examined, as shown in Figure 7b. The sensor response of both materials to acetone is similar at 200 and 300 °C, see the Supporting Information S.2. In the DRIFT spectra recorded at 200 °C, in addition to the decreasing bands ascribed to tungsten−oxygen bonds, various bands attributed to different functional groups of acetone are present.

There is a great deal of the literature which examines the surface adsorption of acetone onto different solids under varying conditions. In the literature, it was found that at lower temperatures, acetone adsorbs through hydrogen bonding with surface hydroxyl groups, while at higher temperatures, the situation is more complicated.[61,62] Würger et al. reported that the adsorption of acetone onto the surface of TiO_2 via the carbonyl group results in a peak shift of the band attributed to the C═O bond.[63] The band attributed to the carbonyl group of free acetone is usually found at approximately 1715 cm^{-1}, while the band of adsorbed acetone is known to shift to 1680 cm^{-1}.[64] In the DRIFT spectra of the SA, in addition to the decreasing bands attributed to tungsten−oxygen, a single broad carbonyl band at 1680 cm^{-1} is increasing. This indicates that acetone adsorbs via the oxygen of its carbonyl into the oxygen vacancy of the WO_3 surface.[63,64] Because of the strong decrease in the bands attributed to the tungsten−oxygen bond for the SA sample, only the band attributed to asymmetric deformation of the methyl groups of acetone is visible at a

https://dx.doi.org/10.1021/acssensors.0c00113
ACS Sens. XXXX, XXX, XXX−XXX

wave number very close to that reported for free acetone.[64] This indicates that the methyl group is not strongly affected by the adsorption of acetone to the surface. As a result of thermal activation, Petrik et al. found the formation of acetone diolates through the reaction of adsorbed acetone with adsorbed surface oxygen.[65] Based on theoretical calculations, Würger et al. attribute a splitting of the band attributed to the carbonyl (two bands at 1700 and 1679 cm^{-1}) to the formation of these diolates. This splitting is clearly visible in the DRIFT spectra of the ME sample at 200 °C. In this case, it appears that the surface reaction is analogous to the one reported for TiO_2.[66] Acetone first adsorbs via the oxygen of the carbonyl to the surface metal.[66] The adsorbed acetone then reacts with surface oxygen to form a diolate. The additional bands visible at 1650 and 1600 cm^{-1} are very close to the bands reported in the literature (1655 and 1595 cm^{-1} on TiO_2 for the C═O and the C═C bond, respectively) for mesityl oxide an intermediate for the condensation reaction of acetone.[56,63] Although it is impossible to infer all the reaction steps of acetone on the surface of WO_3, these results indicate that also for this chemically complex gas, the initial interaction between the surface vacancies and the oxygen of acetone plays a crucial role. From there, acetone reacts with WO_3 resulting in the visible decrease in the bands attributed to tungsten−oxygen and the detected decrease in the resistance, see the schematic Figure 7c.

For the sake of completeness, the interaction between the samples and CO is also considered (Figure 8). Overall, the response of sensors based on pure WO_3 to CO is, however, known to be low. Also, here, the responses of all the sensors are low. In line with the low response, reduction in the samples (decreasing tungsten−oxygen bands) is only weakly or not at all visible in the DRIFT spectra of the samples. The absorption bands belonging to surface adsorbed CO and CO_2 are clearly visible in the spectra. In the literature, it is reported that a strong interaction between the surface cation and the gas should result in a shift toward higher frequencies of the absorption band. In the DRIFT spectra, the absorption band of CO at 2143 cm^{-1} and that of CO_2 at 2350 cm^{-1} are very close to the values expected for the free molecules, indicating a weak interaction with the WO_3 surface.[64] In the DRIFT spectra of the SA sample recorded upon exposure to 400 ppm CO in the presence of only 50 ppm oxygen, although the sensor response is much higher (approximately 30), the absorption band of CO_2 is only weakly visible. For more information about the sample under low oxygen conditions, please see the publication by Staerz et al.[21] Overall, these findings are in line with the reports of Hübner et al. and theoretical findings.[31,67] As a result, the following mechanism is suggested. Although it can interact with WO_3 with either its oxygen or carbon, CO preferentially reacts with surface oxygen to form CO_2. The magnitude of the sensor signal depends on the equilibrium established between the generation of oxygen vacancies and their cancellation (higher sensor response in a low-oxygen background despite less CO_2 production). Based on this, it appears that like H_2, CO directly reduces the surface of WO_3. See the Supporting Information S.8c for the schematic of the reaction.

From the literature and the results shown here, the dominant role of the vacancy in the surface chemistry of WO_3 becomes clear. Gases that can initially adsorb via oxygen into a tungsten oxide vacancy show high signals, for example, NO_2 and acetone. Oppositely, WO_3 shows low sensor responses to gases that prefer to directly reduce the surface, for example, H_2 and CO. This tendency also helps explain the very different behavior of humidity with WO_3 versus SnO_2.

CONCLUSIONS

WO_3 samples prepared using various synthesis methods and with very different morphologies were systematically characterized. It was possible to identify sensor characteristics inherent to WO_3. Overall, it was found that the sensing behavior is surprisingly homogeneous and shows good complementarity to SnO_2-based sensors. All of the sensors showed an increase in the resistance with humidity. All of the sensors showed a decreased sensor response to the only oxidizing gas, NO_2, in the presence of humidity. The sensors responded well to acetone and ethanol and showed practically no response to much higher concentrations of CO. Using operando DIRFT spectroscopy, it was possible to elucidate the surface reactions that result in the sensor response. The sameness of the WO_3 samples was attributed to the initial reaction of the test gases with surface vacancies. As oxygen vacancies are a ubiquitous defect, the findings here indicate that WO_3 will always be sensitive to certain gases with the ability to interact with the vacancy. This is a further indication that selective metal oxides are unattainable because they will always respond to a group of gases with similar features.

ASSOCIATED CONTENT

Supporting Information

The Supporting Information is available free of charge at https://pubs.acs.org/doi/10.1021/acssensors.0c00113.

C 1s superimposed and deconvoluted XPS spectra for the WO_3 samples; sensor profile of SA and ME WO_3 at different temperatures; raw response of a sensor based on SA WO_3 to toluene in 0% RH at different temperatures; DRIFT spectra of the SA sample in dry synthetic air referenced to spectra recorded in N_2 both at 200 and 300 °C; and complete DRIFT spectra of the samples during exposure to 0.75 ppm NO_2, 1.5 ppm acetone, 10% RH humidity, and 500 ppm CO referenced to dry synthetic air (PDF)

AUTHOR INFORMATION

Corresponding Author

Nicolae Barsan − *Institute for Physical and Theoretical Chemistry, Eberhard Karls University of Tuebingen, 72076 Tuebingen, Germany;* orcid.org/0000-0001-6718-9889; Phone: +49 7071 29 78761; Email: nb@ipc.uni-tuebingen.de

Authors

Anna Staerz − *Institute for Physical and Theoretical Chemistry, Eberhard Karls University of Tuebingen, 72076 Tuebingen, Germany*

Simona Somacescu − *Ilie Murgulescu Institute of Physical Chemistry, Romanian Academy, 060021 Bucharest, Romania*

Mauro Epifani − *Consiglio Nazionale delle Ricerche, Istituto per la Microelettronica ed i Microsistemi (C.N.R.−I.M.M.), 73100 Lecce, Italy*

Tetsuya Kida − *Faculty of Advanced Science and Technology, Kumamoto University, 860-8555 Kumamoto, Japan;* orcid.org/0000-0001-9357-9557

https://dx.doi.org/10.1021/acssensors.0c00113
ACS Sens. XXXX, XXX, XXX−XXX

Udo Weimar − *Institute for Physical and Theoretical Chemistry, Eberhard Karls University of Tuebingen, 72076 Tuebingen, Germany*

Complete contact information is available at: https://pubs.acs.org/10.1021/acssensors.0c00113

Author Contributions

The manuscript was written through contributions of all authors. All authors have given approval to the final version of the manuscript.

Funding

Some of the work was funded by the financial support of the Japan Society for Promotion of Science grant number PE19703.

Notes

The authors declare no competing financial interest.

REFERENCES

(1) Seiyama, T.; Kato, A.; Fujiishi, K.; Nagatani, M. A New Detector for Gaseous Components Using Semiconductive Thin Films. *Anal. Chem.* **1962**, *34*, 1502−1503.

(2) Ihokura, K.; Watson, J. *The Stannic Oxide Gas Sensor—Principles and Application*; CRC Press: Boca Raton, Florida, 1994.

(3) Taguchi, N. Gas-Detecting Device. U.S.Patent 3,695,848 A, 1971.

(4) Neri, G. First Fifty Years of Chemoresistive Gas Sensors. *Chemosensors* **2015**, *3*, 1−20.

(5) Persaud, K.; Dodd, G. Analysis of Discrimination Mechanisms in the Mammalian Olfactory System Using a Model Nose. *Nature* **1982**, *299*, 352−355.

(6) Rüffer, D.; Hoehne, F.; Bühler, J. New Digital Metal-Oxide (MOx) Sensor Platform. *Sensors* **2018**, *18*, 1052.

(7) Röck, F.; Barsan, N.; Weimar, U. Electronic Nose: Current Status and Future Trends. *Chem. Rev.* **2008**, *108*, 705−725.

(8) Kim, H.-J.; Lee, J.-H. Highly Sensitive and Selective Gas Sensors Using P-Type Oxide Semiconductors: Overview. *Sens. Actuators, B* **2014**, *192*, 607−627.

(9) Izawa, K.; Ulmer, H.; Anna Staerz, U. W. *Gas Sensors Based on Condcuting Metal Oxides: Basics Understanding, Technology and Applications*; Barsan, N., Schierbaum, K., Eds.; Elseiver, 2018.

(10) Shaver, P. J. Activated Tungsten Oxide Gas Detectors. *Appl. Phys. Lett.* **1967**, *11*, 255.

(11) Choi, S.-J.; Ku, K. H.; Kim, B. J.; Kim, I.-D. Novel Templating Route Using Pt Infiltrated Block Copolymer Micro-Particles for Catalytic Pt Functionalized Macroporous WO3 Nanofibers and Its Application in Breath Pattern Recognition. *ACS Sensors* **2016**, *1*, 1124.

(12) Kato, W.; Hashishin, T.; Tamaki, J.; Kajita, S. K. Pt Loaded WO3 Thin Film Sensors for Highly Sensitive Detection of Ethanol Gas. In 214th ECS *Meeting Abstract*; The Electrochemical Society, 2008; p 3113.

(13) Horprathum, M.; Srichaiyaperk, T.; Samransuksamer, B.; Wisitsoraat, A.; Eiamchai, P.; Limwichean, S.; Chananonnawathorn, C.; Aiempanakit, K.; Nuntawong, N.; Patthanasettakul, V.; et al. Ultrasensitive Hydrogen Sensor Based on Pt-Decorated WO3 Nanorods Prepared by Glancing-Angle Dc Magnetron Sputtering. *ACS Appl. Mater. Interfaces* **2014**, *6*, 22051−22060.

(14) Kim, S.; Park, S.; Park, S.; Lee, C. Acetone Sensing of Au and Pd-Decorated WO3 Nanorod Sensors. *Sens. Actuators, B* **2015**, *209*, 180−185.

(15) Penza, M.; Martucci, C.; Cassano, G. NOx Gas Sensing Characteristics of WO3 Thin Films Activated by Noble Metals (Pd, Pt, Au) Layers. *Sens. Actuators, B* **1998**, *50*, 52−59.

(16) Labidi, A.; Gillet, E.; Delamare, R.; Maaref, M.; Aguir, K. Ethanol and Ozone Sensing Characteristics of WO3 Based Sensors Activated by Au and Pd. *Sens. Actuators, B* **2006**, *120*, 338−345.

(17) Xia, H.; Wang, Y.; Kong, F.; Wang, S.; Zhu, B.; Guo, X.; Zhang, J.; Wang, Y.; Wu, S. Au-Doped WO3 -Based Sensor for NO2 Detection at Low Operating Temperature. *Sens. Actuators, B* **2008**, *134*, 133−139.

(18) Li, F.; Li, C.; Zhu, L.; Guo, W.; Shen, L.; Wen, S.; Ruan, S. Enhanced Toluene Sensing Performance of Gold-Functionalized WO3 ·H2O Nanosheets. *Sens. Actuators, B* **2016**, *223*, 761−767.

(19) Vallejos, S.; Stoycheva, T.; Umek, P.; Navio, C.; Snyders, R.; Bittencourt, C.; Llobet, E.; Blackman, C.; Moniz, S.; Correig, X. Au Nanoparticle-Functionalised WO3 Nanoneedles and Their Application in High Sensitivity Gas Sensor Devices. *Chem. Commun.* **2011**, *47*, 565−567.

(20) Kim, N.-H.; Choi, S.-J.; Kim, S.-J.; Cho, H.-J.; Jang, J.-S.; Koo, W.-T.; Kim, M.; Kim, I.-D. Highly Sensitive and Selective Acetone Sensing Performance of WO3 Nanofibers Functionalized by Rh2O3 Nanoparticles. *Sens. Actuators, B* **2016**, *224*, 185−192.

(21) Staerz, A.; Boehme, I.; Degler, D.; Bahri, M.; Doronkin, D.; Zimina, A.; Brinkmann, H.; Herrmann, S.; Junker, B.; Ersen, O.; et al. Rhodium Oxide Surface-Loaded Gas Sensors. *Nanomaterials* **2018**, *8*, 892.

(22) Staerz, A.; Kim, T.-H.; Lee, J.; Weimar, U.; Barsan, N. Nano-Level Control of Gas Sensing Characteristics via p-n Heterojunction between Rh2O3 Clusters and WO3 Crystallites. *J. Phys. Chem. C.* **2017**, *121*, 24701.

(23) Kim, N.-H.; Choi, S.-J.; Yang, D.-J.; Bae, J.; Park, J.; Kim, I.-D. Highly Sensitive and Selective Hydrogen Sulfide and Toluene Sensors Using Pd Functionalized WO3 Nanofibers for Potential Diagnosis of Halitosis and Lung Cancer. *Sens. Actuators, B* **2014**, *193*, 574−581.

(24) Ding, X.; Zeng, D.; Zhang, S.; Xie, C. C-Doped WO3 Microtubes Assembled by Nanoparticles with Ultrahigh Sensitivity to Toluene at Low Operating Temperature. *Sens. Actuators, B* **2011**, *155*, 86−92.

(25) Government of Canada. *Residential Indoor Air Quality Guidelines*, 2018; Vol. 3.

(26) Kida, T.; Nishiyama, A.; Hua, Z.; Suematsu, K.; Yuasa, M.; Shimanoe, K. WO3 Nanolamella Gas Sensor: Porosity Control Using SnO2 Nanoparticles for Enhanced NO2 Sensing. *Langmuir* **2014**, *30*, 2571.

(27) Nakagawa, H.; Okazaki, S.; Asakura, S.; Fukuda, K.; Akimoto, H.; Takahashi, S.; Shigemori, S. An Automated Car Ventilation System. *Sens. Actuators, B* **2000**, *65*, 133−137.

(28) Cantalini, C.; Pelino, M.; Sun, H. T.; Faccio, M.; Santucci, S.; Lozzi, L.; Passacantando, M. Cross Sensitivity and Stability of NO2 Sensors from WO3 Thin Film. *Sens. Actuators, B* **1996**, *35*, 112−118.

(29) Hermida, I. D. P.; Wiranto, G.; Hiskia; Nopriyanti, R. Fabrication of SnO2 Based CO Gas Sensor Device Using Thick Film Technology. *J. Phys.: Conf. Ser.* **2016**, *776*, 012061.

(30) Baumann, S. L. *Detektions-Mechanismen Auf WO3 Bei Einsatz in Verbrennungsabgasen*; Jutus Liebig Universität Gießen, 2003.

(31) Hübner, M.; Simion, C. E.; Haensch, A.; Barsan, N.; Weimar, U. CO Sensing Mechanism with WO3 Based Gas Sensors. *Sens. Actuators, B* **2010**, *151*, 103−106.

(32) Staerz, A.; Berthold, C.; Russ, T.; Wicker, S.; Weimar, U.; Barsan, N. The Oxidizing Effect of Humidity on WO3 Based Sensors. *Sens. Actuators, B* **2016**, *237*, 54−58.

(33) Akamatsu, T.; Itoh, T.; Izu, N.; Shin, W. NO and NO2 Sensing Properties of WO3 and Co3O4 Based Gas Sensors. *Sensors* **2013**, *13*, 12467−12481.

(34) Pokhrel, S.; Simion, C. E.; Teodorescu, V. S.; Barsan, N.; Weimar, U. Synthesis, Mechanism, and Gas-Sensing Application of Surfactant Tailored Tungsten Oxide Nanostructures. *Adv. Funct. Mater.* **2009**, *19*, 1767−1774.

(35) Wicker, S.; Guiltat, M.; Weimar, U.; Hémeryck, A.; Barsan, N. Ambient Humidity Influence on CO Detection with SnO2 Gas Sensing Materials. A Combined DRIFTS/DFT Investigation. *J. Phys. Chem. C* **2017**, *121*, 25064−25073.

(36) Grossmann, K.; Pavelko, R. G.; Barsan, N.; Weimar, U. Interplay of H2, Water Vapor and Oxygen at the Surface of SnO2

Based Gas Sensors − An Operando Investigation Utilizing Deuterated Gases. *Sens. Actuators, B* **2012**, *166−167*, 787−793.
(37) Heiland, G.; Kohl, D. Physical and Chemical Aspects of Oxidic Semiconductor Gas Sensors. In *Chemical Sensor Technology*; Seiyama, T., Ed.; Elsevier Science, 1992; pp 43−88.
(38) Zheng, H.; Ou, J. Z.; Strano, M. S.; Kaner, R. B.; Mitchell, A.; Kalantar-Zadeh, K. Nanostructured Tungsten Oxide - Properties, Synthesis, and Applications. *Adv. Funct. Mater.* **2011**, *21*, 2175−2196.
(39) Wang, L.; Teleki, A.; Pratsinis, S. E.; Gouma, P. I. Ferroelectric WO3 Nanoparticles for Acetone Selective Detection. *Chem. Mater.* **2008**, *20*, 4794−4796.
(40) Righettoni, M.; Tricoli, A.; Pratsinis, S. E. Thermally Stable, Silica-Doped ε-WO3 for Sensing of Acetone in the Human Breath. *Chem. Mater.* **2010**, *22*, 3152−3157.
(41) Deng, C.; Zhang, J.; Yu, X.; Zhang, W.; Zhang, X. Determination of Acetone in Human Breath by Gas Chromatography-Mass Spectrometry and Solid-Phase Microextraction with on-Fiber Derivatization. *J. Chromatogr. B: Anal. Technol. Biomed. Life Sci.* **2004**, *810*, 269−275.
(42) Khadayate, R. S.; Sali, J. V.; Patil, P. P. Acetone Vapor Sensing Properties of Screen Printed WO3 Thick Films. *Talanta* **2007**, *72*, 1077−1081.
(43) Li, X.-L.; Lou, T.-J.; Sun, X.-M.; Li, Y.-D. Highly Sensitive WO3 Hollow-Sphere Gas Sensors. *Inorg. Chem.* **2004**, *43*, 5442−5449.
(44) Chen, Y.; Qin, H.; Cao, Y.; Zhang, H.; Hu, J. Acetone Sensing Properties and Mechanism of SnO2 Thick-Films. *Sensors* **2018**, *18*, 3425.
(45) Kida, T.; Nishiyama, A.; Yuasa, M.; Shimanoe, K.; Yamazoe, N. Highly Sensitive NO2 Sensors Using Lamellar-Structured WO3 Particles Prepared by an Acidification Method. *Sens. Actuators, B* **2009**, *135*, 568−574.
(46) Epifani, M.; Andreu, T.; Arbiol, J.; Díaz, R.; Siciliano, P.; Morante, J. R. Chloro-Alkoxide Route to Transition Metal Oxides. Synthesis of WO3 Thin Films and Powders from a Tungsten Chloro-Methoxide. *Chem. Mater.* **2009**, *21*, 5215−5221.
(47) Olinger, J. M.; Griffiths, P. R. Quantitative Effects of an Absorbing Matrix on Near-Infrared Diffuse Reflectance Spectra. *Anal. Chem.* **1988**, *60*, 2427−2435.
(48) Choi, Y.-G.; Sakai, G.; Shimanoe, K.; Teraoka, Y.; Miura, N.; Yamazoe, N. Preparation of Size and Habit-Controlled Nano Crystallites of Tungsten Oxide. *Sens. Actuators, B* **2003**, *93*, 486−494.
(49) Simion, C. E.; Somacescu, S.; Teodorescu, V. S.; Osiceanu, P.; Stanoiu, A. H2 S Sensing Mechanim of SnO2 -CuWO4 Operated under Pulsed Temperature Modulation. *Sens. Actuators, B* **2018**, *259*, 258−268.
(50) Stanoiu, A.; Simion, C. E.; Sackmann, A.; Baibarac, M.; Florea, O. G.; Osiceanu, P.; Teodorescu, V. S.; Somacescu, S. Networked Mesoporous SnO2 Nanostructures Templated by Brij 35 with Enhanced H2 S Selective Performance. *Microporous Mesoporous Mater.* **2018**, *270*, 93−101.
(51) Naumkin, A. V.; Kraut-Vass, A.; Gaarenstroom, S. W.; Powell, C. J. *NIST Reference Database*, version 4.1, 2012.
(52) Staerz, A.; Somacescu, S.; Epifani, M.; Russ, T.; Weimar, U.; Barsan, N. WO3 Based Gas Sensors. *Proceedings* **2019**, *2*, 826.
(53) Albanese, E.; Di Valentin, C.; Pacchioni, G. H2O Adsorption on WO3 and WO3-x (001) Surfaces. *ACS Appl. Mater. Interfaces* **2017**, *9*, 23212−23221.
(54) Kanan, S. M.; Lu, Z.; Cox, J. K.; Bernhardt, G.; Tripp, C. P. Identification of Surface Sites on Monoclinic WO3 Powders by Infrared Spectroscopy. *Langmuir* **2002**, *18*, 1707−1712.
(55) Ramis, G.; Cristiani, C.; Elmi, A. S.; Villa, P.; Busca, G. Characterization of the Surface Properties of Polycrystaline WO3. *J. Mol. Catal.* **1990**, *61*, 319−331.
(56) Davydov, A. A. *Infrared Spectroscopy of Adsorbed Species on the Surface of Transition Metal Oxides*; Rochester, C. H., Ed.; John Wiley & Sons, Inc.: Chichester, 1990.
(57) Yang, L.; Marikutsa, A.; Rumyantseva, M.; Konstantinova, E.; Khmelevsky, N.; Gaskov, A. Quasi Similar Routes of NO2 and NO Sensing by Nanocrystalline WO3: Evidence by In Situ DRIFT Spectroscopy. *Sensors* **2019**, *19*, 3405.
(58) Han, X.; Yin, X. Density Functional Theory Study of the NO2 -Sensing Mechanims on a WO3 (001) Surface: The Role of Surface Oxygen Vacancies in the Formation of NO and NO3. *Mol. Phys.* **2016**, *114*, 3546.
(59) Heiland, G. Zum Einfluss von Wasserstoff Auf Die Elektrische Leitfaehigkeit von ZnO-Kristallen. *Z. Phys.* **1957**, *148*, 15−27.
(60) Kohl, D. Surface Processes in the Detection of Reducing Gases with SnO2-Based Devices. *Sensor. Actuator.* **1989**, *18*, 71−113.
(61) Young, R. P.; Sheppard, N. Infrared spectroscopic studies of adsorption and catalysis: Acetone and acetaldehyde on silica and silica-supported nickel. *J. Catal.* **1967**, *7*, 223.
(62) McManus, J. C.; Harano, Y.; Low, M. J. D. Infrared Study of the Interactions of Acetone and Siliceous Surfaces. *Can. J. Chem.* **1969**, *47*, 2545−2554.
(63) Würger, T.; Heckel, W.; Sellschopp, K.; Müller, S.; Stierle, A.; Wang, Y.; Noei, H.; Feldbauer, G. Adsorption of Acetone on Rutile TiO2 : A DFT and FTIRS Study. *J. Phys. Chem. C* **2018**, *122*, 19481−19490.
(64) A., Davydov *Molecular Spectroscopy of Oxide Catalyst Surfaces*; Wiley VCH, 2003.
(65) Petrik, N. G.; Henderson, M. A.; Kimmel, G. A. Insights into Acetone Photochemistry on Rutile TiO2(110). 1. Off-Normal CH3 Ejection from Acetone Diolate. *J. Phys. Chem. C* **2015**, *119*, 12262−12272.
(66) Xia, Y.; Zhang, B.; Ye, J.; Ge, Q.; Zhang, Z. Acetone-Assisted Oxygen Vacancy Diffusion on TiO2(110). *J. Phys. Chem. Lett.* **2012**, *3*, 2970−2974.
(67) Jin, H.; Zhou, H.; Zhang, Y. Insight into the Mechanism of CO Oxidation on WO3(001) Surfaces for Gas Sensing: A DFT Study. *Sensors* **2017**, *17*, 1898.
(68) Salje, E. K. H.; Rehmann, S.; Pobell, F.; Morris, D.; Knight, K. S.; Herrmannsdörfer, T.; Dove, M. T. Crystal structure and paramagnetic behaviour of. *J. Phys. Condens. Matter* **1997**, *9*, 6563−6577.
(69) Salje, E. The Orthorhombic Phase of WO3. *Acta Crystallogr., Sect. B: Struct. Crystallogr. Cryst. Chem.* **1977**, *33*, 574−577.
(70) Loopstra, B. O.; Rietveld, H. M. Further Refinement of the Structure of WO3. *Acta Crystallogr., Sect. B: Struct. Crystallogr. Cryst. Chem.* **1969**, *25*, 1420−1421.

https://dx.doi.org/10.1021/acssensors.0c00113
ACS Sens. XXXX, XXX, XXX−XXX

THE JOURNAL OF PHYSICAL CHEMISTRY Letters

Letter

Cite This: J. Phys. Chem. Lett. 2020, 11, 166−171

pubs.acs.org/JPCL

Direct Microscopic Proof of the Fermi Level Pinning Gas-Sensing Mechanism: The Case of Platinum-Loaded WO_3

Anna Staerz,[†] Mounib Bahri,[‡] Ugur Geyik,[†] Helena Brinkmann,[†] Udo Weimar,[†] Ovidiu Ersen,[‡] and Nicolae Barsan*[,†]

[†]Institute of Physical and Theoretical Chemistry (IPTC), University of Tuebingen, Auf der Morgenstelle 15, D-72076 Tuebingen, Germany

[‡]Institut de Physique et Chimie des Matériaux de Strasbourg (IPCMS), UMR 7504 CNRS-Université de Strasbourg, 23 rue du Lœss, F-67034 Strasbourg cedex 2, France

Supporting Information

ABSTRACT: It is widely known that the sensing characteristics of metal oxides are drastically changed through noble metal oxide surface additives. Using operando infrared spectroscopy it was identified that the Fermi level pinning mechanism dominates the sensor response of platinum-loaded WO_3. Spectroscopy, however, provides information about the sample only on average. Traditional microscopy offers structural information but is typically done in vacuum and on unheated sensors, very different than the operation conditions of metal oxide gas sensors. Here, state-of-the-art in situ scanning transmission electron microscopy offers spatially resolved information on heated samples at atmospheric pressure in varying gas atmospheres. As a result it was possible to directly couple microscopically observed structural changes in the surface noble metal nanoclusters with IR spectra and sensor responses. On the basis of the findings, the dominant Fermi level pinning mechanism could be validated. The presented work demonstrates the benefits of coupling in situ microscopy with operando spectroscopy in order to elucidate the sensing mechanism of metal oxides.

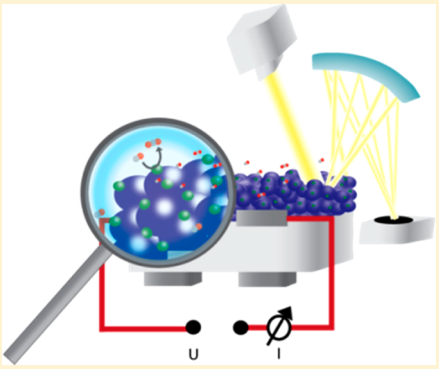

As the world becomes more interconnected, sensors will be needed for a wide array of applications. Gas sensors based on semiconducting metal oxides (SMOX) are an inexpensive, robust, sensitive, and compact option. Reactions on the surface of the heated porous SMOX nanomaterial result in a charge transfer, which causes a detectable change in the material's resistance.[1] In most cases, in order to increase stability and tune the sensing characteristics of SMOX, noble metal additives are used. In fact the first commercially available SMOX-based sensor, introduced in the 1960s by Figaro Engineering Inc., was already based on Pd-modified SnO_2.[2,3] In the 1980s Morrison and Yamazoe suggested two mechanisms, chemical interaction and Fermi level control, which explain how the additives change the surface reactions responsible for the sensor response.[4,5] In the case of a chemical interaction, the reactions between the SMOX with the target gas are activated by the surface loading. In the Fermi level control mechanism, the target gas reacts with the surface additive, changing the electronic coupling between the materials. Recently, operando infrared spectra showed indications of a dominant Fermi level pinning mechanism in the case of sensors based on Rh_2O_3 surface-loaded n-type SMOX (SnO_2, WO_3, and In_2O_3)[6,7] and platinum-loaded SnO_2 and WO_3.[8,9] Infrared spectra, however, only provide information about the sample on average. In order to elucidate the exact mechanism, a more localized, spatially resolved method is needed. Lately the direct visualization via transmission electron microscopy (TEM) was successfully coupled with Fourier transform infrared (FTIR) to elucidate structure−property relationships of catalysts.[10] Here, for the first time for a model system relevant to gas sensing, using in situ environmental gas scanning transmission electron microscopy (STEM), it was possible to observe structural changes in the noble metal nanoclusters during exposure to gas. It was also possible to directly correlate these changes to the sensor response and to infrared spectra taken under similar conditions. These results show that the noble metal additive clusters react predominantly with the reducing test gas, CO. In addition, based on the STEM images, it was possible to explain the drastic decrease of the resistance in highly reducing conditions. Using these inputs it can be understood why the sensor is permanently changed as a result of exposure to the highly reducing atmosphere.

As previously reported, at 300 °C the inherent sensing characteristics of WO_3—a low response to CO, high responses to low concentrations of acetone, practically humidity independent response to ethanol, and decreasing response of NO_2 with humidity—disappear as a result of loading with

Received: October 23, 2019
Accepted: December 13, 2019
Published: December 13, 2019

DOI: 10.1021/acs.jpclett.9b03114
J. Phys. Chem. Lett. 2020, 11, 166−171

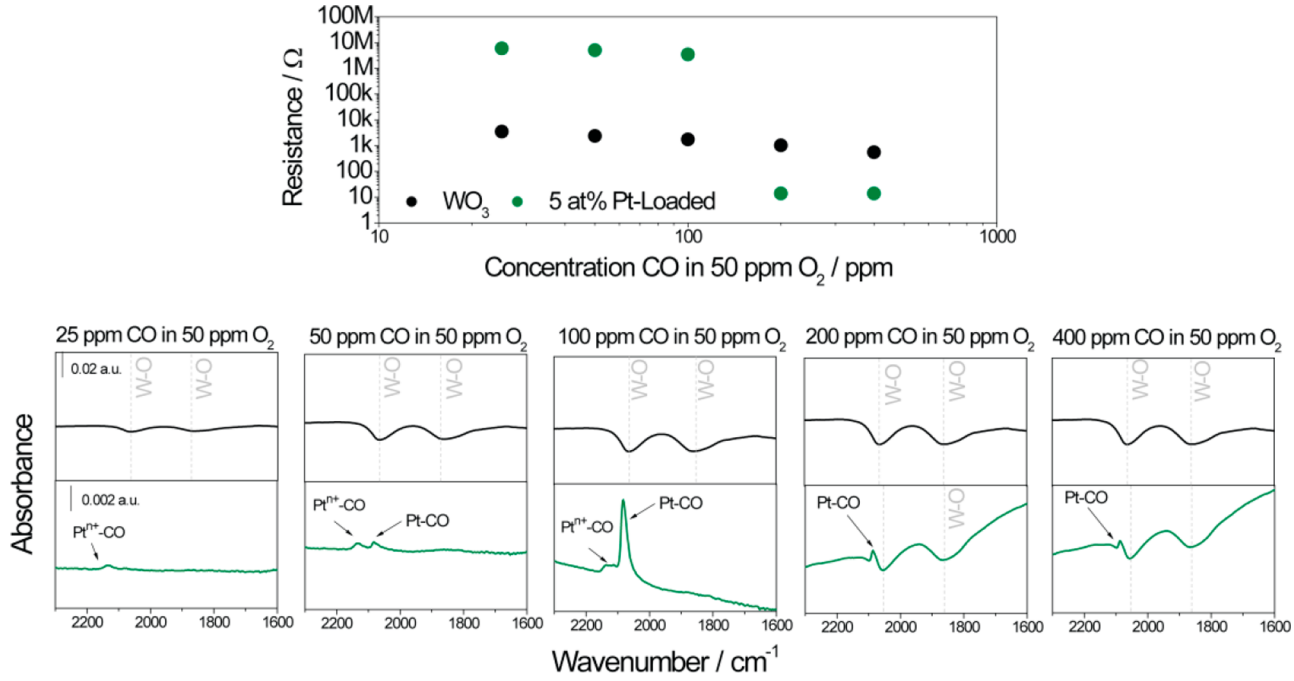

Figure 1. Resistance measurements taken on sensors based on WO_3 and 5 atom % platinum-loaded WO_3 during exposure to increasing concentrations of CO in a dry background of 50 ppm O_2 in N_2. The corresponding diffuse reflectance infrared Fourier transform spectra for the samples under selected conditions are also shown.

platinum (see previous work[9,11]). In all cases, the sensor signal to reducing gases in dry synthetic air decreases as a result of loading with platinum (see the Supporting Information).

On the basis of X-ray photoelectron spectroscopy (XPS) measurements, the platinum clusters on the surface of freshly prepared sensors are found to be dominantly oxidized (see Figure S.3). In the literature, XPS and ultraviolet photoelectron spectroscopy (UPS) was used to experimentally identify the Fermi level pinning mechanism of photocatalysts.[12,13] The conditions of the XPS and UPS measurements (ultrahigh vacuum and room temperature) are extremely different from the operation conditions of the sensors (standard atmospheric pressure and 300 °C). In addition, it is known that carbon contamination on the surface can significantly alter the work function of the sample attained using these techniques.[14,15] The samples examined here were prepared under standard laboratory conditions and calcined in ambient environment. As a result, all samples have a surface carbon contamination visible in the survey XPS (see the Supporting Information). Although the carbon contamination can be reduced using different methods, it is known that these pretreatments can also result in a significant change of the surface properties and the work function.[15] For these reasons, a different method is needed to determine if there is an electronic coupling between the oxidized surface clusters and WO_3. The resistance of the heated sensors in nitrogen is an alternative which enables the coupling of platinum clusters and WO_3 to be probed under more relevant application conditions and despite surface carbon contamination.[8,16] By measuring the resistance of the sensors during operation in nitrogen, it is assumed that the surface acceptor state related to the ionosorption of O_2 can be neglected. In this case the relation for a depletion layer limited charge transport can be used to describe the correlation between the resistance and the surface band bending. For this sample a band bending of 235 meV caused by the presence of noble metal oxide surface loadings was calculated.[8,16] This value indicates that the surface platinum nanoclusters are significantly electronically coupled with the WO_3 nanoparticles and that their presence causes an initial depletion layer.[9]

Based on operando diffuse reflectance Fourier transform (DRIFT) spectra, it was identified that, like for Rh-loaded WO_3, the Fermi level pinning mechanism also dominates in the case of platinum loading. Until now, however, this assumption was made solely on spectroscopic findings which provide only average information about the sample. In order to identify the exact mechanism, more localized information, i.e. at the nanoparticle level, is required. In order to correctly identify the processes responsible for the macroscopic response of the material used in the sensor device, localized information is needed in combination with average information obtained from a significant amount of the nanostructured material.

To obtain local and average information under similar operation conditions, which is relevant for the material behavior in operation conditions, operando diffuse reflectance infrared Fourier transform spectroscopy in low-oxygen background was coupled with in situ environmental gas STEM. The sensors were exposed to increasing concentrations of CO in a background of 50 ppm O_2 in N_2. The goal of these measurements was to compare the sensing behavior between conditions where oxidized platinum is present on the surface and a situation where only metallic platinum clusters remain. In this case the Fermi level pinning should be released when the noble metal clusters are fully metallic.[7−9] The full reduction of Rh_2O_3 surface clusters under these conditions was previously shown using X-ray absorption spectroscopy.[7] The resistance measurements, taken simultaneously to the infrared spectra, indicate a different mechanism between the Pt-loaded sample and the pure sample. The resistance change in correlation to the concentration of CO of the unloaded sample is similar to the behavior in synthetic air (for various

DOI: 10.1021/acs.jpclett.9b03114
J. Phys. Chem. Lett. 2020, 11, 166−171

reducing gases) (Figure S.4). The change in resistance shows a power law behavior, i.e. the decrease in resistance is linear in the log·log scale.[9,17] As expected, in the case of the unloaded sample the bands attributed to combinations and overtones of the tungsten oxide lattice (2055 and 1855 cm^{-1}) are decreasing[18,19] (Figure 1). At low CO concentrations the sensor response of the loaded sample also shows a linear response in log·log scale, at 200 ppm CO, however, there is significant drop in the resistance (Figure 1).

In previous work done on platinum-loaded WO_3 nanofibers, bands attributed to metallic platinum carbonyls were visible in the infrared spectra taken in high CO concentrations.[9] Here more information can be gained from the DRIFT spectra as carbonyls on both oxidized and metallic platinum are visible. During exposure to 25 ppm CO in 50 ppm O_2, only Pt^{n+}-carbonyls are visible.[8,20,21] If the concentration is increased to 50 ppm, carbonyls attributed to both oxidized and metallic platinum are visible. This indicates that both oxidized and metallic platinum clusters exist on the surface. This is different from rhodium surface clusters in which it was found that either the clusters are oxidized or fully reduced.[7] As the concentration is increased to 100 ppm CO, the intensity of the band attributed to metallic platinum increases significantly in comparison to that of oxidized platinum. After exposure to 200 ppm CO, the resistance of the material has significantly dropped and in the DRIFT spectra only the band attributed to metallic platinum carbonyls is still visible. At this point, decreasing bands attributed to combinations and overtones (2055 and 1855 cm^{-1}) of the tungsten oxide lattice also become visible.[18,19] The change of these bands over the concentration ranges indicates an initial interaction between carbon monoxide and the oxidized platinum surface clusters. As the concentration increases the platinum clusters become more reduced, and at 200 ppm, they are fully reduced. As mentioned previously, however, the infrared spectra provide only average information about the sample.

Figure 2 shows a comparison between a fresh sample (a) and a sample that was cooled in 400 ppm CO (b). The fresh sample shows a random dispersion of platinum oxide particles on the WO_3 support. Elemental mapping verifies the homogeneous dispersion of platinum in the fresh sample and can be seen in Figure S.5. After exposure to 400 ppm CO, the Pt particles are found to migrate toward the more uneven and potentially defective areas of the grains of WO_3 (following a hypothetical aggregative growth mechanism schematized by the green arrows). High-resolution images in Figure 2c,d show metallic Pt particles with Pt(200) (c) and Pt(111) (d) which confirm the reduction of PtOx particles to metallic Pt under CO. In order to additionally verify these findings, XPS spectra of a fresh sample and a sample that was cooled in 400 ppm CO were obtained. Also here the reduction of platinum is clearly visible (Figure S.3).

Thus, it is concluded that the surface clusters are fully reduced to their metallic state, which is in agreement with the infrared spectra acquired in similar conditions. In addition, these findings offer an explanation for why the sensor is irreversibly altered as a result of the reduction. The resistance before exposure to CO in low-oxygen background is approximately 20 MΩ, and after it is ca. 5 MΩ (Figure S.6). The presence of homogeneously oxidized platinum clusters on the surface of WO_3 was found to significantly increase the resistance of the samples. It is possible that after exposure to the reducing conditions, the platinum clusters are less oxidized

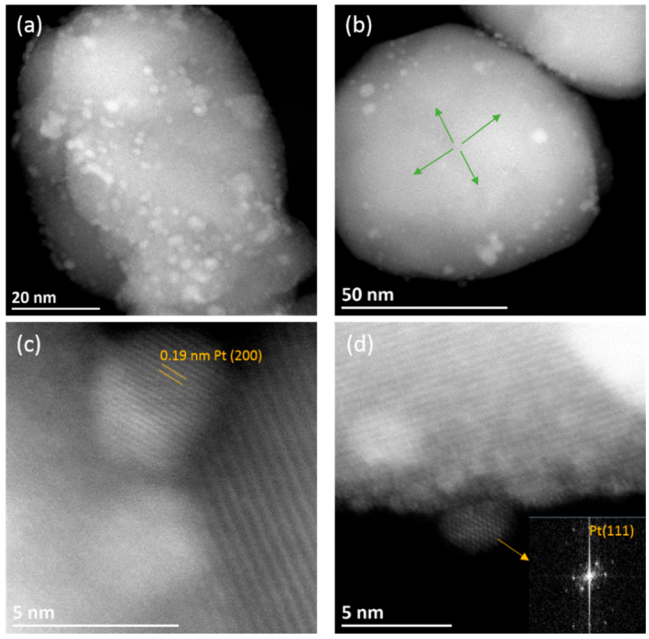

Figure 2. STEM-HAADF images of the PtOx–WO_3 sample before the exposure to CO (a) and after the exposure (b). HR-STEM-HAADF images (c and d) show metallic Pt nanoparticles after cooling in 400 ppm CO. Inset of panel d: Fast Fourier transform of the corresponding high-resolution image.

than before. Moreover, it is known that in addition to the surface additive type, the band bending scales with the contact areas between the materials. As a result of the aggregative growth mechanism, the platinum particles are much larger and more poorly dispersed as a result of the CO exposure, probably reducing the resulting band bending. To verify that these findings are generally valid for the sample, multiple regions were examined, and the STEM images are shown as Figure S.7 (fresh sample) and Figure S.8 (sample cooled in 400 ppm CO).

To better understand the change in particle distribution and the Pt phase transformation, in situ STEM measurements were done in different gas concentrations and under various environments. In particular, after the heated (300 °C) sample was stabilized at atmospheric pressure in 50 ppm oxygen in nitrogen, different concentrations of CO were introduced starting from 50 ppm and ending with 900 ppm. Figure 3 shows how platinum particles in a single area are reduced as a result of increasing CO concentration; based on the before-mentioned morphological changes, the reduction can be inferred. The results of the in situ measurement are then compared to the IR spectra taken under similar conditions. Under exposure to 50 ppm CO, the platinum particles are fully oxidized; very small clusters homogeneously dispersed on the whole surface (Figures 3 and S.7). As the concentration of CO increases, the platinum surface particles are reduced and the small clusters migrate and agglomerate. The green circle in Figure 3 illustrates the sintering of two platinum oxide particles. Note that the STEM high-angle annular dark-field (STEM-HAADF) intensity of the particles increases at 400 ppm CO, in agreement with a transformation to a denser phase, from oxide to metal. The typical particle size decrease associated with a morphological change is more significant for smaller particles and occurs already at low CO concentrations (a comparison can be additionally seen in Figure S.9). It is

DOI: 10.1021/acs.jpclett.9b03114
J. Phys. Chem. Lett. 2020, 11, 166−171

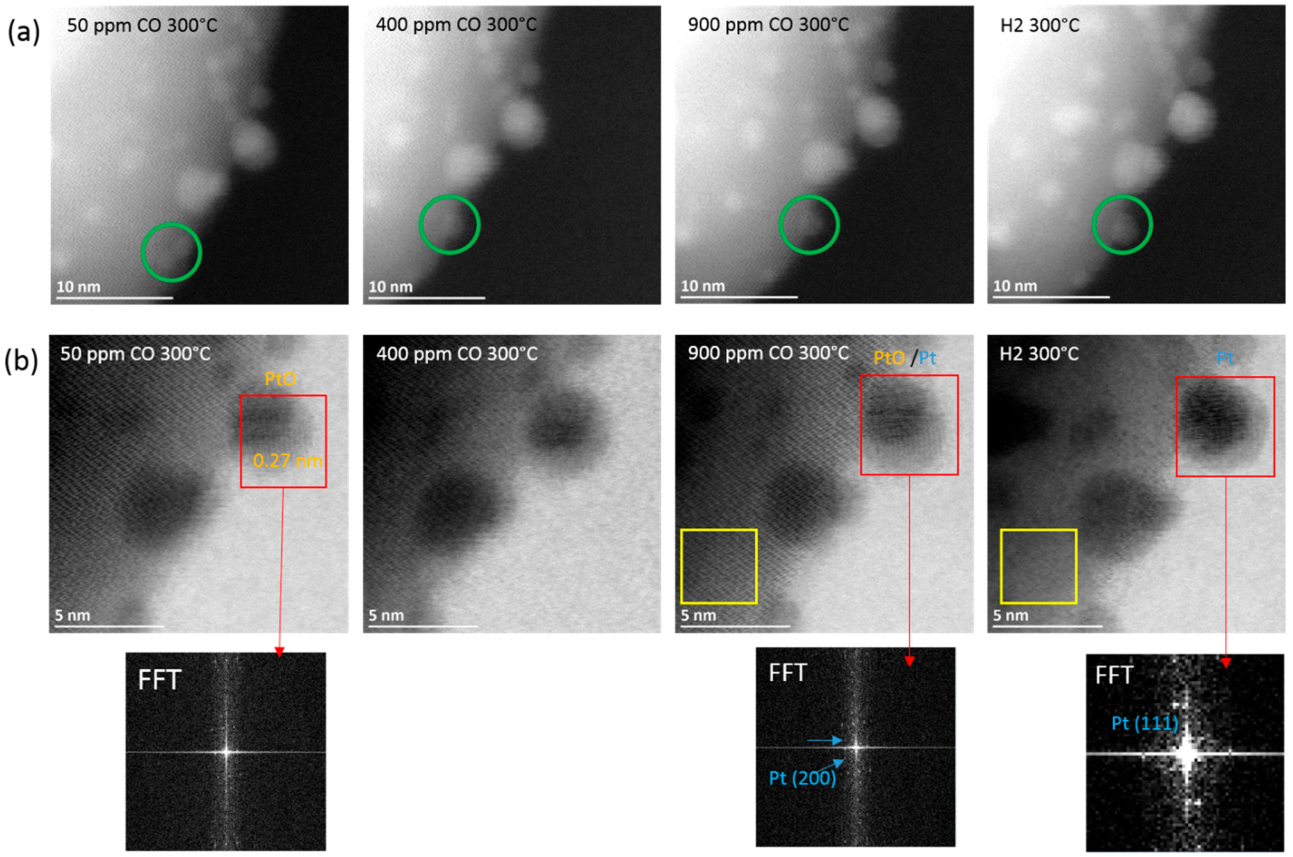

Figure 3. In situ STEM-HAADF images in different environments showing particle coalescence (a) and (b) in situ STEM-BF images showing the PtO_x−Pt structural transformation when increasing the CO concentration and under H_2 at 300 °C.

concluded that, in the examined sensor conditions, the migration and coalescence effect of these small clusters is significant and therefore potentially relevant when using this material as a gas sensor. Note that the effect is more strongly pronounced in the ex situ measurements (sample removed from the fresh gas sensor and one cooled in 400 ppm CO) due to the longer operation time at 300 °C, as well as by the high flow of the used reducing atmosphere.

Another important finding is that at 900 ppm the surface particles are reduced to metallic platinum with the appearance of Pt(200). This situation is in line with that indicated by the infrared spectra taken under exposure to 200 ppm CO. In general, the tendencies seen in the infrared spectra can be correlated to the TEM pictures which are taken under exposure to higher CO concentrations; this discrepancy is most likely due to the much smaller flow rate in the TEM cell. The TEM cell volume is only 1.2 μL, and some fine changes under a few parts per million are observed but the total amount is too small to allow a CO concentration increase in the mass spectrometer connected at the sample holder exit (see the experimental setup in Figure S.2). These two major differences, which are the small volume of the TEM cell and the analysis duration (only 1 h for each concentration), can explain the discrepancy in the typical concentrations where the reduction was observed by in situ DRIFT spectroscopy compared to in situ STEM.

From these results it is clear that unlike the rhodium oxide surface clusters which are either oxidized or metallic, the surface platinum clusters can be in a partially reduced state.[7] The findings indicate, however, that although the partial reduction of the surface platinum clusters is possible, the extreme drop in resistance occurs only once the clusters are entirely reduced and the Fermi level pinning is completely released. There are several possible explanations why the sample becomes conductive under high concentrations of CO in low-oxygen background. It is possible that the WO_3 surface could be extremely depleted as a result of the prior coupling with the platinum oxide clusters and cannot be significantly reoxidized in the low-oxygen conditions. Additionally, once the platinum surface clusters are reduced to their metallic state they could even catalyze the reaction between CO and WO_3, resulting in a significant reduction of the surface. Under 400 ppm CO in 50 ppm O_2, the material becomes conductive (the resistance is so low that the used setup can no longer properly measure it). Al Mohammad examined the electrical properties of WO_3 nanopowder at different reduction levels and found that until the material was reduced to WO_2, it showed *n*-type semiconductor behavior.[22] Venables et al. report that at ca. 300 °C the reduction of WO_3 to WO_2 takes place slowly, needing approximately 40 min to reach completion in a flowing H_2 atmosphere.[23] Upon exposure to pure hydrogen, the reduction of the platinum clusters was fast. In line with the findings of Venables et al. the reduction of the supporting oxide is also visible. In fact, after flushing the TEM cell with 50 μL of hydrogen, the complete reduction of WO_3 to W as well as the amorphization of the crystalline structure (yellow square in Figure 3) was observed. In the sample taken from the sensor cooled in 400 ppm CO in 50 ppm O_2, although the platinum clusters are still metallic, no reduction of the WO_3 is visible. These findings indicate that the significant drop in the

DOI: 10.1021/acs.jpclett.9b03114
J. Phys. Chem. Lett. 2020, 11, 166−171

resistance is most probably a result of a coupling between the metallic surface clusters and the WO_3, e.g. electrons from the metallic Pt are inserted into the base oxide, and not due to a strong reduction of WO_3.

The combination of operando spectroscopic results with more localized information from in situ microscopy was very useful for understanding the gas-sensing mechanism of platinum-loaded WO_3 sensors. Here it was shown that under normal sensing conditions, an oxygen-rich background, the oxidized platinum clusters dominate the surface chemistry of the sample. It was shown both spectroscopically and optically that under low-oxygen background and in high CO concentrations, these clusters are reduced to their metallic state. These findings allow the sensing mechanism of platinum oxide-loaded WO_3 to be fully elucidated. Furthermore, this work is the first time operando spectroscopy and in situ microscopy were combined to examine the sensing mechanism of metal oxides. The results demonstrate the complementarity of these methods and are indicative of their future usefulness.

EXPERIMENTAL SECTION

The platinum-loaded samples were prepared analogously to the Rh_2O_3 loaded samples as previously reported.[7,9] An aqueous solution of $PtCl_2$ (0.07 g, Sigma-Aldrich 99.9% trace metals basis) with WO_3 (1.00 g Sigma-Aldrich, nanopowder, <100 nm particle size (TEM)) and 5 mL of distilled water was brought to pH 1 using hydrochloric acid. The slurry was stirred at 80 °C for 2 h and dried at 70 °C. The procedure was then repeated a second time after which the powder was heat treated at 500 °C for 1 h. The same procedure was done with WO_3 (without the addition of a loading) in order to ensure that the detected changes were not a result of the preparation method.

To fabricate the sensors, the pure and the loaded materials were ground with propane-1,2-diol (Sigma-Aldrich; 99.5+% ACS Reagent) into a thick paste which was screen printed on Al_2O_3 substrates (with a backside Pt heater and Pt electrodes). The sensors were dried for 3 h at room temperature and overnight at 80 °C and then calcined in a tubular furnace (Heraeus ROK 6/30) for 10 min at 400 °C, 10 min at 500 °C, and finally 10 min at 400 °C. The DC resistance measurements were done using a Keithley 617 electrometer and an Agilent E3630A voltage source to heat the sensors. The sensors were mounted in a homemade Teflon chamber and heated to 300 °C using an Agilent E3614A DC power source. The gas flow was regulated using computer automated mass flow controllers with a total flow of 200 mL/min. The resistance was monitored using a Keithley 617 electrometer.

For the XPS measurements the pure and the loaded material were ground with propane-1,2-diol (Sigma-Aldrich; 99.5+% ACS Reagent) into a thick paste which was coated onto a stainless steel chip (half the chip was coated with the pure sample, and the other half was coated with the Pt-loaded sample). A second chip was prepared which contained just the Pt-loaded sample. The chips were dried for 3 h at room temperature and overnight at 80 °C and then calcined in a tubular furnace (Heraeus ROK 6/30) for 10 min at 400 °C, 10 min at 500 °C, and finally 10 min at 400 °C. The chip containing just the Pt-loaded sample was then additionally pretreated at 300 °C with 400 ppm CO in 50 ppm O_2. The experiments were performed in a multichamber ultrahigh vacuum (UHV) system with a base pressure of 1×10^{-10} mbar. X-ray photoelectron spectroscopy (XPS) measurements were performed using a separate UHV chamber equipped with a hemispherical analyzer (EA 125/Omicron), a Mg Kα X-ray source, and a pass energy of 20 eV. The energy scale was calibrated to reproduce the binding energy (BE) of Au $4f_{7/2}$ (84.0 eV).

For the operando DRIFT spectroscopy, a Vertex 80v narrow-band MCT detector with a spectral resolution of 4 cm^{-1} was used. A heated sensor (300 °C) was housed in a custom-made chamber containing a KBr window; the sensor was heated, and the resistance was recorded simultaneously with the infrared measurements. A Praying Mantis Optical unit (Harrick Scientific Products) was used, and the beam was condensed to a 2 mm diameter spot. A single channel spectrum was recorded every 15 min during test gas exposure. A schematic is provided in Figure S.1. In order to obtain the desired absorbance spectra, which provides information about the surface reaction with the target gas, the relation suggested by Olinger and Griffiths was used:[24]

$$A = -\log\left(\frac{\mathrm{SCS}_{\mathrm{exposure}}}{\mathrm{SCS}_{\mathrm{reference}}}\right) \quad (1)$$

The samples for the ex situ STEM measurements were taken from a freshly prepared sensor and from one that had been exposed to 400 ppm CO for 2 h.

Scanning transmission electron microscopy (STEM) was performed on a Cs corrected Jeol 2100F operating at 200 kV. Both HAADF and bright field (BF) spatially correlated images were acquired in STEM mode.

In situ operando gas STEM measurement was carried out using a Protochips Atmosphere device. The sample was placed between two microelectrical−mechanical system (MEMS)-based closed cells (SiN windows). The temperature and the gas flow in the cell are controlled by a heated holder and a gas delivery manifold, respectively. All the indicated temperatures are based on the company-provided calibration. At the sample holder exit, a mass spectrometer Pfeiffer Prisma Plus is connected, which acts as a residual gas analyzer.

The sample was dispersed in ethanol and drop-casted on the SiN membrane acting as a heating element. The in situ experiment was done at atmospheric pressure. The temperature was fixed to 300 °C. After the sample was stabilized in synthetic air for 1 h, the background was changed to 50 ppm O_2 in N_2 and stabilized for an additional hour. The CO concentration was increased stepwise, 50, 100, 400, and 900 ppm, in a background of 50 ppm O_2 in N_2. Each concentration was held for 1 h. The last gas environment chosen was 100% H_2 in order to compare the reduction phenomena to 900 ppm CO. Before each gas environment change, the temperature was slightly decreased to 200 °C and then increased again to 300 °C in order to avoid any unsuited microstructural modification of the specimen.

ASSOCIATED CONTENT

Supporting Information

The Supporting Information is available free of charge at https://pubs.acs.org/doi/10.1021/acs.jpclett.9b03114.

Schematics of the experimental setup; XPS surveys; STEM-HAADF, STEM-BF, and EDS images; in situ STEM images (PDF)

DOI: 10.1021/acs.jpclett.9b03114
J. Phys. Chem. Lett. 2020, 11, 166−171

AUTHOR INFORMATION

Corresponding Author

*E-mail: nb@ipc.uni-tuebingen.de.

ORCID

Mounib Bahri: 0000-0002-8336-9158
Ovidiu Ersen: 0000-0002-1553-0915
Nicolae Barsan: 0000-0001-6718-9889

Notes

The authors declare no competing financial interest.

ACKNOWLEDGMENTS

For assistance with XPS measurements, the authors thank Axel Belser and Benjamin Junker.

REFERENCES

(1) Barsan, N.; Koziej, D.; Weimar, U. Metal Oxide-Based Gas Sensor Research: How To? *Sens. Actuators, B* **2007**, *121* (1), 18−35.
(2) Taguchi, N. Gas-Detecting Device. U.S. Patent US3695848, 1971.
(3) Neri, G. First Fifty Years of Chemoresistive Gas Sensors. *Chemosensors* **2015**, *3* (1), 1−20.
(4) Morrison, S. R. Selectivity in Semiconductor Gas Sensors. *Sens. Actuators* **1987**, *12*, 425−440.
(5) Yamazoe, N.; Kurokawa, Y.; Seiyama, T. Effects of Additives on Semiconductor Gas Sensors. *Sens. Actuators* **1983**, *4*, 283−289.
(6) Staerz, A.; Kim, T.-H.; Lee, J.; Weimar, U.; Barsan, N. Nano-Level Control of Gas Sensing Characteristics via p-n Heterojunction between Rh_2O_3 Clusters and WO_3 Crystallites. *J. Phys. Chem. C* **2017**, *121*, 24701.
(7) Staerz, A.; Boehme, I.; Degler, D.; Bahri, M.; Doronkin, D.; Zimina, A.; Brinkmann, H.; Herrmann, S.; Junker, B.; Ersen, O.; et al. Rhodium Oxide Surface-Loaded Gas Sensors. *Nanomaterials* **2018**, *8* (11), 892.
(8) Degler, D.; Müller, S. A.; Doronkin, D. E.; Wang, D.; Grunwaldt, J.-D.; Weimar, U.; Barsan, N. Platinum Loaded Tin Dioxide: A Model System for Unravelling the Interplay between Heterogeneous Catalysis and Gas Sensing. *J. Mater. Chem. A* **2018**, *6* (5), 2034.
(9) Staerz, A.; Liu, Y.; Geyik, U.; Brinkmann, H.; Weimar, U.; Zhang, T.; Barsan, N. The Effect of Platinum Loading on WO_3 Based Sensors. *Sens. Actuators, B* **2019**, *291*, 378−384.
(10) Resasco, J.; Dai, S.; Graham, G.; Pan, X.; Christopher, P. Combining In-Situ Transmission Electron Microscopy and Infrared Spectroscopy for Understanding Dynamic and Atomic-Scale Features of Supported Metal Catalysts. *J. Phys. Chem. C* **2018**, *122* (44), 25143−25157.
(11) Staerz, A.; Somacescu, M. S.; Epifani, M.; Russ, T.; Weimar, U.; Barsan, N. WO3 Based Gas Sensors. *Proceedings* **2018**, *2* (826), 826.
(12) Kashiwaya, S.; Toupance, T.; Klein, A.; Jaegermann, W. Fermi Level Positions and Induced Band Bending at Single Crystalline Anatase (101) and (001) Surfaces: Origin of the Enhanced Photocatalytic Activity of Facet Engineered Crystals. *Adv. Energy Mater.* **2018**, *8* (33), 1802195.
(13) Lohaus, C.; Klein, A.; Jaegermann, W. Limitation of Fermi Level Shifts by Polaron Defect States in Hematite Photoelectrodes. *Nat. Commun.* **2018**, *9* (1), 4309.
(14) Helander, M. G.; Greiner, M. T.; Wang, Z. B.; Tang, W. M.; Lu, Z. H. Work Function of Fluorine Doped Tin Oxide. *J. Vac. Sci. Technol., A* **2011**, *29* (1), No. 011019.
(15) Kashiwaya, S.; Morasch, J.; Streibel, V.; Toupance, T.; Jaegermann, W.; Klein, A. The Work Function of TiO2. *Surfaces* **2018**, *1* (1), 73−89.
(16) Staerz, A.; Kim, T.-H.; Lee, J.-H.; Weimar, U.; Barsan, N. Nanolevel Control of Gas Sensing Characteristics via p−n Heterojunction between Rh_2O_3 Clusters and WO_3 Crystallites. *J. Phys. Chem. C* **2017**, *121* (44), 24701−24706.
(17) Yamazoe, N.; Shimanoe, K. Theory of Power Laws for Semiconductor Gas Sensors. *Sens. Actuators, B* **2008**, *128* (2), 566−573.
(18) Akamatsu, T.; Itoh, T.; Izu, N.; Shin, W. NO and NO_2 Sensing Properties of WO_3 and Co_3O_4 Based Gas Sensors. *Sensors* **2013**, *13* (9), 12467−12481.
(19) Hübner, M.; Simion, C. E.; Haensch, A.; Barsan, N.; Weimar, U. CO Sensing Mechanism with WO_3 Based Gas Sensors. *Sens. Actuators, B* **2010**, *151*, 103−106.
(20) Davydov, A. A. *Infrared Spectroscopy of Adsorbed Species on the Surface of Transition Metal Oxides*; Rochester, C. H., Ed.; John Wiley & Sons, Inc.: Chichester, 1990.
(21) Hadjiivanov, K. I. IR Study of CO and H_2O Coadsorption on Ptn+/TiO2 and Pt /TiO2 Samples. *J. Chem. Soc., Faraday Trans.* **1998**, *94* (13), 1901−1904.
(22) Al Mohammad, A. Synthesis, Separation and Electrical Properties of WO3-x Nanopowders via Partial Pressure High Energy Ball-Milling. *Acta Phys. Pol., A* **2009**, *116* (2), 240−244.
(23) Venables, D. S.; Brown, M. E. Reduction of Tungsten Oxides with Hydrogen and with Hydrogen and Carbon. *Thermochim. Acta* **1996**, *285*, 361−382.
(24) Olinger, J. M.; Griffiths, P. R. Quantitative Effects of an Absorbing Matrix on Near-Infrared Diffuse Reflectance Spectra. *Anal. Chem.* **1988**, *60* (21), 2427−2428.

DOI: 10.1021/acs.jpclett.9b03114
J. Phys. Chem. Lett. 2020, 11, 166−171

ACS APPLIED MATERIALS & INTERFACES

www.acsami.org

Research Article

Dominant Role of Heterojunctions in Gas Sensing with Composite Materials

Anna Staerz, Xing Gao, Faruk Cetmi, Zhang Ming, Udo Weimar, Tong Zhang, and Nicolae Barsan*

Cite This: *ACS Appl. Mater. Interfaces* 2020, 12, 21127–21132

Read Online

ACCESS | Metrics & More | Article Recommendations | Supporting Information

ABSTRACT: It is well known that composite materials, consisting of at least two metal oxides, show qualities and sensing behavior very different from the single components. Recently, the preparation of core–shell nanomaterials for gas sensors has become extremely popular. Specifically, these materials have been found to show desirable sensor responses. The preparation of core–shell nanomaterials is, however, complex, limiting the commercial applicability. Composite materials can be more easily attained simply through the mechanical mixing of the various components. Although some studies exist that attempt to compare mechanically mixed composites to those prepared via a synthetic route, these examinations are often flawed, as due to varying preparation methods, the basic characteristics of the materials are not the same. Here, it was possible to separate the role of the contacts between the materials from that of the secondary core–shell structure, by using a soft method to mechanically break apart the structure. This ensures that the difference in morphology is the only change in the material characteristics. It was verified that the composite materials show a different sensing behavior from that of the pure materials. It was also found that regardless of the secondary structure, the composite materials showed very similar sensor responses. By examining materials containing different ratios of Cr_2O_3 to SnO_2, it was possible to attribute the sensor behavior changes to the contacts between the different metal oxides. It was shown that by varying the concentration of each oxide it is possible to attain either an n- or p-type response and at a certain concentration even no response. This work is significant because it identifies that the contact between the materials plays the dominant role in the sensor response and it shows the viability of mechanical mixing for composite sample preparation.

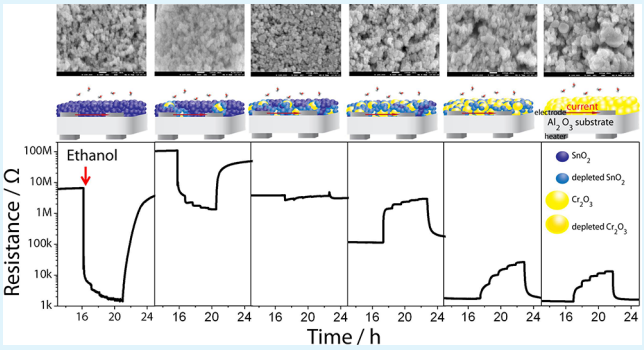

KEYWORDS: *heterojunction, composite materials, metal oxides, gas sensor*

INTRODUCTION

Academic interest in the preparation of core–shell nanomaterials (CSNs) has grown significantly in recent years. The core–shell nanoparticle structure consists of an inner layer of nanoparticles encapsulated by a different material.[1] Specifically, the use of CSNs in metal oxide-based gas sensors has become increasingly popular in the last 10 years. This can be seen in the number of yearly citations for the search: core–shell gas sensors, in the Web of Science, which increased from 400 in 2010 to over 3500 in 2018. The main advantage of CSNs is reported to be that through the combination of a core and shell material improved or new sensor properties are attained which cannot be reached using the individual components.[2] The preparation method, however, is very complex which limits the commercial applicability.[2] A simpler way to create composite materials would be through mechanical mixing. Although there are reports of interesting sensor effects,[3] this method appears to be less commonly used. Yamazoe and Shimanoe report that the contact geometry between materials dominants the sensor response.[4] They theorize that even when the arrangement of the grains in the sensitive layer is not random but is made up of secondary structures, if the contact geometry remains the same and changes in gas diffusion are negligible, then the result remains unchanged.[4] In contrast, when comparing the sensor responses of co-precipitated oxides with those of mechanical mixtures containing the same Sn/Ti ratio, Shaposhnik et al. found that the responses differ.[5] In this case however, the crystallite size was found to vary as a result of the co-precipitation, indicating that other factors besides the packing structure of the sample may be responsible for the detected changes.

From this survey of the literature, it becomes clear that in order to truly isolate the role of the secondary structure from

Received: March 19, 2020
Accepted: April 14, 2020
Published: April 14, 2020

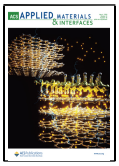

https://dx.doi.org/10.1021/acsami.0c05173
ACS Appl. Mater. Interfaces 2020, 12, 21127–21132

that of the contacts between the materials, it is very important that samples remain unchanged in all other respects. Here, composite samples of the n-type material SnO_2 and the p-type Cr_2O_3 were examined. In general, p-type semiconductors have received significantly less attention than n-type materials.[6] It is considered that the adsorbed oxygen on the Cr_2O_3 surface act as an acceptor and its interaction with the valence band determines the generation of holes.[7] The simultaneously performed work function and resistance change measurements of Pokhrel et al. support these findings.[8] In general, it is assumed that the exposure of a metal oxide to a reducing gas, like ethanol, decreases the concentration of surface oxygen. The electrons go back into the valence band and decrease the concentration of holes.[8] Overall, however, the sensor response of Cr_2O_3 to ethanol was found to be low due to the large influence of the gas insensitive resistive component of the metal oxide and electrode junction.[8] In order to make p-type semiconductors relevant for gas sensing, their response must be enhanced.[6]

The combination of Cr_2O_3 with the commonly used n-type SnO_2 is a promising solution. SnO_2 and Cr_2O_3 CSNs reportedly show a good p-type response to acetylene.[9] The addition of SnO_2 to Cr_2O_3 is, also, reported to increase the response to ethanol.[10]

Through a systematic study, the role of both the heterostructure and secondary morphology on the gas sensing will be examined. In order to isolate the role of the secondary structure from that of the contacts between the different oxides, it is very important that samples remain unchanged in all other respects. Here in order to achieve this, CSNs were mechanically broken to create randomly dispersed samples. The sensor behavior of these samples was then compared to CSN samples. Strikingly, it is found that the secondary structure has no influence on the sensor characteristics. It was, however, found that, in line with the literature, the sensor response of the composite materials was higher than of the pure materials. In order to identify the origin of this enhanced response, different ratios of mechanically mixed SnO_2−Cr_2O_3 were prepared. Based on the combination ratio of the materials, the sensors showed either an n- or p-type response. At a certain ratio, no sensor response was visible. In total, the results here show that the contact between the oxides plays a dominant role in defining the sensing characteristics of nanocomposite materials. These findings indicate that in the future the mechanical mixing of metal oxides is a viable method for the development of gas sensors based on composite materials.

EXPERIMENTAL SECTION

Synthetic Procedures. For comparison purposes, samples with and without the core−shell structure were desired. In a first step, the core−shell nanofibers were prepared by electrospinning. The two different precursors ($Cr(NO_3)_2{\cdot}9H_2O$ and $SnCl_2{\cdot}2H_2O$) were dissolved and transferred into two syringes which were equipped with a coaxial nozzle. The inner fluid formed the core of the nanofibers. A voltage of 16 kV was applied. After spinning for 20 min, the samples could be collected and then the samples were annealed at 550 °C for 2 h.[11] In order to limit differences as a result of preparation methods, randomly packed samples were prepared by breaking apart the core−shell structure using mechanical grinding via a mortar and pestle. The samples were ground by hand for 10 min in a mortar and pestle. The sensors were prepared using the following procedure. Each of the metal oxide powders were mixed with 1,2-propanediol (Sigma-Aldrich, 99.5+% ACS reagent) and then ground with mortar and pestle into a viscous paste. The paste was then screen-printed onto an alumina substrates containing platinum electrodes and a backside platinum heater (300 μm electrode gap, 300 μm width and 5 μm thickness; CeramTec AG, Germany) using an EKRA Microtronic II. The sensors were dried at room temperature for 1 h and then overnight at 80 °C (Heraeus UT12). The sensors were annealed for 10 min each at 400−500−400 °C with two steps to cool down in a tube furnace (Heraeus ROK 6/30). Based on the used screen, a layer thickness of approximately 50 μm is achieved. In the case of the various ratios, pure SnO_2 and Cr_2O_3 nanofibers were combined and then mechanically broken apart into nanoparticles.

Sensor Measurements. The sensors are installed in a homemade measurement chamber and heated to 200 °C using an Agilent E3614A dc power source. The gas flow was regulated using a computer monitored mass flow controller unit. The resistance was monitored using a Keithley 617 electrometer.

Morphology and microstructure of the samples were analyzed by using scanning electron microscopy (SEM; JOEL JSM-6500F) and transmission electron microscopy (TEM; JEM-2100F). The chemical binding energy and elemental analysis were investigated by an X-ray photoelectron spectrometer with Mg as the exciting source.

Additionally, the composite materials have been examined using scanning TEM (STEM), and experiments were performed using a Cs-corrected JEM-2100F (JEOL Akishima, Tokyo, Japan) operated at 200 kV.

RESULTS AND DISCUSSION

Two composite core−shell materials were prepared via electrospinning, see Figure 1. In order to ensure that the secondary nanofiber structures were successfully broken apart, SEM images were compared, Figure 2. They were obtained on the sensitive layer of finished sensors. From Figure 2a,c, it can be seen that the secondary nanofiber structure remains intact during the sensor preparation process. In Figure 2b,d, it can be seen that the soft mechanical grinding method was successful in breaking apart the secondary structure.

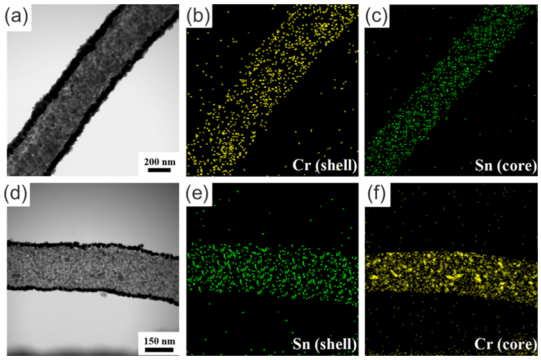

Figure 1. TEM image and elemental mapping of (a−c) SnO_2−Cr_2O_3 core−shell nanofibers and (d−f) Cr_2O_3−SnO_2 core−shell nanofibers.

The responses of the sensors to different gases in three different background humidity levels were examined. A sensor operation temperature of 200 °C was selected for this study based on the literature. Singh et al. found that above 300 °C the response of SnO_2 activated with Cr_2O_3 significantly decreases, while Liu et al. already report stable and high responses to ethanol at 150 °C.[10,12] The gases were selected due to their relevance in different applications, and the appropriate concentrations were applied: acetone (breath analysis[13]), ethanol (volatile organic compound to which metal oxides respond well to), and CO (exhaust[14]). In order to identify what role the secondary nanofiber structure has on the

https://dx.doi.org/10.1021/acsami.0c05173
ACS Appl. Mater. Interfaces 2020, 12, 21127−21132

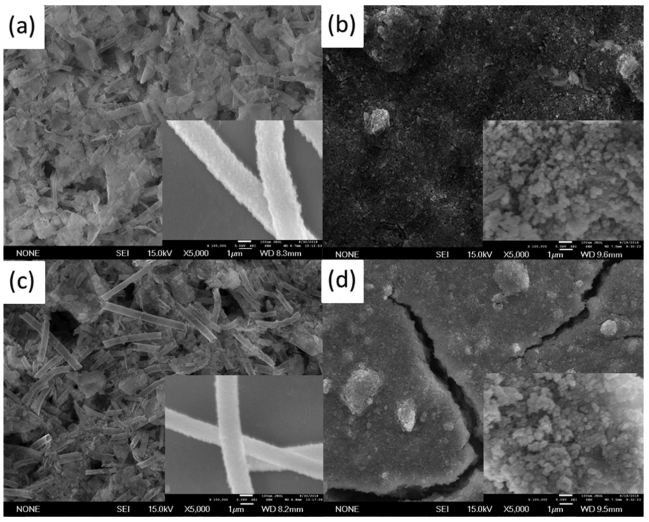

Figure 2. SEM image of the (a) Cr_2O_3– SnO_2 core–shell sensitive layer of a sensor, (b) crushed SnO_2–Cr_2O_3 core–shell sensitive layer of a sensor, (c) SnO_2–Cr_2O_3 core–shell sensitive layer of a sensor, and (d) crushed Cr_2O_3– SnO_2 core–shell sensitive layer of a sensor. The higher magnification insets are taken of powder samples.

response, sensors based on the Cr_2O_3–SnO_2 and SnO_2–Cr_2O_3 core–shell structures were compared to sensors based on the respective crushed materials, see Figure 3. For this comparison only one concentration of each gas was used, for information about the sensitivity of the samples see the Supporting Information, Figure S.1.

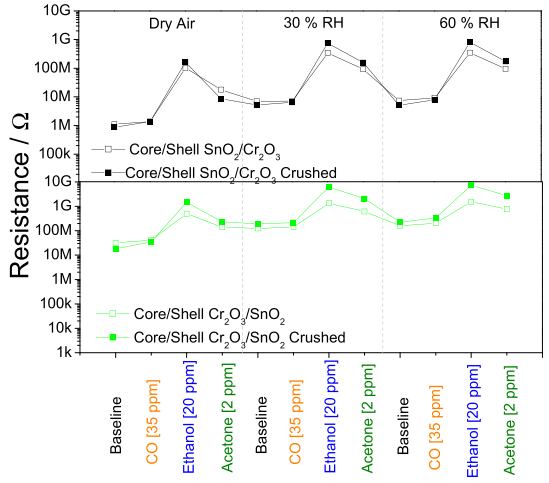

Figure 3. Sensor response of sensors based on the nanofiber composite material and the crushed composite materials.

The results are very surprising. The responses of the sensors based on the nanofibers and the respective crushed material are practically identical. In order to ensure that not only the secondary structure was destroyed but also the distribution of Cr_2O_3 and SnO_2 within the sample is homogeneous, energy-dispersive X-ray (EDX) was done on the crushed Cr_2O_3–SnO_2 core–shell materials and on the pure samples, see the Supporting Information, see Figure S.2. From these results, it appears that the nanofiber morphology provides no significant sensor advantage. There is, however, an identifiable difference between sensors based on the Cr_2O_3–SnO_2 and the SnO_2–Cr_2O_3 core–shell materials. Although both core–shell samples show p-type sensing behavior, the response of the SnO_2–Cr_2O_3 core–shell is higher than that of the Cr_2O_3–SnO_2 core–shell. This could be due to the different ratio of the metal oxides to each other in the two samples (different thickness of SnO_2 and Cr_2O_3 shells), see Figure 1. For reference, measurements of the pure SnO_2 and Cr_2O_3 materials were done. Again sensors based on nanofibers and on the respective crushed sample were examined, see Figure 4.

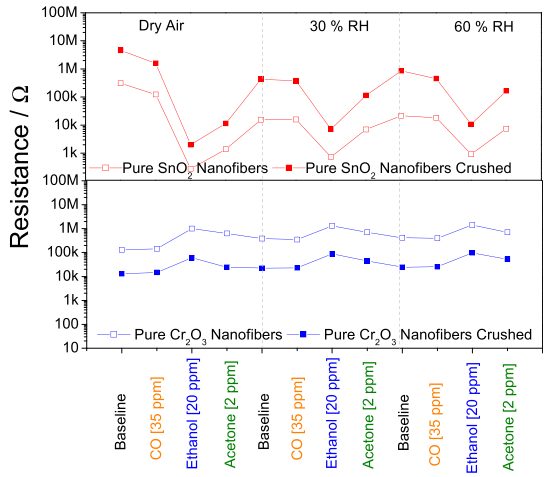

Figure 4. Sensor response of sensors based on the pure nanofiber material and the crushed pure materials.

As expected, the pure SnO_2-based sensors show an n-type response, while the Cr_2O_3 sensors show a p-type response. Similarly, to the composite materials, the nanofibers and the respective crushed materials of the pure samples show very similar sensor behavior. In most cases, the resistance of the samples containing the nanofibers is higher than the corresponding crushed materials. This result can be explained by the inverse dependence of the resistance on the cross-sectional area

$$R = \frac{\rho L}{A} \tag{1}$$

where ρ is the resistivity (Ω·m), L is the length (m), and A is the cross-sectional areas (m^2). The only exception is pure SnO_2, in this case the resistance is higher for the crushed sample. Based on X-ray diffraction (XRD) spectra, see the Supporting Information Figure S.3, taken of the pure nanofibers and the crushed materials, there is no significant change in the primary crystallite size (comparable full width half intensity values). From the SEM, see Figure 5, it can be seen that the soft mechanical crushing however not only broke the nanofibers apart but also separated the crystallites that formed larger agglomerated particles. This additional change in morphology is possibly responsible for the increase in the sensor resistance. In the case of the nanofibers, "necks", conduction paths between the grains which are only partially depleted, can readily form in the more agglomerated SnO_2 particles.[15] In the case of the sample after the crushing process, fewer "necks" between the grains could exist and as a result the resistance overall of the sample is higher.

From these measurements it is clear that the secondary nanofiber structure of the material provides no significant enhancement of the sensing properties both for the pure and the composite materials. Overall, however, the combination of

https://dx.doi.org/10.1021/acsami.0c05173
ACS Appl. Mater. Interfaces 2020, 12, 21127–21132

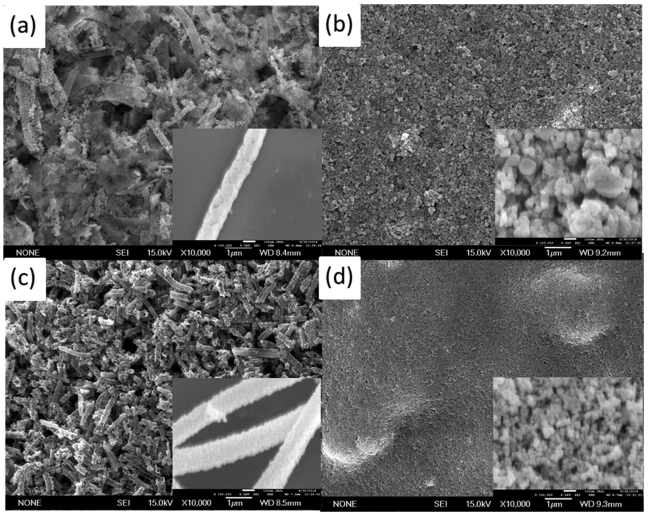

Figure 5. SEM image of the (a) pure Cr_2O_3 nanofiber sensitive layer of a sensor, (b) crushed Cr_2O_3 sensitive layer of a sensor, (c) pure SnO_2 nanofiber sensitive layer of a sensor, and (d) crushed SnO_2 sensitive layer of a sensor. The higher magnification insets are taken of a powder samples.

Cr_2O_3 with SnO_2 resulted in an enhanced p-type response. For both composite materials, (crushed and CSNs) the response to ethanol and acetone are significantly higher than that of pure Cr_2O_3. These results indicate that the interaction between the materials is responsible for the increased response.

In order to understand how the interaction between SnO_2 and Cr_2O_3 enhances sensing, additional measurements were done on samples of crushed SnO_2 containing various wt % of crushed Cr_2O_3. SEM images of the samples can be found in the Supporting Information, Figure S.3 and XRD Figure S.3. Homogenous dispersion and complete destruction of the fiber structure is verified by (EDS) mapping, see Supporting Information Figures S.5−S.7.

In Figure 6, the response of the sensors to one concentration of each gas is shown, to see how the sensor responds over a range of concentrations please see the calibration curves in the Supporting Information, Figure S.1. The most striking result is the drastic increase of the baseline resistance after the addition of 5 wt % Cr_2O_3 to SnO_2. As more Cr_2O_3 is added, the resistance then decreases. A heterojunction could occur at the

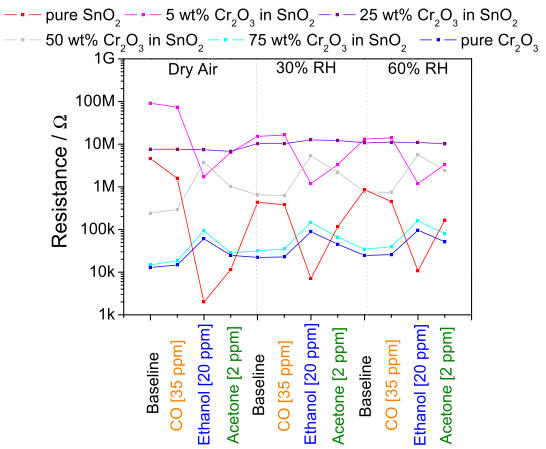

Figure 6. Sensor response of sensors based on the crushed mixed and pure materials.

interface between Cr_2O_3 and SnO_2 because the two are dissimilar crystalline semiconductors. For more detailed information about heterojunctions in general please see the review by Calow et al.[16] This change in baseline resistance could be the result of the heterojunction formed between the n-type SnO_2 and the p-type Cr_2O_3. In order to rule out the effect of adsorbed oxygen on the resistance, that is, have a flat band situation between grains of the same material, measurements were done in nitrogen, see Figure 7.[17−19] In this case, it

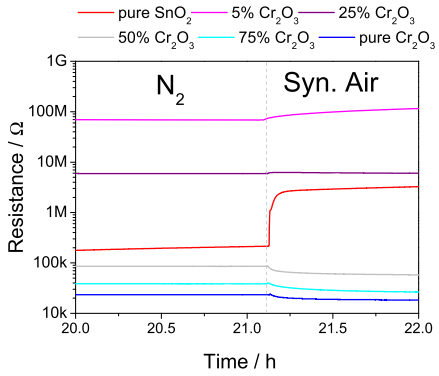

Figure 7. Resistance of the crushed samples in nitrogen and synthetic air.

is assumed that any difference in the resistance of the composite samples versus the pure samples is as a result of the contact between the materials. The drastic increase of the resistance as a result of the addition of only 5 wt % of $Cr_2O_3$is also present in this measurement, supporting the idea that a heterojunction occurs at the interface between the two dissimilar crystalline semiconductors.

In the literature, there are large ranges reported for the work function of the two materials: SnO_2 between 4.7 and 5.7 eV[20] and for Cr_2O_3 between 4.6[21] and 5.9.[22] From the measurements however, it appears that the electrons migrate from SnO_2 to Cr_2O_3, resulting in a majority charge carrier depletion layer in both oxides. The predicted band edge positions of Cr_2O_3 and SnO_2 are shown in Table 1, and Figure 8a illustrates

Table 1. Energy Band Gap, Calculated Conduction Band Edge, and Work Function of Cr_2O_3 and SnO_2[11,23,24]

semiconductors	Cr_2O_3	SnO_2
energy band gap[11,24] E_g (eV)	3.4	3.5
work function[11,24] W (eV)	5.68	4.9
conduction band edge[23] E_c (eV)	−3.93	−4.5
valence band edge[23] E_v (eV)	−7.43	−8

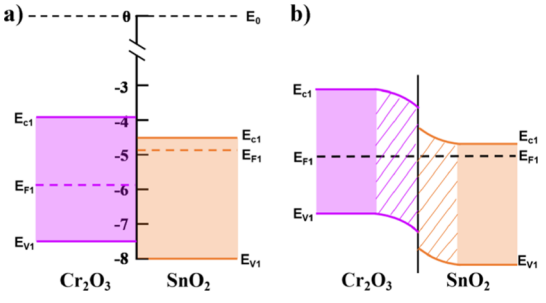

Figure 8. Energy band structure diagram for (a) p-type Cr_2O_3 and n-type SnO_2, (b) p-type Cr_2O_3−n-type SnO_2 heterojunction.

https://dx.doi.org/10.1021/acsami.0c05173
ACS Appl. Mater. Interfaces 2020, 12, 21127−21132

the energy band structure of Cr_2O_3 and SnO_2 before contact. Based on Table 1, the energy band structure diagram for p-type Cr_2O_3–n-type SnO_2 heterojunction is obtained, see Figure 8b. In the literature, the Fermi level of SnO_2 (an n-type semiconductor meaning it has donor levels in the band gap) is higher than that of Cr_2O_3 (a p-type semiconductor meaning it has acceptor levels in the band gap). As a result, when in contact electrons will move from SnO_2 to Cr_2O_3 resulting in an electron depletion layer within SnO_2 (upwards band bending) and a depletion layer for holes in Cr_2O_3 (downwards bending).

The grains of SnO_2 are very small; see Figure 5d inset, meaning it is possible that they are completely depleted as a result of their interaction with the grains of Cr_2O_3/formation of heterojunctions. The 5 wt % sample, where the current flows predominantly through the SnO_2, shows the most drastic resistance increase and shows an n-type response. As a result of the heterojunction with Cr_2O_3, SnO_2 has fewer electrons explaining the drastic resistance increase in nitrogen; that means that there are now fewer electrons which can be captured on the surface by adsorbed oxygen explaining the decreased effect of synthetic air on the resistance. At 25 wt % Cr_2O_3, the resistance is still significantly higher than both pure materials, but the presence of oxygen has no effect on the baseline resistance and no sensor response is visible. A possible explanation is that the current flows between both Cr_2O_3 and SnO_2, and the effects compensate each other. In the case of the 50 and 75 wt % Cr_2O_3, the current predominantly flows through the Cr_2O_3. The sensors show a p-type response. The resistance in nitrogen is under that of the pure SnO_2 sample, but is above the pure Cr_2O_3 sensor. Overall, the increase of the resistance as a result of the heterojunction is potentially less significant in this case due to the larger size of the Cr_2O_3 grains. The difference in size between the grains of the two materials can be seen in the SEM shown in Figure 5 and is verified by comparing the grain size calculated from the X-ray diffractograms using the Debye Scherrer equation. Here, the average Cr_2O_3 grain is over 20 nm while those of SnO_2 are approximately 10 nm, see Supporting Information Figure S.4. In other words, while the resistance of a large part of Cr_2O_3 grains is not affected by the heterojunction, a significantly larger portion of the smaller SnO_2 grains may be depleted. The effect of oxygen on the baseline of the 50 wt % and the 75 wt % Cr_2O_3 sample is more significant that on the pure chromium oxide sample. As a result of the heterojunction Cr_2O_3 has more electrons available, and thus the reactivity with atmospheric oxygen (more electrons can be captured by oxygen on the surface) increases. From these results it can be seen that the heterojunction between the materials is responsible for the improved sensor response. Here, it can also be identified that through optimization of the material concentration, different sensor characteristics can be attained.

CONCLUSIONS

It is known that by combining different metal oxides, it is possible to drastically alter sensor characteristics and to attain results not possible with pure materials. Composite materials are often prepared using complex synthesis methods in order to attain secondary morphological structures, for example, electrospinning to produce CSNs. In the past, studies that have tried to separate the role of the contact from that of the secondary morphology did not ensure that the characteristics of the samples remained otherwise unchanged. Here, by comparing samples, in which, the secondary structure had been mechanically broken with CSN material, it was possible to identify the dominant effect of the contact between the materials. By varying the ratio of the material, the materials showed varying sensor characteristics, showing both p- and n-type behavior. It was also found that at a certain ratio, the sample shows no sensor response. This finding shows the viability of mechanically mixing materials together to attain optimized sensing characteristics. It furthermore reveals that, by varying the ratio between the materials, different sensing behavior becomes attainable.

ASSOCIATED CONTENT

Supporting Information

The Supporting Information is available free of charge at https://pubs.acs.org/doi/10.1021/acsami.0c05173.

Calibration curves of all of the sensors to ethanol, CO, and acetone; EDX of the crushed core–shell samples; XRD spectra of the nanofiber and crushed pure Cr_2O_3 and SnO_2 samples; SEM and XRD of the composite materials; and STEM images and EDS mapping of the 25, 50, and 75 wt % of Cr_2O_3 in SnO_2 (PDF)

AUTHOR INFORMATION

Corresponding Author

Nicolae Barsan – *Institute of Physical and Theoretical Chemistry (IPTC), University of Tübingen, Tübingen D-72076, Germany*; orcid.org/0000-0001-6718-9889; Email: nb@ipc.uni-tuebingen.de

Authors

Anna Staerz – *Institute of Physical and Theoretical Chemistry (IPTC), University of Tübingen, Tübingen D-72076, Germany*

Xing Gao – *State Key Laboratory on Integrated Optoelectronics, College of Electronic Science and Engineering, Jilin University, Changchun 130012, People's Republic of China*

Faruk Cetmi – *Institute of Physical and Theoretical Chemistry (IPTC), University of Tübingen, Tübingen D-72076, Germany*

Zhang Ming – *State Key Laboratory on Integrated Optoelectronics, College of Electronic Science and Engineering, Jilin University, Changchun 130012, People's Republic of China*

Udo Weimar – *Institute of Physical and Theoretical Chemistry (IPTC), University of Tübingen, Tübingen D-72076, Germany*

Tong Zhang – *State Key Laboratory on Integrated Optoelectronics, College of Electronic Science and Engineering, Jilin University, Changchun 130012, People's Republic of China*; orcid.org/0000-0002-2690-859X

Complete contact information is available at: https://pubs.acs.org/10.1021/acsami.0c05173

Author Contributions

The manuscript was written through contributions of all the authors. All the authors have given approval to the final version of the manuscript.

Notes

The authors declare no competing financial interest.

ACKNOWLEDGMENTS

The authors would like to thank Prof. Dr. Ovidiu Ersen and Dr. Walid Baaziz from the University of Strasbourg for providing STEM images and EDS elemental mapping of the samples.

REFERENCES

(1) Wang, H.; Chen, L.; Feng, Y.; Chen, H. Exploiting Core-Shell Synergy for Nanosynthesis and Mechanistic Investigation. *Acc. Chem. Res.* **2013**, *46*, 1636−1646.

(2) Kalambate, P. K.; Dhanjai, Z.; Huang, Z.; Li, Y.; Shen, Y.; Xie, M.; Huang, Y.; Srivastava, A. K. Core@Shell Nanomaterials Based Sensing Devices: A Review. *Trends Anal. Chem.* **2019**, *115*, 147−161.

(3) Naik, A. J. T.; Parkin, I. P.; Binions, R. Gas Sensing Studies of an n-n Heterojunction Metal Oxide Semiconductor Sensor Array Based on WO_3 and ZnO Composites. *IEEE Sensors*; IEEE, 2013; No. November.

(4) Yamazoe, N.; Shimanoe, K. Basic approach to the transducer function of oxide semiconductor gas sensors. *Sens. Actuators, B* **2011**, *160*, 1352−1362.

(5) Shaposhnik, D.; Pavelko, R.; Llobet, E.; Gispert-guirado, F.; Vilanova, X. Hydrogen sensors on the basis of SnO_2−TiO_2 systems. *Procedia Eng.* **2011**, *25*, 1133−1136.

(6) Kim, H.-J.; Lee, J.-H. Highly Sensitive and Selective Gas Sensors Using P-Type Oxide Semiconductors: Overview. *Sens. Actuators, B* **2014**, *192*, 607−627.

(7) Morrison, S. Surface states on a chromia catalyst. *J. Catal.* **1977**, *47*, 69−78.

(8) Pokhrel, S.; Simion, C. E.; Quemener, V.; Bârsan, N.; Weimar, U. Investigations of Conduction Mechanism in Cr_2O_3 Gas Sensing Thick Films by Ac Impedance Spectroscopy and Work Function Changes Measurements. *Sens. Actuators, B* **2008**, *133*, 78−83.

(9) Gao, X.; Zhou, Q.; Lu, Z.; Xu, L.; Zhang, Q.; Zeng, W. Synthesis of Cr_2O_3 Nanoparticle-Coated SnO_2 Nanofibers and C_2H_2 Sensing Properties. *Front. Mater.* **2019**, *6*, 163.

(10) Singh, R. C.; Kohli, N.; Singh, M. P.; Singh, O. Ethanol and LPG Sensing Characteristics of SnO_2 Activated Cr_2O_3 Thick Film Sensor. *Bull. Mater. Sci.* **2010**, *33*, 575−579.

(11) Li, F.; Gao, X.; Wang, R.; Zhang, T.; Lu, G.; Barsan, N. Design of Core-Shell Heterostructure Nanofibers with Different Work Function and Their Sensing Properties to Trimethylamine. *ACS Appl. Mater. Interfaces* **2016**, *8*, 19799−19806.

(12) Liu, H.; Du, X.; Xing, X.; Wang, G.; Qiao, S. Z. Highly ordered mesoporous Cr_2O_3 materials with enhanced performance for gas sensors and lithium ion batteries. *Chem. Commun.* **2012**, *48*, 865−867.

(13) Deng, C.; Zhang, J.; Yu, X.; Zhang, W.; Zhang, X. Determination of Acetone in Human Breath by Gas Chromatography-Mass Spectrometry and Solid-Phase Microextraction with on-Fiber Derivatization. *J. Chromatogr. B: Anal. Technol. Biomed. Life Sci.* **2004**, *810*, 269−275.

(14) Wiegleb, G.; Heitbaum, J. Semiconductor Gas Sensor for Detecting NO and CO Traces in Ambient Air of Road Traffic. *Sens. Actuators, B* **1994**, *17*, 93−99.

(15) Bârsan, N.; Hübner, M.; Weimar, U. Conduction Mechanisms in SnO_2 Based Polycrystalline Thick Film Gas Sensors Exposed to CO and H_2 in Different Oxygen Backgrounds. *Sens. Actuators, B* **2011**, *157*, 510−517.

(16) Calow, J. T.; Deasley, P. J.; Owen, S. J. T.; Webb, P. W. A Review of Semiconductor Heterojunctions. *J. Mater. Sci.* **1967**, *2*, 88−96.

(17) Staerz, A.; Boehme, I.; Degler, D.; Bahri, M.; Doronkin, D.; Zimina, A.; Brinkmann, H.; Herrmann, S.; Junker, B.; Ersen, O.; et al. Rhodium Oxide Surface-Loaded Gas Sensors. *Nanomaterials* **2018**, *8*, 892.

(18) Degler, D.; Müller, S. A.; Doronkin, D.; Wang, D.; Grunwaldt, J.-D.; Weimar, U.; Barsan, N. Platinum loaded tin dioxide: a model system for unravelling the interplay between heterogeneous catalysis and gas sensing. *J. Mater. Chem. A* **2018**, *6*, 2034.

(19) Staerz, A.; Kim, T.-H.; Lee, J.; Weimar, U.; Barsan, N. Nano-Level Control of Gas Sensing Characteristics via p−n Heterojunction between Rh_2O_3 Clusters and WO_3 Crystallites. *J. Phys. Chem. C* **2017**, *121*, 24701−24706.

(20) Klein, A.; Körber, C.; Wachau, A.; Säuberlich, F.; Gassenbauer, Y.; Harvey, S. P.; Proffit, D. E.; Mason, T. O. Transparent Conducting Oxides for Photovoltaics: Manipulation of Fermi Level, Work Function and Energy Band Alignment. *Materials* **2010**, *3*, 4892−4914.

(21) Dillmann, B.; Rohr, F.; Seiferth, O.; Klivenyi, G.; Bender, M.; Homann, K.; Yakovkin, I. N.; Ehrlich, D.; Bäumer, M.; Kuhlenbeck, H.; et al. Adsorption on a Polar Oxide Surface: O_2, C_2H_4 and Na on $Cr_2O_3(0001)/Cr(110)$. *Faraday Discuss.* **1996**, *105*, 295−315.

(22) Singh, K. K.; Senapati, K. K.; Borgohain, C.; Sarma, K. C. Newly Developed Fe_3O_4−Cr_2O_3 Magnetic Nanocomposite for Photocatalytic Decomposition of 4-Chlorophenol in Water. *J. Environ. Sci.* **2017**, *52*, 333−340.

(23) Xu, Y.; Schoonen, M. A. A. The Absolute Energy Positions of Conduction and Valence Bands of Selected Semiconducting Minerals. *Am. Mineral.* **2000**, *85*, 543−556.

(24) Kim, T.-H.; Yoon, J.-W.; Kang, Y. C.; Abdel-Hady, F.; Wazzan, A. A.; Lee, J.-H. A Strategy for Ultrasensitive and Selective Detection of Methylamine Using P-Type Cr_2O_3: Morphological Design of Sensing Materials, Control of Charge Carrier Concentrations, and Configurational Tuning of Au Catalysts. *Sens. Actuators, B* **2017**, *240*, 1049−1057.

https://dx.doi.org/10.1021/acsami.0c05173
ACS Appl. Mater. Interfaces 2020, 12, 21127−21132

Sensors & Actuators: B. Chemical 291 (2019) 378–384

Contents lists available at ScienceDirect

Sensors and Actuators B: Chemical

journal homepage: www.elsevier.com/locate/snb

The effect of platinum loading on WO_3 based sensors

Anna Staerz[a], Yunshi Liu[b], Ugur Geyik[a], Helena Brinkmann[a], Udo Weimar[a], Tong Zhang[b,*], Nicolae Barsan[a,*]

[a] Institute of Physical and Theoretical Chemistry (IPTC), University of Tuebingen, Auf der Morgenstelle 15, D-72076, Tuebingen, Germany
[b] State Key Laboratory on Integrated Optoelectronics, College of Electronic Science and Engineering, Jilin University, Changchun, 130012, People's Republic of China

ARTICLE INFO

Keywords:
Gas sensors
WO_3
Platinum surface loading
Fermi level pinning

ABSTRACT

In order to increase the stability of semiconducting metal oxides and to modify their gas sensing behavior, noble metal surface additives are often used. In literature, there are numerous papers that report the drastic effect of platinum loading on the sensing characteristics of WO_3. Here a thorough characterization of two different platinum loaded WO_3 samples was coupled with operando diffuse reflectance infrared Fourier transform spectroscopy. Based on the results, it was possible to identify the mechanism which is responsible for the changed sensor behavior. It was found that in this case a Fermi level pinning mechanism dominates. In addition, by comparing the two samples prepared with different impregnation methods, it could be shown that the dispersion on the surface of the material determines how strong the effect of the loading is. This work complements recent findings in which the Fermi level pinning mechanism was identified for Rh_2O_3 loaded samples (SnO_2, In_2O_3 and WO_3) and Pt-loadings on SnO_2. The results help in understanding reports already found in literature and provides useful inputs for the intentional tuning of sensor characteristics.

1. Introduction

Semiconducting metal oxide (SMOX) based gas sensors are an inexpensive, robust and compact alternative to other gas detection methods. The first commercially available gas sensor was developed by Naoyoshi Taguchi in the 1960s [1]. In order to increase the stability of this SnO_2 based gas sensor and to tune its sensor response, the noble metal catalyst Pd was added [1]. Even today most commercially available SMOX based gas sensors contain noble metal additives. Already in the late 1980s and early 1990s, Morrison and Yamazoe et al. suggested two possible modes of interaction between the noble metal loading and the base metal oxide: spillover effect and the Fermi level pinning mechanism [2,3]. In the case of the spillover effect, the target gas adsorbs onto the loading. This adsorbate is then transferred to the metal oxide where the decomposition reaction takes place [2,3]. In the case of the Fermi level pinning mechanism, the Fermi level of both materials is pinned by the contact between the loading and the base material. The reaction takes place entirely on the noble-metal loading. If, as a result of the interaction with the target gas, the work function of the noble metal loading changes, then the charge layer in the base material caused by the contact is altered [2,3]. Experimental observations of either mechanism are limited. Today, the optimization of sensors still largely occurs based on empirical findings. Recently it has been found that in the case of Rh_2O_3 loaded SnO_2, WO_3 and In_2O_3 as well as Pt-loaded SnO_2, the Fermi level pinning mechanism dominates [4–6]. More research is needed to verify the general applicability of the Fermi level pinning mechanism for gas sensors based on noble metal loaded n-type semiconductors. Based on the findings reported here, the mechanism can be expanded to include Pt-loaded WO_3. In addition to the catalyst type, it is known that the size of the noble metal oxide affects its reactivity [7] and can, thus, have an effect on the sensor response. Here two different loading methods are examined and in both cases the Fermi level pinning mechanism is identified. This proves that the results are generally true for WO_3 loaded with platinum. It additionally highlights that through a homogeneous dispersion, the noble metal catalyst more efficiently dominates the sensor response via the Fermi level pinning mechanism. This is an application relevant finding, as it shows how a lower amount, i.e. less expensive solution, of loading with a noble metal catalyst can be effective. The drastic effect of loading with platinum is shown by examining how the response of WO_3 sensors, to five different gases, changes. The gases were selected due to their relevance in different applications. There are numerous publications that report WO_3 to be a good sensor for acetone [8]. The detection of acetone in a concentration range (0.5 ppm and 2 ppm) is relevant for the monitoring of diabetes via breath analysis [9]. Low concentrations of toluene are relevant for monitoring indoor air quality. The Canadian

* Corresponding authors.
E-mail addresses: zhangtong@jlu.edu.cn (T. Zhang), nb@ipc.uni-tuebingen.de (N. Barsan).

https://doi.org/10.1016/j.snb.2019.04.088
Received 18 February 2019; Received in revised form 17 April 2019; Accepted 17 April 2019
Available online 18 April 2019
0925-4005/

government has set an indoor air exposure limit at 4 ppm [10]. CO (30 ppm and 100 ppm) and NO_2 (2 ppm and 10 ppm) are both exhaust pollutants, between [11,12]. In addition the response to ethanol was examined because there are several reports in literature that through surface loading with platinum WO_3 becomes better suited to detect ethanol [13,14].

Through the complete characterization presented here, it is possible to expand a previously suggested mechanism to platinum loaded WO_3, indicating a general validity. In addition, based on these findings, which indicate a dominant Fermi level pinning mechanism, it is possible to understand the origin of results found in literature.

2. Material and methods

The sol gel loaded samples were prepared according to the procedure described in Ref. [4]. 0.073 g of $PtCl_2$ (Sigma-Aldrich 99.9% trace metals basis) with 1 g of WO_3 (Sigma-Aldrich, nanopowder, < 100 nm particle size (TEM)) were stirred in deionized water at a pH value of 1.0 (attained through the addition of HCl) at 80 °C for 2 h and dried at 70 °C. Afterwards, the attained powders were calcined at 500 °C for 1 h. In addition, to ensure that the changes in sensor response were not caused by the presence of the surface-loading and not due to the preparation procedure itself, the pure samples were also stirred in deionized water at a pH value of 1.0 (attained with HCl). The suspension was also stirred at 80 °C for 2 h and then dried at 70 °C. The powders were calcined at 500 °C for 1 h.

The nanofibers were prepared using the following method. 0.7 g of $(NH_4)_6H_2W_{12}O_{40}{\cdot}H_2O$ and 6 mL of deionized water were mixed together and stirred vigorously for 3 h. Then, 0.8 g of polyvinyl pyrrolidone (PVP, M_w = 1,300,000) was added to the mixture and it was allowed to stir overnight. This viscous solution was used to fabricate $(NH_4)_6H_2W_{12}O_{40}$/PVP as-spun fibers. A typical electrospinning setup composed of a high voltage DC power supply, a capillary and a grounded collector, was used. The solution was filled into a 5 mL syringe equipped with a stainless steel needle having an inner diameter of 0.7 mm. A high DC voltage of 15 kV was applied and the feeding rate was 0.7 mL/h. The as-prepared fibers were collected at a distance of 20 cm. All the as-prepared fibers were calcined at 550 °C for 2 h with a heating rate of 1 °C. After natural cooling, WO_3 was obtained. A certain amount of WO_3 nanofibers was added to deionized water with ultrasonication for 30 s. After stirring for 6 h, a milky suspension was obtained. Then 0.01 mmol H_2PtCl_6 aqueous solution was added to the above mixture and the Pt/W atomic ratio was 1/100. Pt NPs were formed by adding $NaBH_4$ solution into the mixture dropwise over 30 min. The molar ratio of H_2PtCl_6 and $NaBH_4$ was 1/2. Finally, the mixture was washed using ethanol and deionized water three times and dried at 60 °C. Surface loaded Pt/WO_3 sample was obtained.

To fabricate the sensors, the pure and loaded materials were ground with 1,2-propanediol (Sigma-Aldrich; 99.5 + % ACS Reagent) into a thick paste which was screen-printed on Al_2O_3 substrates (with a backside Pt-heater and Pt electrodes). The sensors were dried for 3 h at room temperature, overnight at 80 °C and then calcined in a tubular furnace (Heraeus ROK 6/30)) for 10 min. at 400 °C, 10 min. at 500 °C and finally 10 min. at 400 °C. The DC resistance measurements were done using a Keithley 617 electrometer and an Agilent E3630A voltage source to heat the sensors. The sensors were mounted in a PTFE sensor chamber and the gases were supplied using a computer operated gas mixing system (the total flow was held constant at 200 ml/min). The sensor signal was calculated using the following equation for reducing gases:

$$s = \frac{R_{reference}}{R_{Test\ Gas}} \tag{1}$$

In the case of oxidizing gases (NO_2), the inverse relationship was used. For the operando diffuse reflectance infrared Fourier transform (DRIFT) spectroscopy a Vertex80v narrow-band MCT detector with a spectral resolution of 4 cm^{-1} was used. A heated sensor (300 °C) was housed in a custom-made chamber containing a KBr window. As during standard operation the sensor was heated and the resistance was recorded. A single channel spectrum was recorded every 15 min during test gas exposure. In order to obtain the desired absorbance spectra which provides information about the surface reaction with the target gas the relationship suggested by Olinger and Griffiths was used [14]:

$$A = -log\left(\frac{SCS_{exposure}}{SCS_{reference}}\right) \tag{2}$$

As an example, the evaluation of the pure WO_3 from Sigma Aldrich during exposure to 18 ppm ethanol is given in the supplementary information.

Morphology and microstructure of the samples were analyzed by using scanning electron microscopy (SEM; JOEL JSM-6500F) transmission electron microscopy (TEM; JEM-2100F). The chemical binding energy and elemental analysis were investigated by an X-ray photoelectron spectrometer (XPS) with Mg as the exciting source.

3. Results and discussion

The sensors were operated at 300 °C, a commonly used temperature for WO_3 based sensors. The doping levels were selected for a number of reasons. In previous studies, it was found that high loadings were necessary to achieve significant changes of the sensing characteristics [4]. This is in line with literature in which high loadings between 1 at% and 7 at% are often reported [13,15–18]. The sensor response to different gases, selected due to their relevance in various applications was investigated. In Fig. 1, the sensor signals, calculated using Eq. (1), to one concentration of each gas are shown. For real applications the effect of humidity is important, so the responses in dry air and in 30% RH at room temperature were measured. Both pure WO_3 materials show the expected sensor behavior [19]. The sensors respond well to acetone and ethanol, show low responses to CO and the response to NO_2 decreases significantly with humidity [19]. The sensors respond well to very low concentrations of toluene [19]. Despite the difference in the preparation method, the loading has a similar effect in both cases. The sensor response to NO_2 and toluene disappears. In both cases the samples still respond to acetone and ethanol. It has been previously reported that loading with platinum increases the selectivity of WO_3 to ethanol [13,14]. Similar to the results here, platinum loaded WO_3 has been reported to respond well to acetone, with a significant decrease, however, of the response in humidity [20]. No explanation supported by operando findings, however, for the results exists. To identify what causes these changes, additional measurements and structural information about the sample are needed.

Using XPS measurements, information about the state of the surface additives is gained. The used material underwent the same preparation and thermal treatment as the sensors. As shown in the high-resolution Pt 4f spectra (Fig. 2) the raw data can be separated into several fitted peaks, indicating the existence of different chemical states for the Pt component. The peaks with binding energies (BEs) located at 71.3 and 74.5 eV can be assigned to the metallic Pt species. Meanwhile, the BEs at 72.5 and 75.3 eV with two shakeup satellite peaks correspond to oxidized Pt, i.e. PtO and PtO_2 [9]. Thus, both metallic and oxidized Pt components can be found on the surface of the two samples

From SEM pictures taken of the sensitive layer of the sensors, it can be clearly ascertained that the morphology, specifically the grain size, is not affected by either of the used loading methods, see Fig. 3. As

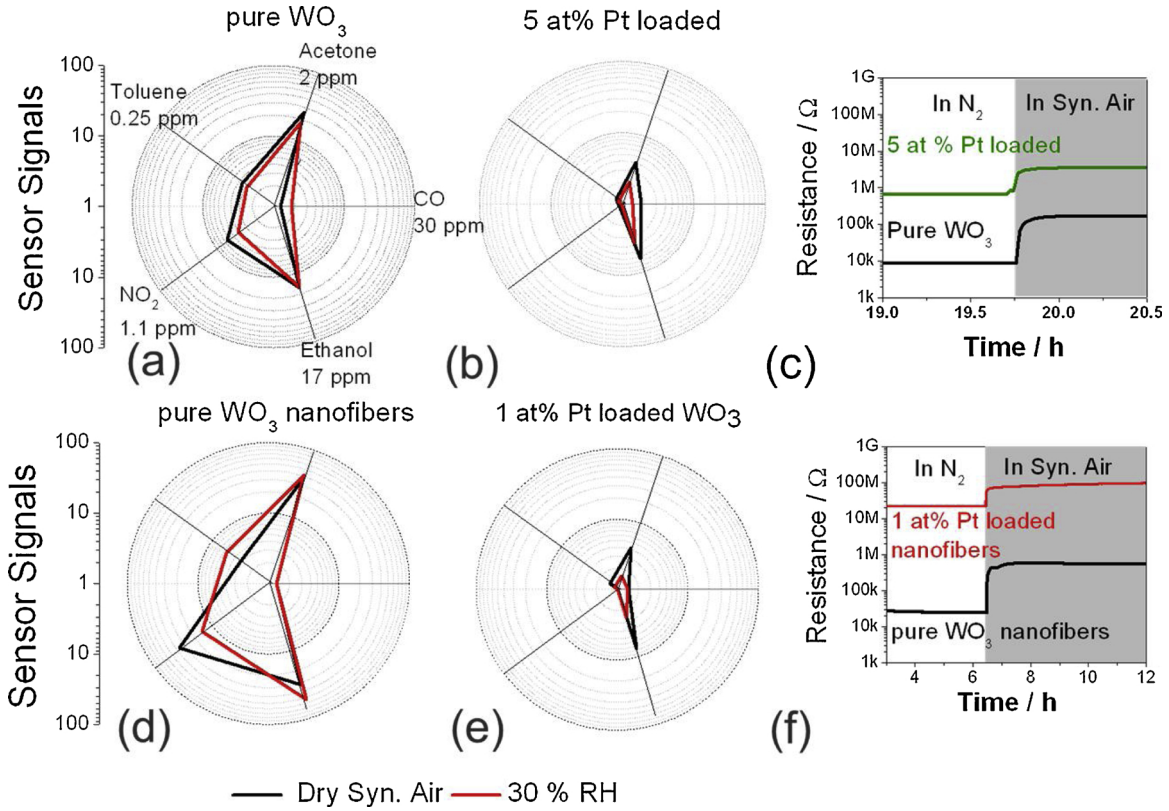

Fig. 1. (a) Sensor profile of pure WO_3 from Sigma Aldrich after treatment in an aqueous solution at pH 1. (b) Sensor profile of the Sigma Aldrich sample sol gel loaded with 5 at % Pt. (c) Resistance of the loaded and the pure Sigma Aldrich sample during exposure to N_2 and then syn. air. (d) Sensor profile of pure WO_3 nanofibers. (e) Sensor profile of the 1 at % Pt loaded nanofibers. (f) Resistance of the loaded and the pure nanofibers sample during exposure to N_2 and then syn. air.

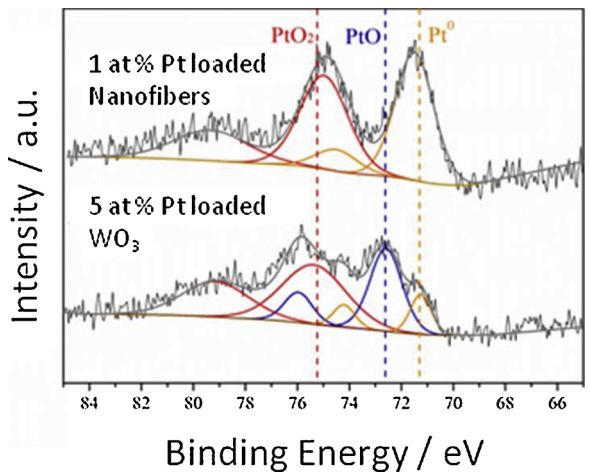

Fig. 2. The high-resolution XPS spectra of Pt 4f for 1 at% Pt loaded WO_3 nanofibers and 5 at% Pt loaded WO_3 particles.

previously reported, it is possible to identify if there is a significant electronic coupling between the base material and the surface clusters by comparing the resistances of the loaded and the pure samples in nitrogen [5,6].

Under nitrogen exposure, it is assumed that the acceptor states related to adsorbed oxygen are negligible and that the relationship between surface band bending and resistance can be described as follows [5,6]:

$$eV_s = k_B T \cdot ln\left(\frac{R}{R_0}\right) \quad (3)$$

In both cases loading with platinum results in a significant increase of the resistance in nitrogen, see Fig. 1. Based on Eq. (3), the presence of the platinum surface clusters on the sol gel sample resulted in a bending of ca. 213 meV. In the case of the nanofibers, the band bending was found to be 335 meV. These values indicate that the surface platinum species are significantly electronically coupled with the WO_3 nanoparticles. The work function of platinum is reported to span between 4.6 eV [21] and 5.93 eV [22]. In all cases, however, it is reported that the oxidation of platinum results in an increase of the work function [21,23]. The work function of tungsten trioxide is reported to be 5.05 eV [24]. Based on this information, coupling between all three of the Pt species, metallic Pt, PtO and PtO_2, could be responsible for the detected increase of the resistance.

To understand the role of the Pt species during sensing, operando DRIFT spectroscopy is useful. The absorbance spectra were calculated using Eq. (2). Both the pure and the loaded samples show a significant decrease of the resistance as a result of ethanol exposure. In the case of the pure WO_3 samples, decreasing bands at 2062 and 1861 cm^{-1} are visible during ethanol exposure, see Fig. 4. These bands have been attributed to various overtones and combination modes of the bond between tungsten and oxygen in the lattice of WO_3 [25–27]. This decrease indicates that ethanol reduces the surface of WO_3, and is in line with the large detected decrease of the resistance. In the case of the loaded samples no bands are visible in the DRIFT spectra, despite the large detected resistance change (see signals Fig. 1). This indicates that the sensing mechanism changes and that the surface reaction with ethanol

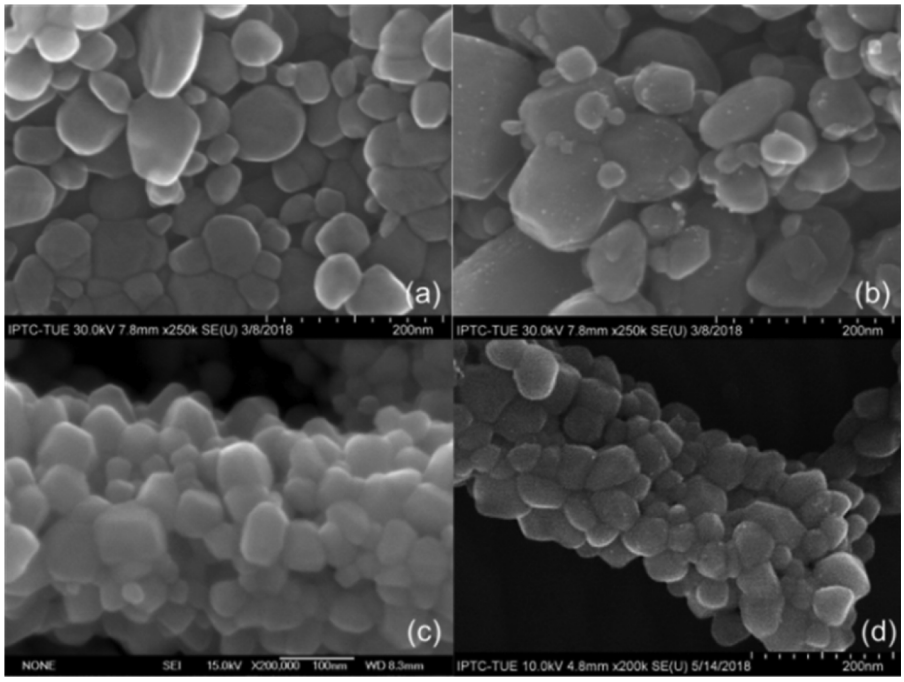

Fig. 3. SEM images of the sensitive layers based on the (a) pure WO_3 from Sigma Aldrich after the acidic wet treatment, (b) the 5 at % Pt loaded WO_3 sample from Sigma Aldrich, (c) the pure WO_3 nanofibers, and (d) the 1 at% Pt loaded WO_3 nanofibers.

no longer takes place on the WO_3. This makes the spillover mechanism improbable as in this case the reduction of WO_3 would be more significantly visible. Instead it is likely that the reaction takes place on the oxidized platinum clusters, indicating a Fermi level mechanism. It is known that the oxidation of platinum increases its work function. Inversely, a reduction of the clusters would decrease the work function difference between WO_3 and the platinum species (electrons are released from the heterojunction back into WO_3). This would explain the decrease in the resistance although no surface reduction of WO_3 is visible. Very similar results have been reported for platinum surface loaded SnO_2 and for Rh_2O_3 loadings on SnO_2, WO_3 and In_2O_3 [4–6]. The sensor response of the sol gel loaded samples and the nanofibers are very similar, even though in the case of the nanofibers only 1 at % Pt was used while in the sol gel sample 5 at % was applied. The band bending is even more significant in the case of the nanofibers. In addition to the nature of the loading, it is also known that the morphology also plays an important role [28]. Morphological information about the loadings was gained from TEM images, see Fig. 5.

In the case of the sol gel sample, the dispersion of Pt nanoparticles is not uniform in the sample. The diameters of particles range between 15 and 30 nm. The lattice spacing with 0.279 nm is assigned to (200) of PtOx (JCPDS 21-1284). In the case of the nanofibers homogeneously dispersed loadings with diameters below 5 nm were observed. The better dispersion of the particles in the case of the nanofibers explains why the same change in the sensor response can be attained with a lower loading concentration. In addition the higher change of the resistance in nitrogen as a result of loading for the nanofibers can also be explained by the smaller cluster size, as band bending scales with the contact areas between the materials.

To further verify the mechanism indicated by the results found under normal operating conditions, low oxygen measurements were used. Due to the better controlled preparation and thus more homogenous dispersion of the nanoclusters, the nanofibers were used for further measurements. Ideally by using high concentrations of a reducing gas in low oxygen background, it is possible to fully reduce the platinum oxide clusters, thus, inducing a mechanism switch. This method has been successfully applied in the past [4,5].

The pure nanofibers barely respond to CO. As expected in the DIRFT spectra, a decrease of the bands attributed to overtones and combination modes of the bond between tungsten and oxygen [25–27] is visible, see Fig. 6. This indicates that CO reacts with surface oxygen, which explains the detected decrease in resistance. As the concentration of CO

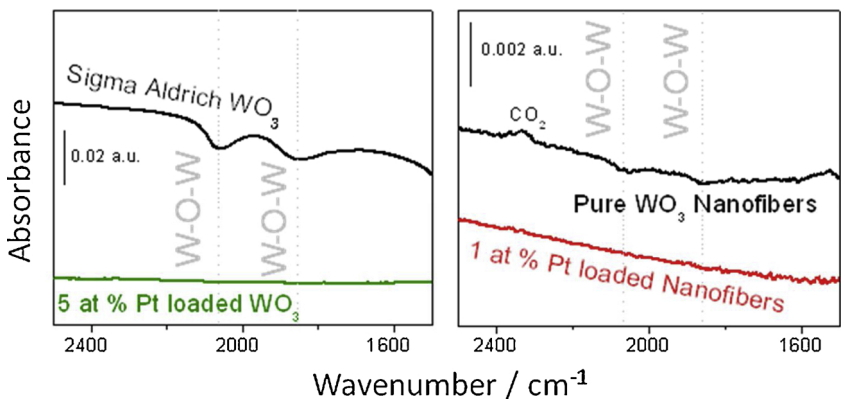

Fig. 4. DRIFT spectra taken during exposure to 18 ppm ethanol referenced to the spectrum taken in dry synthetic air.

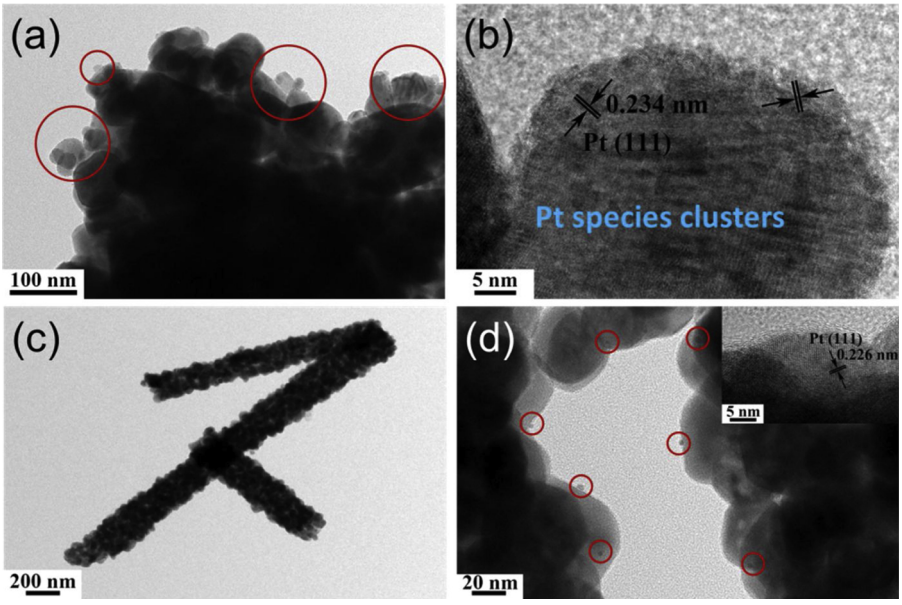

Fig. 5. TEM images of (a, b) 5 at% Pt loaded WO_3 particles and (c, d) 1 at% Pt loaded WO_3 nanofibers. The inset in (d) is the corresponding HRTEM images.

increases, the resistance decreases further and the reduction of the surface is more readily visible.

In the case of the 1 at% Pt loaded nanofibers, there is a significant change in the resistance at high CO concentrations (beginning with 100 ppm CO). Despite the significant decrease of the resistance (high sensor signal), no reduction of WO_3 is visible in the DRIFT spectra during exposure to 100 ppm CO, see the enlarged spectra in Fig. 7. At this point however a band (20,170 cm^{-1}) attributed to Pt° carbonyls becomes visible [5,29,30]. As the concentration of CO increases the resistance continues to fall strongly, and in addition to the formation of platinum carbonyls the reduction of WO_3 becomes visible in the DRIFT spectra, see Fig. 7. These results are very similar to those reported for Rh_2O_3 surface loaded n-type metal oxides [4,6]. These results further confirm the Fermi level pinning mechanism. At low CO concentrations the reduction of the oxidized platinum dominates. As a result its work function is reduced meaning fewer electrons are captured from WO_3. This release of electrons is responsible for the strong decrease in the resistance. At higher concentrations, the platinum clusters become dominantly metallic and the CO begins to react with WO_3.

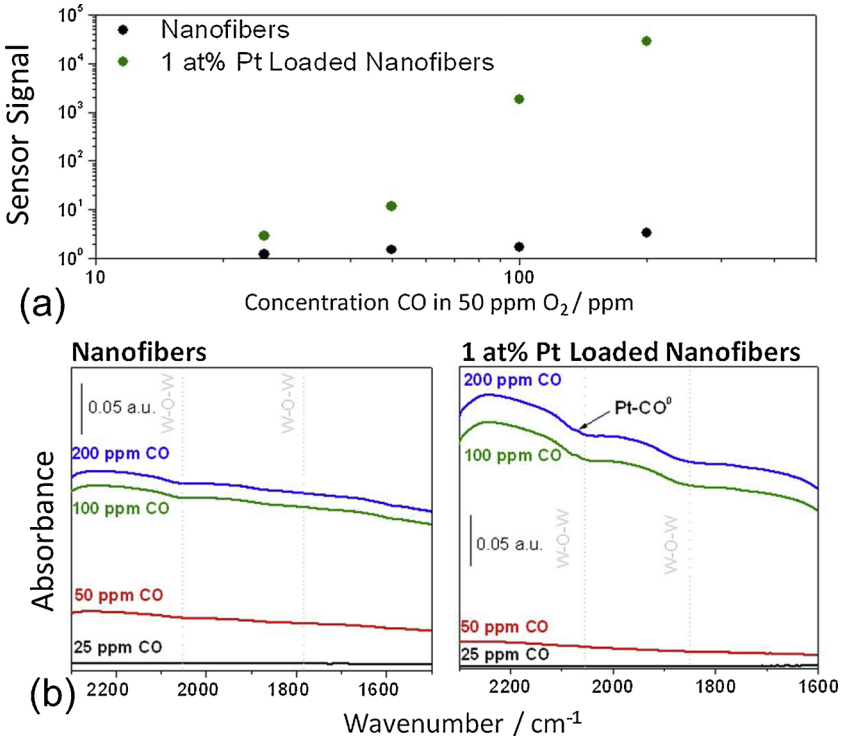

Fig. 6. (a) The change in resistance of the sensors, based on the nanofibers and the 1 at% Pt loaded nanofibers during exposure to different CO concentrations in a low-oxygen background, measured simultaneously to the DRIFT spectra. (b) The DRIFT spectra of the nanofibers and the 1 at% Pt loaded nanofibers during exposure to different concentrations of CO, the spectra were referenced to a spectrum taken in 50 ppm O_2 in N_2.

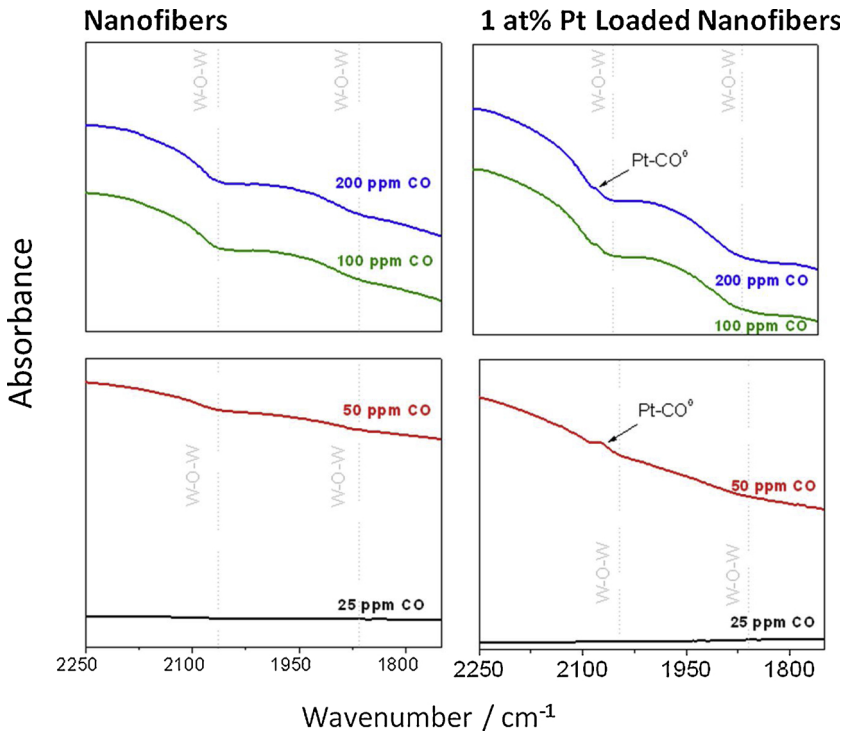

Fig. 7. Enlarged section of the DRIFT spectra of the nanofibers and the 1 at% Pt loaded nanofibers during exposure to different concentrations of CO. The spectra were referenced to a spectrum taken in 50 ppm O_2 in N_2.

4. Conclusion

Here it was shown that under normal conditions sensing is dominated by the Fermi level pinning mechanism in the case of Pt surface loaded WO_3. Very similar results were attained with two differently prepared samples indicating a generality of the results. These results, in the context of recent reports, show the dominance of the Fermi level pinning mechanism for noble metal surface loadings [4–6]. Here it was additionally shown that not only the nature of the loading clusters, but also their dispersion on the surface can have a significant effect on the sensing performance. By more homogenously dispersing the Pt clusters on the surface, it was possible to attain similar results for 1 at% loading as for 5 at%. In total and in the context of existing literature, these results are very significant for understanding existing reports and for the intentional tuning of sensing characteristics in the future.

Acknowledgements

This work was supported by the Natural Science Foundation Committee (Granted No. 61673191) and the High Tech Project of Jilin Province (No. 20180414025GH).

Appendix A. Supplementary data

Supplementary material related to this article can be found, in the online version, at doi:https://doi.org/10.1016/j.snb.2019.04.088.

References

[1] N. Taguchi, Gas-Detecting Device, US3695848, 1971.
[2] N. Yamazoe, Y. Kurokawa, T. Seiyama, Effects of additives on semiconductor gas sensors, Sensors Actuators B Chem. 4 (1983) 283–289, https://doi.org/10.1016/0250-6874(83)85034-3.
[3] S.R. Morrison, Selectivity in semiconductor gas sensors, Sens. Actuators B Chem. 12 (1987) 425–440.
[4] A. Staerz, I. Boehme, D. Degler, M. Bahri, D. Doronkin, A. Zimina, H. Brinkmann, S. Herrmann, B. Junker, O. Ersen, J.-D. Grunwaldt, U. Weimar, N. Barsan, Rhodium oxide surface-loaded gas sensors, Nanomaterials 8 (2018) 892, https://doi.org/10.3390/nano8110892.
[5] D. Degler, S.A. Müller, D.E. Doronkin, D. Wang, J.-D. Grunwaldt, U. Weimar, N. Barsan, Platinum loaded tin dioxide: a model system for unravelling the interplay between heterogeneous catalysis and gas sensing, J. Mater. Chem. A 6 (5) (2018) 2034–2046, https://doi.org/10.1039/C7TA08781K.
[6] A. Staerz, T.-H. Kim, J.-H. Lee, U. Weimar, N. Barsan, Nanolevel control of gas sensing characteristics via p–n heterojunction between Rh_2O_3 clusters and WO_3 crystallites, J. Phys. Chem. C 121 (2017) 24701–24706, https://doi.org/10.1021/acs.jpcc.7b09316.
[7] C.T. Campbell, The active site in nanaoparticle gold catalysis, Science (80-.) 30 (2004) 6.
[8] M. Righettoni, A. Tricoli, S.E. Pratsinis, Thermally stable, silica-doped ε-WO3 for sensing of acetone in the human breath, Chem. Mater. 22 (2010) 3152–3157, https://doi.org/10.1021/cm1001576.
[9] C. Deng, J. Zhang, X. Yu, W. Zhang, X. Zhang, Determination of acetone in human breath by gas chromatography-mass spectrometry and solid-phase microextraction with on-fiber derivatization, J. Chromatogr. B Anal. Technol. Biomed. Life Sci. 810 (2004) 269–275, https://doi.org/10.1016/j.jchromb.2004.08.013.
[10] Government of Canada, Residential Indoor Air Quality Guidelines, (2018) http://healthycanadians.gc.ca/healthy-living-vie-saine/environment-environnement/air/guidelines-lignes-directrices-eng.php#a1.
[11] G. Wiegelb, J. Heitbaum, Semiconductor gas sensor for detecting NO and CO traces in ambient air of road traffic, Sens. Actuators B Chem. 17 (1994) 93–99.
[12] H. Nakagawa, S. Okazaki, S. Asakura, K. Fukuda, H. Akimoto, H. Takahashi, S. Shigemori, An automated car ventilation system, Sens. Actuators B Chem. (2000) 133–137.
[13] W. Kato, T. Hashishin, J. Tamaki, S. Kajita, Pt loaded WO3 thin film sensors for highly sensitive detection of ethanol gas, 214th ECS Meet. (2008) p. Abstract#3113.
[14] S. Roy, A. Dey, B. Biswas, S.K. Sarkar, Investigation of Pt and Pd Modified WO3 and ZnO Based Thin Film Sensors for Ethanol Sensing, (2017).
[15] J. Zhang, X. Liu, M. Xu, X. Guo, S. Wu, S. Zhang, S. Wang, Pt clusters supported on WO_3 for ethanol detection, Sensors Actuators B Chem. 147 (2010) 185–190, https://doi.org/10.1016/j.snb.2010.03.017.
[16] H. Lin, C. Hsua, H. Yang, P. Lee, C. Yang, Nanocrystalline W03-Based H2S Sensors vol. 22, (1994), pp. 63–68.
[17] T. Samerjai, N. Tamaekong, C. Liewhiran, A. Wisitsoraat, A. Tuantranont, S. Phanichphant, Selectivity towards H2 gas by flame-made Pt-loaded WO3 sensing films, Sensors Actuators B Chem. 157 (2011) 290–297, https://doi.org/10.1016/j.snb.2011.03.065.
[18] M. Horprathum, T. Srichaiyaperk, B. Samransuksamer, A. Wisitsoraat, P. Eiamchai, S. Limwichean, C. Chananonnawathorn, K. Aiempanakit, N. Nuntawong, V. Patthanasettakul, C. Oros, S. Porntheeraphat, P. Songsiriritthigul, H. Nakajima, A. Tuantranont, P. Chindaudom, Ultrasensitive hydrogen sensor based on Pt-decorated WO3 nanorods prepared by glancing-angle dc magnetron sputtering, ACS Appl. Mater. Interfaces 6 (2014) 22051–22060, https://doi.org/10.1021/am505127g.
[19] A. Staerz, M.S. Somacescu, M. Epifani, T. Russ, U. Weimar, N. Barsan, WO3 based gas sensors, Proceedings (2018) 826, https://doi.org/10.3390/proceedings2130826.
[20] T. Hyodo, T. Kaino, T. Ueda, K. Izawa, Y. Shimizu, Acetone-Sensing Properties of WO3 –Based Gas Sensors Operated in Dynamic Temperature Modulation Mode — Effects of Loading of Noble Metal and / or NiO onto WO3 vol. 28, (2016), pp. 1179–1189.
[21] J.K. Schaeffer, L.R.C. Fonseca, S.B. Samavedam, Y. Liang, P.J. Tobin, B.E. White, Contributions to the effective work function of platinum on hafnium dioxide, Appl. Phys.

Lett. 85 (2004) 1826–1828, https://doi.org/10.1063/1.1786656.
[22] David R. Lide, CRC Handbook of Chemistry and Physics, CRC Publisher, Boca Raton, Florida, USA, 2005, https://doi.org/10.1016/0022-2860(92)85083-S.
[23] O.A. Otegbade, Theoretical Investigations of Surface Oxides on Platinum and Platinum Alloy Catalysts for Fuel Cell Applications, Dr. Thesis, UCL (University Coll. London), 2012.
[24] P. Suchorska-Woźniak, O. Rac, M. Fiedot, H. Teterycz, Analysis of SnO_2|WO_3 hetero-contact properties during the detection of hydrogen sulphide, Sensors 14 (2014) 20480–20499, https://doi.org/10.3390/s141120480.
[25] S.M. Kanan, Z. Lu, J.K. Cox, G. Bernhardt, C.P. Tripp, Identification of surface sites on monoclinic WO_3 powders by infrared spectroscopy, Langmuir 18 (2002) 1707–1712, https://doi.org/10.1021/la011428u.
[26] T. Akamatsu, T. Itoh, N. Izu, W. Shin, NO and NO_2 sensing properties of WO_3 and Co_3O_4 based gas sensors, Sensors (Basel) 13 (2013) 12467–12481, https://doi.org/10.3390/s130912467.
[27] M. Hübner, C.E. Simion, A. Haensch, N. Barsan, U. Weimar, CO sensing mechanism with WO_3 based gas sensors, Sensors Actuators B Chem. 151 (2010) 103–106, https://doi.org/10.1016/j.snb.2010.09.040.
[28] N. Yamazoe, G. Sakai, K. Shimanoe, Oxide semiconductor gas sensors, Catal Surv. Asia 7 (2003) 63–75, https://doi.org/10.1023/A:1023436725457.
[29] A.A. Davydov, Infrared Spectroscopy of Adsorbed Species on the Surface of Transition Metal Oxides, John Wiley & Sons, Inc., Chichester, 1990.
[30] K.I. Hadjiivanov, IR study of CO and H2O coadsorption on Ptn+ / TiO2 and Pt /TiO2 samples, J. Chem. Soc. Faraday Trans. 94 (1998) 1901–1904.

nanomaterials

MDPI

Article

Rhodium Oxide Surface-Loaded Gas Sensors

Anna Staerz [1], Inci Boehme [1], David Degler [2], Mounib Bahri [3], Dmitry E. Doronkin [4], Anna Zimina [4], Helena Brinkmann [1], Sina Herrmann [1], Benjamin Junker [1], Ovidiu Ersen [3], Jan-Dierk Grunwaldt [4], Udo Weimar [1] and Nicolae Barsan [1,*]

1 Institute of Physical and Theoretical Chemistry (IPTC), University of Tuebingen, Auf der Morgenstelle 15, D-72076 Tuebingen, Germany; anna.staerz@ipc.uni-tuebingen.de (A.S.); inci.can@ipc.uni-tuebingen.de (I.B.); helena.brinkmann@student.uni-tuebingen.de (H.B.); sina.herrmann@ipc.uni-tuebingen.de (S.H.); benjamin.junker@ipc.uni-tuebingen.de (B.J.); upw@ipc.uni-tuebingen.de (U.W.)

2 European Synchrotron Radiation Facility (ESRF), 71 Avenue des Martyrs, 38043 Grenoble, France; david.degler@esrf.fr

3 Institut de Physique et Chimie des Matériaux de Strasbourg (IPCMS), UMR 7504 CNRS-Université de Strasbourg, 23 rue du Lœss, F-67034 Strasbourg cedex 2, France; mounib.bahri@ipcms.unistra.fr (M.B.); ovidiu.ersen@ipcms.unistra.fr (O.E.)

4 Institute of Catalysis Research and Technology (IKFT) and Institute for Chemical Technology and Polymer Chemistry (ITCP), Karlsruhe Institute of Technology, Kaiserstr. 12, 76131 Karlsruhe, Germany; dmitry.doronkin@kit.edu (D.E.D.); anna.zimina@kit.edu (A.Z.); grunwaldt@kit.edu (J.-D.G.)

* Correspondence: nb@ipc.uni-tuebingen.de; Tel.: +49-(0)7071-29-78761

Received: 4 October 2018; Accepted: 25 October 2018; Published: 1 November 2018

Abstract: In order to increase their stability and tune-sensing characteristics, metal oxides are often surface-loaded with noble metals. Although a great deal of empirical work shows that surface-loading with noble metals drastically changes sensing characteristics, little information exists on the mechanism. Here, a systematic study of sensors based on rhodium-loaded WO_3, SnO_2, and In_2O_3—examined using X-ray diffraction, high-resolution scanning transmission electron microscopy, direct current (DC) resistance measurements, operando diffuse reflectance infrared Fourier transform (DRIFT) spectroscopy, and operando X-ray absorption spectroscopy—is presented. Under normal sensing conditions, the rhodium clusters were oxidized. Significant evidence is provided that, in this case, the sensing is dominated by a Fermi-level pinning mechanism, i.e., the reaction with the target gas takes place on the noble-metal cluster, changing its oxidation state. As a result, the heterojunction between the oxidized rhodium clusters and the base metal oxide was altered and a change in the resistance was detected. Through measurements done in low-oxygen background, it was possible to induce a mechanism switch by reducing the clusters to their metallic state. At this point, there was a significant drop in the overall resistance, and the reaction between the target gas and the base material was again visible. For decades, noble metal loading was used to change the characteristics of metal-oxide-based sensors. The study presented here is an attempt to clarify the mechanism responsible for the change. Generalities are shown between the sensing mechanisms of different supporting materials loaded with rhodium, and sample-specific aspects that must be considered are identified.

Keywords: gas sensors; surface-loading; DRIFT spectroscopy; X-ray absorption spectroscopy; Fermi-level pinning

1. Introduction

As the world becomes more automated and connected, sensors will play an increasing role. Gas sensors based on semiconducting metal oxides (SMOX) are a compact, inexpensive, sensitive,

and robust alternative to other detection methods. Over the last five decades, SMOX-based sensors were widely used for automated air flap control in cars and in domestic alarms for explosive gases [1,2]. A great deal of research is being done on the use of SMOX sensors in a wide array of applications. However, in order for SMOX-based sensors to be effectively used in the future, their sensitivity, selectivity, and stability must be increased [3]. Numerous different methods were examined in order to address these issues, ranging from the optimization of morphology to the use of composite materials based on metal oxides coupled with organics or silica [3–5]. Traditionally, these limitations were addressed through loading with noble metals [6]. Already in the 1960s, palladium was added to the first commercially available SnO_2-based sensor from Figaro Engineering [7,8]. Even today, most commercial sensors are not based on pure materials, but contain low quantities of noble-metal-oxide additives [8]. These additives are usually chosen based on empirically attained knowledge. However, in the late 1980s and early 1990s, Yamazoe and Morrison suggested two mechanisms, spillover and Fermi-level pinning, which could explain the effect of surface-loading on the sensor response; experimental results supporting the theories remain limited [9–11]. In the case of the spillover mechanism, the target/analyte molecule is adsorbed onto the noble-metal-oxide cluster which leads to a weakening of its molecular bond. The adsorbate is transferred onto the support material where the reaction takes place [12]. In the Fermi-level pinning mechanism, the gas detection reaction takes place on the surface of the noble metal cluster. The cluster electronically interacts with the base material and the contact pins the Fermi levels of both materials. If the work function of the noble-metal-oxide cluster is changed upon interacting with an analyte gas, the depletion layer in the base material caused by the contact is also affected. It was recently reported that the Fermi-level pinning mechanism explains the change in the sensing characteristics of WO_3 surface-loaded with oxidized rhodium clusters and the effect of oxidized platinum clusters on the surface of SnO_2 [13]. Here, a systematic study of three commonly used oxides for gas sensors, WO_3, SnO_2, and In_2O_3 [3], loaded with rhodium oxide clusters was done to examine the general validity of these findings. The response of the sensors to five chemically different and application-relevant gases was examined. The gases were picked in concentrations relevant for different applications. There is currently a large interest in detecting acetone in the breath as a means for diabetes monitoring [14]. For diabetes monitoring, an acetone concentration between 0.5 ppm and 2 ppm (0.001–0.005 mg/L) is relevant [14]. CO and NO_2 are both relevant pollutants found in automobile exhaust measurements [15]. Values between 30 ppm and 100 ppm (ca. 0.035–0.116 mg/L) are relevant for CO, and between 2 ppm and 10 ppm (0.004–0.019 mg/L) for NO_2 [16]. Often, however, indoor air is more polluted than outdoors. As people spend more and more time inside, governments and even the World Health Organization released guidelines regarding indoor air quality [17,18]. Indoor air quality is often diminished by the presence of volatile organic compounds due to outgassing of furniture and other household objects. The Canadian government, for example, set a short-term indoor air exposure limit of toluene at 4 ppm (0.015 mg/L) [18]. Ethanol is another volatile organic compound which metal-oxide-based gas sensors are known to respond well to. In total, these gases show high variation in their chemical characteristics and allowing their use in sensors for a wide array of relevant applications.

A full characterization of the samples was done using X-ray diffraction (XRD) and high-resolution scanning transmission electron microscopy (HR-STEM). In order to understand the effect of oxidized noble-metal surface clusters on sensing, operando diffuse reflectance infrared Fourier transform (DRIFT) spectroscopy and operando X-ray absorption spectroscopy (XAS) were used. The results show that the Fermi-level pinning mechanism accurately describes the effect of the clusters on sensing. This work indicates the general validity of the Fermi-level pinning mechanism for sensors based on oxygen-deficient *n*-type SMOX-containing surface noble-metal-oxide clusters. This finding is very significant, as the sensor characteristics of SMOX are often tuned using loading with noble metals.

2. Materials and Methods

2.1. Sample Preparation

The loaded samples were prepared as described in Reference [19]. $SnO_2/WO_3/In_2O_3$ and $RhCl_3 \cdot xH_2O$ from Sigma Aldrich (Saint Louis, MI, USA) were stirred in deionized water at a pH value of 1.0 at 80 °C for 2 h and dried at 70 °C. The powders were calcined at 500 °C for 1 h. To ensure that the detected results were caused by the presence of the surface-loading and not due to the preparation procedure itself, the pure samples were also suspended in deionized water at a pH value of 1.0, which was set using a concentrated HCl solution. Then, the suspension was stirred at 80 °C for 2 h and the powders were dried at 70 °C and calcined at 500 °C for 1 h. The powders were deposited onto alumina substrates as described elsewhere [20]. More information regarding the loading can be found in the Table S1.

2.2. Direct Current (DC) Resistance Measurements

The measurements were performed using a Keithley 617 electrometer for WO_3 and SnO_2 and an Agilent 34972 multimeter for In_2O_3. Agilent E3630A and E3614A voltage sources were used to heat the sensors. The sensors were mounted in a homemade Teflon sensor chamber, and the various test gas concentrations in dry synthetic air were supplied using a computer-controlled gas-mixing system. As the standard for work done using gas sensors, the concentration of the target gas is given in ppm. The following relationship was used [21]:

$$\text{Gas Concentration (ppm)} = \frac{\text{Mole Volume}}{\text{Mole Mass}} \times \text{Gas Concentration}\left(\frac{\text{g}}{\text{m}^3}\right) = \frac{0.241\text{m}^3}{\text{Mole Mass}} \times \text{Gas Concentration}\left(\frac{\text{g}}{\text{m}^3}\right) \quad (1)$$

The sensors were measured at 300 °C. The sensor signal for reducing gases was calculated using the following Equation (2):

$$s = \frac{R_{\text{reference}}}{R_{\text{test gas}}} \quad (2)$$

In the case of oxidizing gases, the inverse relationship was used. The reference was the resistance measurement in dry synthetic air.

2.3. DRIFT Spectroscopy

For the operando DRIFT spectroscopy, a Vertex70v containing a narrow-band mercury cadmium telluride (MCT) detector (Bruker, Billerica, MA, USA) with a spectral resolution of 4 cm^{-1} was used. The sensors were mounted in a homemade chamber containing a KBr window. The sensors were heated to 300 °C, and the DC resistance was recorded simultaneously. Every 15 min, a single-channel spectrum was recorded during the gas exposure. To obtain the absorbance spectra, information about the surface reaction was provided with the target gas. The single-channel spectra taken under exposure to the target gases were referenced to the spectra taken under the carrier gas using Equation (3).

$$\text{Absorbance} = -\log\left(\frac{\text{single channel test gas}}{\text{single channel reference}}\right) \quad (3)$$

As previously reported, it is possible to estimate the band-bending caused by the presence of noble-metal-oxide surface-loadings from these measurements [13,22,23]. In N_2, the surface acceptor state related to the ionosorption of O_2 is considered negligible, and the relationship between resistance and surface band-bending (eV_S) for depletion layer limited charge transport can be estimated using the Equation (4) [13,22,23]:

$$eV_s = kT \cdot \ln\left(\frac{R_{\text{loaded}}}{R_{\text{pure}}}\right) \quad (4)$$

where k represents the Boltzmann constant, T is the temperature, R_{pure} is the resistance of the unloaded material, and R_{loaded} is the resistance of the loaded material in N_2.

2.4. XRD Measurements

XRD diffractograms were collected with a Philips X'Pert apparatus (PANalytical Spectris, Egham, UK). A monochromatic Cu Kα radiation source (λ = 1.540598 Å) was used. The diffractograms were recorded from a 2θ-ω angle of 25° to 45° with a step size of 0.01° at a rate of 0.01°/s. The XRD data were analyzed using the Match! 3 software (CRYSTAL IMPACT, Bonn, Germany).

2.5. X-ray Absorption Spectroscopy (XAS) Measurements

All X-ray absorption spectroscopy (XAS) experiments were recorded at beamline P65 at the PETRA III synchrotron radiation source (DESY, Hamburg, Germany). X-rays were provided by an undulator (11 periods, seventh harmonic, DESY, Hamburg, Germany); higher harmonics were rejected using Pt-coated mirror layers mounted before the monochromator, and the incident X-ray energy was selected using a double crystal monochromator with Si (311) crystals. Using slits, the beam size was set to 1.5 × 0.3 mm. X-ray absorption near-edge structure (XANES) and extended X-ray absorption fine structure (EXAFS) spectra were recorded at the Rh K-edge in fluorescence geometry using an energy-dispersive Vortex P80 detector. For operando XAS, the samples were placed in a homemade in situ cell, which allowed controlling the atmosphere and heating voltage, while simultaneously recording XAS and DC resistance of the sensor placed in the cell [24]. XAS data analysis was done using the ATHENA and ARTEMIS software form the IFEFFIT package (developed by Ravel and Newville from the US Naval Research Laboratory and the University of Chicago, for details see [25]). ATHENA was used for calibrating and normalizing all spectra, and for subtracting the background of the EXAFS. Fourier transformation (FT) of k^1, k^2, and k^3-weighted EXAFS was done in a k range of 2.5 $Å^{-1}$ to 10 $Å^{-1}$, using a Hanning window with a sill size of 1 $Å^{-1}$. Using ARTEMIS, EXFAS fitting was done by adjusting theoretical backscattering paths, which were obtained from FEFF 6.0 calculations (The FEFF Project, University of Washington, WA, USA, to experimental data using the least-squares method in R space (1 Å to 3.5 Å) [26].

2.6. Scanning Transmission Electron Microscopy

Scanning transmission electron microscopy (STEM) experiments were performed using a Cs-corrected JEM-2100F (JEOL Akishima, Tokyo, Japan) operated at 200 kV.

3. Results

3.1. Material Characterization

WO_3, SnO_2, and In_2O_3 are all oxygen-deficient *n*-type semiconductors that are commonly used for gas sensors. The sensors are typically operated between 200 °C and 500 °C. Here, in order to minimize the measurement variables, an operation temperature of 300 °C was selected.

XRD measurements were taken at room temperature for SnO_2 and In_2O_3, while that of WO_3 was taken at 300 °C (see Figure 1). For SnO_2, the tetragonal rutile structure was verified [27], and, as it only has one stable crystal structure, it can be assumed that the same structure exists at the operation temperature. As already reported in the case of WO_3, the sample is found to be in a mixed γ- and β-phase at 300 °C [28–30]. For In_2O_3, the cubic structure was verified by XRD [31]. This structure is stable until 800 °C, which is well above the operation temperature; thus, no change was anticipated [32]. Using the Debye-Scherrer equation, the crystallite diameters of the base materials were approximated as 30 nm for WO_3, 20 nm for SnO_2, and 40 nm for In_2O_3.

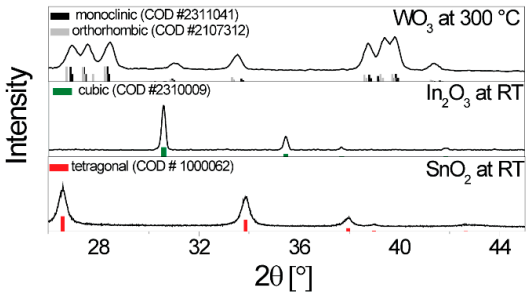

Figure 1. X-ray diffractograms taken of the sensitive layer on the sensors (SnO_2 and In_2O_3 at room temperature; WO_3 was recorded on a heated sensor). The reference patterns are from the Crystallography Open Database.

In HR-STEM images, however, it can be seen that the In_2O_3 clusters were larger than 100 nm, meaning that the crystallite size could not be accurately determined using the Debye-Scherrer equation [33]. The average size of the In_2O_3 clusters was approximately 300 nm. In the case of the SnO_2 sample, the grain size was between 7 nm and 25 nm. In the case of the WO_3 sample, the crystallite size varied between 25 nm and 65 nm. These findings are in line with the XRD measurements. The Rh-oxide loading is marked with yellow arrows in Figure 2. The STEM measurements revealed that, for loaded WO_3 and SnO_2, the rhodium-oxide particle size was between 1 nm and 2.5 nm with a good dispersion on the surface (Figure 2).

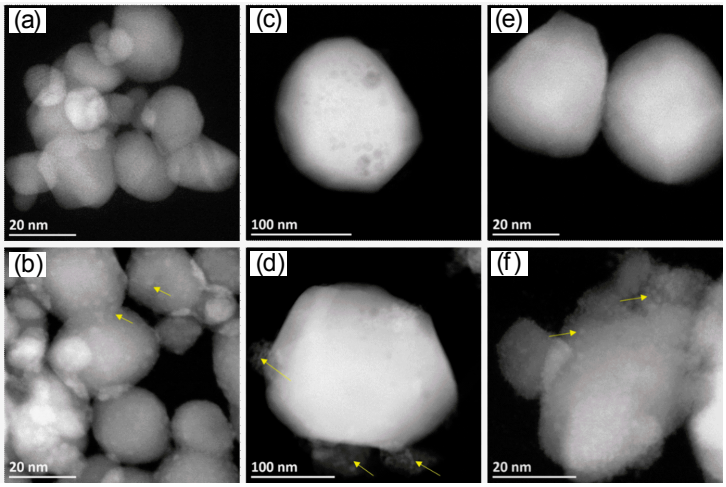

Figure 2. Scanning transmission electron microscopy (STEM) high-angle annular dark-field (HAADF) images of pure and Rh-loaded clusters on three different supports: SnO_2 (**a**) pure and (**b**) 3.00 at.% Rh-loaded SnO_2; In_2O_3 (**c**) pure and (**d**) 2.75 at.% Rh-loaded In_2O_3; WO_3 (**e**) pure and (**f**) 5.00 at.% Rh-loaded WO_3. Yellow arrows show the Rh_2O_3 particles and clusters.

For loaded In_2O_3, however, there were two kinds of structures: one with a high amount of Rh_2O_3 on a small amount of In_2O_3 (yellow arrow, Figure 3a), and the second with large crystals of In_2O_3 and a small quantity of rhodium oxides (Figure 2d; blue arrow Figure 3a; barely visible in Figure 3b). The high amount of Rh_2O_3 is shown as a layer formed around a highly crystalline small In_2O_3 grain (Figure 3c,d). Energy-dispersive X-ray spectroscopy (EDS) elemental mapping images support these findings (see Figure S1).

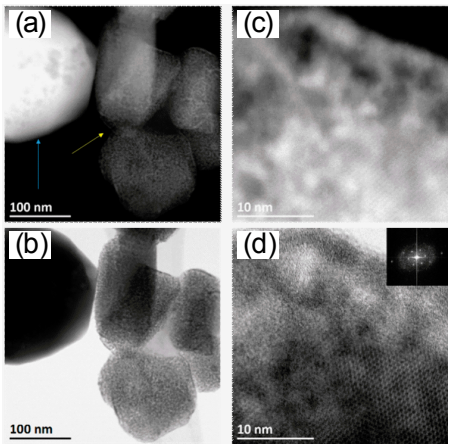

Figure 3. STEM images of 2.75 at.% Rh-Loaded In_2O_3. (**a**) STEM HAADF and (**b**) STEM bright-field (BF) images show two kinds of structures: low Rh-loaded (blue arrows) and high Rh-loaded (yellow arrow). (**c**) High-resolution (HR)-STEM HAADF and (**d**) HR-STEM BF images show high crystalline In_2O_3 and a rich Rh layer around In_2O_3. The inset in (**d**) is the fast Fourier transform (FFT) of the STEM BF image.

The XANES spectra, at room temperature, of all sensing materials and two reference compounds are shown in Figure 4. All three sensing materials showed similar XANES spectra which corresponded to the Rh_2O_3 reference compound, i.e., Rh was present as Rh^{3+}. Further information on the structure of the Rh loadings was gained through analysis of the EXAFS. The visual inspection of the FT EXAFS (Figure 4b) shows good agreement with Rh_2O_3 in the first coordination shell and, thus, confirms the presence of oxidized Rh structures. The strongly decreased magnitude of features related to the outer shells suggests a small size of the Rh loadings. Quantitative information on the Rh structure was obtained by fitting the calculated EXAFS based on Rh_2O_3 to the experimentally obtained EXAFS. The results of the best fits are shown in Table 1.

Table 1. Structural parameters obtained from fitted extended X-ray absorption fine structure (EXAFS). Coordination number, N; distance, R; Debye–Waller factor, σ^2; energy shift, δE_0; passive electron reduction factor, $S_0{}^2$; misfit, ρ.

Sample	Atom	N	R (Å)	σ^2 (10^{-3} Å^2)	$S_0{}^2$	δE_0 (eV)	ρ (%)
5.0 at.% Rh WO_3	O	6.0 [f]	2.02 ± 0.01	4.01 ± 1.75	0.72 ± 0.09	−2.10 ± 1.14	1.7
	Rh	2.0 [f]	3.09 ± 0.02	5.25 ± 2.52			
3.0 at.% Rh SnO_2	O	5.5 [f]	2.04 ± 0.01	3.22 ± 1.38	0.84 ± 0.08	−0.65 ± 0.94	1.1
	Rh	2.0 [f]	3.14 ± 0.03	4.39 ± 3.75			
	Rh	2.5 [f]	3.34 ± 0.03				
2.75 at.% Rh In_2O_3	O	5.5 [f]	2.04 ± 0.01	3.45 ± 1.18	0.72 ± 0.06	−1.14 ± 0.86	0.9
	Rh	1.5 [f]	3.15 ± 0.03	5.95 ± 4.41			
	Rh	1.5 [f]	3.38 ± 0.04				

[f] fixed.

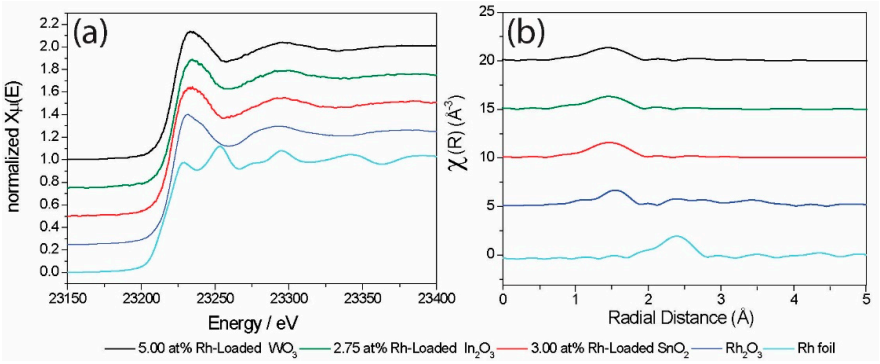

Figure 4. Rh K-edge X-ray absorption near-edge structure (XANES) spectra (**a**) and Fourier transform (FT) k^3-weigthed extended X-ray absorption fine structure (EXAFS) spectra (**b**) of Rh-loaded sensing materials (amplitude × 2), Rh_2O_3 reference (amplitude × 2), and Rh foil $\left(\frac{\text{amplitude}}{2}\right)$.

For the 5.0 at.% Rh-loaded WO_3 sample, the best EXAFS fit was obtained by a model with two coordination shells. The first shell consisted of six O atoms at a distance of 2.02 Å, while the second shell featured two Rh atoms at a distance of 3.09 Å. The coordination of Rh by six O atoms corresponds to the theoretical coordination number. The fitted Rh–O distance was shorter than expected for bulk Rh_2O_3 (2.04 Å), but still closer to that of Rh_2O_3 than the average W–O distance of the supporting WO_3 (1.93 Å). The coordination number of the second shell was smaller than the theoretical value of 3, and the obtained Rh–Rh distance was longer than the expected value of the corresponding shell in bulk Rh_2O_3 (2.99 Å). The introduction of additional Rh shells found for bulk Rh_2O_3 at either at 2.72 Å (N of bulk Rh_2O_3: 1.0) or 3.58 Å (N of bulk Rh_2O_3: 3.0) did not improve the fit model.

For the 3.0 at.% Rh-loaded SnO_2 and the 2.75 at.% Rh-loaded In_2O_3, the best fits were obtained by a model with three coordination shells. In both cases, the best fits were obtained by adjusting the coordination number of oxygen (first shell) to 5.5, which was smaller than the theoretical value of 6.0, but still matched an octahedral coordination of Rh by O. The fitted Rh–O distance (2.04 Å) was similar for both materials and corresponded to that of bulk Rh_2O_3. The second and third coordination shells were fitted by Rh atoms at distances of 3.14 and 3.34 Å for 3.0 at.% Rh-loaded SnO_2, and 3.15 and 3.38 Å for 2.75 at.% Rh-loaded In_2O_3. Considering the calculated errors, the second and third shells were within similar distances for both materials. The used coordination numbers (Table 1) were smaller than the theoretically expected value of 3.0 for each shell in bulk Rh_2O_3. The Rh-loaded In_2O_3 sample was fitted with significantly lower coordination numbers than the Rh-loaded SnO_2 sample.

All three materials were successfully fitted with fit models derived from Rh_2O_3. Thus, an incorporation of Rh into the lattice of the supporting oxide could be excluded. Rh-loaded SnO_2 and In_2O_3 showed a similar Rh_2O_3-like structure, and the decreased coordination numbers and high disorder of the second and third shells suggested a small size of Rh_2O_3 clusters on SnO_2 and In_2O_3. The coordination numbers of the second and third shells of an oxide decrease with decreasing particle size, e.g., as reported for NiO [34]. Thus, based on the coordination number, the Rh_2O_3 clusters on SnO_2 were expected to be larger than those on In_2O_3. For Rh-loaded WO_3, the quantitative analysis of the EXAFS showed a less Rh_2O_3-like structure. However, based on the Rh–O distance, which was still close to that of Rh_2O_3, and based on the presence Rh in the second coordination shell, the structure was assumed to still be Rh_2O_3-like. The shortened Rh–O distance, high disorder, low coordination number of the second shell, and atypical Rh–Rh distance suggested the presence of very small and highly disordered Rh_2O_3-like clusters on WO_3.

3.2. Resistance Measurements

The goal of the study was to understand how the presence of the oxidized noble-metal clusters changes sensing. In order to identify changes in the sensor characteristics, sensors based on the pure base material must show significant and stable responses. Although it is known that sensors based on

materials which are highly loaded with noble metals show responses at lower temperatures, the sensors based on pure base materials need a higher operation temperature. For this reason, the DC resistance measurements were conducted at 300 °C (see Figures 5 and 6). The sensor signals were calculated using Equation (2), and the results are shown in Figure 5. Although, for real world applications, the effect of humidity must be considered, the work here sought to understand the fundamental mechanism responsible for the change in sensor response. Thus, for the sake of simplicity, the sensor response measurements were done in dry air. In all three cases, the loading resulted in a drastic change of the sensing characteristics. It was previously reported in the 1990s, by Buedy et al., that loading with rhodium drastically changes the sensor response of SnO_2 [35]. The change in the sensing mechanism, as a result of loading WO_3 with Rh_2O_3 nanoclusters, was recently reported [13]. In this work, a surface-loading of 2.50 at.% was used, and, to corroborate the previous results, a similar loading level was selected here. Based on the crystallite size calculated from the XRD spectra, loadings of 2.75 at.% for In_2O_3 and 3.00 at.% for SnO_2 were selected in order to attain comparable surface-loadings. In both cases, however, the effect of the loading was more significant (negligible sensor responses to all gases) than for the WO_3 sample [36,37]. For these cases, a lower loading of 0.50 at.% was then additionally examined, while, for WO_3, a higher loading of 5 at.% was added. In the case of In_2O_3, the total surface area was much lower than expected from the XRD measurements (Figure 1), and from the large grains visible in the STEM images (Figure 2). This is a possible explanation for the stronger effect of loading on In_2O_3 (comparable results at much lower concentrations) in comparison to WO_3. Due to the large crystallite size of In_2O_3, the ratio of surface area to volume was much smaller than for SnO_2 and WO_3 (ca. 0.02 for In_2O_3, 0.22 for SnO_2, and 0.20 for WO_3). In the case of SnO_2, there was no identifiable microstructural reason for the stronger effect of the loading. This indicates that the different electronic properties of the base materials also play a role. The results for 2.50 at.% loaded WO_3 are similar to those previously reported on a differently prepared sample [13]. The 2.50 at.% loading led to the disappearance of the NO_2 response. Rh_2O_3 is a known catalyst for the oxidation of NO to NO_2, indicating it would be a poor sensing material for NO_2 [38]. The response to CO increased; CO is known to react with the lattice oxygen of Rh_2O_3 to form CO_2 [39]. The response to acetone decreased, and there was practically no change in the response to toluene. Here, it was additionally found that the response to ethanol increased. For sensors based on the 5.00 at.% loaded WO_3 sample, the response to all gases except ethanol became negligible.

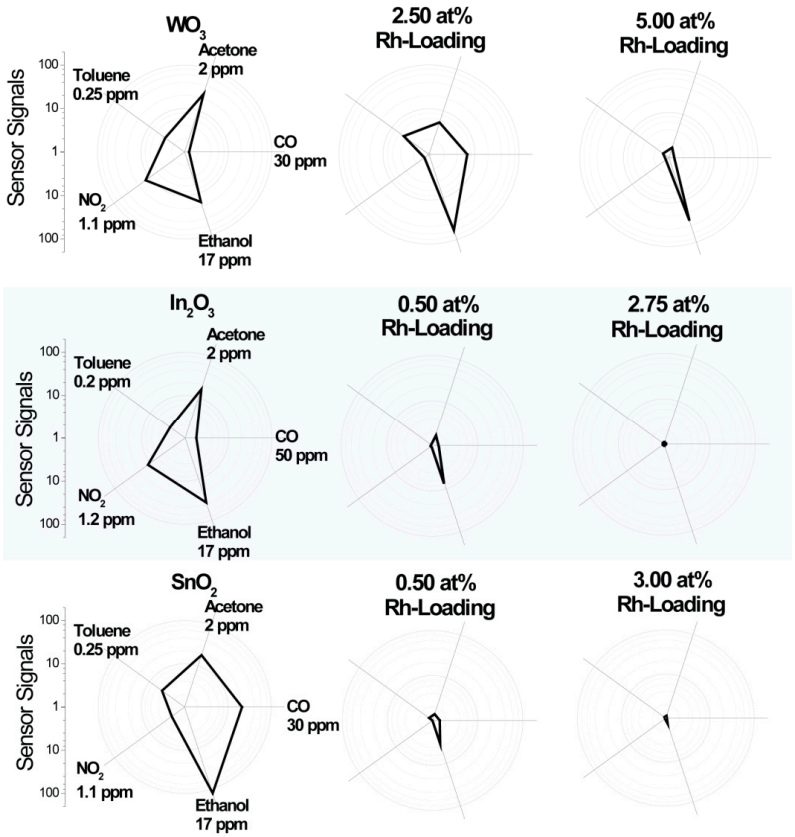

Figure 5. Signals of the sensors based on the different materials with various test gases in dry air at an operation temperature of 300 °C. The results are shown in a polar plot in order to highlight the general qualities of the sensors.

A very significant change in the sensing characteristics of In_2O_3 can already be seen for the 0.50 at.% loaded sample. Like WO_3, In_2O_3 is known to respond well to NO_2. This inherent characteristic of In_2O_3 disappeared as a result of the loading. Similar to the loaded WO_3 sample, the response to acetone decreased. The response to CO remained practically unchanged. The response of the 2.75 at.% to all gases was indeterminable. The effect of 0.50 at.% loading also had a significant effect on SnO_2. The sensor response was very similar to that of the 0.50 at.% loaded In_2O_3 sensor. The response of the 3 at.% loaded SnO_2 sample was negligible for all gases.

In order to examine the electronic coupling between the oxidized rhodium clusters and the host oxide, resistance measurements were conducted in N_2.

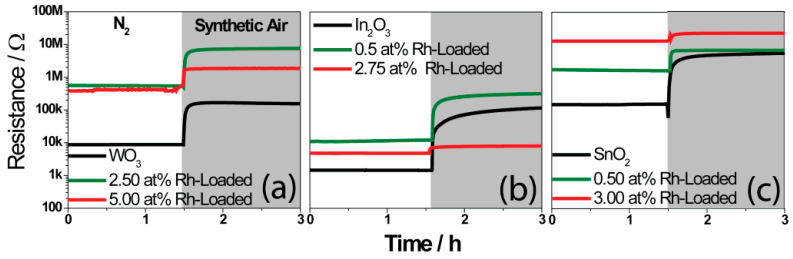

Figure 6. The resistances of the sensors, based on WO_3 (**a**), In_2O_3 (**b**), and SnO_2 (**c**), are shown in N_2 and dry synthetic air background (80% N_2 and 20% O_2).

The large increase of the resistance in nitrogen as a result of the loading indicates a strong electronic coupling between the surface clusters and the base material. The heterojunction resulted in a depletion layer which extended into the *n*-type base material, resulting in a higher resistance. Using the resistance

values in nitrogen (Figure 6) of the pure base materials and of the loaded materials, it is possible to calculate the band-bending caused by the noble-metal surface clusters [13,22]. The calculated band-bending of the Rh_2O_3 loaded materials are shown in Table 2. This was done using Equation (4).

Table 2. A list of the calculated band-bending values.

Material	Band-bending (meV)
2.50 at.% Rh-Loaded WO_3	ca. 198
5.00 at.% Rh-Loaded WO_3	ca. 200
0.50 at.% Rh-Loaded In_2O_3	ca. 105
2.75 at.% Rh-Loaded In_2O_3	ca. 98
0.50 at.% Rh-Loaded SnO_2	ca. 119
3.00 at.% Rh-Loaded SnO_2	ca. 222

In the presence of synthetic air, the resistance increased due to the adsorption of the oxygen. The pure materials all showed large changes in resistance (Figure 6). The effect of oxygen was lower for the loaded samples. While the oxidation of the Rh-clusters by atmospheric oxygen (dominant effect on loaded samples) would also lead to an increase in the resistance, it appears to be less effective than the direct oxidation of the base material (effect of atmospheric oxygen on the pure materials). Interestingly, for the WO_3 sample, the band-bending caused by the surface clusters was similar for the 2.50 at.% and the 5 at.% loaded samples. The effect of oxygen was, however, much more significant for the 2.50 at.% loaded sample [36]. One possible explanation is that the dispersion of the clusters was similar for the two samples, but the clusters on the 5.00 at.% sample were significantly larger. A similar situation was most probably true for In_2O_3. In the case of SnO_2, the calculated band-bending was significantly smaller for the lower loading versus the higher sample. The effect of atmospheric oxygen was also, however, lower for the higher-loaded sample. This could indicate that the clusters were larger but also more homogeneously dispersed in the case of the 3.00 at.% loaded sample. When comparing the results of the nitrogen and synthetic air measurements with the sensor response, it becomes clear that the reactivity to oxygen is correlated with the strength of the response to the test gases.

3.3. DRIFT Measurements

Following surface-loading with oxidized rhodium clusters, the responses of the different base materials became similar (see Figure 5). In order to examine how the presence of the surface additives unified the sensing characteristics, the interaction between the sensors and CO, an exemplary gas, was examined in greater detail. To examine the surface reactions, operando DRIFT spectroscopy was used. This method was proven to be a powerful tool [40]. In order to examine the role of the oxidized rhodium clusters in sensing and to induce a mechanism switch by reducing the clusters to their metallic state, the samples were exposed to different CO concentrations (between 25 ppm and 400 ppm) in a low-oxygen background (50 ppm O_2). The simultaneously obtained electrical measurements are shown in Figure 7.

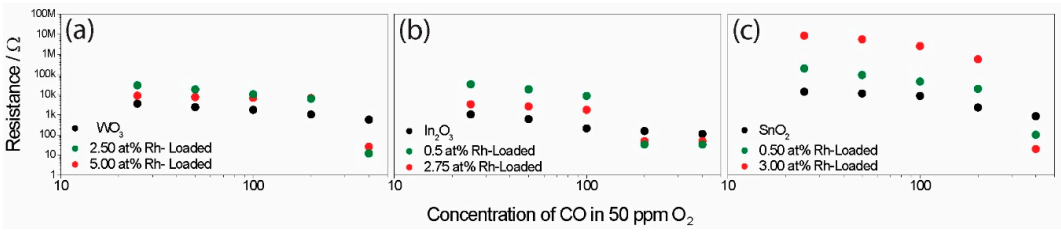

Figure 7. The change in resistance of the sensors, based on WO_3 (**a**), In_2O_3 (**b**), and SnO_2 (**c**), during exposure to different CO concentrations in a low-oxygen background, measured during the simultaneously measured diffuse reflectance infrared Fourier transform (DRIFT) spectroscopy, is plotted in log–log.

As expected, the sensor signals for the unloaded samples initially increased with higher concentrations, and, at higher concentrations, the sensitivity (the change in sensor response per ppm) decreased as a result of saturation (Figure 7). In the case of the loaded sample, there was a significant jump in the sensor response at higher CO concentrations (in the cases of WO_3 and SnO_2, this jump occurred between 200 ppm and 400 ppm, while, for indium, the jump occurred between 100 ppm and 200 ppm). The simultaneously acquired DRIFT spectra also showed a much higher absorbance at this point (Figure 8). It is known that the free-carrier absorption is proportional to the density of conduction electrons. For this reason, the resistance is inversely proportional to the absorbance, explaining the large change in the overall absorbance in the spectra taken under high CO concentrations [41]. In the 1960s, this phenomenon was examined in detail by Harrick for an oxidized silicon surface [42]. In addition, discrete adsorption bands in the DRIFT spectra provide information about the surface reactions responsible for the sensing at this point. In the case of pure WO_3 (Figure 8a), the exposure to CO determined the decrease of the W–O lattice bands at 2061 cm^{-1} and 1853 cm^{-1} [43]. This indicates the reduction of the material's surface.

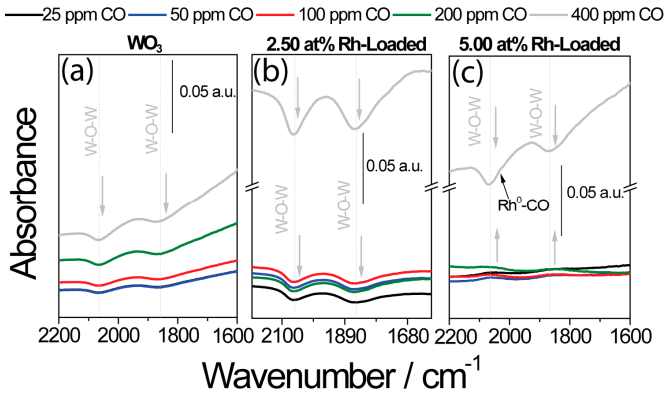

Figure 8. DRIFT spectra taken during exposure to different CO concentrations in low-oxygen (50 ppm O_2) backgrounds for (**a**) unloaded WO_3 sample, (**b**) 2.50 at.% Rh_2O_3 loaded WO_3, and (**c**) 5 at.% Rh_2O_3 loaded WO_3.

The sensing mechanism was different for 5 at.% loaded WO_3 (Figure 8c). Here, an increase of the W–O bands was visible for low CO concentrations. This finding was previously reported for Rh-loaded WO_3 during exposure to reducing gases such as acetone under normal sensing conditions [13]. As a result of the surface Rh_2O_3 clusters, the surface of WO_3 is highly depleted (see Table 2). As a result of the reaction between CO and the Rh_2O_3 clusters, electrons are released back into WO_3. With these electrons, WO_3 can react with atmospheric oxygen. This oxidation would, in turn, result in an increase in resistance. The mechanism changed as a result of exposure to 400 ppm, resulting in only the reduction of WO_3 being visible. This mechanism change was again correlated with the significant decrease in the resistance seen in the electrical measurements. In the DRIFT spectra of the 2.50 at.% loaded WO_3 sample, the reduction of WO_3 was visible even at low CO concentrations. Once the Rh_2O_3 cluster was reduced, however, CO reacted entirely with the base oxide, and the intensity of the decreasing bands attributed to the reduction of the WO_3 lattice was significantly heightened. This correlates with the stronger decrease in resistance detected in the electrical measurements.

The DRIFT spectra taken of the pure and loaded In_2O_3 samples showed a similar situation (Figure 9). The simultaneously acquired DRIFT spectra of pure In_2O_3 showed the reduction in the number of In–O bands centered at 1517 cm^{-1}, 1274 cm^{-1}, 1108 cm^{-1}, and 1022 cm^{-1}, which indicates the reduction of the surface by CO [37,44]. In the case of the highly loaded sample, the decrease in the number of In–O bands appeared only in higher CO concentrations (200 ppm and 400 ppm CO) [45]. In these concentrations, the jump in the sensor signal appeared. There was also an additional band centered at 2028 cm^{-1}, which was assigned to metallic rhodium carbonyls (Rh–CO) [37,44,46].

The DRIFT spectra of the loaded SnO_2 samples were more difficult to interpret, but showed a similar situation.

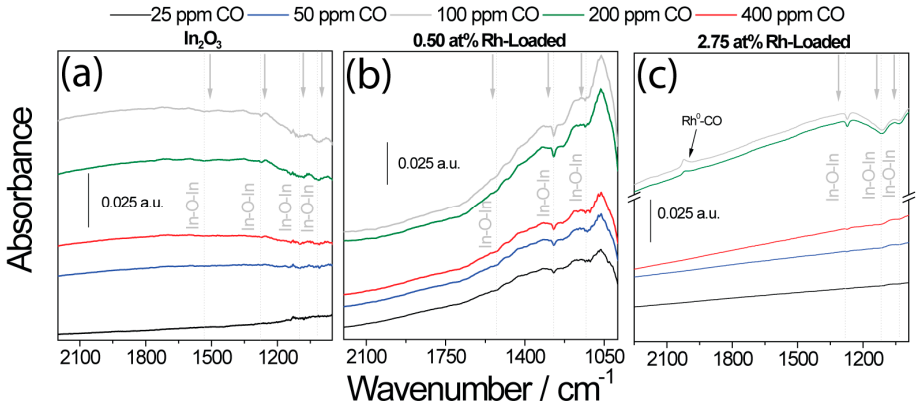

Figure 9. DRIFT spectra taken during exposure to different CO concentrations in low-oxygen (50 ppm O_2) backgrounds for (**a**) unloaded In_2O_3 sample, (**b**) 0.50 at.% Rh_2O_3 loaded In_2O_3, and (**c**) 2.75 at.% Rh_2O_3 loaded In_2O_3.

The DRIFT spectra of the sensors based on the SnO_2 samples are shown in Figure 10. It was previously reported that the reduction of the SnO_2 lattice by CO is the initial step of the surface reaction [47]. The formed CO_2 subsequently reacts with the SnO_2 surface to form carbonates. The DRIFT spectra taken of the pure SnO_2 sample were in line with this mechanism (Figure 10a). There were decreasing bands visible at 1060 cm^{-1} [48], 1120 cm^{-1} [48], and 1270 cm^{-1} [47], which were attributed to the lattice oxygen of SnO_2. The increasing bands at 1302 cm^{-1}, 1348 cm^{-1}, 1442 cm^{-1}, and 1561 cm^{-1} were attributed to surface carbonates [49]. In the case of the highly loaded sample (Figure 10c), there was no visible reduction of SnO_2 or carbonate formation during exposure to low CO concentrations.

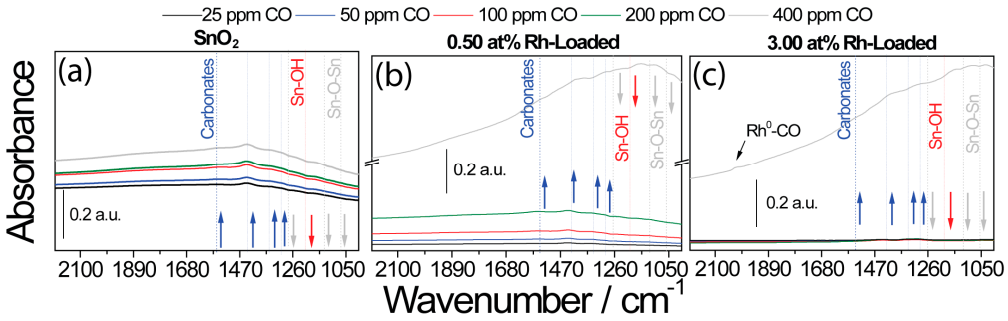

Figure 10. DRIFT spectra taken during exposure to different CO concentrations in low-oxygen (50 ppm O_2) backgrounds for (**a**) unloaded SnO_2 sample, (**b**) 0.50 at.% Rh_2O_3 loaded SnO_2, and (**c**) 3.00 at.% Rh_2O_3 loaded SnO_2.

In total, the DRIFT spectra provided good insight into how the presence of the Rh_2O_3 nanoclusters changed sensing. All three base oxides were reduced by the presence of CO in low-oxygen backgrounds. As expected, the sensitivity of the materials decreased with higher CO concentrations.

In the case of the highly loaded samples, the reduction of the base material only took place in high CO concentrations. This indicates that the reaction mechanism for each material was different at low CO concentration from that of the pure material.

3.4. X-ray Absorption Spectroscopy (XAS)

The DRIFT spectra predominantly provided insight into how the interaction between the base oxides and CO changed as a result of loading. In order to gain insight into how the Rh_2O_3 clusters

changed during sensing, operando XAS was used. Here, the sensors were again exposed to CO (between 25 ppm and 400 ppm CO) in low-oxygen (50 ppm) concentrations. XAS is an element-selective technique, and the shape of the XANES spectra is sensitive to the oxidation state and chemical surrounding of the absorbing element [50,51]. In order to study the behavior of Rh, the same measurements investigated by operando DRIFT spectroscopy of the higher-loaded samples were repeated, simultaneously recording XANES spectra at the Rh K-edge and the sensor response.

The electrical response (Figure 11) of the sensors was very similar to that attained during the DRIFT spectroscopy measurements (Figure 7). The loaded WO_3 and SnO_2 samples showed a significant resistance jump under exposure to 400 ppm CO. In the case of In_2O_3, the resistance jump was already visible during exposure to 200 ppm CO.

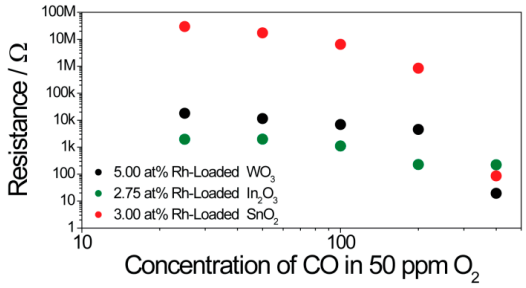

Figure 11. The change in resistance of the sensors during exposure to different CO concentrations in low-oxygen background, acquired during simultaneously measured X-ray absorption spectroscopy (XAS), is plotted in log-log.

For Rh-loaded WO_3 and SnO_2, the XANES spectra showed a change from Rh^{3+} to Rh^0 between 200 ppm and 400 ppm CO, and, for Rh-loaded In_2O_3, the change was already visible between 100 ppm and 200 ppm CO (Figure 12). The oxidation state change of Rh agreed well with the resistance jump and the distinct changes in the DRIFT spectra. Prior to the resistance jump, no indications of metallic Rh were visible in the XANES spectra, i.e., metallic Rh was only found in strongly reducing conditions, while, in oxygen-rich conditions, Rh was oxidized (Rh^{3+}). Here, it is important to note that, once the rhodium clusters were completely reduced to their metallic state, the sensors were irreversibly changed, i.e., the resistance in dry air did not return to the same value, and the color of the sensitive layer was different compared to that of a new sensor. In the case of normal operation conditions, the clusters were not reduced to their metallic state, and the sensor response showed good recovery (see XANES spectra recorded during exposure to CO in dry and humid synthetic air; Figure S2).

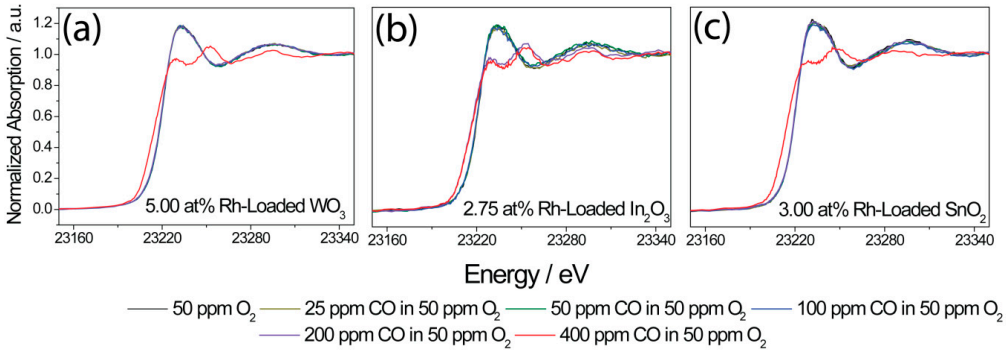

Figure 12. Rh K-edge XANES spectra of 5.00 at.% Rh-loaded WO_3 (**a**), 2.75 at.% Rh-loaded In_2O_3 (**b**), and 3.00 at.% Rh-loaded SnO_2 (**c**), recorded during different CO exposures in a low-oxygen background (50 ppm O_2) at 300 °C.

4. Discussion and Conclusion

It was found that, through surface-loading with oxidized rhodium clusters, it is possible to drastically change the sensing characteristics of WO_3, In_2O_3 and SnO_2. The three metal oxides, which are very commonly used for gas sensors, show very different responses in their pure states. The surface-loading with Rh resulted in more unified responses; none of the sensors responded to NO_2, while the response of all sensors to acetone decreased, and, at lower loadings, the response to CO was detectable. In all cases, the rhodium-loaded samples showed the highest responses to ethanol. It was previously reported that the Fermi-level pinning mechanism explains the change in the sensing characteristics of WO_3 surface-loaded with oxidized rhodium clusters, and also the effect of oxidized platinum clusters on the surface of SnO_2 [13].

In order to generally validate these findings, it was examined whether the change in sensor response of the three most commonly used materials as a result of Rh_2O_3 loading could be explained using the Fermi-level pinning mechanism. In all cases, the oxidized rhodium surface clusters caused a significant increase in the material's resistance in nitrogen, indicating significant electronic coupling between the clusters and the base material. By increasing the loading concentration, the effect of oxygen on the resistance of the materials was lowered and, in all cases, the response of the sensors decreased; this can be explained by the increase in the size of the Rh_2O_3 nanoclusters, limiting the charge transfer between the cluster and the base material during the reaction with the target gas. Using measurements in low-oxygen backgrounds, it was possible to identify the effect of the oxidation state of rhodium on the sensing mechanism. The XANES measurements revealed that, under normal sensing conditions, the surface rhodium clusters were oxidized. This was also true for measurements conducted at low CO concentrations in low-oxygen backgrounds. At higher CO concentrations, our results indicate that the clusters were reduced, and only metallic rhodium was present on the surface. A great deal of work was previously done on the interaction between rhodium and CO in catalysis [52,53]. The findings here are in line with those of Basini et al., who found that, at or above 300 °C, for rhodium clusters on various support oxides, only linear or bridged carbonyls were visible, indicative of Rh^0 [54]. In operando DRIFT spectra taken under the same conditions, the reduction of the base material could only be seen once the surface rhodium clusters were metallic. In the case of WO_3, the oxidation of the material was visible even in conditions where the rhodium clusters were still oxidized. This indicates that, in normal sensing conditions, when the rhodium clusters are oxidized (Figure S2), reactions between the rhodium clusters and the target gases are responsible for the sensor response. These findings are significant for the intentional tuning of sensors characteristics; the surface chemistry, and, as a result, the sensing characteristics of the sensor are dominated by the noble-metal loading. Although this was true for the three base materials, different loading levels were needed to attain similar results. This indicates that the base material still plays a role in the sensing mechanism. In order to verify this finding and examine it more closely, in the future, base materials with comparable crystallite size and morphology are needed. Hence, it is crucial that a preparation method is developed in which the Rh_2O_3 surface cluster size and dispersion are homogeneous among the different samples.

The work presented here provides significant evidence for the general validity of the Fermi-level pinning mechanism for sensors based on Rh_2O_3-loaded *n*-type oxides. For decades, sensors based on oxides loaded with noble metals were used in numerous applications. Although theories were developed to explain the changes in sensing characteristics as a result of the loading, experimental evidence is still scarce. The comprehensive study presented here is a crucial first step in understanding the effect of surface-loading. It identifies generalities between different supporting materials, as well as the additional sample-specific aspects that must be considered.

Supplementary Materials: The following are available online at http://www.mdpi.com/2079-4991/8/11/892/s1, Table S1: Concentrations used for the loading preparations, Figure S1: STEM images of 2.75 at.% Rh-Loaded In_2O_3. (a) STEM-HAADF (b) STEM-BF and EDS elemental mapping images (c), STEM images of 5 at.% Rh-Loaded WO_3. (d) STEM-HAADF (e) STEM-BF and EDS elemental mapping images (f), Figure S2: Rh K-edge XANES spectra

of 5 at.% Rh-loaded WO_3 (a), 2.75 at.% Rh-loaded In_2O_3 (b) and 3.00 at.% Rh-loaded SnO_2 (c), recorded during different CO exposure in dry syn. air at 300 °C.

Author Contributions: A.S. and I.B. contributed equally to this work; Conceptualization, N.B., U.W., O.E. and J.-D.G.; Formal analysis and experiments, A.S., I.B., D.D., M.B. and D.E.D.; Investigation, A.S., I.B., D.D., M.B., D.E.D., A.Z., H.B., S.H. and B.J.; Writing-original draft preparation, A.S., I.B., D.D. and M.B.; Writing-review and editing, A.S., D.D., J.-D.G. and N.B.; Supervision, N.B.

Funding: Parts of this research were carried out at PETRA III at DESY, a member of the Helmholtz Association (HGF), and we acknowledge the granted beamtime at beamline P65 and their financial support. Edmund Welter and Matthias Hermann (DESY) are thanked for their help during XAS measurements.

Conflicts of Interest: The authors declare no conflicts of interest.

References

1. Yamazoe, N. Toward innovations of gas sensor technology. *Sens. Actuator B Chem.* **2005**, *108*, 2–14. [CrossRef]
2. Chemical and Biochemical Sensors. *Ullmann's Encyclopedia of Industrial Chemistry*; Wiley VCH GmbH & Co KGaA. Posted September 29, 2016. Available online: https://doi.org/10.1002/14356007.b06_121.pub2 (accessed on 17 August 2018).
3. Hoa, N.D.; Duy, N.V.; El-Safty, S.A.; Hieu, N.V. Meso-/nanoporous semiconducting metal oxides for gas sensor applications. *J. Nanomater.* **2015**, *2015*. [CrossRef]
4. Lee, J.H. Gas sensors using hierarchical and hollow oxide nanostructures: Overview. *Sens. Actuator B Chem.* **2009**, *140*, 319–336. [CrossRef]
5. Hoa, N.D.; El-Safty, S.A. Highly sensitive and selective volatile organic compound gas sensors based on mesoporous nanocomposite monoliths. *Anal. Methods* **2011**, *3*, 1948–1956. [CrossRef]
6. Sun, Y.F.; Liu, S.B.; Meng, F.L.; Liu, J.Y.; Jin, Z.; Kong, L.T.; Liu, J.H. Metal oxide nanostructures and their gas sensing properties: A review. *Sensors* **2012**, *12*, 2610–2631. [CrossRef] [PubMed]
7. Neri, G. First Fifty Years of Chemoresistive Gas Sensors. *Chemosensors* **2015**, *3*, 1–20. [CrossRef]
8. Taguchi, N. Gas-Detecting Device. US3695848, 3 October 1972.
9. Yamazoe, N.; Kurokawa, Y.; Seiyama, T. Effects of Additives on Semiconductor Gas Sensors. *Sens. Actuators B* **1983**, *4*, 283–289. [CrossRef]
10. Morrison, S.R. Selectivity in semiconductor gas sensors. *Sens. Actuators* **1987**, *12*, 425–440. [CrossRef]
11. Yamazoe, N. New Approaches for improving semiconductor gas sensors. *Sens. Actuators B* **1991**, *5*, 7–19. [CrossRef]
12. Matsushima, S.; Teraoka, Y.; Miura, N.; Yamazoe, N. Electronic interaction between metal additives and tin dioxide in tin dioxide-based gas sensors. *JPN J. Appl. Phys.* **1988**, *27*, 1798–1802. [CrossRef]
13. Staerz, A.; Kim, T.-H.; Lee, J.-H.; Weimar, U.; Barsan, N. Nanolevel control of gas sensing characteristics via p–n heterojunction between Rh_2O_3 clusters and WO_3 crystallites. *J. Phys. Chem. C* **2017**, *121*, 24701–24706. [CrossRef]
14. Deng, C.; Zhang, J.; Yu, X.; Zhang, W.; Zhang, X. Determination of acetone in human breath by gas chromatography-mass spectrometry and solid-phase microextraction with on-fiber derivatization. *J. Chromatogr. B* **2004**, *810*, 269–275. [CrossRef]
15. Wiegelb, G.; Heitbaum, J. Semiconductor gas sensor for detecting NO and CO traces in ambient air of road traffic. *Sens. Actuators B* **1994**, *17*, 93–99. [CrossRef]
16. Nakagawa, H.; Okazaki, S.; Asakura, S.; Fukuda, K.; Akimoto, H.; Takahashi, H.; Shigemori, S. An automated car ventilation system. *Sens. Actuators B* **2000**, *65*, 133–137. [CrossRef]
17. Guidelines for indoor air quality. *WHO Regional Office for Europe*. 2010. Available online: http://www.euro.who.int/__data/assets/pdf_file/0009/128169/e94535.pdf (accessed on 21 July 2017).
18. Residential Indoor Air Quality Guidelines. *Government of Canada*. 2018. Available online: http://healthycanadians.gc.ca/healthy-living-vie-saine/environment-environnement/air/guidelines-lignes-directrices-eng.php#a1 (accessed on 16 October 2018).
19. Choi, K.-I.; Hwang, S.-J.; Dai, Z.; Kang, Y.C.; Lee, J.-H. Rh-catalyzed WO_3 with anomalous humidity dependence of gas sensing characteristics. *RSC Adv.* **2014**, *4*, 53130–53136. [CrossRef]
20. Wicker, S.; Guiltat, M.; Weimar, U.; Hémeryck, A.; Barsan, N. Ambient humidity influence on CO detection with SnO_2 gas sensing materials. A combined DRIFTS/DFT Investigation. *J. Phys. Chem. C* **2017**, *121*, 25064–25073. [CrossRef]

21. Harris, D.C. Measurements. In *Quantitative Chemical Analysis*, 7th ed.; China Lake: Kern County, CA, USA, 2007; pp. 13–15.
22. Degler, D.S.; Müller, A.; Doronkin, D.E.; Wang, D.; Grunwaldt, J.-D.; Weimar, U.; Barsan, N. Platinum loaded Tin dioxide: A model system for unravelling the interplay between heterogeneous catalysis and gas sensing. *J. Mater. Chem. A* **2018**. [CrossRef]
23. Bârsan, N.; Hübner, M.; Weimar, U. Conduction mechanisms in SnO_2 based polycrystalline thick film gas sensors exposed to CO and H_2 in different oxygen backgrounds. *Sens. Actuators B* **2011**, *157*, 510–517. [CrossRef]
24. Koziej, D.; Hübner, M.; Barsan, N.; Weimar, U.; Sikora, M.; Grunwaldt, J.-D. Operando X-ray absorption spectroscopy studies on Pd-SnO_2 based sensors. *Phys. Chem. Chem. Phys.* **2009**, *11*, 8620–8625. [CrossRef] [PubMed]
25. Ravel, B.; Newville, M. ATHENA, ARTEMIS, HEPHAESTUS: Data analysis for X-ray absorption spectroscopy using IFEFFIT. *J. Synchrotron Radiat.* **2005**, *12*, 537–541. [CrossRef] [PubMed]
26. Ravel, B. *Quantitative EXAFS Analysis*; van Bokhoven, J.A., Lamberti, C., Eds.; John Wiley & Sons, Ltd.: Chichester, UK, 2016; pp. 281–302.
27. Baur, W.H.; Khan, A. Rutile-type compounds. IV. SiO_2, GeO_2 and a comparison with other rutile-type structures. *Acta Crystallogr. B* **1971**, *27*, 2133–2139. [CrossRef]
28. Loopstra, B.O.; Boldrini, P. Neutron diffraction inverstigation of WO_3. *Acta Crystallogr. B* **1966**. [CrossRef]
29. Staerz, A.; Weimar, U.; Barsan, N. Understanding the Potential of WO_3 Based Sensors for Breath Analysis. *Sensors* **2016**, *16*, 1815. [CrossRef] [PubMed]
30. Salje, E. The Orthorhombic Phase of WO_3. *Acta Crystallogr. B* **1977**, *33*, 574–577. [CrossRef]
31. Marezio, M. Refinement of the crystal structure of In_2O_3. *Acta Crystallogr. B* **1966**, *20*, 723–728. [CrossRef]
32. Prewitt, C.T.; Shannon, R.D.; Rogers, D.B.; Sleight, A.W. The C rare earth oxide-corundum transition and crystal chemistry of oxides having the corundum structure. *Inorg. Chem.* **1969**, *8*, 1985–1993. [CrossRef]
33. Birkholz, M. *A Thin Film Analysis by X-ray Scattering*; Wiley-VCH Verlag: Weinheim, Germany, 2006.
34. Kuzmin, A.; Chaboy, J. EXAFS and XANES analysis of oxides at the nanoscale. *IUCrJ* **2014**, *1*, 571–589. [CrossRef] [PubMed]
35. Anton, M.; Buedy, B. The influence of rhodium on SnO_2-CO gas sensor. *Sens. Actuators B* **1994**, *19*, 500–501. [CrossRef]
36. Brinkmann, H. An Investigation of Rh_2O_3-Loaded n-Type Semiconducting Metal Oxide Sensors. Teacher's Thesis, University of Tuebingen, Tuebingen, Germany, 2017.
37. Herrmann, S. Eine untersuchung von Rh_2O_3 geladenen In_2O_3 Gassensoren. Teacher's Thesis, University of Tuebingen, Tuebingen, Germany, 2018.
38. Weiss, B.M.; Artioli, N.; Iglesia, E. Catalytic NO oxidation pathways and redox cycles on dispersed oxides of rhodium and cobalt. *ChemCatChem* **2012**, *4*, 1397–1404. [CrossRef]
39. Watson, P.R.; Somorjai, G.A. Interaction of carbon monoxide, carbon dioxide, and deuterium with rhodium oxide: its reduction and catalytic stability. *J. Phys. Chem.* **1982**, *20*, 3993–3996. [CrossRef]
40. Barsan, N.; Koziej, D.; Weimar, U. Metal oxide-based gas sensor research: How to? *Sens. Actuators B* **2007**, *121*, 18–35. [CrossRef]
41. Mijalković, S. Optical properties and photoelectric effects. In *Semiconductor Physical Electronics*; Li, S.S., Ed.; Springer: New York, NY, USA, 1997; Chapter 9; pp. 248–256.
42. Harrick, N.J. Optical spectrum of the semiconductor surface states from frustrated total internal reflections. *Phys. Rev.* **1962**, *125*, 1165–1170. [CrossRef]
43. Hübner, M.; Simion, C.E.; Haensch, A.; Barsan, N.; Weimar, U. CO sensing mechanism with WO_3 based gas sensors. *Sens. Actuators B* **2010**, *151*, 103–106. [CrossRef]
44. Can, I.; Weimar, U.; Barsan, N. Operando investigations of differently prepared In_2O_3-Gas sensors. *Proceedings* **2017**, *1*, 432. [CrossRef]
45. Boehme, I.; Herrmann, S.; Staerz, A.; Brinkmann, H.; Weimar, U. Understanding the sensing mechanism of Rh_2O_3 loaded In_2O_3. *Proceedings* **2018**, in press.
46. Hecker, W.C.; Rasband, P.B. Catalyst characterization using quantitative FTIR: CO on supported Rh. *J. Catal.* **1993**, *139*, 551–560.
47. Degler, D.; Wicker, S.; Weimar, U.; Barsan, N. Identifying the active oxygen species in SnO_2 based gas sensing materials: An operando IR spectrsocopy study. *J. Phys. Chem. C* **2015**, *119*, 11792–11799. [CrossRef]

48. Amalric Popescu, D.; Herrmann, J.-M.; Ensuque, A.; Bozon-Verduraz, F. Nanosized tin dioxide: Spectroscopic (UV–VIS, NIR, EPR) and electrical conductivity studies. *Phys. Chem. Chem. Phys.* **2001**, *3*, 2522–2530. [CrossRef]
49. Wicker, S. Influence of Humidity on the Gas Sensing Characteristics of SnO_2: DRIFTS Investigation of Different Base Materials and Dopants. Ph.D. Thesis, University of Tuebingen, Tuebingen, Germany, 2016.
50. De Groot, F. High-resolution X-ray emission and X-ray absorption spectroscopy. *Chem. Rev.* **2001**, *101*, 1779–1808. [CrossRef] [PubMed]
51. Kowalska, J.K.; Lima, F.A.; Pollock, C.J.; Rees, J.A.; DeBeer, S. A practical guide to high-resolution X-ray spectroscopic measurements and their applications in bioinorganic chemistry. *Isr. J. Chem.* **2016**, *56*, 803–815. [CrossRef]
52. Koningsberger, D.C.; Prins, R. *X-ray Absorption: Principles, Applications, Techniques of EXAFS, SEXAFS and XANES*; John Wiley & Sons: Hoboken, NJ, USA, 1987.
53. Grunwaldt, J.D.; Basini, L.; Clausen, B.S. In situ EXAFS study of Rh/Al_2O_3 catalysts for catalytic partial oxidation of methane. *J. Catal.* **2001**, *200*, 321–329. [CrossRef]
54. Basini, L.; Marchionna, M.; Aragno, A. Drift and mass spectroscopic studies on the reactivity of rhodium clusters at the surface of polycrystalline oxides. *J. Phys. Chem.* **1992**, *96*, 9431–9441. [CrossRef]

THE JOURNAL OF PHYSICAL CHEMISTRY C

Article

Cite This: J. Phys. Chem. C 2017, 121, 24701-24706

pubs.acs.org/JPCC

Nanolevel Control of Gas Sensing Characteristics via p−n Heterojunction between Rh_2O_3 Clusters and WO_3 Crystallites

Anna Staerz,[†] Tae-Hyung Kim,[‡] Jong-Heun Lee,[‡] Udo Weimar,[†] and Nicolae Barsan*[,†]

[†]Institute of Physical and Theoretical Chemistry (IPTC), University of Tuebingen, Auf der Morgenstelle 15, D-72076, Tuebingen, Germany

[‡]Department of Materials Science and Engineering, Korea University, Seoul 136-713, Republic of Korea

ABSTRACT: Today semiconducting metal oxide (SMOX) based gas sensors are used in a wide array of applications. Dopants, e.g., rhodium, are often used to change the sensor response of SMOXs. The adjustment of sensing characteristics with dopants is usually done empirically, and there is a knowledge gap surrounding how the presence of dopants alters the chemistry of sensing. Here using X-ray photoelectron spectroscopy (XPS), transmission electron microscopy (TEM), dc resistance measurements, and operando diffuse reflectance infrared Fourier transform (DRIFT) spectroscopy, it was understood how surface loading with Rh_2O_3 changes sensing with WO_3. As a result of uniform surface loading, reactions between the Rh_2O_3 clusters and the analyte gas dominate the reception. Changes in the p−n heterojunction between Rh_2O_3 and WO_3 are responsible for the transduction. These results in combination with existing literature indicate that, through controlled surface doping, it is possible to intentionally tune the sensor characteristics of SMOXs.

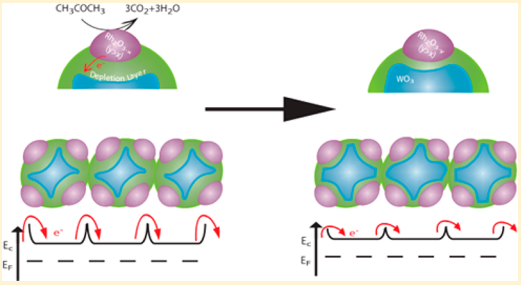

INTRODUCTION

Metal oxide heterojunctions are relevant for a host of applications, e.g., water splitting, memory drives, etc.[1−3] Specifically, dopants resulting in nanoscale p−n junctions have a large effect on the responses of semiconducting metal oxide (SMOX) based sensors.[4,5] In their review, however, Miller et al. report that most research done on heterostructured gas sensors is strictly empirical.[4] Although numerous papers have proposed that the heterojunction interface plays a significant role in the sensor response and some even suggest specific mechanisms,[6] to the best of the authors' knowledge no conclusive experimental evidence has previously been reported. The most commonly used SMOXs for commercial gas sensors are SnO_2, WO_3, and In_2O_3. There are several reports that the sensor response of WO_3 drastically changes through the incorporation of nanoscale Rh_2O_3.[7−9] Here, characterization with X-ray photoelectron spectroscopy (XPS), transmission electron microscopy (TEM), dc resistance measurements, and operando diffuse reflectance infrared Fourier transform (DRIFT) spectroscopy of a WO_3 sample uniformly surface loaded with Rh_2O_3 led to remarkable results. It was identified that the reaction between Rh_2O_3 and the analyte gas is responsible for the reception of the sensor. The resulting change in the heterojunction between p-Rh_2O_3 and n-WO_3 induces the change in charge (transduction). These findings are an initial step in understanding the underlying physical chemistry responsible for gas sensing. Only with this understanding is the design of high performance gas sensors possible.[10]

Pure WO_3 is known to show a high sensor response to NO_2.[11,12] Remarkably, by loading the WO_3 based sensors with rhodium, the signal to NO_2 practically disappeared and the signals to CO became less humidity dependent. Although already in 1994 Buedy et al. reported a similar influence of rhodium on SnO_2 based sensors,[13] until now no explanation exists for why the sensor characteristics so drastically change as a result of Rh loading. In the present study, special focus was directed at understanding the role of Rh loading on the gas sensing characteristics of WO_3.

EXPERIMENTAL SECTION

Pure WO_3 hollow spheres were synthesized by the following process: 2.3 g of tungsten oxide (Sigma-Aldrich; 99.995%), 2.1 g of citric acid monohydrate (Sigma-Aldrich; 99.0%), and 6.0 g of polyethylene glycol (MW 1500, Samchun Chemical) were dissolved in 500 mL of a 2.8−3.0% diluted ammonium hydroxide aqueous solution and stirred until the solution became clear. The solution was transferred to a droplet generator for the spray pyrolysis. Six ultrasonic transducers (resonant frequency 1.7 MHz) were used to generate a large number of droplets, which were carried into the high-temperature (700 °C) quartz tube reactor (inner diameter 55 mm) by a carrier gas (air, 40 L min^{-1}) and then condensed. The W-precursor spheres were collected with a Teflon bag filter in the particle-collecting chamber and converted into WO_3

Received: September 19, 2017
Revised: October 18, 2017
Published: October 24, 2017

DOI: 10.1021/acs.jpcc.7b09316
J. Phys. Chem. C 2017, 121, 24701−24706

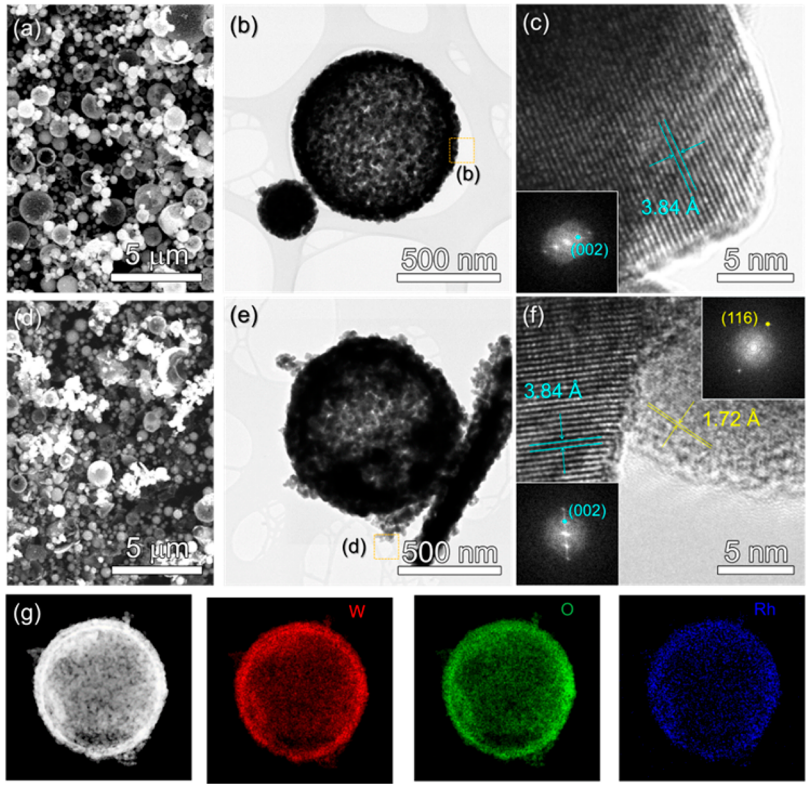

Figure 1. Low magnification SEM image of (a) WO_3 hollow spheres and (d) Rh-loaded WO_3 hollow spheres. TEM images of (b, c) WO_3 hollow spheres and (e, f) Rh-loaded WO_3 hollow spheres. (g) EDS elemental mapping images of Rh-loaded WO_3 hollow spheres.

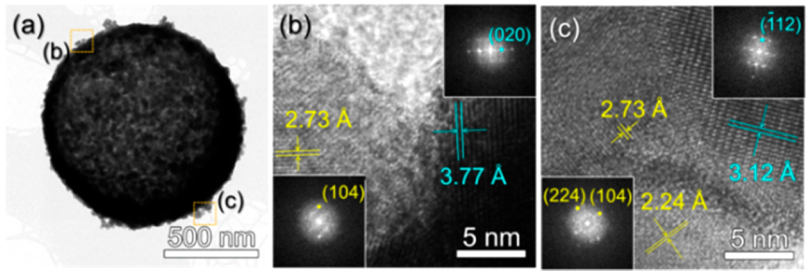

Figure 2. TEM image of Rh-loaded WO_3 hollow spheres.

spheres via heat treatment at 500 °C for 1 h. The resulting hollow spheres were then loaded with 2.5 atom % Rh using the previously described method.[8] In order to fabricate sensors, the pure and Rh-loaded materials were each ground with 1,2-propanediol (Sigma-Aldrich; 99.5+% ACS Reagent) into a paste which was then screen printed onto Al_2O_3 substrates containing Pt electrodes and a backside Pt heater. The printed sensors were dried for 3 h at room temperature (RT) followed by 14 h at 70 °C. The sensors were calcined in a tubular furnace at 400 °C for 10 min, 500 °C for 10 min, and 400 °C for 10 min. An electrometer (Keithley 100) was used for the resistance measurements, and the sensors were heated using a power source (Agilent E3630A) to 300 °C. The samples were examined using TEM analysis (Talos F200X, FEI Co., USA) and X-ray photoelectron spectra (XPS; PHI 5000 VersaProbe, Ulvac-PHI, Japan). The surface reactions of the samples during sensing were examined using operando diffuse reflectance infrared Fourier transform (DRIFT) spectroscopy (Vertex80v narrow-band MCT detector with a spectral resolution of 4 cm^{-1}). A heated sensor (300 °C) was housed in a chamber containing a KBr window, and the resistance of the sensing layer was recorded using an electrometer (Keithley 617 programmable electrometer). The test gases were added using a computer controlled gas mixing system (total flow constant 200 mL/min). A spectrum was recorded every 15 min. A reference spectrum was measured before each test gas exposure, and the sample spectrum was taken at the end of each test gas exposure from which the absorbance spectra were then attained as previously described by Grossmann et al.[14] using the following:

$$\text{absorbance} = -\log\left(\frac{\text{single channel test gas}}{\text{single channel reference}}\right) \quad (1)$$

RESULTS AND DISCUSSION

The hollow morphology of pure and Rh-loaded WO_3 was confirmed by scanning electron microscopy (SEM) and TEM analysis; see Figure 1. The shell thicknesses of the pure and Rh-loaded WO_3 hollow spheres were similar (~40 nm). The EDS elemental mapping of the Rh-loaded WO_3 hollow spheres also

DOI: 10.1021/acs.jpcc.7b09316
J. Phys. Chem. C 2017, 121, 24701−24706

clearly shows that Rh is uniformly distributed over the hollow spheres (Figure 1g).

The lattice fringes of the WO_3 were observed in the pure hollow spheres (Figure 1c), whereas lattice fringes of both the WO_3 and Rh_2O_3 were observed in the Rh-loaded hollow spheres (Figure 1f and Figure 2). Rh_2O_3 is known to crystallize in three structures; the interval distance of 2.73 Å for the (104) plane is most consistent with the presence of the Rh_2O_3 (I) phase.[15] The Rh_2O_3 (I) phase is known to be a p-type semiconductor (Figure 2b,c).[16]

At 300 °C, the resistance of sensors based on the unloaded sample in N_2 is ca. 700 Ω (R_0) while the resistance of the loaded sample is approximately 550 kΩ (R); see Figure 3. The

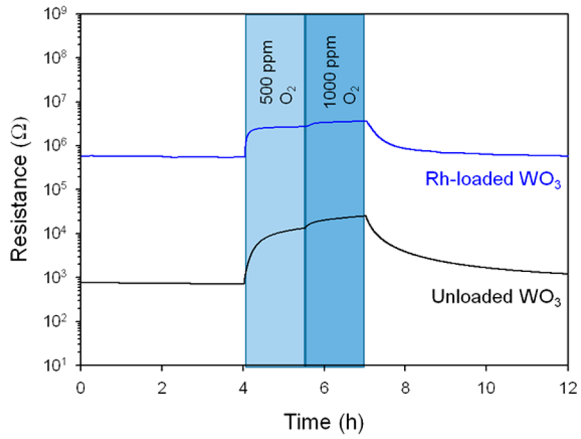

Figure 3. Depiction of dc resistance measurements taken during exposure to O_2 pulses in N_2.

drastic increase in the resistance indicates an electronic coupling between the base metal oxide and the surface Rh_2O_3. From EDS mapping and the TEM pictures it can be deduced that crystalline Rh_2O_3 particles are uniformly present on the WO_3 surface. The loading of WO_3 with the p-type Rh_2O_3 results in the wide distribution of nanoscale p−n heterojunctions on the surface of the sample. At the heterojunctions, electrons from WO_3 migrate toward Rh_2O_3 and conversely holes migrate from Rh_2O_3 to WO_3. The resistance difference between the two samples under exposure to N_2 can be used to approximate the band bending resulting from the surface loading with Rh_2O_3. In N_2, the surface acceptor state related to the ionosorption of O_2 can be neglected. In this case the following relationship between the resistance and the surface band bending can be used for a depletion layer limited charge transport:[17]

$$q\Delta V_S = kT \ln\left(\frac{R}{R_0}\right) \tag{2}$$

The presence of Rh_2O_3 results in a band bending ($q\Delta V_S$) of approximately 330 meV. This indicates a strong electronic coupling between the WO_3 and the Rh_2O_3 clusters. As a result, a depletion layer extends into WO_3, and the potential barrier at the grain boundary is higher. This situation is depicted in Scheme 1.

These results are supported by the findings of the X-ray photoelectron spectra (Figure 4). In the XPS spectra the binding energies of W $4f_{7/2}$ and W $4f_{5/2}$ peaks for the Rh-loaded hollow sphere were 0.1 eV lower than those for the pure hollow

Scheme 1. Grain Surface of Unloaded and Rh-Loaded Samples in the Absence and Presence of Oxygen

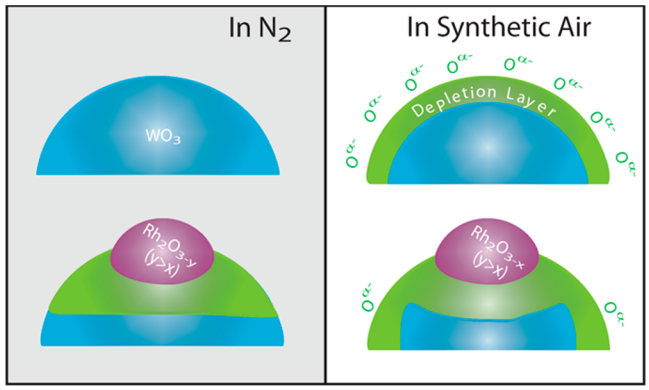

sphere (Figure 4a). This is indicative of increased tungsten−oxygen surface vacancies[7,8,18] on the loaded sample.

The results are further supported by the effect of oxygen on the sensor resistance (Figure 3). It is lower on the Rh-loaded sample than on the unloaded sample. In the presence of oxygen the Rh_2O_3 clusters become more oxidized, which leads to an overall increase in the number of holes and an increase of its work function. More electrons are captured from the supporting WO_3, and as a consequence the sensor resistance increases. The lack of electrons in the WO_3 regions electrically affected by the presence of the Rh_2O_3 clusters hinders the ionosorption of atmospheric oxygen (see Scheme 1). In 2015, Ma et al. proposed a very similar explanation for the hindered OH^- adsorption onto PdO doped SnO_2 in the presence of oxygen.[19]

The presence of Rh_2O_3 on the surface not only has a drastic effect on the base resistance at 300 °C but also changes the sensing characteristics, as shown in Figure 5. Different concentrations of analyte gases (CO, toluene, acetone, and NO_2) were supplied into the homemade gas chamber at a constant flow rate of 200 mL/min using a computer controlled gas mixing system with mass flow controllers. Each gas concentration was pulsed for 1 h, and the system was flushed with synthetic air at the respective humidity level between test gases for several hours. The signals were calculated so that they are always greater than 1, for reducing gases:

$$\text{sensor signal}_{\text{reducing}} = \frac{R_{bg}}{R_{tg}} \geq 1 \tag{3}$$

and for oxidizing gases (NO_2):

$$\text{sensor signal}_{\text{oxidizing}} = \frac{R_{tg}}{R_{bg}} \geq 1 \tag{4}$$

R_{bg} is the resistance during the background gas, and R_{tg} is the resistance during test gas exposure.

The sensor signals are plotted in a logarithmic scale in order to allow for a better comparison between the changes of the sensor signals (relative change of the resistance). At all temperatures the tendencies of the sensor response as a result of Rh loading are very similar. The largest effect is visible for the sensor's response to NO_2 and CO (Figure 5). The sensor signal to NO_2 becomes negligible as a result of Rh loading, while the signal to CO increases. In the application relevant conditions between 30 and 80% relative humidity (RH), the sensor signal of the loaded sensor to CO is practically humidity

DOI: 10.1021/acs.jpcc.7b09316
J. Phys. Chem. C 2017, 121, 24701−24706

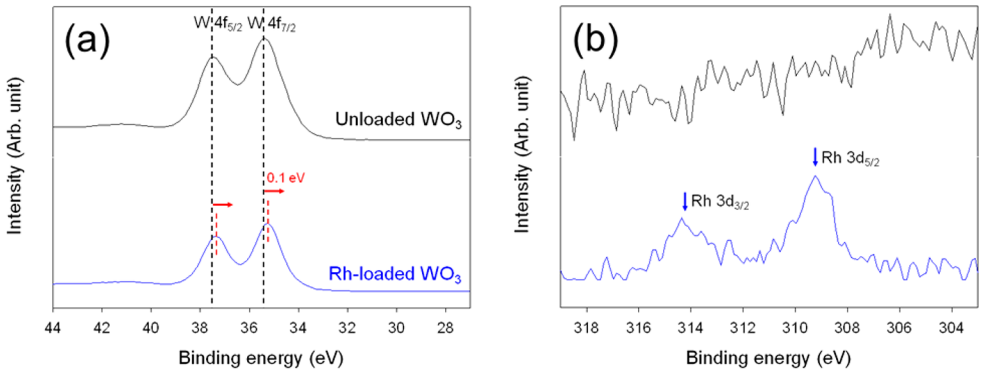

Figure 4. XPS spectra of pure and Rh-loaded WO_3 hollow spheres: (a) W 4f binding energy spectra; (b) Rh 3d binding energy spectra.

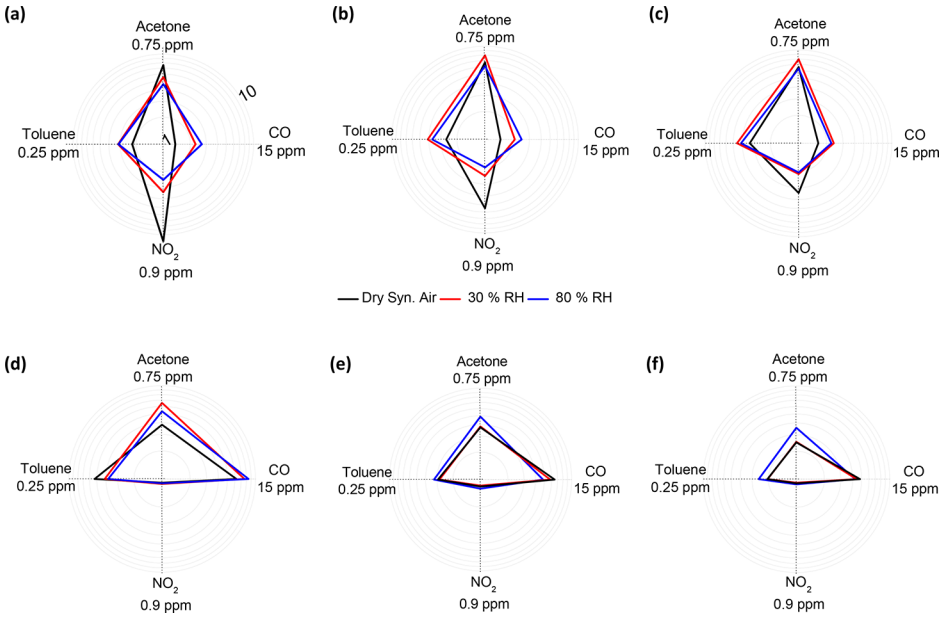

Figure 5. Polar plots of sensor responses at 250, 300, and 350 °C, unloaded (a–c) and Rh-loaded WO_3 (d–f) in different relative background humidity levels. The scale is the same for all depicted graphs.

independent. The signal to toluene is similar, but the response of the loaded sample is less humidity dependent. Overall the signal to acetone decreases slightly and remains humidity dependent although in a different manner when one compares the pure with the doped sensors. Due to the similarity in the sensor responses at the different temperatures and because at 300 °C the sensors show fast responses and high stability, further investigations were done at 300 °C.

Operando DRIFT spectroscopy was used to examine how the presence of Rh_2O_3 changes the surface reactions responsible for gas detection (Figure 6). The DRIFT results attained during acetone exposure gave the best insight into how the surface chemistry changes as a result of the surface loading. Sensors based on both samples respond well to low concentrations of acetone. In the absorbance spectrum attained by referencing the spectrum taken during acetone exposure to the spectrum taken in dry synthetic air, there is a visible decrease in bands attributed to tungsten–oxygen overtones (bands at 2055 and 1855 cm^{-1}).[12,20] In addition, an increase of two bands (1036 and 997 cm^{-1}) is visible. Bands in this region can be attributed to the symmetric stretching mode of short terminal metal–oxygen double bonds.[21,22] From these results it can be inferred that the WO_3 surface of the unloaded sample is

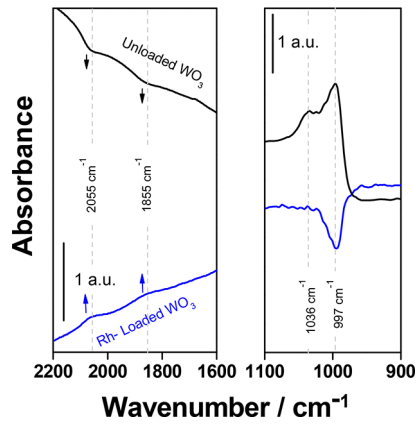

Figure 6. DRIFT absorbance spectra taken during exposure to acetone in dry synthetic air at 300 °C.

reduced during the combustion of acetone on the surface. The increase in surface oxygen vacancies is then compensated by the formation of tungsten–oxygen double bonds. The situation changes for the Rh_2O_3-loaded sample. In the spectrum taken of the sensors based on it, the bands attributed to tungsten–

DOI: 10.1021/acs.jpcc.7b09316
J. Phys. Chem. C 2017, 121, 24701–24706

Scheme 2. Grain Surface of Unloaded and Loaded Samples during Acetone Exposure

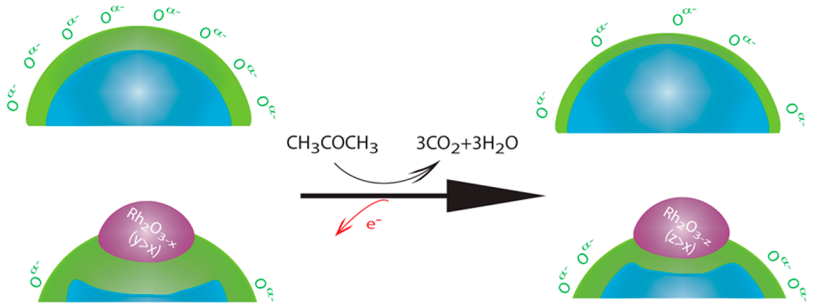

oxygen overtones are slightly increasing (see arrows) while a band at 997 cm^{-1} attributed to tungsten−oxygen double bonds is decreasing. Initially this result is very surprising because it indicates an increase of the surface oxidation of WO_3 in spite of a very significant decrease of the sensor resistance. In fact, this finding indicates that the detection of acetone is dominated by what happens on the Rh_2O_3 clusters. Their reduction by acetone decreases the concentration of holes and its work function. Because of the latter, fewer electrons are captured from the WO_3. This results in a decrease of the sensor resistance. As a secondary effect, the availability of more electrons in WO_3, determined by the reduction of the heterojunction-related depletion layer, makes it possible for more oxygen to be adsorbed at its surface (which is the explanation for the increase of tungsten−oxygen bonds). Overall, the dominant process is still the pinning of the Fermi level of WO_3 by that of the Rh_2O_3 clusters. This situation is depicted in Scheme 2.

From the results it can be deduced that the sensing is dominated by the Rh_2O_3 clusters. At 300 °C, WO_3 is known to show high sensor signals to oxidizing gases, such as NO_2, while in general the response to CO is lower and humidity dependent.[23] As a result of high surface loading with Rh_2O_3, however, the signals to NO_2 become negligible. Here, as for oxygen, there are no electrons available from WO_3 for its ionosorption, which makes it insensitive to NO_2. On the other hand, Rh_2O_3 is known to be a good catalyst for the oxidation of NO to NO_2,[24] which means that it should not react with NO_2. That means both possibilities for NO_2 sensing, directly on the supporting oxide and with the Rh_2O_3 clusters, are eliminated. This explains why the signal to NO_2 is low in the case of the loaded sample.

On the other hand, the signals to CO increase and become less humidity dependent. These results confirm that the reactions between the surface Rh_2O_3 and analytes gases are responsible for the reception. CO is known to react strongly with the lattice oxygen of Rh_2O_3 to yield CO_2. Conversely, CO_2 is known to desorb from the Rh_2O_3 surface essentially intact.[25] The results are in accordance with those attained here for the Rh-loaded WO_3 sample. Similar sensor characteristics have been reported by Anton and Buedy for SnO_2 loaded samples.[13] Additionally, in both cases the base resistance of the sensors dramatically increases as a result of the loading indicating an electronic coupling via a heterojunction between the host oxide and the surface Rh_2O_3.The effect of changes in the heterojunction properties on the host oxide dominates transduction.

CONCLUSION

In conclusion, it was possible, through characterization with XPS, TEM, dc resistance measurements, and DRIFT spectroscopic measurements, to understand how surface Rh_2O_3 changes gas sensing in WO_3. Reactions between Rh_2O_3 and the analyte gases are responsible for the reception, and the transduction is the result of changes in the p−n heterojunction characteristics. These findings are groundbreaking and finally provide conclusive evidence for how the surface chemistry and the transduction can be tuned through the presence of p−n heterojunctions. This provides a means through which the sensing characteristics of SMOXs can be intentionally tuned and a template on how the gas sensing p−n heterojunctions can be studied.

AUTHOR INFORMATION

Corresponding Author

*E-mail: nb@ipc.uni-tuebingen.de.

ORCID

Jong-Heun Lee: 0000-0002-3075-3623

Nicolae Barsan: 0000-0001-6718-9889

Notes

The authors declare no competing financial interest.

REFERENCES

(1) Steirer, K. X.; Ou, K. L.; Armstrong, N. R.; Ratcliff, E. L. Critical Interface States Controlling Rectification of Ultrathin NiO−ZnO p−n Heterojunctions. *ACS Appl. Mater. Interfaces* **2017**, *9*, 31111−31118.

(2) Faber, H.; Das, S.; Lin, Y.; Pliatsikas, N.; Zhao, K.; Kehagias, T.; Dimitrakopulos, G.; Amassian, A.; Patsalas, P. A.; Anthopoulos, T. D. Heterojunction Oxide Thin-Film Transistors with Unprecedented Electron Mobility Grown from Solution. *Sci. Adv.* **2017**, *3*, e1602640.

(3) Wang, M.; Pyeon, M.; Gonullu, Y.; Kaouk, A.; Shen, S.; Guo, L.; Mathur, S. Constructing Fe_2O_3/TiO_2 Core−shell Photoelectrodes for Efficient Photoelectrochemical Water Splitting. *Nanoscale* **2015**, *7*, 10094−10100.

(4) Miller, D. R.; Akbar, S. A.; Morris, P. A. Nanoscale Metal Oxide-Based Heterojunctions for Gas Sensing: A Review. *Sens. Actuators, B* **2014**, *204*, 250−272.

(5) Hoa, L. T.; Hur, S. H. Highly Sensitive NO_2 Sensors Based on Local P−n Heterojunctions Composed of 0D CuO Nanoparticles and 1D ZnO Nanorods. *Phys. Status Solidi A* **2013**, *210*, 1213−1216.

(6) Wang, Z.; Li, Z.; Sun, J.; Zhang, H.; Wang, W.; Zheng, W.; Wang, C. Improved Hydrogen Monitoring Properties Based on P-NiO/N-SnO_2 Heterojunction Composite Nanofibers. *J. Phys. Chem. C* **2010**, *114*, 6100−6105.

(7) Kim, N. H.; Choi, S. J.; Kim, S. J.; Cho, H. J.; Jang, J. S.; Koo, W. T.; Kim, M.; Kim, I. D. Highly Sensitive and Selective Acetone Sensing Performance of WO_3 Nanofibers Functionalized by Rh_2O_3 Nanoparticles. *Sens. Actuators, B* **2016**, *224*, 185−192.

DOI: 10.1021/acs.jpcc.7b09316
J. Phys. Chem. C 2017, 121, 24701−24706

(8) Choi, K.-I.; Hwang, S.-J.; Dai, Z.; Chan Kang, Y.; Lee, J.-H. Rh-Catalyzed WO_3 with Anomalous Humidity Dependence of Gas Sensing Characteristics. *RSC Adv.* **2014**, *4*, 53130−53136.
(9) Kim, S.-J.; Choi, S.-J.; Jang, J.-S.; Kim, N.-H.; Hakim, M.; Tuller, H. L.; Kim, I.-D. Mesoporous WO_3 Nanofibers with Protein Templated Nanoscale Catalysts for Detection of Trace Biomarkers in Exhaled Breath. *ACS Nano* **2016**, *10*, 5891−5899.
(10) Zu, B.; Lu, B.; Yang, Z.; Guo, Y.; Dou, X.; Xu, T. Gas Adsorption Thermodynamics Deduced from the Electrical Responses in Gas-Gated Field-Effect Nanosensors. *J. Phys. Chem. C* **2014**, *118*, 14703−14710.
(11) Akiyama, M.; Tamaki, J.; Miura, N.; Yamazoe, N. Tungsten Oxide-Based Semiconductor Sensor Highly Sensitive to NO and NO_2. *Chem. Lett.* **1991**, *20*, 1611−1614.
(12) Akamatsu, T.; Itoh, T.; Izu, N.; Shin, W. NO and NO_2 Sensing Properties of WO_3 and Co_3O_4 Based Gas Sensors. *Sensors* **2013**, *13*, 12467−12481.
(13) Anton, M.; Buedy, B. The Influence of Rhodium on SnO_2-CO Gas Sensor. *Sens. Actuators, B* **1994**, *19*, 500−501.
(14) Grossmann, K.; Pavelko, R. G.; Barsan, N.; Weimar, U. Chemical Interplay of H_2, Water Vapor and Oxygenat the Surface of SnO_2 Based Gas Sensors−An Operando Investigation Utilizing Deuterated Gases. *Sens. Actuators, B* **2012**, *166−167*, 787−793.
(15) *Catalysis by Ceria and Related Materials*; Trovarelli, A., Ed.; Catalytic Science Series 2; World Scientific Publishing: 2002; p 508.
(16) Koffyberg, F. P. Optical Bandgaps and Electron Affinities of Semiconducting Rh_2O_3(I) and Rh_2O_3(III). *J. Phys. Chem. Solids* **1992**, *53*, 1285−1288.
(17) Barsan, N.; Hübner, M.; Weimar, U. Conduction Mechanisms in SnO2 Based Polycrystalline Thick Film Gas Sensors Exposed to CO and H_2 in Different Oxygen Backgrounds. *Sens. Actuators, B* **2011**, *157*, 510−517.
(18) Shpak, A. P.; Korduban, A. M.; Medvedskij, M. M.; Kandyba, V. O. XPS Studies of Active Elements Surface of Gas Sensors Based on WO_{3-X} Nanoparticles. *J. Electron Spectrosc. Relat. Phenom.* **2007**, *156−158*, 172−175.
(19) Ma, N.; Suematsu, K.; Yuasa, M.; Kida, T.; Shimanoe, K. Effect of Water Vapor on Pd-Loaded SnO_2 Nanoparticles Gas Sensor. *ACS Appl. Mater. Interfaces* **2015**, *7*, 5863−5869.
(20) Hübner, M.; Simion, C. E.; Haensch, a.; Barsan, N.; Weimar, U. CO Sensing Mechanism with WO_3 Based Gas Sensors. *Sens. Actuators, B* **2010**, *151*, 103−106.
(21) Weckhuysen, B. M.; Jehng, J.-M.; Wachs, I. E. In Situ Raman Spectroscopy of Supported Transition Metal Oxide Catalysts: $^{18}O_2$ − $^{16}O_2$ Isotopic Labeling Studies. *J. Phys. Chem. B* **2000**, *104*, 7382−7387.
(22) Ramis, G.; Cristiani, C.; Elmi, A. S.; Villa, P.; Busca, G. Characterization of the Surface Properties of Polycrystalune WO_3. *J. Mol. Catal.* **1990**, *61*, 319−331.
(23) Pokhrel, S.; Simion, C. E.; Teodorescu, V. S.; Barsan, N.; Weimar, U. Synthesis, Mechanism, and Gas-Sensing Application of Surfactant Tailored Tungsten Oxide Nanostructures. *Adv. Funct. Mater.* **2009**, *19*, 1767−1774.
(24) Weiss, B. M.; Artioli, N.; Iglesia, E. Catalytic NO Oxidation Pathways and Redox Cycles on Dispersed Oxides of Rhodium and Cobalt. *ChemCatChem* **2012**, *4*, 1397−1404.
(25) Watson, P. R.; Somorjai, G. A. Interaction of CO, CO_2, and D_2 with Rhodium Oxide: Its Reduction and Catalytic Stability. *J. Phys. Chem.* **1982**, *86*, 3993−3996.

DOI: 10.1021/acs.jpcc.7b09316
J. Phys. Chem. C 2017, 121, 24701−24706

Sensors and Actuators B 237 (2016) 54–58

Contents lists available at ScienceDirect

Sensors and Actuators B: Chemical

journal homepage: www.elsevier.com/locate/snb

The oxidizing effect of humidity on WO_3 based sensors

A. Staerz[a,b], C. Berthold[c], T. Russ[a,b], S. Wicker[a,b], U. Weimar[a,b], N. Barsan[a,b,*]

[a] Institute of Physical and Theoretical Chemistry (IPTC), University of Tuebingen, Auf der Morgenstelle 15, D-72076, Tuebingen, Germany
[b] Centre for Light-Matter Interaction, Sensors & Analytics (LISA+), University of Tuebingen, Auf der Morgenstelle 15, D-72076 Tuebingen, Germany
[c] Angewandte Mineralogie, University of Tuebingen, Wilhelmstraße 56, D-72076, Tuebingen, Germany

ARTICLE INFO

Article history:
Received 19 February 2016
Received in revised form 7 June 2016
Accepted 12 June 2016
Available online 15 June 2016

Keywords:
Operando DRIFTS
Gas sensing with WO_3
Detection of CO and NO_2
Effect of humidity

ABSTRACT

Semiconducting metal oxide based gas sensors are used in a wide spectrum of fields, ranging from the detection of hazardous gases within the environment to monitoring air quality. WO_3 is the second, after SnO_2, most commonly used semiconducting metal oxide in commercial gas sensors. Despite its frequent application, the surface reactions responsible for sensing are largely unknown. Here, for the first time, a mechanism for the surface reaction between WO_3 and humidity can be concluded from experimental results. DC resistance measurements and operando diffuse reflectance infrared Fourier transform spectroscopy show an oxidation of the WO_3 lattice during humidity exposure. The filling of oxygen vacancies by water explains the effects atmospheric humidity has on WO_3 based sensors, specifically the increase in resistance, the higher sensor signals to CO and the lower sensor signals to NO_2. These findings are a basis for understanding how sensing occurs with WO_3 based sensors.

1. Introduction

WO_3 is an oxygen deficient n-type semiconductor, whose gas sensing attributes have been intensely studied since 1991 [1]. The gas sensing qualities of WO_3 are complementary to SnO_2. SnO_2 is reported to show high signals to i.e. CO [2], ethanol [3] and H_2 [2]; comparatively, a multitude of published results report high signals of WO_3 to ammonia [4], toluene [5], hydrogen sulfide [6], and acetone [7]. This complementary behavior is a possible explanation why SnO_2 and WO_3 are the only two semiconducting metal oxides (SMOx) used in commercial sensors. Using sensors for diagnostic breath analysis is an exciting new application field. In 2008, the United States Food and Drug Administration first approved a breath detector based on an electrochemical cell for clinical diagnostics [8]. The electrochemical sensor used in the Niox Mino from Aerocrine is an amperometric liquid electrolyte sensor [9]. SMOx is a more inexpensive and robust alternative to sensing with an electrochemical cell. In fact, in 2012, Righettoni et al. already reported the successful monitoring of acetone in human breath using a prototype detector containing a sensor based on silicon doped WO_3 [10]. In addition to acetone, many other gases, hydrogen sulfide [11] and toluene [12], detectable with a WO_3 sensor are relevant for breath analysis, making it a very promising material for breath analysis.

Despite its widespread use, the sensing mechanism of WO_3 is poorly understood. For years it was thought that the sensing of all n-type metal oxides emulates that of SnO_2. This is clearly a misconception, as the gas sensing attributes of WO_3 are very different from those of SnO_2. For example, the two oxides are reported to interact very differently with humidity. The SnO_2 surface is reduced by water, leading to a resistance decrease during humidity exposure [13]. This resistance decrease is also observed for most other oxygen deficient n-type semiconductors, i.e. In_2O_3 [14] and ZnO [15]. We have recently shown that for WO_3 based gas sensors, even if the sensitive material is differently prepared, exposure to humidity leads to an increase in resistance [16,17]. Additionally, the sensor signals to the reducing gas, CO, increased with humidity, while those to the oxidizing gas, NO_2 decreased with increasing humidity [17]. This shows that WO_3 clearly interacts very differently with humidity than SnO_2.

2. Material and methods

To fabricate the sensors, commercially available WO_3 nanopowder (Sigma Aldrich >100 nm) was ground with 1,2-Propandiol (Sigma Aldrich; 99,5+ % A.C.S. Reagent) into a printable paste using a mortar and pestle. The paste was screen printed onto Al_2O_3-substrates with a Pt-electrode and a Pt-heater. The sensitive layer of WO_3 was dried for several hours at room temperature and then

* Corresponding author at: The Institute of Physical and Theoretical Chemistry (IPTC), University of Tuebingen, Auf der Morgenstelle 15, D-72076, Tuebingen, Germany.
E-mail address: nb@ipc.uni-tuebingen.de (N. Barsan).

http://dx.doi.org/10.1016/j.snb.2016.06.072
0925-4005/

overnight at 70 °C. The sensors were calcined in a tubular furnace at 400 °C for 10 min, 500 °C for 10 min followed by 10 min at 400 °C. The resistance of the sensor was measured using a Keithley 100 electrometer. Different concentrations of CO and NO_2 were supplied by a computer regulated gas mixing system containing mass flow controllers. Each of the five test gas concentrations was pulsed for two hours. Between different test gases the system was flushed with synthetic air. The complete measurement protocol was done in a dry synthetic air background as well as in 30% and 80% relative humidity (RH). The resistance change of two identically prepared WO_3 sensors was simultaneously measured. The sensor signals for reducing gases were calculated using the following formula:

$$Sensor\ Signal_{reducing} = \frac{R_{bg}}{R_{tg}} \geq 1 \quad .$$

The inverse relationship was used for oxidizing gases:

$$Sensor\ Signal_{oxidizing} = \frac{R_{tg}}{R_{bg}} \geq 1 \quad .$$

Here R_{bg} is the resistance during exposure to the background gas and R_{tg} is the resistance during exposure to the test gas. Operando diffuse reflectance infrared spectroscopy was used to examine the surface reactions of the sensor under working conditions. The measurements were done in a Bruker VERTEX 80v spectrometer. A homemade test chamber and a liquid nitrogen cooled MCT (mercury cadmium tellurium) detector were used. A spectrum was recorded every 15 min. A reference spectrum was measured before each test gas exposure and the sample spectrum was taken at the end of each test gas exposure. The absorbance spectra were calculated from the single channel spectra using the following equation:

$$\text{absorbance} = -\log\left(\frac{\text{single channel test gas}}{\text{single channel reference}}\right)$$

Using operando DRIFT spectroscopy, we address the knowledge deficit surrounding sensing with WO_3. Here the main focus is on understanding the impact of humidity on the baseline resistance and how it effects the sensing of an exemplary reducing and oxidizing gas.

In addition to phase characterization of the calcined WO_3-sensor layer directly on the Al_2O_3-substrate at RT, measurements were also performed during heating and cooling of the sensor using a BRUKER D8 discover GADDS microdiffractometer. This system is equipped with a Co-X-ray tube, HOPG-primary monochromator, X-ray optics and a large 2dimensional VANTEC-500 detector covering 40° 2Θ and 40° ψ for fast and local resolved measurements directly on the sensor [18]. Measurement times for each diffractogram were 1 min and the beam diameter was app. 300 μm.

3. Results and discussion

Unlike SnO_2, WO_3 can exist in different crystal phases. Between 17 °C and 330 °C, the γ-monoclinic phase is considered to be stable [19]. Although when annealed to higher temperatures WO_3 transforms to other crystal phases, the phase change is reported to be reversible [19]. The X-ray diffraction pattern of the calcined WO_3 sensor before use indicated that the γ-monoclinic phase is predominantly present. After a complete DC resistance measurement under measurement conditions with the sensor at an operating temperature of 300 °C for over 100 h at 80% RH and under analyte gas exposure, an additional XRD measurement was done under normal atmosphere of the sensor at RT. The diffraction of the used sensor is identical to that of the unused sensor at RT, this indicates that any changes in the crystal structure which may occur during sensing are entirely reversible, see Fig. 2.

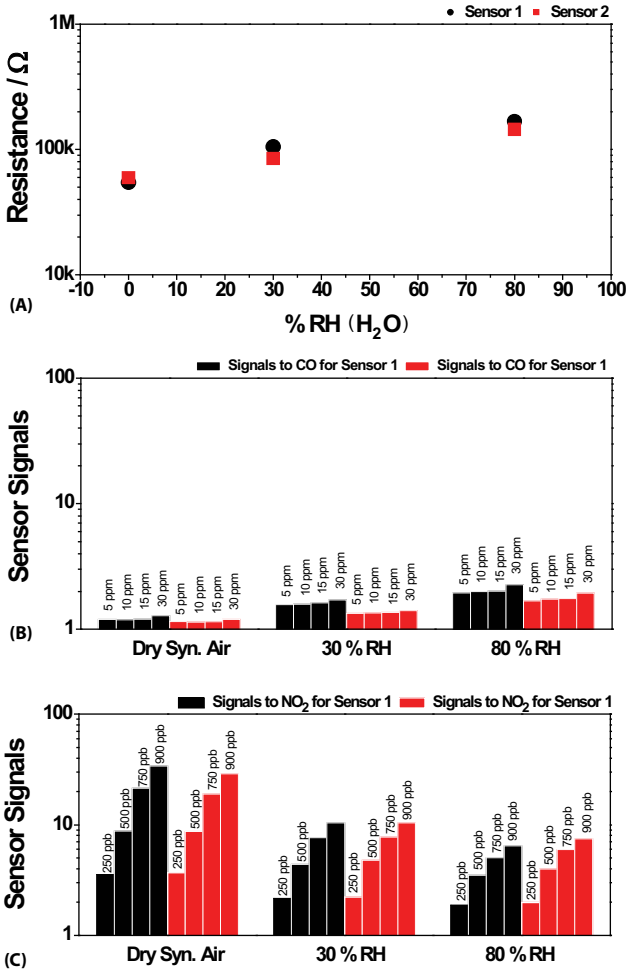

Fig. 1. Evaluation based on DC resistance measurements; the sensor signals for each of the two identically prepared WO_3 based sensors are plotted individually. A) The humidity dependence of the resistance of the sensor based on WO_3 shown. B) The effect of humidity on the sensor signals to CO and NO_2 is depicted.

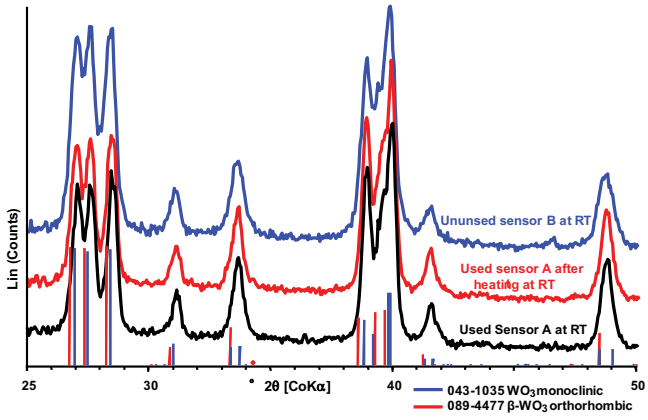

Fig. 2. The diffractograms of the used sensor A at room temperature (black) and after heating (red) up to 400 °C are compared to diffractogram of the unused sensor B (blue) at RT. Prior to the XRD measurements the used sensor A was operated at 300 °C for over 100 h under various target gases and at different RH (up to 80%). (For interpretation of the references to colour in this figure legend, the reader is referred to the web version of this article.)

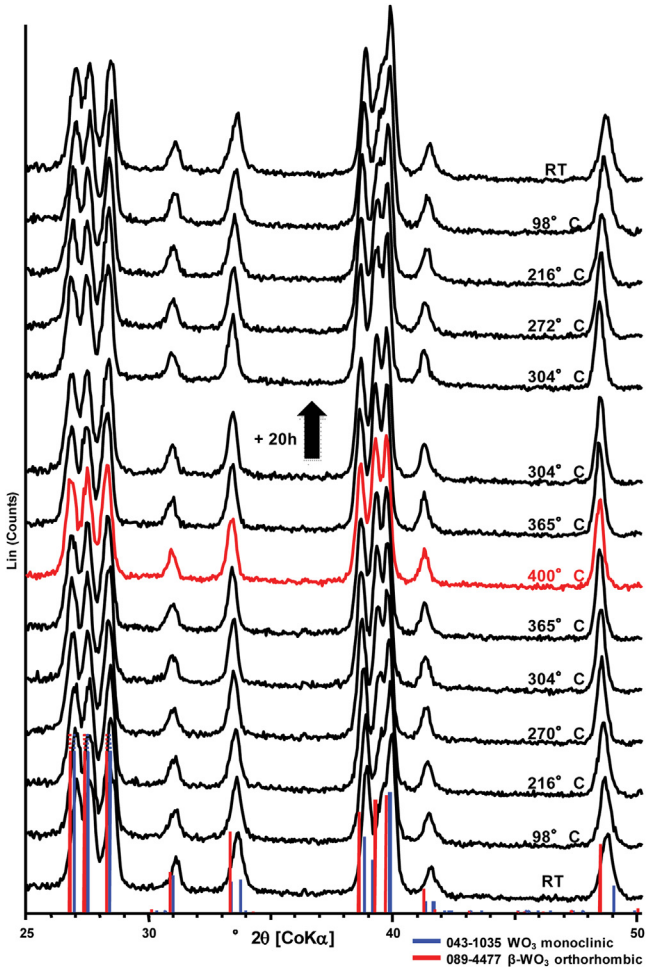

Fig. 3. The cyclic heating measurement in laboratory air from RT up to 400 °C, a holding time of app. 20 h at 303 °C and subsequent cooling to RT is shown. At app. 300 °C the phase transformation from the monoclinic to the orthorhombic β-phase structure is visible. The phase is state remains stable during the 20 h. The reverse phase transformation was already observed at app. 272 °C during cooling.

For sensing the situation at 300 °C is important. An additional cyclic measurement of the used sensor A in laboratory air heating the sensor from RT up to 400 °C, a holding time of over 15 h at 303 °C and subsequent cooling to RT is shown in Fig. 3. At app. 300 °C the described phase transformation is detectable from the monoclinic to the orthorhombic β-phase structure which remains stable during the holding time at 303 °C. During cooling, the reverse phase transformation was already observed at app. 272 °C.

Based on the XRD measurements of the used and the unused sensors, it can be concluded that any phase transitions which occur during sensing are reversible. Moreover, we can also state that the material is not changed because of exposure to target gases and humidity (Fig. 3).

The effect of humidity on the electrical response of the sensor to CO and NO_2 was examined using DC resistance measurements. The previously reported results were confirmed. In addition to the increase of the samples resistance with humidity (see Fig. 1), the sensor signals to CO were also higher in humidity than in dry synthetic air (see Fig. 1). This indicates that unlike on SnO_2, the reducing gas CO does not compete with water for reaction partners on the WO_3 surface. In fact, the interaction of the WO_3 surface with CO seems to be promoted by humidity. Operando DRIFT spectroscopy allows the examination of surface reactions under normal sensing conditions. Here the sensor was operated at 300 °C and under standard pressure, typical operating conditions for SMOx based gas sensors. The DRIFT spectra taken on the Sigma Aldrich sample during CO exposure in dry air show similar results to those previously published (see Fig. 4) [20]. There were also no remarkable differences between the spectra taken of CO in 10% RH versus dry air. The visible decrease in the absorbance bands at 1847 cm^{-1} and 2049 cm^{-1} are attributed to a decrease in overtones of tungsten-oxygen lattice bonds. It was reported that the first M-O overtones are typically visible in this wavenumber region (2150–1850 cm^{-1}) [21]; additionally, several different infrared studies have specifically attributed these two bands to overtones of W-O bonds [22–24]. Additionally in the DRIFT spectra taken during exposure to CO in the presence and the absence of humidity, the band attributed to gaseous CO_2 is visible. From this information it can be concluded that CO reduces the WO_3 surface, resulting in oxygen vacancies [20]:

$$CO_{gas} + O_O \rightarrow CO_{2,gas} + V_O^{\cdot\cdot} + 2e^-.$$

WO_3 is an oxygen deficient n-type semiconductor. An oxygen vacancy results in two-electron donors explaining the detected decrease in resistance during CO exposure. Contrarily NO_2 leads to an increase in the resistance of the WO_3 based sensors. The classic nitro symmetric and asymmetric bands are not visible in the spectra taken during NO_2 exposure. An increasing band at 1424 cm^{-1} is, however, visible during NO_2 exposure, Akamatsu et al. associated this band with nitrate groups [24]. The formation of nitrate groups

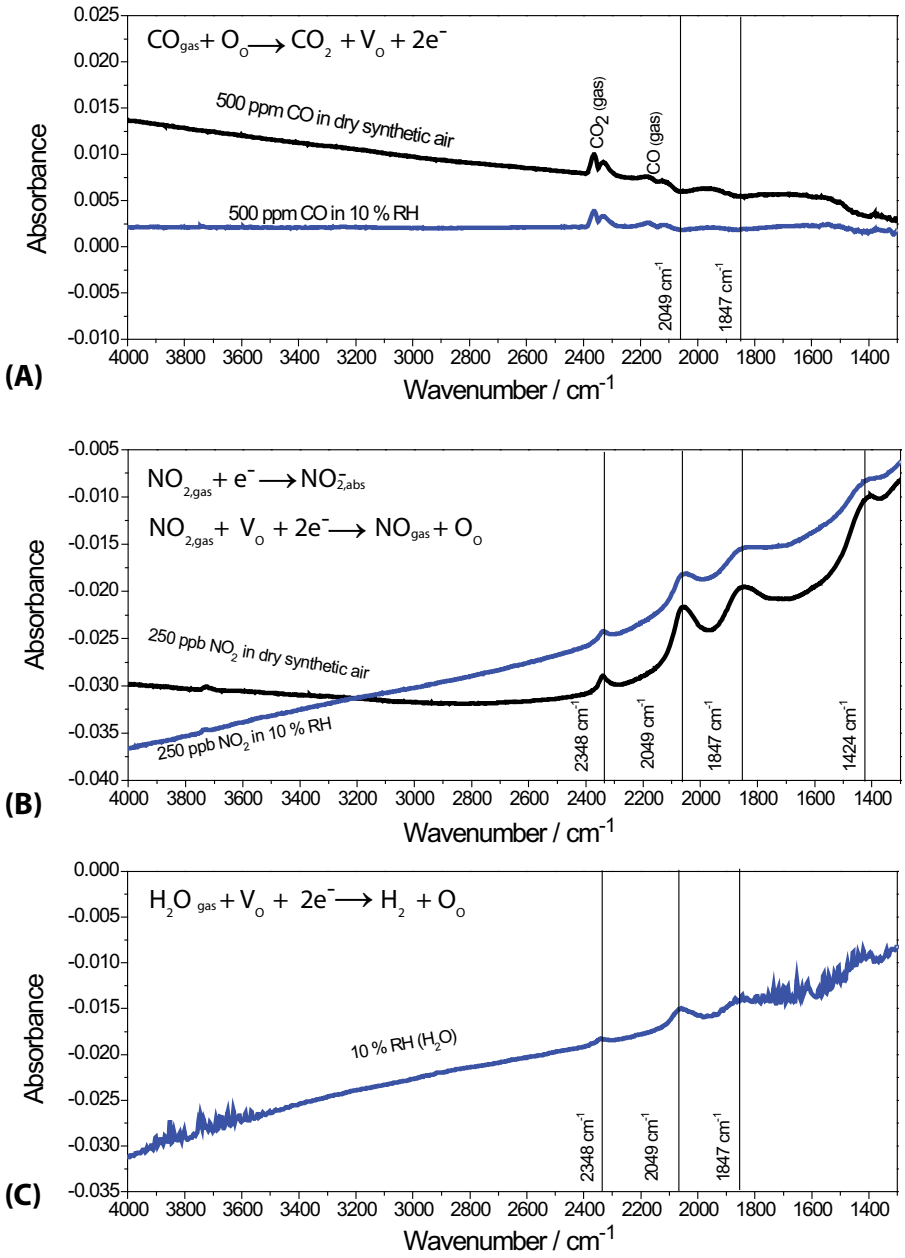

Fig. 4. Operando DRIFT spectra taken with the sensor heated to 300 °C. The spectra taken during exposure to CO and NO_2 in a dry synthetic background are referenced to a spectrum taken in dry synthetic air, while those taken in a humid background are referenced to a spectrum taken in synthetic air with 10% RH. The spectrum shown during exposure to 10% RH is referenced to a spectrum taken in dry synthetic air. A) Operando DRIFT spectra taken during exposure to 500 ppm CO in the presence and absence of 10% RH are shown. B) Operando DRIFT spectra taken during exposure to 250 ppb NO_2 in the presence and absence of 10% RH are depicted. C) An Operando DRIFT spectrum taken during exposure to 10% RH is shown.

on the surface would lead to a decrease of the resistance based on the following reaction:

$$NO_{2,gas} + e^- \rightarrow NO^-_{2,abs}$$

The oxidation of the surface is more clearly visible due to the increasing bands 1847 cm^{-1} and 2049 cm^{-1} (see Fig. 4). As previously stated these bands are attributed to WO overtones. The increase in the band at 2348 cm^{-1} may also be a tungsten oxygen lattice overtone. Its decrease is most likely not visible in the spectra taken during CO exposure due to an overlap with the bands attributed to gaseous CO_2. These bands show the filling of oxygen vacancies by NO_2 indicating the following previously suggested mechanism [25]:

$$NO_{2,gas} + V_O^{\cdot\cdot} + 2e^- \rightarrow O_O + NO_{gas}$$

In the DRIFT spectrum taken during humidity exposure (see Fig. 4) the rotational fine structure of water is visible in the region above 3500 cm^{-1} and below 1700 cm^{-1}. No bands attributed to the formation of hydroxyl groups are present. Overall the spectrum is similar to those taken during exposure to NO_2. The bands at 1847 cm^{-1}, 2049 cm^{-1}, and 2348 cm^{-1} are all increasing. This indicates that the oxygen in water, similar to the oxygen in NO_2,

fills the oxygen vacancies. This explains the detected increase in resistance. The following mechanism is suggested:

$$H_2O_{gas} + V_{\ddot{O}} + 2e^- \rightarrow O_0 + H_{2,gas}.$$

The oxidation of the surface also explains the detected effect of humidity on the sensor signals to CO and NO_2. Through the oxidizing effect of humidity the resistance of the sensors is increased (see Fig. 1), and more reaction partners for CO are present on the surface than in dry air. The latter explains the increase in the sensor signals to CO resulting from humidity (see Fig. 1). NO_2 and water both oxidize the surface meaning they compete for the reaction partners. This explains the detected decrease of the sensor signals to NO_2 in humidity (see Fig. 1).

4. Conclusion

Using a combination of analytical methods, significant insight was gained into how sensing occurs on the surface of the WO_3 sample. This understanding in turn is crucial for the development of more selective and sensitive gas sensors It was shown using XRD that measurements done at RT are not necessarily relevant for characterization of sensors operated at higher temperatures due to reversible temperature dependent crystal phase changes. Therefore it is necessary to have operando XRD studies in the future. The reduction of the WO_3 lattice by CO and the oxidation by NO_2 was visible in operandi DRIFT spectra. Based on the infrared results in combination with DC resistance measurements, it is concluded that for this sample of WO_3, contrary to what generally occurs with SnO_2, the lattice is oxidized by humidity. This oxidation explains the experimentally detected increase in resistance for the WO_3 sample during humidity exposure. It explains why the sensor signals to the reducing gas, CO, increase and why those to the oxidizing gas, NO_2, decrease in humidity. This result is an indication that the surface reactions of WO_3 are unlike those of SnO_2, and that to understand the sensing of more complex gases additional operando research is necessary. To check the general validity of these results additional WO_3 samples will be examined in operando in the future. This basic understanding is not only essential for optimizing sensing, but for all fields in which the surface reactions of WO_3 play a key role.

References

[1] M. Akiyama, J. Tamaki, N. Miura, N. Yamazoe, Tungsten oxide-based semiconductor sensor highly sensitive to NO and NO_2, Chem. Lett. (1991) 1611–1614, http://dx.doi.org/10.1246/cl.1991.1611.

[2] S.W. Lee, P.P. Tsai, H. Chen, Comparison study of SnO_2 thin- and thick-film gas sensors, Sens. Actuators B Chem. 67 (2000) 122–127, http://dx.doi.org/10.1016/S0925-4005(00)00390-7.

[3] G. Neri, A. Bonavita, G. Micali, N. Donato, F.A. Deorsola, P. Mossino, et al., Ethanol sensors based on Pt-doped tin oxide nanopowders synthesised by gel-combustion, Sens. Actuators B Chem. 117 (2006) 196–204, http://dx.doi.org/10.1016/j.snb.2005.11.032.

[4] G. Wang, Y. Ji, X. Huang, X. Yang, P.I. Gouma, M. Dudley, Fabrication and characterization of polycrystalline WO_3 nanofibers and their application for ammonia sensing, J. Phys. Chem. B. 110 (2006) 23777–23782, http://dx.doi.org/10.1021/jp0635819.

[5] K.-I. Choi, S.-J. Hwang, Z. Dai, Y. Chan Kang, J.-H. Lee, Rh-catalyzed WO_3 with anomalous humidity dependence of gas sensing characteristics, RSC Adv. 4 (2014) 53130–53136, http://dx.doi.org/10.1039/C4RA06654E.

[6] C.S. Rout, M. Hegde, C.N.R. Rao, H_2S sensors based on tungsten oxide nanostructures, Sens. Actuators B Chem. 128 (2008) 488–493, http://dx.doi.org/10.1016/j.snb.2007.07.013.

[7] R.S. Khadayate, J.V. Sali, P.P. Patil, Acetone vapor sensing properties of screen printed WO_3 thick films, Talanta 72 (2007) 1077–1081, http://dx.doi.org/10.1016/j.talanta.2006.12.043.

[8] K.M. Paschke, A. Mashir, R.A. Dweik, Clinical applications of breath testing, F1000 Med. Rep. 2 (2010) 56, http://dx.doi.org/10.3410/M2-56.

[9] H.G. Nicolas Roxhed, Goran Stemme, No Title, Patent Number: 9304100 (2013).

[10] M. Righettoni, A. Tricoli, S. Gass, A. Schmid, A. Amann, S.E. Pratsinis, Breath acetone monitoring by portable Si:WO_3 gas sensors, Anal. Chim. Acta. 738 (2012) 69–75, http://dx.doi.org/10.1016/j.aca.2012.06.002.

[11] F.L. Suarez, J.K. Furne, J. Springfield, M.D. Levitt, Morning breath odor: influence of treatments on sulfur gases, J. Dent. Res. 79 (2000) 1773–1777, http://dx.doi.org/10.1177/00220345000790100701.

[12] D. Poli, P. Carbognani, M. Corradi, M. Goldoni, O. Acampa, B. Balbi, et al., Exhaled volatile organic compounds in patients with non-small cell lung cancer: cross sectional and nested short-term follow-up study, Respir. Res. 6 (2005) 71, http://dx.doi.org/10.1186/1465-9921-6-71.

[13] D. Degler, S. Wicker, U. Weimar, N. Barsan, Identifying the active oxygen species in SnO_2 based gas sensing materials: an operando IR spectrsocopy study, J. Phys. Chem. C. 119 (2015) 11792–11799, http://dx.doi.org/10.1021/acs.jpcc.5b04082.

[14] G. Korotcenkov, M. Ivanov, I. Blinov, J.R. Stetter, Kinetics of indium oxide-based thin film gas sensor response: the role of redox and adsorption/desorption processes in gas sensing effects, Thin Solid Films 515 (2007) 3987–3996, http://dx.doi.org/10.1016/j.tsf.2006.09.044.

[15] Y. Zhang, K. Yu, D. Jiang, Z. Zhu, H. Geng, L. Luo, Zinc oxide nanorod and nanowire for humidity sensor, Appl. Surf. Sci. 242 (2005) 212–217, http://dx.doi.org/10.1016/j.apsusc.2004.08.013.

[16] J.A. Kemmler, S. Pokhrel, L. Mädler, U. Weimar, N. Barsan, Flame spray pyrolysis for sensing at the nanoscale, Nanotechnology 24 (2013) 442001, http://dx.doi.org/10.1088/0957-4484/24/44/442001.

[17] S. Pokhrel, C.E. Simion, V.S. Teodorescu, N. Barsan, U. Weimar, Synthesis, mechanism, and gas-sensing application of surfactant tailored tungsten oxide nanostructures, Adv. Funct. Mater. 19 (2009) 1767–1774, http://dx.doi.org/10.1002/adfm.200801171.

[18] C. Berthold, A. Bjeoumikhov, L. Bruegemann, Fast XRD^2 microdiffraction with focusing X-Ray microlenses, Part. Part. Syst. Charact. 26 (2009) 107–111, http://dx.doi.org/10.1002/ppsc.200800038.

[19] H. Zheng, J.Z. Ou, M.S. Strano, R.B. Kaner, A. Mitchell, K. Kalantar-Zadeh, Nanostructured tungsten oxide – Properties, synthesis, and applications, Adv. Funct. Mater. 21 (2011) 2175–2196, http://dx.doi.org/10.1002/adfm.201002477.

[20] M. Hübner, C.E. Simion, A. Haensch, N. Barsan, U. Weimar, CO sensing mechanism with WO_3 based gas sensors, Sens. Actuators B Chem. 151 (2010) 103–106, http://dx.doi.org/10.1016/j.snb.2010.09.040.

[21] M.A. Vuurman, D.J. Stufkens, A. Oskam, G. Deo, I.E. Wachs, Combined raman and IR study of MOx-V_2O_5/Al_2O_3(MOx = MoO_3, WO_3, NiO, CoO) catalysts under dehydrated conditions, J. Chem. Soc. Faraday Trans. 92 (1996) 3259, http://dx.doi.org/10.1039/ft9969203259.

[22] S.M. Kanan, Z. Lu, J.K. Cox, G. Bernhardt, C.P. Tripp, Identification of surface sites on monoclinic WO_3 powders by infrared spectroscopy, Langmuir 18 (2002) 1707–1712, http://dx.doi.org/10.1021/la011428u.

[23] G. Ramis, G. Busca, C. Cristiani, L. Lietti, P. Forzatti, F. Bregani, Characterization of tungsta-titania catalysts, Langmuir 8 (1992) 1744–1749, http://dx.doi.org/10.1021/la00043a010.

[24] T. Akamatsu, T. Itoh, N. Izu, W. Shin, NO and NO_2 sensing properties of WO3 and Co3O4 based gas sensors, Sensors (Basel) 13 (2013) 12467–12481, http://dx.doi.org/10.3390/s130912467.

[25] S.L. Baumann bei Einsatz in Verbrennungsabgasen (2003).

Biographies

Anna Staerz received her master's degree in Chemistry at the University of Tuebingen in 2015. She is currently a Ph.D. student at the Institute of Physical Chemistry at the University of Tuebingen.

Christoph Berthold received his diploma in Mineralogy in 1991 and in 1997 his Dr. rer. nat. at the Faculty in Geoscience of the University of Tuebingen. Since 1993 he works as scientific assistant and since 2000 as senior researcher in the Applied Mineralogy Group of Prof. K.G. Nickel at the University of Tuebingen.

Tamara Russ is enrolled in the chemistry master's program at the University of Tuebingen.

Susanne Wicker received her diploma in Chemistry at the University of Tuebingen in 2013. Since then, she has been a Ph.D. student at the Institute of Physical Chemistry at the University of Tuebingen. Her work is in the field of metal oxide gas sensors.

Udo Weimar received his diploma in physics in 1989, his PhD in chemistry in 1993 and his Habilitation in 2002 from the University of Tuebingen. Since 2010, he is a full professor in the Department of Chemistry at the University of Tuebingen. His research interest focuses on chemical sensors as well as on multicomponent analysis and pattern recognition.

Nicolae Barsan received his diploma in Physics from the Faculty of Physics of the Bucharest University in 1982. In 1993 he received his Ph.D. in Solid State Physics from the Institute of Atomic Physics, Bucharest, Romania. Since 1995 he has been a senior researcher at the Institute of Physical Chemistry of the University of Tuebingen, where he and Udo Weimar lead the Gas Sensors Group.